Transfer and Characterisation of Graphene for Integration with Gaseous Electron Multipliers

Thuong Thuong Nguyen
London Centre for Nanotechnology
Electronic and Electrical Engineering

University College London

Thesis submitted for the degree of Doctor of Philosophy (PhD)

2015

Abstract

Graphene is the latest material to join the large family generated by the high versatility of carbon. Building on the extensive knowledge and large research of its predecessors, graphene has proven to be of a higher potential due to the versatility of its applications. Its most promising properties, a very good electrical conductivity, its two-dimensional nature, combined with its in-plane strength makes it a very good candidate for integration as a membrane in existing electronics. The latter is an important criterion as it allows potential electronic data collection, a technique widely necessary in current technologies.

In high-energy physics, the quality of the detection setup is critical to identification of the particles. The gaseous electron multiplier (GEM), a particle detector derived from the multi-wire proportional chamber for which the Nobel Prize was awarded in 1992 is one of the current technologies in use in CERN. Although the GEM currently boosts one of the best quality signal detection, ions produced in the avalanche process have been flowing back into conversion regions of the detector, interfering with the low signals in that section. As a result of this interference, the amplified signals from the particles detected, suffer from induced noise. To remedy to this, this work has overseen the integration of graphene to the device between the amplification and the conversion regions. Due to the thinness of graphene, electrons are expected to flow through it, while ions, of much larger size, are expected to be blocked by the layer. This would make graphene an ideal membrane to prevent ion backflow, while keeping the disturbance of the electron signal to a minimum.

In this work, graphene production and integration methods were investigated, and a suitable transfer method was developed for the incorporation of the material into the existing GEMs. The results were the successful transfer of high quality graphene across holes of up to 70 µm, a step up from the 5 µm achieved by previous existing techniques in literature. The integrated layers were then tested within custom built setups in order to insure compatibility and measure graphene transmission properties. This work included a systematic characterisation and optimisation of all parameters

to be monitored for the new setups. The properties of graphene were then tested under low electric field configurations in order to avoid potential damage. Results showed the resilience of graphene in low fields, repeatability and the isolation of a field dependence effect which was attributed to field focusing. Secondly, while aiming to improve the electron yield through graphene, the layers were tested in high field conditions. The experiments revealed the possibility of induced permanent damage in the event of high frequency of discharges but a very good resilience of graphene under normal operating conditions. In order to achieve larger coverage, bilayer and trilayer graphene were also tested alongside monolayers. The latter were found to have to low coverage to distinguish field focusing from actual transmission, trilayers were found to be opaque to ions but also to electrons. Finally, bilayers were also found to be opaque to ions as expected, but showed a variable positive electron transmission, a very promising result towards the integration of graphene in GEMs.

Declaration

I, Thuong Thuong Nguyen confirm that the work presented in this thesis is my own. Where information has been derived from other sources, I confirm that this has been indicated in the thesis.

London,

Acknowledgements

First of all, I would like to thank Professor Richard B. Jackman for giving me the opportunity to work on this project. I would also like to thank him for his support and for entrusting me with a large freedom, which has had ups and downs but allowed me to grow during these past four years. As importantly, I would like to acknowledge Professor Glenn Tyrell and Applied Scintillation Technologies Ltd (now Scintacor Ltd) for their sponsorship, without which this work would not have been possible.

I wanted to address sincere thanks to all the IT and administration staff for their time. I would like to thank Steve Etienne, Vijay Krishnan, Dr. Suguo Huo, Dr. Richard Thorogate, Dr. Steve Hudziak and the cleanroom staff for their patience and help with equipment. I am especially thankful to Mark Turmaine, whose expertise, and volunteer help have been invaluable. I would like to thank Prof. Lescek Ropelewski and his research group in CERN: Silvia Franchino, Diego Gonzalez, Rui de Oliveira, Eraldo Oliveri, Filippo Resnati, Patrik Thuiner, and Miranda Van Stenis for the lunch breaks, many coffee breaks, and the hard (but successful) work during my visits in CERN.

I am equally grateful to all the people from the LCN that I have spent time with during daytime and late night lab work, conferences and climbing sessions. I would like to thank all the present DEGs: Abdul Afandi, Suguru Amakubo, Steven Evans, Mo Golsharifi, Marie Hicks, Ralph Moors, Alex Pakpour, Will Parfitt, Alice Taylor, Joe Welch for all the conferences, QPs and lunch times. I would also like to acknowledge past DEGs such as Aysha Chaudhary, Carolina Parada, Joe Smith, Niall Tumilty, Fang Zhao and especially Rob Edgington for all his useful advice.

I would like to thank Arnaud Blois, Phil Crowley, Ivan Isakov, Henry Montagu, Marion Sourribes, Dr. Ed Romans and Prof. Paul Warbuton and their group for the fun times during various trips and events. I am also grateful to Abu Adan for the write-up sessions, Nick Constantino and Gregor Hannappel for their feedback, and also Nuno Braz for his late night EBL sessions, and the (much needed) coffee breaks from the library.

Finally I would like to thank my family and friends who have supported me during these four years, especially Vlad, Saad, Grace, Oana, and Cyrille.

Contents

List of Figures

Acronyms

AFM atomic force microscopy. 45–48, 50, 51, 79–83, 161

BSE back-scattered electron. 40

CERN Centre Europeen pour la Recherche Nucleaire. 16, 25, 60, 88

CVD chemical vapour deposition. 7, 12, 30, 35, 58

DI deionised. 36, 59, 60, 62

EBL electron beam lithography. 31

ET Everhart-Thornley. 41

FWHM full width at half maximum. 78, 83–85

GEM gaseous electron detector. 25, 26, 87, 88, 90, 111, 140

HDMS hexadimethylsilazane. 33

HOPG highly ordered pyrolitic graphite. 58

IBF ion backflow. 28, 29

IPA isopropyl alcohol. 60, 62

IR infrared. 34, 44

LHC large hadron collider. 16

LOR lift-off resist. 34

NMP n-methyl-2-pyrrolidone. 34

PDMS polydimethylsiloxane. 36, 58

PMGI polydimethylglutarimide. 34

PMMA poly(methyl methacrylate). 35, 36, 58–70, 162

PVD physical vapour deposition. 30

QCM quartz crystal microbalance. 31

RIE reactive ion etching. 34

SE secondary electron. 41

SEM scanning electron microscope. 36, 65, 67, 68, 70–74, 81, 83, 126, 147, 161, 164

TMAH tetramethylammoniumhydroxide. 34

UV ultraviolet. 31–34, 88, 120

vdW van der Waals. 11

WD working distance. 70

Chapter 1

Introduction to Graphene

1.1 Carbon Allotropes

In the current race to harness all the aspects of the emerging field of nanotechnology, one element has been attracting worldwide attention. The fourth most abundant element in our galaxy after hydrogen, helium and oxygen is carbon. It is the most versatile material out of the four due to the diversity of bonds it can form. Quantum mechanics states that the electrons in carbon should be arranged in the following orbitals 1s, 2s, 2px, 2py, 2pz with 2 electrons in the 1s orbital. The lower state 2s should also have two electrons and the remaining two electrons can occupy interchangeably any of the 2p orbitals. However the energy required in order to move a 2s electron to a free 2p state is higher than the energy released by the formation of a bond. This leads to the electrons in the 2s state being more stable within bonds. This effect is called hybridisation of the s and p orbitals. According to hybridisation theory, the orbitals can hybridise into sp, sp^2 and sp^3.

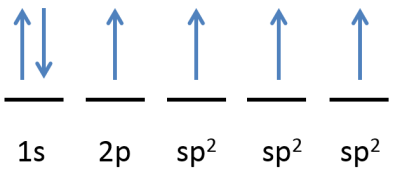

Figure 1.1: Diagram showing the electron distribution in the sp^2 hybridisation: the full 1s orbital and the 2p, sp^2, sp^2, sp^2 states.

The diagram above illustrates an example of sp^2 hybridisation. Similarly, sp^3 has 1s, sp^3, sp^3, sp^3, sp^3 states, and sp has 1s, 2p, 2p, sp, sp states. This leads to the formation of single bonds (sp^3), double bonds (sp^2) and triple bonds (sp) between carbon atoms, the combination of which leads to very diverse chemical structures. A pure network of sp^3 bonds between the carbon atoms can exist, such network results in tetrahedral structures (such as in methane) called diamond. On the other hand, an amorphous mix of sp^2 and sp^3 carbon is called diamond-like carbon.

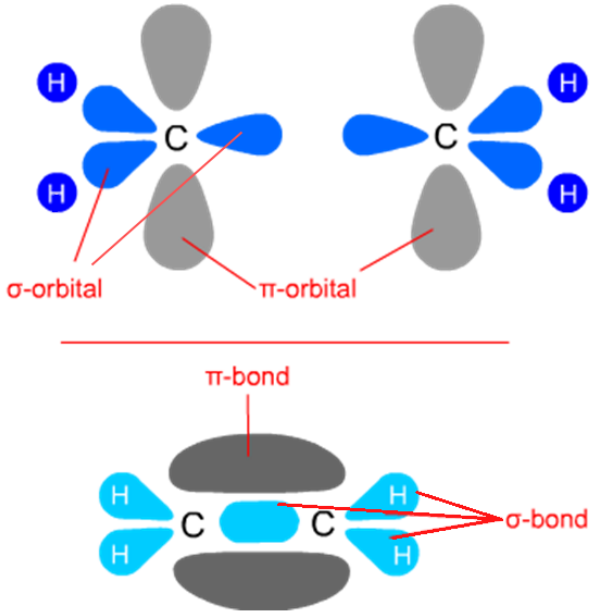

Figure 1.2: Diagram of two sp^2 hybridised molecules above, then at the bottom, the combination of the two σ bonds into a double bond, and the bonding of the π orbitals into π bonds, forming a C_2H_4 molecule.

The sp^2 form of carbon, which is the one of interest in this work, is called graphite. In this form, the 3 sp^2 electrons are bonded together in a plane into "sigma (σ) bonds" and the remaining 2p orbital bonds above and below to other planes of sp^2 networks as shown in Figure 1.2. These 2p-2p bonds are called "π bonds" and are weaker than the σ bonds. This makes the material more brittle along the planes.

One could break up the π bonds of graphite to isolate each plane of sp^2 networks from the others, such an isolated 2D surface would be called graphene. This plane has been produced for more than 400 years allegedly from simple writing with graphite pencils. However, it wasn't until 2004 that the material was formally investigated

and isolated as a free standing 2D layer, with its physical properties by Konstantin Novoselov and Andre Geim [1]. This plane can also be rolled up into a tube or a ball, which are named carbon nanotubes and fullerenes respectively. Carbon can therefore take a wide range of shapes (the most common crystalline forms known are summarised in Figure 1.3). However, out of all these materials, graphene has been the most widely researched one in the past decade since its discovery with a record number of patents and publications.

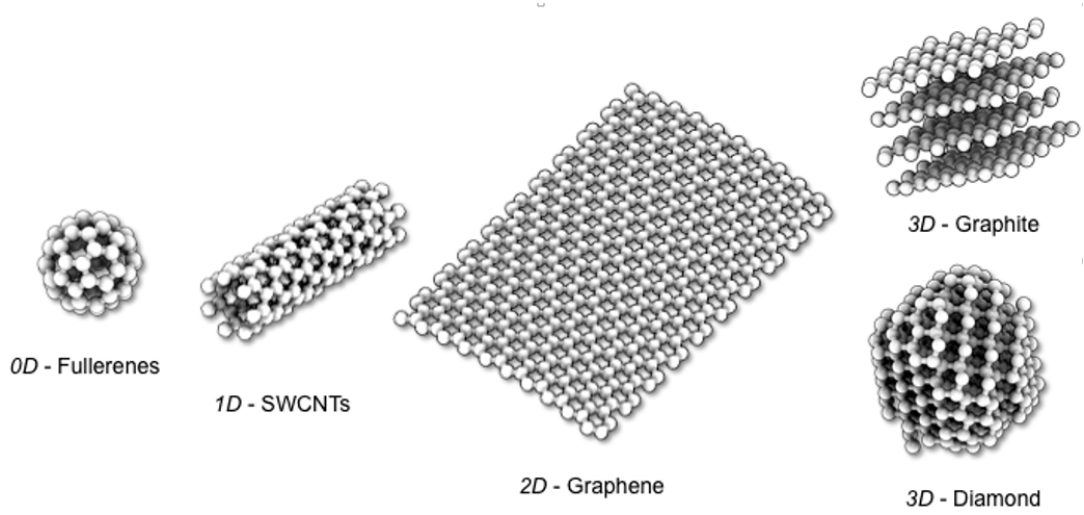

Figure 1.3: Some examples of carbon allotropes spanning many dimensions from 0D fullerenes to 3D diamond (Credit: Italian national research council)

The term "graphene" has now been widely used to describe any form of two-dimensional carbon material, which unit cell is a hexagon formed of six carbon atoms arranged at each corner of the hexagon. These forms of graphene can span from a multilayer, multi-domain meter-sized graphene plane to flakes of nano-size single-layer graphene dispersed in a solution. As described previously, the main feature of graphene over sp^2 forms of carbon, which have been praised worldwide for its durability and exception capabilities, are the dangling π-bonds perpendicular to the plane of the material.

These π-bonds make graphene very sensitive to any surface or molecule it comes into contact with. As a result, graphene is readily available to functionalisation, but also very tunable by modifying its substrate. These π-bonds can also be seen as delocalised electrons readily available as carriers for transport and therefore make

graphene a material with outstanding properties.

Before discussing the properties of graphene in further detail, it is important to introduce the fabrication, production and integration methods of graphene in applications or experiments. As the graphene family encompasses a wide umbrella of extremely thin carbon materials with a honeycomb structure, its properties are therefore strongly influenced by its origins, and therefore are indissociable from them.

1.2 Fabrication and Production of Graphene

Here the current fabrication and production methods of graphene will be briefly reviewed. The literature on the subject is extensive and the most relevant publications will be discussed but the following references are recommended for further reading: [2–4].

The very first method discovered to produce graphene was mechanical exfoliation from graphite using scotch tape [1]. The tape could then be subsequently dissolved away in a solution to obtain solutions of graphene flakes or the tape could be applied directly onto a substrate as shown in Figure 1.4 a). This method has had the advantage of producing the best known quality of graphene to date, with the suspended version of exfoliated graphene reaching mobilities up to 200 000 cm^2 V^{-1} s^{-1} [5]. On the other hand, this method had the clear drawbacks that it could not be scaled industrially, and that the layers of graphene obtained this way could only be of limited sizes and of random shapes.

Based on this pioneering method, a few more controlled techniques have been naturally developped to source graphene from the exfoliation of high quality graphite. One of them for example, is liquid exfoliation [6] shown in Figure 1.4 d). Such method involves dispersion of thin graphite into a liquid solution, which affects the bonds between the layers. Ultrasonification then separates the layers into a graphene flakes suspension. The most obvious advantage of this procedure is the possibility to create very large amounts of graphene. Unfortunately the graphene flakes produced tend to be multilayer and only yield 28 % [6] of monolayer. Additionally the layers obtained contain high amounts of chemical residues (10 %), are small in size (hundreds of nm) and can contain curved or distorted layers.

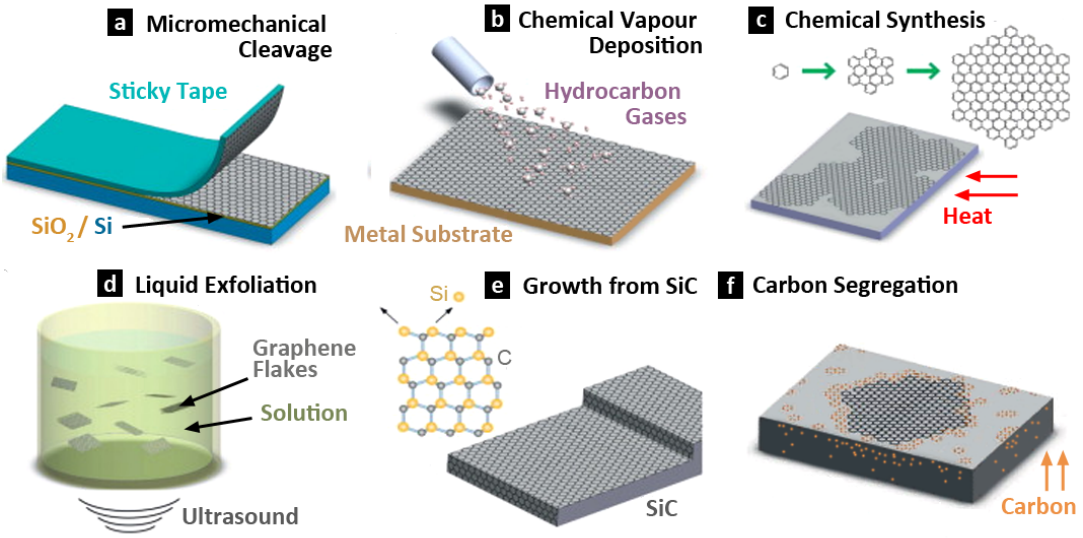

Figure 1.4: Schematic diagram of fabrication methods discussed here: a) the original exfoliation method of graphene from graphite then application onto an SiO_2/Si substrate, b) the deposition of graphene onto metallic substrate from gas precursors, c) the chemical bottom-up assembly from polycyclic carbons, d) exfoliation of graphite in a liquid environment, e) the evaporation of Si from SiC to form a layer of graphene and f) the solubilisation of carbon into a metallic substrate then the subsequent precipitation of the carbon to the surface (adapted from reference [3]).

Graphene can also be produced from the reduction of graphite oxide [7]. Graphite is oxidised using a mixture of H_2SO_4, $NaNO_3$, $KMnO_4$ (Hummers method). The graphite oxide is then exposed to dialysis and ultrasonicated to separate the graphite oxide into graphene oxide sheets. The sheets are then reduced using a solution of water, ammonium and hydrazine (N_2H_4) which gives a suspension of graphene sheets which are then filtered out. Similarly to the two previous methods, the graphene produced is small in size and also contains a high amount of oxygen (about 10 %). A reported way of reducing the amount of oxygen in the graphene is to apply an electric arc between two graphite electrodes in the solution of graphite oxide, reducing the oxygen to about 6 to 7 % [8]. These previous methods tend to produce graphene flakes, or graphene powders, a name used depending on the size and shape of the graphene pieces generated.

Another material from which to produce graphene, would be silicon carbide (SiC) [9–11]: upon heating of SiC (around 1100°C − 1600°C), the silicon desorbs, leaving

behind a graphene layer as illustrated in Figure 1.4 e). This method can also produce large amounts of graphene with large areas that depend on the size of and quality the SiC substrate. The graphene made is generally of good quality and the number of layers can be controlled by changing exposure time and temperature conditions. Unfortunalely, high prices of SiC means large scale production is difficult. Additionally, the graphene is not easily detachable from the SiC substrate, making it unsuitable for further applications.

An interesting method of production is the assembly of graphene by chemical methods [12, 13]: polycyclic hydrocarbons can be dispersed onto a substrate as shown in Figure 1.4 c); and upon a series of step-by-step controlled thermal annealing processes, these precursors can be assembled in a bottom-up fashion due to surface chemical reactions. The graphene produced with this method however is termed "nano-graphene" due to the small size of the units produced (nanoribbons and dots).

The most widely used source of large-area graphene production nowadays lies in the decomposition of gaseous precursors containing carbon, onto substrates with low carbon solubility [14–20]. The most commonly used technique consists in chemical vapour deposition (CVD) of graphene onto polycrystalline copper, shown in Figure 1.4 b). The crystallinity and orientation of the supporting materials have been shown to yield very different qualities of graphene depending on various physical properties of the substrate: for example lattice matching, strain, thermal expansion etc. [17, 21–24]. However polycrystalline copper is the cheapest material which can be used to produce large areas of monolayer graphene, albeit with small crystal grain sizes of a few micrometers on average, with reported grain sizes up to cm size if growth condition are precisely controlled ([15]: largest grain sizes obtained with synthesized graphene). However where monolayer properties are preferred over high electronic performance, this growth method proves cheap, scalable and versatile. Indeed, if the precursors, substrates and conditions are well controlled, flakes and multilayers can also be produced [17, 25].

Finally, after mentioning the low carbon solubility substrates, a method of producing disordered graphene also exists through the solubilisation of a carbon containing material (this can be a solid source such as a polymer [26], or a gas [27]) into a high

solubility substrate at high temperatures [28–30]. Upon cooling, the solubility of carbon will decrease, and the material releases its carbon content to its surface producing graphene as shown in Figure 1.4 f). This method called segregation or precipitation of graphene, can be used to produce large areas layers. However, these are highly disordered and are of a highly varying number of layers when compared to the low solubility substrates. Molecular beam epitaxy also produces layer of similar quality to segregated graphene due to the lack of control of the number of layers [31].

Other methods also exist but do not produce the quality, quantity or type of graphene required for this work but can be found in the reviews cited earlier.

1.3 Integration of Techniques for Graphene

Due to the varied ways of producing graphene and as a result, the many shapes and forms graphene can take, its integration in applications requires a large range of methods. Unfortunately, as discussed previously, graphene cannot be produced directly on any non-metallic substrates and is fabricated preferentially on metallic substrates. For this reason, its integration often constitutes an additional necessary step towards a final application.

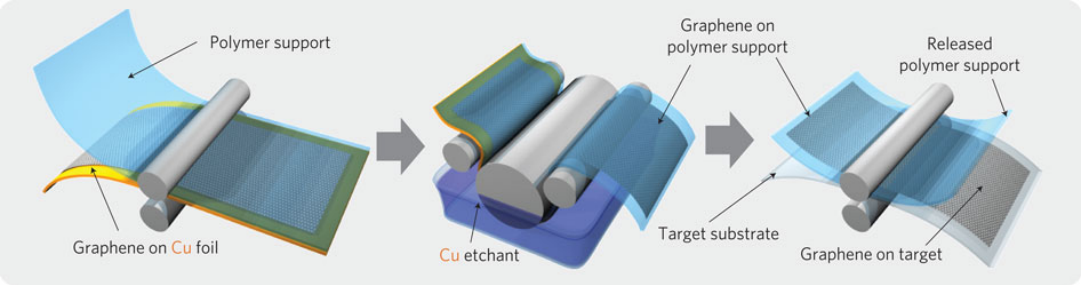

Figure 1.5: Illustration of the rolling method used to transfer graphene, adapted from reference [32].

Graphene flakes and powders (i.e. small sizes of graphene) can simply be sonicated into solutions or mixed with other powders. This type of graphene is generally used as an alloy for industrial applications to produce stronger and lighter composites, for coatings, as a bulk material or even in metallic inks for circuit printing [33, 34]. A more interesting way of integrating graphene flakes is anodic bonding [35]: graphite is pressed against the destination substrate: an insulating heated piece of glass at 200°C

and the subsequent application of voltages between 0.5 kV and 2 kV causes some flakes of graphene to stick to the charged glass via electrostatic interaction.

For larger layers of graphene, the first method developed, briefly mentioned in the previous section, was simply to take very thin sheets of graphene and mechanically 'applying' the layers onto the desired substrates. In fact due to the relatively weak Van der Waals forces holding the graphene against its supporting substrates, as well as dangling π bonds, the layers tend to adhere easily to surfaces.

Presently, the most widely used method [36, 37] to transfer graphene exploits this property directly. The graphene is grown on a substrate, and then coated with a flexible polymer layer via spin-coating and curing. The original support is then dissolved away by wet etching. This leaves behind graphene on the polymer. The graphene side is then adhered onto the destination substrate and the polymer is dissolved away leaving graphene. The details of this method will be explained further in Section 3.3. The main drawback of this technique is the remaining polymer residues after dissolution, and the damage from mechanical manipulation.

A solution to this was provided by changing the flexible polymer for a solid polymer [38] and the subsequent "stamping" of graphene method which avoids the polymer dissolution. A "self release" intermediate method using mechanical detachment was also suggested [39], and various thermal annealing methods [40–42] to reduce the polymer remaining. Alternatives to the etching of the original substrate exists and consists in the intercalation of bubbles between the graphene and the substrate [43] or the creating of capillary bridges between them [44]. These techniques allow higher flexibility in the selection of the original growth substrate but still rely on the use of a flexible polymer and are therefore still subject to residues. Finally a larger-scale version [32] of this method was developed by "rolling" a solid polymer onto the growth substrate, adhering the graphene with the polymer and then re-rolling them onto the destination support as illustrated in Figure 1.5. The obvious advantage of this techniques was the high scalability, but the mechanical application of graphene onto the new substrate meant that repeated rolling is needed to achieve large areas.

We follow this section on integration with a discussion of the resulting properties of the graphene produced.

1.4 Graphene Property: Ion Impermeability

The most interesting property of this carbon layer of interest for this work is its selective permeability. Graphene, despite being formed from a layer of single atoms, is very mechanically resistant in the plane of the lattice due to its aromatic rings with strong delocalised double bonds. These same bonds also allow, to a lesser extent, high mechanical stability in the direction orthogonal to its lattice. The two-dimensional (2D) yield strength was measured [45] in 2008 to be $42\,\mathrm{N.m^{-1}}$ for a defect-free layer. Similarly the Young's modulus was found [45] to be about $1.0 \pm 0.1\,\mathrm{TPa}$ as opposed to 200 GPa as for alloyed steels [46] for example. This value is comparable to that of diamond: 1.2 TPa, one of the stiffest materials measured. These remarkable mechanical properties allow resistance to large molecules up to certain pressures, despite the atomic thickness of graphene. This property is commonly observed [47] when transferring graphene onto metals, providing observable protection against the oxidation of the underlying substrate in air up to 400°C.

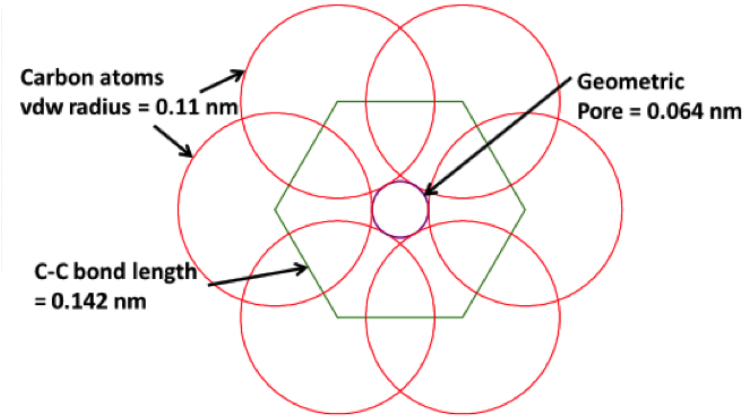

Figure 1.6: Diagram showing the effective pore size of an aromatic ring in graphene, the bond length between the carbons and the van der Waals (VDW) radius of the atoms.

In addition to this resistance to large molecules, graphene also shows impermeability to small ions and atoms. This property arises from its structure which consists in aromatic rings arranged in a honeycomb lattice. The hexagonal ring has a bond length of 0.142 nm and therefore an inner radius [48] of 0.246 nm. Although this is relatively large, the π bonds orthogonal to the lattice can be seen as a delocalised

cloud of electrons which overlaps the hole in the hexagon. This reduces the opening pore to be significantly smaller, yielding an effective diameter of 0.064 nm. This is significantly smaller than the van der Waals (vdW) radius of most atoms, some of the smallest ones for instance being helium with 0.28 nm and hydrogen with 0.314 nm. The pi-bonds therefore should allow impermeability to atoms, molecules and ions assuming they do not have enough energy to go through the electron cloud. Experimentally, suspended graphene has been measured to withstand an irradiation dose up to approximately 1016 ions/cm^2 at tens of keV energies [49]. Similar experiments have shown that graphene is completely impermeable to helium atoms up to 6 atm [50].

On the other hand, suspended graphene has been shown to exhibit high transparency to electrons using transmission electron microscopes with energies ranging from tens of keV up to 300 keV [51, 52]. Although this electron permeability has been shown at high electron energies, its interaction with incoming low energy electrons (i.e.: below 10 eV) has not yet been studied. The next section will now describe the electrical properties of graphene, which will be used in this work along with its permeability.

1.5 Electrical Properties and Electron Permeability

The most remarkable property of graphene is without doubt, its atomic thickness. Such materials have been investigated theoretically for a long time but the existence of such a thin, free-standing layer was thought to be impossible until the discovery of graphene. This thinness allows confinement of charge transport along a two dimensional plane and has given rise to very peculiar physical effects.

1.5.1 General Electrical Properties

The computed dispersion relation of pure infinite graphene was originally computed by Wallace [53] in 1947 as a unit of study for graphite and predicts the 2D structure was a zero bandgap semimetal, with a linear dispersion dispersion about the K point of symmetry. Such linearity gives rises to classically massless charge carriers also called Dirac fermions. Due to their effective absence of mass, their mobilities have been shown able to reach incredibly high values up to 200 000 cm^2 V^{-1} s^{-1} for suspended

layers [5]. This mobility value was obtained at around 5 K and at a carrier density of 2×10^{11} cm^{-2}, the intrinsic carrier density of graphene [1], but is also expected to be true for a large range of carrier densities and were expected to be even higher if defect-free suspended graphene could be successfully produced [54].

However due to the lack of systematic method for the production and integration of graphene as discussed previously, this value is usually measured to be between 2 000 cm^2 V^{-1} s^{-1} and 15 000 cm^2 V^{-1} s^{-1} for adhered graphene [55]. These large numbers illustrate the deterioration of the properties of graphene in the presence of a substrate. It is also important to discuss the effects of structural defects on the properties of graphene: regarding this subject, induced periodic defects such as the tailoring of consistent armchair or zigzag edges can improve some properties of graphene either by further confinement (such as nanoribbons [12]). Similarly, induced periodic patterns of defects can be used to improve the mechanical properties of graphene [56] or decrease it in the case of sp^3 type of defects [57].

In this work the graphene used was grown by CVD technique and therefore exhibits non negligible grain boundaries [17], but very little structural defects (as characterised later in this work). These grain boundaries have been shown to weaken the transverse mechanical resistance of suspended graphene, but only on a small scale relative to the large strength of graphene [58, 59]. Additionally the grain were shown to slightly deteriorate their mobility while supported on a substrate (mobilities around $10^3 - 10^4$ cm^{2}V^{-1}s^{-1} were obtained for individual inter-grain transport [17]). Although there has been a lot of work on suspended graphene, most suspended grain boundary work focus their effort on TEM and AFM, and do their transport measurement on supported graphene [23, 60–62]. However, from the figures, it is expected that the exceptional properties of the layer could be deteriorated but only by an amount which is negligible compared to the large numbers.

1.5.2 Graphite Properties and Transverse Transport

Although the electrical conductivity of the layer was a necessary criteria for choosing graphene in the application discussed in this work, this property has been well investigated enough that no extra work was necessary to show its semimetallic behaviour.

The main scope of this work was the investigation of graphene as a membrane for trans-diffusion of low energy (below 10 eV) electrons across it. Hence the other critical property of graphene for this work was the transverse electron transmission of graphene at this energy range. Most of the research on graphene transport has been on in-plane effects due to the exceptional capabilities in that direction and tunnelling experiments involving graphene have mainly been focused on the looking at in-plane tunnelling [63, 64].

On the other hand, transverse transport has had very little coverage and although a very large amount of literature exists of transmission electron microscopy of graphene, such experiments are conducted at energies in keV. Here the limited literature which does exist on low energy transport is discussed.

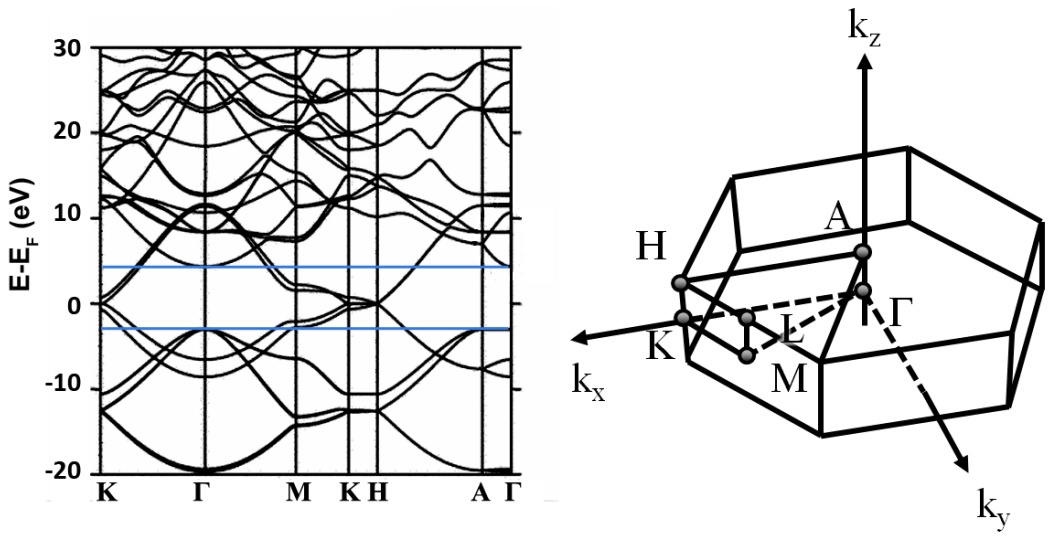

Figure 1.7: Dispersion relation of graphite between points of high symmetry (adapted from reference: [65]) and the corresponding lattice in K-space. The blue lines indicate the bandgap at the Γ point.

Most experimental data using low energy electrons were obtained in vacuum using a modified low energy electron diffraction (LEED) method but show conflicting results, indicating either transmission or the opposite effect: reflection and in some studies, a mix of both effects. Not only the effects observed were different, but the works indicating both effects did not match over varying energy ranges [66–69]. The common point found in most works was that each seemed to agree that electron transmission

below 1 eV does not occur or is very weak, above that, electrons then experience a transmission local maximum which could be located anywhere up to 20 eV. Above that value, the transmission drops again then starts rising steadily after much larger values. Unfortunately the precise value of such local maximum was found experimentally and theoretically to range everywhere between 1 and 20 eV, with varying widths. For instance a work which has focused on developing an electron transparent graphene window has also predicted a maximum graphene transparency around 1-2 eV while the transparency decreases until 100 eV and goes up at high values beyond this [70].

A work which has had a different approach [71], has interpreted transverse electron transmission as electron transport and considered the dispersion relation of graphite rather than that of graphene. This is one of the two mechanisms of transmission possible for transverse electron, the other being transverse tunnelling. The idea of electron transport perpendicular to the layer would only be a rough approximation valid for multilayer graphene, i.e. bilayer or trilayer graphene in this work. The mapped out band structure of graphite is shown in Figure 1.7 along high symmetry points, which are labelled in a diagram of the reciprocal lattice of graphite. The reciprocal lattice of multilayer graphene is very similar to that of graphite, only with some local variations of the order of a few eV depending on stacking orientation of layers [72]. However for simplicity, the band structure of graphite will be considered here (while keeping in mind there may be variations to be expected).

The points of interest in this discussion are the ones lying along k_z: Γ and A and the mapping between them as shown in the figure. At A, a large bandgap of almost 10 eV appears, while the gap becomes smaller at Γ where it is about 6-7 eV. This is very promising and indicates that if transport is concerned, electrons could transmit through graphene above 7 eV, assuming they are incident perfectly normal to it. This latter consideration is very promising because in the application discussed in this work, the electrons are incident with momentum from random directions, meaning the whole band structure could be explored and not only the region between Γ and A.

The other possible effect which could be responsible for electron transmission across graphene is tunnelling. Assuming the graphene as a finite potential barrier

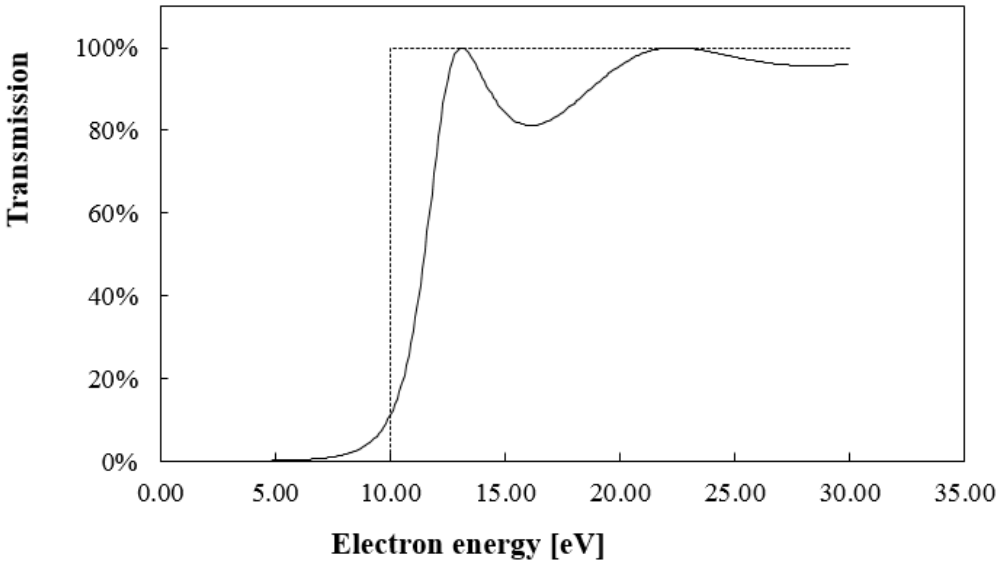

Figure 1.8: Simulation of the transmission probability of an electron through graphene if modelled as a potential barrier with dimensions L = 0.35 nm and U = 10 eV, calculated using [73]. The dashed line indicates tunnelling barrier energy.

of height U and of length L, basic quantum mechanics dictates that the probabillity that a particle of kinetic energy E and mass m, incident on the barrier will transmit through the barrier is given by:

$$T = e^{-2kL}, k = \frac{\sqrt{2m(U-E)}}{\hbar} \tag{1.1}$$

This implies that for a fixed barrier height and length, the higher the energy of the electron, the higher its probability of transmission through it. The electrons used were of energy between 0.1 eV and 10 eV depending on the setup, the energy of the bandgap was about 10 eV or lower as discussed above, and the effective thickness of monolayer graphene is $t = 0.35$ nm. Given this data, a graph of the transmission probability was plotted as a function of energy [73]. The probability of transmission below the barrier height is low but still sizeable and roughly 10 % of electrons of 10 eV may be expected to tunnel through for instance. This gives us an idea of what we can expect in terms of results.

After this introduction to graphene, its fabrication, processing and its most relevant properties, particle detectors will now be introduced.

Chapter 2

Introduction to GEM detectors

2.1 A Brief Introduction to Particle Detectors

The large hadron collider (LHC) at the Centre Europeen pour la Recherche Nucleaire (CERN) hosts seven different experiments in which various types of detectors are used to identify and analyse particles generated from collisions. These detectors are wrapped in a cylindrical shape around collision points as shown in a quarter cross-section diagram in Figure 2.1. Detectors can be divided into three categories depending on their position in the experiment and on their function: the innermost ones are tracking devices destined to detect the presence and path of charged particles. These are then surrounded by calorimeters, which will absorb and determine the energy of the particles through the radiation emitted by the absorption process. The outermost layer consists of spectrometers and is generally used to identify particles (muons for example) which have not been identified by the previous devices.

The detectors used in most of these layers share the sample principles: they are all based on the fact that a particle or radiation traversing a medium will transmit some energy to it. The medium is therefore chosen depending on the particle to be detected. For example if a photon with high enough energy passes through a chamber filled with a gas, the gas molecules can be ionised by the energy loss of the photon. The electrons resulting from the interaction then need to be collected in order to analyse them. To do so, they are subjected to a high voltage, which accelerates them towards an anode. They are collected there in the form of an electric current, which can

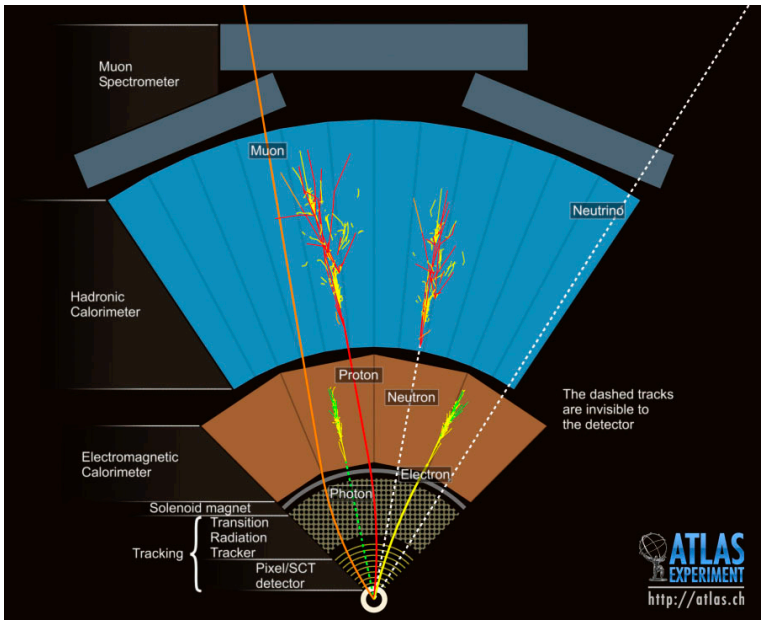

Figure 2.1: Illustration of detection principles inside CERN experiments showing the various layers required to detect different type of particles (credit: ATLAS experiment at CERN).

subsequently be analysed. Additionally, because of the rarity of the energy transfer events, as well as the small energy transferred, all detectors are also equipped with electron amplification steps.

The first crude 'particle detector' was developed by Rutherford and Geiger in 1908 [74], during a period of pioneering discoveries on light and the atom. Indeed X-rays had only been discovered in 1895 by Röntgen, and Rutherford would develop his model of the atom a few years later in 1911.

That detector was then be refined in 1928 by Geiger and Müller, into the now famously used 'Geiger counter' for the measurement of ionising particles. It originally consisted of a tube filled with an inert gas with a wire passing through the middle. A voltage of about 100 V was applied between the wire and the external tube. Due to the concentric geometry of the the tube, the electric field will have a higher field line density towards the wire than on the outside of the tube as shown in Figure 2.2 a). The increase in the density of field lines will not only cause a charged particle of the right polarity to be accelerated towards the centre of the tube (i.e. its kinetic energy to increase), but it will also cause the density of electrons to be larger closer to the

anode. The first effect combined with the second one, lead to an very high collision cross-section overall, which leads to an electron avalanche as illustrated in b), and therefore amplification of the initial electron signal.

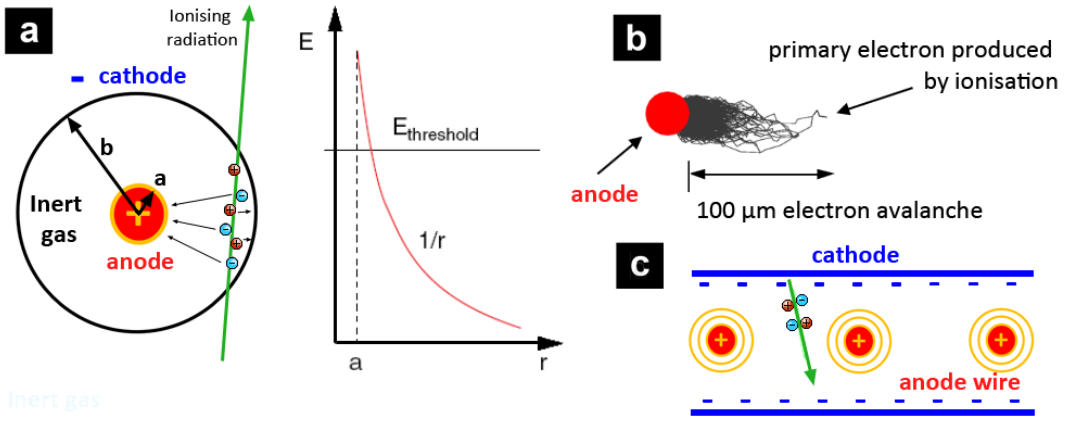

Figure 2.2: a) Diagram of the working principle of the Geiger-Müller counter, showing a cross-section of the counter on the left, and a graph of the electric field as a function of distance r from the centre of the tube. b) Illustration the avalanche process following a primary electron ionisation. c) Cross-sectional diagram of the multi-wire proportional chamber.

Since then, various types of detectors have been developed to measure different properties of radiation but mostly relied on photographic methods. George Charpak received the Nobel prize in 1992 for the development multi-wire proportional chamber (MWPC) in 1968 [75], the first chamber incorporating electronic processing, thus allowing for mass data collecting and subsequent automation of data analysis. This chamber consists of a series of wires running through a chamber filled with a gas as shown in Figure 2.2 c). The surrounding walls are grounded. When incoming radiation ionises the gas in the chamber, the resulting charges get collected by the wires as an electrical signal. The critical difference between these wires and the Geiger counter discussed previously, was that the diameter of the wires was reduced from a centimetre to a few millimetres, with the incorporation of electronic amplifiers on each of them, allowing for operation at lower voltages in the proportional regime. This regime and its significance will now be discussed.

2.2 Proportional Counters

Detectors can be classified by their operating regime. Figure 2.3, shows the trend of a typical experimental graph of the dependence of current collected from the detector as a function of applied voltage across it. The graph assumes a given fixed source of radiation with a constant rate.

When the voltage is increased slightly from zero, the electric field resulting from the applied voltage in the chamber is not enough to prevent the ionised molecules from recombining with their electrons before reaching the electrodes. As the voltage is increased, the recombination processes are gradually overcome, and the amount of current collected increases steadily. The current measured will then rise until no more recombination occurs and all electron-ion pairs in the chamber are detected. As the rate of the radiation source is fixed, then the current will finally reach a saturation maximum no matter how much the voltage is increased. This current is directly equivalent to the amount of electrons generated by the radiation source losing energy to the detector. Detectors which operate in this regime are called ionisation chambers.

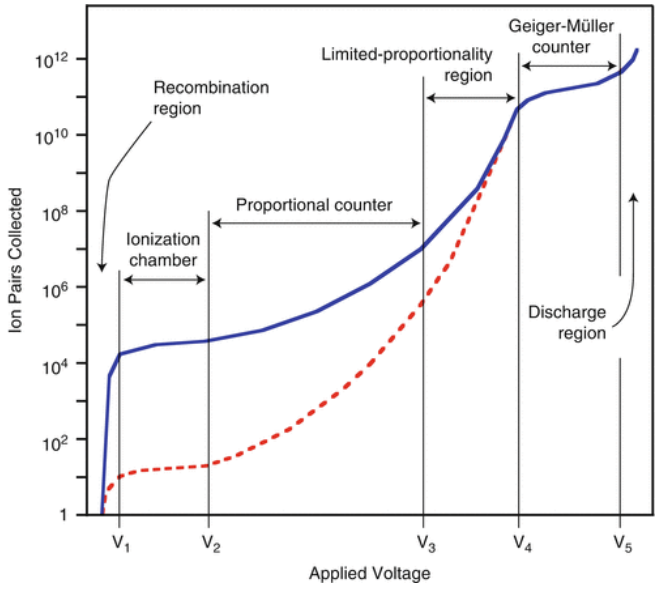

Figure 2.3: Graph illustrating the different operating regimes of particle detectors on a plot of gas amplification on a logarithmic scale, as a function of voltage applied across the detector (linear scale). The red dash line represents the number of ion pairs collected for incoming particles of relative lower energy, while the blue line is for more energetic particles (adapted from reference [76]).

After the voltage is increased further, the electric field lines start becoming denser, and the electrons will gain enough energy in the field to start ionising other gas molecules. The signal collected starts being amplified from the original number of ion-electron pairs generated. As each electron gains on average the same energy between further ionising collisions, the amount of electrons generated by the amplification is then roughly proportional to the initial charge. In this regime, the amount of further amplification is linearly dependent on the applied voltage. This regime is called the region of 'true proportionality', the counters which operate in this voltage window are called proportional counters.

As more and more electron-ion pairs are produced, the speed of the respective particles needs to be taken into account. The particles generated from the processes have a speed which depends on their thermal energy, the kinetic energy gained in the electric field, as well as their collision cross-section. As ions are much larger and heaver than electrons, their collision cross section will consequently be larger, and their overall drift velocity v_{Di} towards the cathode will be much lower than the speed at which electrons are collected v_{De}.

As the number of ions is increased further, and their electrons are being collected away, their presence will start inducing local space charges which will distort the local electric field. This effect will cause the linear dependence of amplification to diminish at higher voltages, leading to the region of 'limited-proportionality'.

When enough ions are produced, the space charges present in the detector distort the electric field to the point that no more amplification occurs even when increasing the voltage. Then the current reaches another saturation state, this region is called the Geiger-Müller region, in which the eponymous detectors operate. An event passing by a detector operating in this regime will give rise to a current. However the current collected at the electrodes will be completely independent from the initial amount of electron-ion pairs originally created and all proportionality relation is lost in these type of counters.

Finally when the voltage is high enough, the gas medium contains so many ions that the medium becomes conductive, this leads to a breakdown and continuous current can flow directly from the cathode to the anode can occur. This region is called

the arc discharge regime, in which plasmas start occurring, and particle detection is therefore not relevant anymore.

As illustrated in Figure 2.3, a less energetic radiation will (as expected) give rise to a similar I-V dependence than a higher energy one but to a lower saturation current. However when the ion-induced space charge effects start being non-negligible the curves start converging together until their energy becomes indistinguishable in the Geiger-Müller regime.

The detectors used in this work are proportional counters. However it is important to understand the influence of the applied voltage on the current collected as the detectors need to be calibrated to operate in the correct regime, so that effects observed at the limits of their operating regime can be interpreted accordingly. The physics behind the effects observed will now be discussed, in the particular case of the proportional regime.

2.3 Photon Detection

2.3.1 Ionisation

Particle detectors can have slightly different designs, and can be made of different materials in order to specialise in the detection of certain types of particles, depending on their nature, energy and other physical properties. The particles of interest in this work are photons, in particular X-rays and therefore the mechanism for the detection of other particles will not be discussed in detail in this thesis.

When a beam of photons of intensity I_0 passes through a material, their intensity I will decreased with respect to I_0, after distance x according to the Beer-Lambert law:

$$I(\lambda) = I_0(\lambda)\, e^{-\mu(\lambda)x} \tag{2.1}$$

where λ is the wavelength of the photon beam and $\mu(\lambda)$ is called the linear attenuation coefficient, a value which varies depending on the material, its density and the wavelength of the incoming beam λ. Assuming that all the energy lost in the attenuation process is converted into electron-ion pairs, then the average number of

electron-pairs generated by these photons passing through the material is proportional to e^{-x}. In a more general form, a primary ionisation event can be approximated as a random binary event (resulting in two outcomes only: either success or failure), resulting from uncorrelated and independent interactions with the molecules in the gas. In this case, the distribution of event successes (or 'counts' for this application) would follow the Poisson's distribution. This can be expressed as follow: the probability P of having k counts (successes), after a distance x would follow:

$$P(k) = \left(\frac{(x/\lambda_i)^k}{k!} \right) e^{-x/\lambda_i} \tag{2.2}$$

where $\lambda_i = \frac{1}{\mu}$ is the mean free path of the photon before producing an electron-ion pair. This value depends on the gas used, the incoming radiation and the interaction between the two, which we will now discuss.

2.3.2 Light Interactions

When a photon (considered as uncharged radiation) is incident upon a gas, quite a few interactions can result. In this section, we will discuss each type of interaction and subsequently show that the only non-negligible interaction in the detector system used in this work is the photo-electric effect. Two main types of interactions can occur from light being incident on an atom: scattering and absorption.

- Rayleigh scattering

  This type of scattering occurs when the photons are being scattered by particles much smaller than their wavelength. This typically occurs for visible light (hundreds of nm) travelling through a medium (lattice spacings of the order of Å) and causes no shift in the wavelength. As in our case λ= 0.152 nm, this type of interaction can therefore be neglected.

- Photo-electric effect

  In this interaction, the photon of energy $h\nu$ is absorbed in its entirety by a molecule in the absorber. This leads to the subsequent ejection of a photoelec-

tron with kinetic energy:

$$E_{e-} = h\nu - E_b \tag{2.3}$$

where E_b is the energy required to remove an electron from its orbital (or its binding energy). This leaves behind a hole in the shell which can be filled with an electron from a higher energy shell loosing energy to fill up the vacancy. The lost energy is strictly dependent on the energy levels in the given absorbing material. This energy can be transferred to another electron in the shell, which will be ejected from the molecule (Auger electron), but the rest of the time it will be emitted in the form of a photon in the X-ray range, called characteristic X-rays.

- Compton scattering

  This type of scattering, also more generally called inelastic scattering, is when the incoming photon is simply deviated from its initial path by an angle θ, transferring the difference in energy to an electron of the molecule. This type of energy transfer is a momentum to momentum transfer rather than a momentum to energy transition transfer. This occurs when the energy of the photon is large enough to be comparable to the rest mass energy of an electron $m_0c^2 = 0.51\,\mathrm{MeV}$. As this momentum transfer is not quantized, the photon can be deviated by any angle, the energy gained by the electron varies on a range from 0 up to almost the entire energy of the initial photon. The energy lost to Compton scattering can be expressed in terms of a wavelength shift.

$$\lambda - \lambda_0 = \frac{h}{m_0 c}\,(1 - cos\theta) \tag{2.4}$$

The largest energy loss would be at a 90^{o} angle which amounts to $\Delta\lambda = h/(m_0c) = 2.43\,\mathrm{pm}$, which in the case of the X-ray source used in this work: 8.04 keV or 0.154 nm, would correspond to an energy difference of $0.17\,\mathrm{keV}$, which is about $2\,\%$ of the original X-ray energy.

The proportion in which each of these interactions occurs is of interest in order to estimate the energies and outcomes expected in a given system. In this work characteristic Kα copper X-ray are used as a photon source. These X-rays have an energy of 8 keV, and the gas mixture used only consists of argon and carbon dioxide (CO_2) in varying proportions. Figure 2.4 illustrates the proportions of the two first interaction mechanisms, and the black line delimitates the points at which the two interactions are equally probable. Moving to the right of the line increases the probability of Compton scattering, while moving the other way increases the probability of photoelectric effect occurring. Placing the atomic number of argon and CO_2 on the diagram vs the X-ray source used in the experiment show that the apparatus used in this work lies in the predominantly photoelectric effect region.

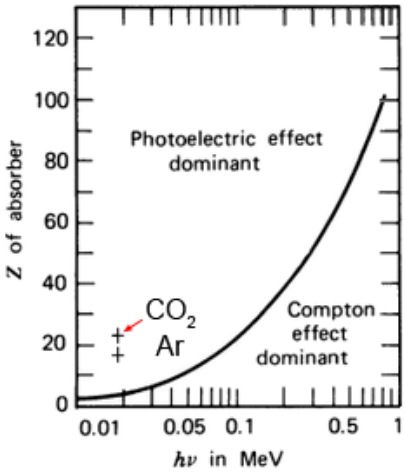

Figure 2.4: Diagram showing the relative importance of various types of light interactions as a function of incident energy (hν) and the atomic number of the 'absorber' material Z. The region in which the detectors used in the work operate are shown by the crosses illustrating both Argon and CO_2 gases under X-ray radiation of energy 8keV. This diagram is adapted from reference [77].

An analytic expression of the exact probability of absorption of an photon by photoelectric effect as a function of photon energy does not exist [76], but a quantitative approximation can be derived from the following rough expression, derived from stopping power and light absorption properties of different materials:

$$P \simeq constant \times \frac{Z^n}{(h\nu)^N} \tag{2.5}$$

where n is larger with increasing photon energy, and N is lower with increasing photon energy. For our particular case of X-rays at 8 keV [77,78], this scales as Z^3/E^3.

2.3.3 Amplification

Considering one electron-ion pair produced during an ionisation process, if accelerated under a high enough electric field (in hundreds of kV generally), the primary electron will collide with more gas molecules and generate further ionisation. It is this process of successive collisions, called Townsend avalanche which generates the amplification of the signals inside GEMs. Let λ_a be the mean free path for an electron before producing ionisation, then the number n of electrons generated after a distance x away from the initial ionisations, is given by:

$$n = n_0 e^{\frac{x}{\lambda}} = n_0 e^{\alpha x} \tag{2.6}$$

Where n_0 is the number of primary electrons produced by initial ionisation, and $\alpha = \lambda^{-1}$ is called the Townsend coefficient, which depends on the nature of the medium, its homogeneities (from local variations in pressure, temperature, impurities) and physical defects in the making of the chamber (for example irregularities in the GEM hole sizes/positions etc.).

2.4 Gaseous Electron Multiplier

The gaseous electron detector is a proportional counter developed by F. Sauli in 1997 at CERN [79]. Its operating principle is derived from the multiwire proportional chamber, but instead of wires, the central part consists of a gaseous electron multiplier (GEM).

A single gaseous electron detector (GEM), as shown in Figure 2.5 a) can be broken down to into a $50\,\mu\text{m} - 70\,\mu\text{m}$ thick sheet of insulating layer (kapton) coated on both sides with 5 µm thin layers of copper. The layer is then patterned with periodic holes of tens of microns size as shown on the scanning electron microscope (SEM) image in b). A high voltage of the order or hundreds of volts is applied across the GEM between the top and the bottom copper coatings, resulting in an electric field being generated

in the holes of the GEM. Such resulting electric field is illustrated in diagram a).

The GEM is placed in the middle of a chamber filled with an inert gas, and a voltage is applied across the top and the bottom of the chamber (respectively the cathode and the anode). The overall electric fields resulting from all these applied voltages are illustrated by the red field lines in a). The electric field in the region above the GEM is called the drift field (or conversion region), as it draws the electrons generated from a passing radiation into the holes of the GEM, and the one below it is the induction field.

Due to the very strong electric field inside the holes, the electrons will collide inside the GEM, and an electron avalanche will result within the gap. For this reason, the zone inside the GEM is called the amplification zone, and the electric field inside is termed the amplification field.

The amplification of a single GEM is can reach up to 10^4 under optimal conditions, with an applied voltage of around 500 V. One could argue that the voltage across the GEM could be increased to obtain similar gain to the MWPC of 10^5 or more [81]. However, an applied voltage of 100 V, across a gap of 50 µm, results in an electric field of 20 000 V.cm^{-1}. At atmospheric conditions of pressure and temperature, such magnitude of electric field results in electric arcs and discharges, which not only disturbs the signal to be measured but also causes damage to the apparatus due to the high currents generated. At this point, one of the advantage of a GEM compared to the MWPC, becomes more apparent: as the anode is separated from the amplification stage, such stages can therefore be stacked up (also called "in cascade") to reach higher gains. Bachmann et al. [82] showed that such GEMs cascaded with a shared load did not affect the gains. Two, three and four GEMs in cascade have been studied and compared systematically in literature [82–84], and the triple GEM was found to exhibit reduced ion backflow effects (which will be discussed later) and therefore had the highest quality of detection and will be the one studied in this work.

Figure 2.5 c) shows a schematic diagram of the triple GEM. The zone between one GEM and the next one is called a transfer zone. This setup also boosts the advantage of a higher radiation stopping power than a single GEM. As a consequence, GEMs can be used in calorimeters either for the detection of hadrons or muons, in alternation

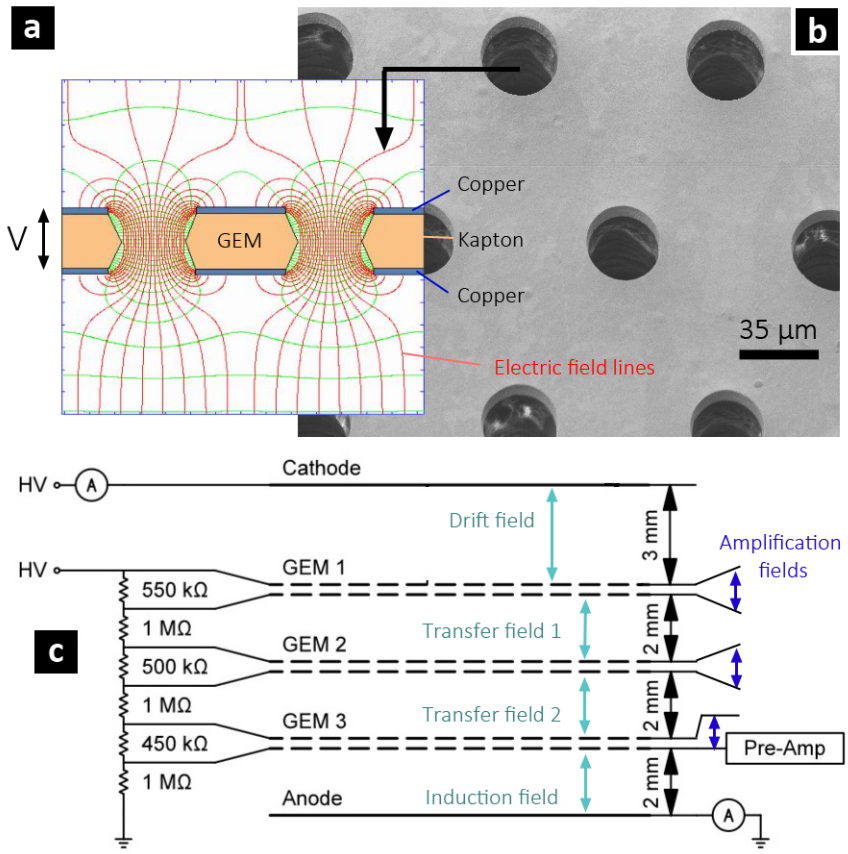

Figure 2.5: a) Cut-out side view of a single GEM. When a voltage V is applied across the GEM, and an overall voltage is applied in the region above and below the GEM, the electric field lines in red form as a result (adapted from [80]), b) SEM image taken at UCL at 10 kV accelerating voltage of a GEM viewed from the top (at a slight angle), showing the patterned periodic holes, c) schematic diagram of the whole triple GEM detector setup, showing the three stages of amplification.

with layers of heavy stopping material such as uranium or steel.

2.5 Factors Affecting the Resolution of Detectors

In practice, the detection resolution of detectors are limited by quite a few factors:

2.5.1 Detector Efficiency

When radiation enters the active area of the detector, it will in principle interact with the gas in the detector enough to give rise to a number of ion pairs which can then subsequently be detected via amplification. In an ideal scenario where all radiations

passing through the detector give rise to a signal, the detector is said to be 100% efficient. Thus it is possible to define a quantity called detector efficiency ϵ, given by the number of pulses recorded, divided by the number of radiation quanta passing through the detector.

2.5.2 Dark Counts

These are the counts registered by the detector in the absence of the radiation counted, considered as noise, they can arise from cosmic rays and other background radiation, electronic noise, etc.

2.5.3 Dead Time

This is the minimum amount of time needed between two events, to result into two distinct pulses. Due to the probabilistic nature of radiation interaction, there is also a probability of two events occurring within a very small amount of time, which could be lost in the counting. If the dead time in a system is fixed, and any counts occurring in such time are simply lost, the detector is called non-paralysable. On the other hand, if an event that occurs during a dead time causes an further increase in the dead time, the system is called paralysable. A typical example is when the dead time corresponds to the time that a pulse needs to decay, then a second pulse appearing within the decay time of the first pulse, will also need to decay, this will then increase the overall dead time. This dead time can also be related to the speed of electronics and depends on the detector system used. The dead time in paralysable setups (such as the one used in this work) manifests itself in the form of pile-ups, which is when multiple pulses overlap each other. The system will count this as one pulse of higher amplitude. Theses high amplitude pulses will appear as a peak towards the highest energy point of the spectrum, and the intensity of the peak will depend on the rate.

2.5.4 Ion Backflow

In the pursuit for further improvements of the detectors, the signal to noise ratio in the readouts is constantly refined. One of the main problems [85, 86] interfering with the signal is ion backflow ion backflow (IBF). In an avalanche, the ions generated

from the collisions slowly drift back to the top due to the field. In theory all ions produced in amplification regions should be collected onto the bottom of the GEM above. However due to the presence of holes, and due to inverse field focusing, some of them feed back into the region above. As a result, not only they distort the field inside the holes, causing loss of electrons, but they also affect the signal collected in the region above. The overall IBF in a detector is defined as the ions issued from below the mesh/first GEM, also called secondary ionisation region, feeding back into the region above towards the anode. In order to differentiate the current from the two ionisation areas, the IBF calculated from this experiment is based on the following formula:

$$IBF = \frac{I_C - I_P}{I_M + (I_C - I_P)} \tag{2.7}$$

where I_C is to the total current on the cathode, I_P is the current collected on the cathode due to primary ionisation only and I_M is the overall current from the mesh. The term $I_C - I_P$ therefore corresponds to the current from the ions flowing back through the mesh due to secondary ionisation. The IBF is therefore defined as the ion current due to the ions feeding back through the mesh divided by the overall current from the secondary ionisation. As a result, this is expressed as a ratio dependent on the total current out of the cathode-mesh system. A property of note is that IBF is independent of pressure and of the gas mixture.

2.5.5 Discharges

Even when operated in the proportional regime, discharges can still occur due to impurities in the gas [87]. These discharges can be reduced by optimising the electric field strengths, the gas mixture, and other parameters in the chamber. Further details will be given in the experimental results.

Chapter 3

Methods

In this section, the existing techniques used in this work will be discussed briefly. Firstly, fabrication techniques will be presented and then characterisation techniques and methods.

3.1 Physical Vapour Deposition

Thin film deposition methods can be separated into CVD and physical vapour deposition (PVD). The CVD method relies on chemical processes and precursor materials to form the film on the substrate whereas PVD makes use of physical processes and the film forms directly from the individual atoms of the source landing on the substrate. Physical vapour deposition does not involve any chemical reactions on the surface of the sample and grows films directly from the source material, which is put under vapour form. This fabrication technique was used in this work to deposit various types of metals (Au, Ag, Ni, Cu, Cr etc.) for contacts and thin film layers.

3.1.1 Resistive Evaporation

In this technique, the material to be deposited is brought to higher vapour pressure by contact with a refractory metal heated via Joule heating. This heat-resistant metal can be either under the form of a helical filament or a boat through which is passed a current of high intensity (typically 20 A to 100 A). Typical materials for this are molybdenum or tungsten, and the choice of the refractory support needs to take into

account the current needed for the source as well as the potential chemical reactions with it. In the case of a filament, the material to be evaporated melts and flows onto the helical wire (also called wetting), and evaporates in all directions into the chamber, depositing along the walls and onto the substrates. In the other case, the molten source becomes a liquid within the boat and evaporates upwards. For this reason, resistive thermal evaporation chambers generally places the source materials at the bottom of the chamber and the substrates for the films upside down inside above them. Lowering or increasing the current passing through the refractory metal can achieve quite accurate control of the deposition rate. This rate is monitored via a quartz crystal microbalance (QCM) placed upside down near the samples. This piezoelectric crystal is subjected to an alternating current, which makes it oscillate at a given frequency. Metal depositing onto its surface will induce a change in frequency that is used to compute the deposition rate.

3.1.2 Electron Beam Evaporation

This evaporation method is very similar to resistive evaporation. In this technique, the film is evaporated by focusing a high-energy electron beam onto a large plate of the source element. The advantage compared to resistive evaporation is that higher melting point materials can also be evaporated, as there is no restriction of an intermediate element being heated.

3.2 Photolithography

Device fabrication on the nano-scale requires the patterning of materials, contacts and labels in order to obtain a suitable device. The technique used for the transfer of patterns onto materials is called lithography. The most common forms of lithography are photolithography, electron beam lithography (EBL) and X-ray lithography. In this project only photolithography was used so far and will be described below. This technique is commonly used in the integrated circuit industry to transfer patterns from a stencil onto thin films. The principle of photolithography is based on the change of structure of some polymers, also called “resist”, upon exposure to ultraviolet (UV) light. After selectively exposing the polymer through a patterned stencil called

"mask", the resist will exhibit differential solubility depending on whether it has or has not been exposed. It can then be selectively removed by dissolving soluble parts into a "developer" solution. There are two types of photoresists: most positive photoresists are linked chains of polymers which de-crosslink after exposure to UV light, allowing the exposed areas to be dissolved away. Conversely, a negative photoresist polymerises and links upon irradiation, which leaves the exposed areas on the substrate after dissolution (as shown in Figure 3.1 a). Different photoresists have different sensitivities depending on their nature and the way they are processed. There are two ways of transferring a pattern onto a given thin film: etching or lift-off. The first method can be anisotropic if a dry etching method (such as plasma) is used, and can also be isotropic if a wet etching method is used (such a solution). The advantages of an etching lithographic process are the high resolution of the pattern obtained and the possibility to remove thick layers of material.

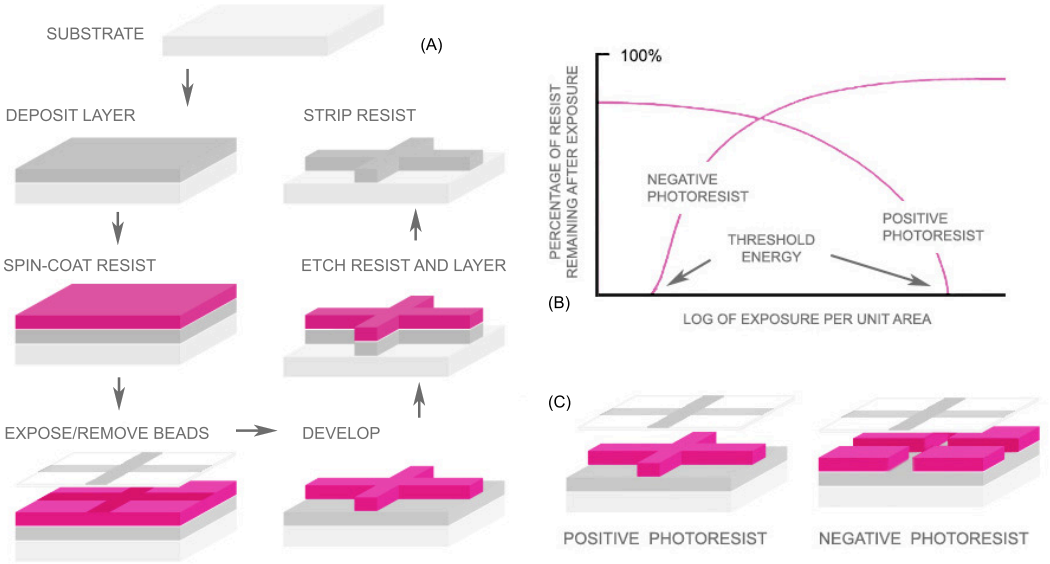

Figure 3.1: a) Typical etching lithography process, b) Effect of exposure energy on different resists and c) Effect of positive and negative resists.

On the other hand the lift-off process has the advantage of not exposing the layer below to the etching solution. This method however, cannot be used for thick films, or for materials deposited at high energies (such as sputtering or furnaces). It is better used for evaporated metals but can give rise to edge depositions if the deposition is

isotropic. A common process recipe for an etching photolithography used in this work is presented as follow:

1. **Deposition**: the layer to be patterned is laid on the substrate (see in section 3.1 for a deposition method).

2. **Adhesion promotion steps**: these steps consist in cleaning the sample from organic or inorganic contamination, then a dehydration bake to remove any remaining water to promote adhesion to the substrate (rather than to adsorbates). On silicon layers, water often reacts with the surface to form a SiOH layer which can be removed by coating the substrate with a layer of hexadimethylsilazane (HDMS) which reacts with the –OH termination to form Si-O-Si$(CH_3)_3$, a hydrophobic termination. This layer cannot be removed easily as it is reacted with the silicon substrate.

3. **Spin coating**: the resist is often kept in a solvent under liquid form. It can then spin coated on the substrate at high speed (typically a multiple of 10^3 of revolutions per minutes or rpm). This step can control the thickness of the resist and its homogeneity. For small samples with corners, the resist can form beads in the corners due to surface tension. These beads therefore create an uneven surface, which will affect in step 5 the homogeneous contact between the resist and the mask. These can be removed by performing steps 5 and 6 with a mask, which will take away the excess resist at the corners of the sample.

4. **Soft baking**: also called pre-bake step, this process consists in heating the resist until most of the solvent is evaporated (approximately 95 %), leaving only the resist. This step is necessary, as the solvent will evaporate with time if left at room temperature, reducing the thickness and the viscosity of the resist. This ensures the resist stays stable and adheres better to the substrate.

5. **UV exposure**: the samples are then aligned to a patterned mask below a UV source. Masks generally consist in fused silica (an amorphous form of glass) coated with chromium (Cr). The glass being transparent to UV, and Cr absorbing these radiations. The exposed areas of the resist will then undergo a

chemical reaction modifying their solubility. Figure 3.1 a) shows the relation between the exposure energy and the amount of resist which is cross-linked after the exposure. In this step an edge bead removal mask can be added to remove spin-coating artefacts forming from surface tension on small substrate with sharp edges.

6. **Development**: the exposed substrate is immersed in a solvent to remove the soluble parts of the resist. Common developers used are based on low concentrations of tetramethylammoniumhydroxide (TMAH) in aqueous solution; others can also be based on sodium hydroxide (NaOH) or potassium hydroxide (KOH) in aqueous solution.

7. **Etch step**: this step removes the layer of material that isn't covered by the resist. Removal can be done by a dry or wet method. The etching method used in section 3.3 for instance is a wet etching method. Dry etching refers to all plasma etching methods such as reactive ion etching (RIE). This step can be preceded by a post-bake (or hard-bake) process, which hardens the resist and increases its stability to etch processes. Alternatively, a "hard mask" can be patterned onto the sample (such as metals) using the steps above. This hard mask can replace the resist as a mask during the etch process and can be removed selectively afterwards.

8. **Resist strip**: the resist on top of the material then needs to be removed. Acetone is often used for this step for normal resists but cross-links lift-off resists. n-methyl-2-pyrrolidone (NMP)), also commercially called 1165, is used as a universal resist remover and can be heated up to 70°C to improve removal.

In a lift-off process, the same steps are followed except the material to be patterned is deposited after the resist development. Remaining resist can be plasma cleaned to improve adhesion of the material to be deposited. The sacrificial resist used for this process, often called lift-off resist (LOR), is based on polydimethylglutarimide (PMGI), a deep UV positive resist. It can be exposed itself or can be coated with a subsequent layer of another resist, which is photosensitive in a different infrared (IR)

region. The sacrificial resist and subsequent layers can then be removed using 1165 (acetone is incompatible with it however).

3.3 Transfer of CVD Grown Graphene

3.3.1 Standard Transfer Process

Graphene has so far only been grown on selected substrates. A transfer method therefore allows a wider variety of interfaces to be used as well as a larger array of devices to be tested. The importance of this transfer method can be highlighted by its role as one of the first pioneers of the principles behind the new field of flexible electronics.

This section will only describe in detail the method used in the scope of this work. The technique has many variations, which are based on similar principles. The main idea behind all known graphene transfer processes lies in the ease of adherence of the material. Being monolayer with dangling π-bonds on each side of the layer makes graphene adhere easily to any substrate in contact with it.

The method used in this thesis is based on providing a soft support for graphene, which can be removed upon adhesion with the target substrate. For this, a resist is spin-coated on to the graphene. The most common resist used for this purpose is poly(methyl methacrylate) (PMMA). This section is based on graphene transfer reviews from 2013 [39]. After coating the graphene with PMMA, the substrate used for CVD growth is then etched away in an aqueous solution. Usual copper etchants such as nitric acid (HNO_3), hydrochloric acid (HCl) and ammonium hydroxide (NH_4OH) need to be avoided as they can chemically modify the graphene or remove it. A commonly used etchant for this purpose in the literature is $FeCl_3$, but it has been shown recently to cross-link PMMA, which prevents its removal and leaves unclean graphene. The etchant used for this transfer process is iron(III) nitrate ($Fe(NO_3)_3$), a salt used for gently etching silver for jewellery.

The coated graphene is left floating on the surface of an aqueous solution of $Fe(NO_3)_3$, with the coat facing upwards until the copper is fully etched away (typically a few hours depending on the concentration of the etching solution). The remaining

coated graphene is then transferred to a deionised (DI) water solution to wash off the etchant and then transferred onto the desired substrate. The PMMA is then removed by immersing the sample in acetone and then rinsed with DI water.

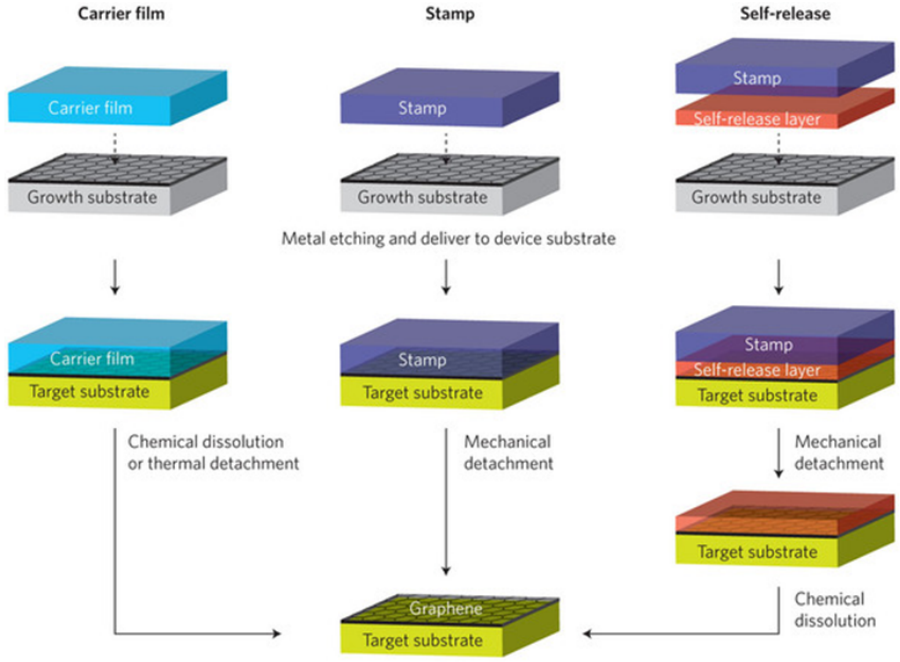

Figure 3.2: Typical transfer methods for graphene. Left: PMMA/Polymer spinning onto substrate followed by etching of metal, then adhesion to a substrate in a wet transfer, and finally chemical dissolution of the support polymer. Middle: Stamp transfer where graphene is coated with a stamp (e.g. polydimethylsiloxane (PDMS)) and applied mechanically onto a substrate. Right: Self-release method using an intermediate layer. Adapted from reference: [38].

Another common transfer method involves PDMS, a stamp often used in soft lithography for the direct transfer of patterns. This layer can be coated on top of the graphene and then used to stamp specific patterns. This is a mechanical method where the layer is pressed onto the substrate. The main obvious advantage of the method is the elimination of the chemical removal step used in order to dissolve the support film, while its main drawback is a low yield of graphene on the target substrate.

3.3.2 Critical Point Drying

This method is commonly used for the drying of cells for the purpose of scanning electron microscope (SEM) imaging. The principal cause for this is the high surface

tension of the water at its interface with air. Water is immiscible with nitrogen and this leads to a high force at the surface (such as that of micelles formed by hydrophobic liquids in water, or a water-oil mixture). In atmospheric conditions and at room temperature, water has a relatively high surface tension compared to other solvents, which can be used as substitute for water.

Substance	**Surface tension** ($nN.m^{-1}$)	**Temperature coefficient** ($nN.m^{-1}K^{-1}$)
Water, H_2O	72.80	0.151
Acetone, $(CH_3)_2CO$	25.20	0.112
Isopropyl alcohol, C_3H_7OH	23.00	0.079
Ethanol, C_2H_5OH	25.20	0.083

Table 3.1: Surface tension of some common solvents in atmospheric conditions and at room temperature, and the change in surface tension per increase in temperature.

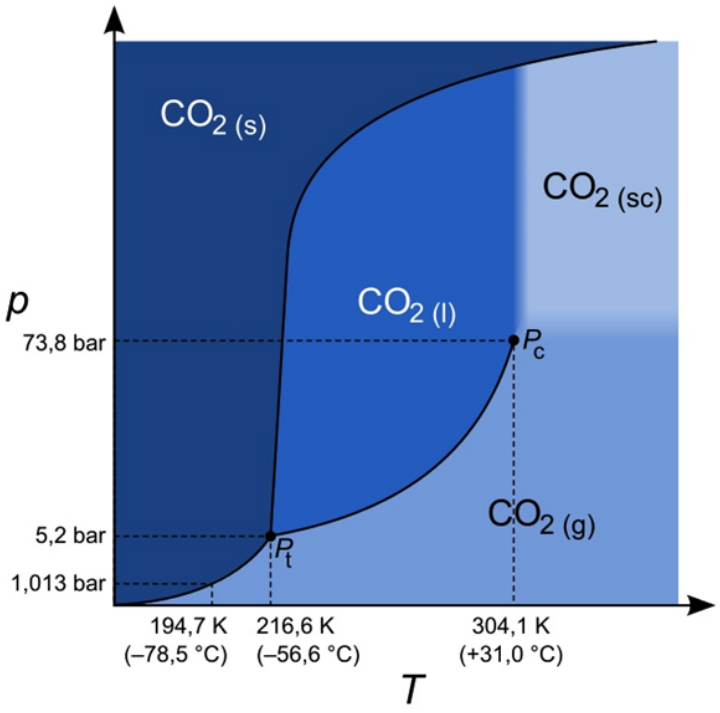

Figure 3.3: Phase diagram of CO_2 showing the critical point P_c and the triple point P_t (the letters S, L, G and SC stand for solid, liquid, gas and supercritical fluid.

Substituting the water in the samples by a solvent with a lower surface tension can therefore reduce some of the damage on the membrane. However the surface tension of the liquid can be completely removed by increasing the temperature and

pressure to the critical point of the material where the densities of the gaseous phase and liquid phase converge to become the same. Because the two phases merge into one, the boundary between the phases disappears and the surface tension vanishes. In this particular case, the liquid used is CO_2 and a phase diagram is shown in Figure 3.3, with its triple and critical points.

In this technique, the sample is placed in acetone in a closed chamber. The solution is then replaced with liquid CO_2. The chamber is then taken to its critical point of CO_2 at 31°C, 73.8 bar (constant volume), at which point it becomes a supercritical fluid and the boundaries between liquid and gas phase cease to exist. Finally, it is cooled back down into its gas phase and exchanged with air or nitrogen. In this way, the sample undergoes a transition between its liquid environment to a gas one without seeing any surface tension.

3.4 Scanning Electron Microscope

Diffraction and interference effects limit the resolution of current microscopes by making images appear blurrier above the resolution limit.

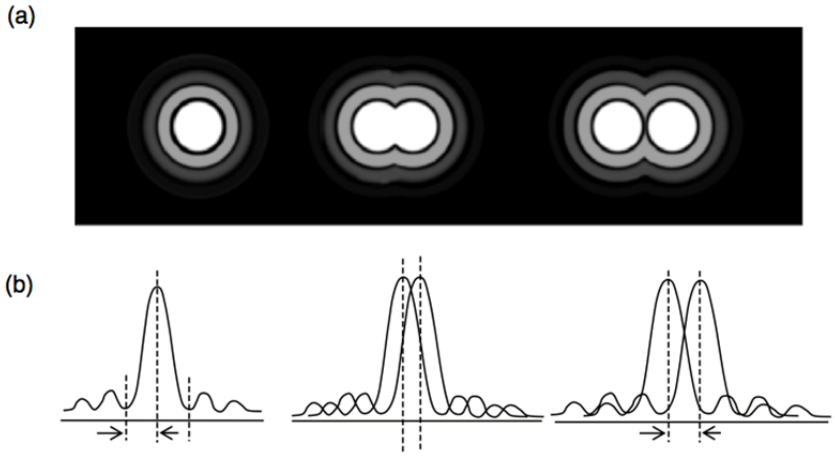

Figure 3.4: Schematic of the resolution based on a) Airy disks and on b) The intensity at a point (adapted from reference: [88])

Ernst Abbe showed in 1873 that the resolution of a microscope is directly proportional to the wavelength of the incident light. Such resolution is defined as the smallest distance between two images that can still be distinguished as separate ob-

jects. When light passes uniformly through an aperture, the resulting image will be subject to diffraction and will appear as a bright disk with faded concentric rings surrounding it. The central disk is called an Airy disk. When two Airy disks of the same size are separated by the diameter of one of the Airy disks, the two images can be resolved as illustrated in Figure 3.4. Abbe expressed the concept in mathematical terms and defined the diffraction limit as:

$$l = \frac{\lambda}{2n\sin(\theta)} \tag{3.1}$$

where l is the smallest size that can be resolved with the microscope, $n\sin(\theta)$ is the numerical aperture (n being the refractive index of the medium and θ being half the angle of diffraction) and λ is the wavelength of the incident light. This equation shows that the resolution can be improved by decreasing the wavelength of light or by increasing the numerical aperture (high refractive index).The scanning electron microscope was invented in the early 1930s quickly after the discovery of the de Broglie's equations:

$$E = \frac{hc}{\lambda} \tag{3.2}$$

As a consequence, for an electron of energy 30 keV, the corresponding wavelength would be 4×10^{-5} nm, which is even smaller than gamma rays. Standard scanning electron microscopes use a range of electron energies from 0.1 to 30 keV, providing electron wavelengths from a few nanometres to 4×10^{-5} nm. The images formed from the interaction of the electrons with the sample depend on the processes that occur when the electrons reach the sample. The overall region excited by the incident beam in the sample is called "interaction volume". This volume will be deeper and pear-shaped with specimens of low atomic number and higher accelerating voltages. Conversely it will be shallower and flat-hemisphere shaped for heavier samples and lower applied voltages.

3.4.1 Back-Scattered Electrons

If the electron is just deflected from its path by a nucleus or by the electrons in the sample, the scattering is considered elastic. Electrons resulting from elastic scattering can be scattered further into the sample or scattered back at the electron source.

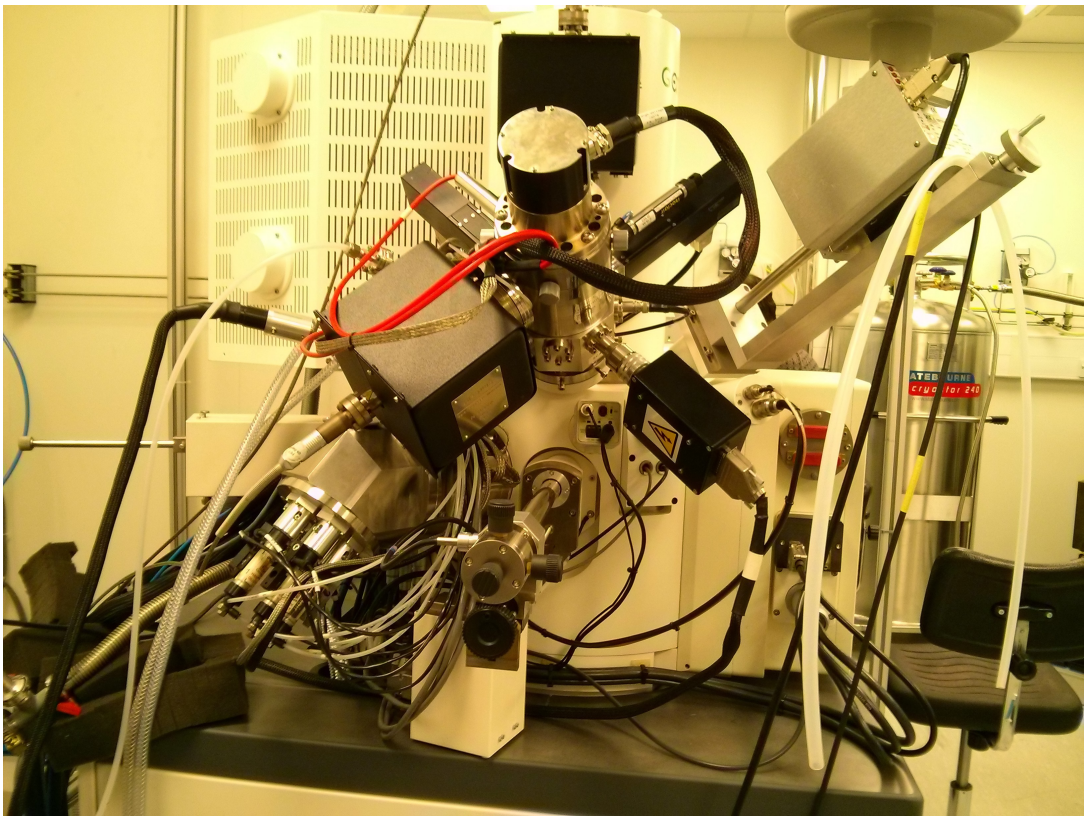

Figure 3.5: Photo of the Leo Gemini scanning electron microscope at the LCN.

Electrons which have undergone one or multiple scatterings and which leave the sample with high energies of more than 50 eV (about 60 % to 80 % of their original energy) are considered back-scattered electrons. The collection of these electrons will constitute the back-scattered electron (BSE) image. These electrons generally constitute between 5 to 50 % of the original beam source intensity. Heavier elements have larger nucleus and therefore generate more BSE. This makes it this imaging technique better for heavier elements (carbon only generates 6 % of BSE).

3.4.2 Secondary Electrons

When primary electrons from the source interact inelastically with the electrons and the nuclei in the sample, the most probable resulting interaction is the emission of secondary electron (SE). Incident electrons ionize the atoms from the surface of the sample. The outer electrons ejected from the atoms will have a very low energy (around 4 eV) and will come from a few nanometres below the surface of the sample. These will be collected in a secondary electron detector and will result in an image with good topography (because the electrons penetrate a few nanometres inside the sample).

These electrons have low energy and therefore need a bias to drift them into the detector. There are generally two types of SE detectors. The most common detector is called the Everhart-Thornley (ET) detector and applies a bias of +10 kV between the sample and the detector. A Faraday cage shields this detector, and a field of 300 V is applied on the outer shell of the cage to channel all low eV electrons onto its surface. This leads to the detection of only higher energy secondary electrons, which are emitted from deeper inside the sample, making the final image more sensitive to topography. This detector is generally set at an angle from the sample as the higher energy electrons come from deeper within the sample. The second type of detector is located inside the source column. All SE, which are scattered back through the aperture opening, are accelerated towards this detector.

3.4.3 X-ray Generation

There are two types of X-rays generated by electron interactions with the sample: the bremsstrahlung and the characteristic radiations. The first type of emission, also called continuum X-rays, is a continuous background due to the deceleration of electrons inside the electric field generated by the sample.

The beam can also ionize electrons in inner shells of an atom. This leads to another electron in the outer shell to lower its energy to fill the vacancy. Characteristic X-rays come from the excess energy being dissipated through the emission of an X-ray. These not only more intense but they are also characteristic of the materials in the sample and are used to characterise its elemental content through what is called energy

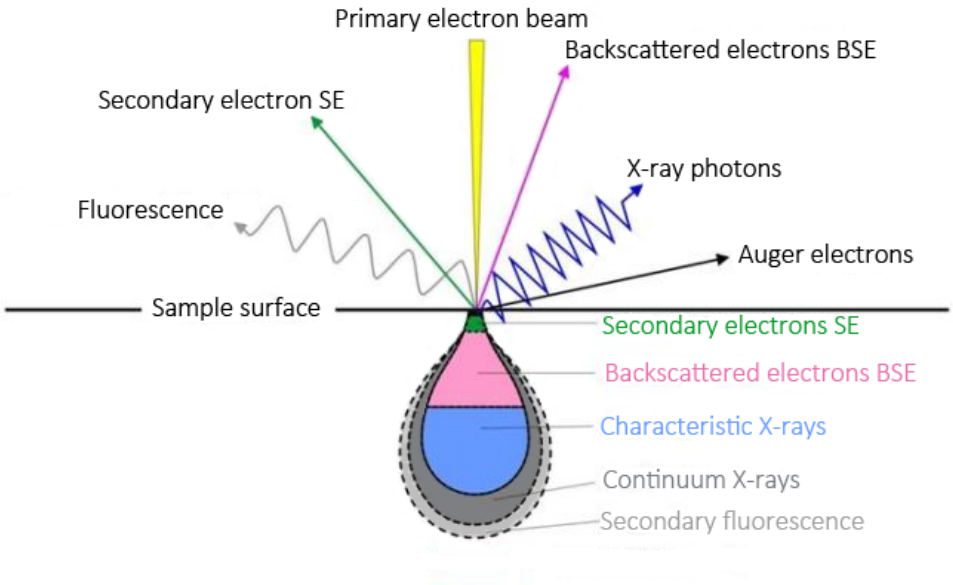

Figure 3.6: Diagram illustrating the different radiations which can be measured from an SEM system with their relative interaction ranges (adapted from University of Glasgow).

dispersive X-ray (EDX) spectroscopy.

3.4.4 Other Emissions

The excess energy from an electron transiting to a lower state can also be transferred to another outer shell electron, which is ejected from the atom. These are called Auger electrons and are used to determine elemental content for light elements (heavier elements valence shells are more difficult to ionize). Characteristic X-ray generation and Auger effect are competing processes, for this reason this type of spectroscopy is often used with EDX as complementing techniques. The different types of radiations which can be measured from an SEM system are summarised in Figure 3.6, with their relative range they originate from in the sample. This depth determines the information which can be extracted from each. The absolute range (of the order of nanometres as a general rule) depends on the atomic number of a material which is probed: the higher the atomic number, the less penetration depth of the incoming electrons. Spectroscopic techniques will be discussed in the next section in more detail.

3.5 Raman Spectroscopy

3.5.1 Spectroscopy

Spectroscopy studies the energy interaction between electromagnetic radiation and matter. The radiative energies used to probe matter in this technique are generally photons, electrons or neutrons. The interactions that occur with matter can be absorption, scattering or reflection of the incident energy, impedance or slowing of the energy transmission and resonance with the energy of excitation. In the case of absorption, the spectrum of the transmitted light can be detected and therefore the amount of absorbed light can be determined, this is called absorption spectroscopy. The absorbed energy is always re-emitted after absorption through various processes. Such processes include fluorescence, phosphorescence and the detection of re-emitted energy is called emission spectroscopy.

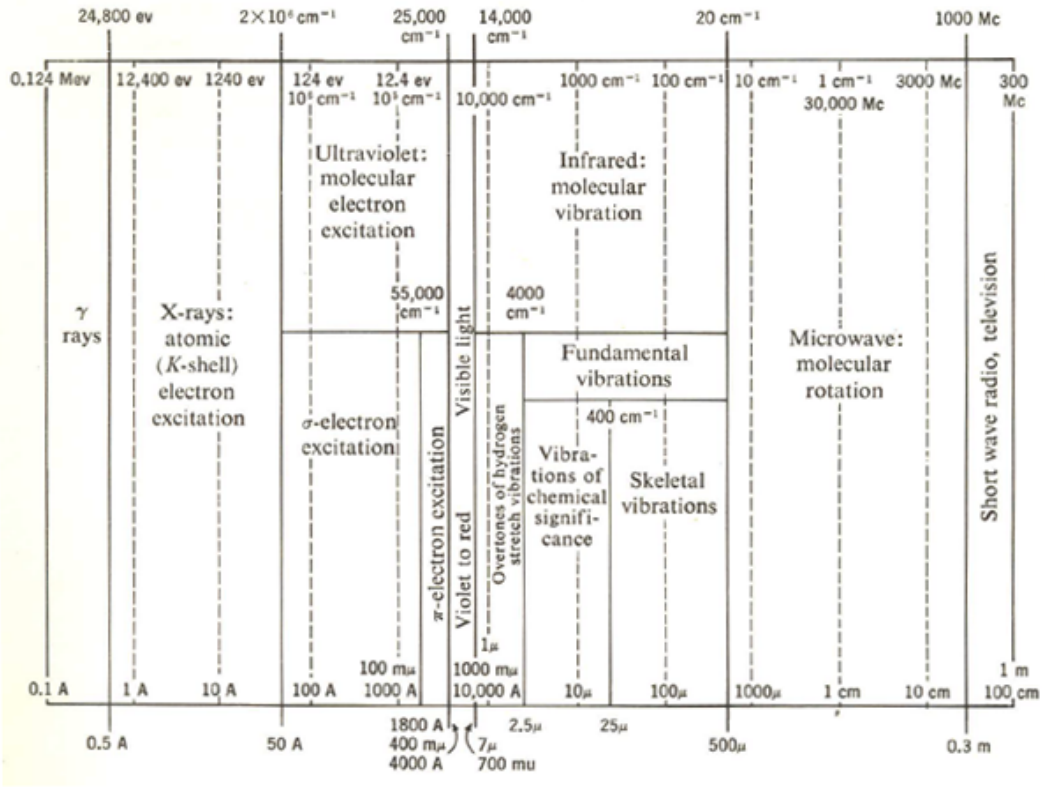

Figure 3.7: Electromagnetic spectrum with the transitions excited by the corresponding radiation (adapted from reference [89]).

In the case of scattering and reflection, the scattering and reflection can either be elastic or inelastic. Elastic scattering is called Rayleigh scattering as discussed previously. Vibrations in the sample can deflect higher energy photons inelastically; this is the basis of Raman spectroscopy. If the scattering event results in an enhancement of the vibration and therefore a lower energy photon, the resulting shift is called Stokes shift. In a less likely event, the photon can leave the sample with a higher energy by causing an already excited vibration to return to its ground state. This scattering result in an equal but opposite energy shift as the Stokes shift, it is called the anti-Stokes shift.

When a molecule absorbs a photon, the molecule is promoted to an existing allowed excited state. Available energy levels arise from electronic configuration, spin, rotation, vibration etc. and thus allow a wide range of transitions. Figure 3.7 shows the electromagnetic spectrum with the various processes that are responsible for transitions in different parts. The diagram shows that low energy radiations excite thermal and molecular transitions, giving information on the bonds and the geometry of the system. As the energy of the interacting radiation increases, the higher energy and more detailed structures are probed, such as electronic transitions giving information about the elemental content of the system.

3.5.2 Raman Spectroscopy

Raman spectroscopy is a lower energy spectroscopy technique and provides very similar information to infrared spectroscopy on the samples. The main difference resides in the fact that infrared spectroscopy is an absorption technique whereas Raman spectroscopy is a scattering technique (in particular inelastic scattering). This makes infrared spectroscopy a more bulk-sensitive technique and Raman spectroscopy a surface sensitive technique (Raman transmission spectroscopy also exists but is not commonly used technique as it requires the sample to be transparent to the radiation). Raman spectroscopy is based on excitations by photons in the visible spectrum and provides information on the bonding between the atoms through excitation of the vibrational degrees of freedom. The Raman signal is weaker than infrared absorption and therefore requires longer integration times. Although IR and Raman spectroscopy

are related as discussed in the previous sections, the Raman signal does not arise from the resonance of the incoming beam with the vibrational energy levels but from a temporary distortion of the electron clouds by the passing photon. This results in a change of the vibration and therefore a change in the polarisability of the molecule. The selection rule for Raman spectroscopy therefore states that the mode excited by the photon needs to cause a change in polarisability of the molecule.

Because of the hexagonal lattice structure of graphene, its Raman spectrum will exhibit a large peak corresponding to the vibration of the hexagon. This signature peak is called the G peak and is located around 1560-1580 cm^{-1} Raman shift. In the presence of structural defects in the lattice, the vibrations will be different and will therefore give rise to a different signal. Such imperfections in graphene give rise to what is called called the D peak (around 1340-1360 cm^{-1}) and can be caused by any types of defects in the structure including addition of a functional group (which will change the vibration of the lattice), addition of dopants, reconstructions, edge effects, structural out of plane defects etc. This peak can therefore be used as an indication of the quality of the graphene and the nature of the defects in the layer [90, 91]. A typical graphene spectrum will be described in detail in Chapter 4, Figure 4.2. The other peaks (for example D+D", 2D) arise from either double resonant (the photon creates a virtual electron-hole pair which are both scattered by lattice phonons and/or defects) or overtone (promotion of the vibration to an energy level higher than the nearest vibrational level) Raman processes. The exact origin of each of these peaks however is still a topic under discussion [92] and is not of interest within the scope of this work.

3.5.3 Raman Setup

The Raman measurements in this work were done using an Invia Raman Renishaw spectrometer. All measurements were done at a laser wavelength of 532 nm unless stated otherwise. The laser had with a maximum power of 30 mW and all the measurements were conducted at 1 % of the max power at a magnification of x100.

The setup is described in Figure 3.8: the laser signal passes through a beam expander that increases its size. The laser beam then proceeds through a beam splitter.

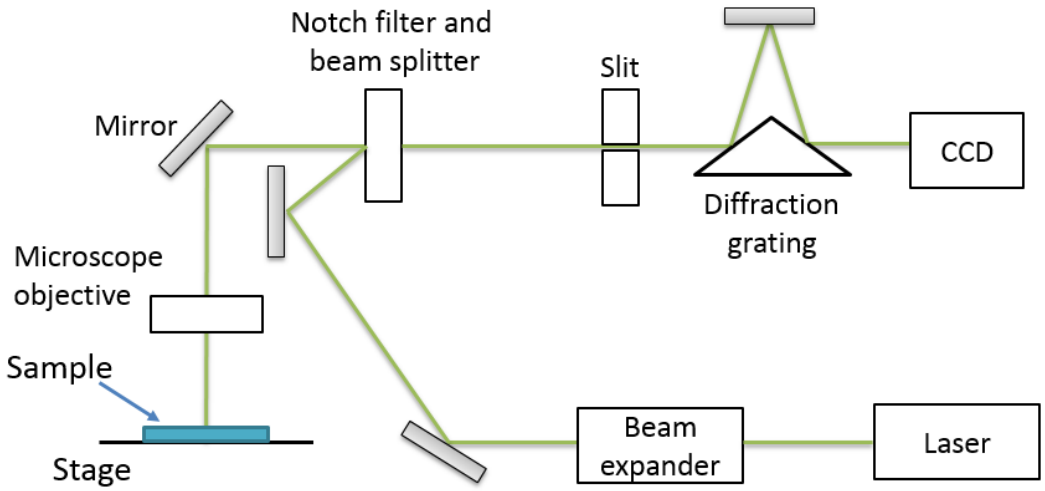

Figure 3.8: Schematic diagram of the setup of the Invia Raman Renishaw spectrometer used in this work.

Half the laser beam is then focused through the microscope objective onto the sample. In our setup the spot size on the sample (a higher magnification and a shorter wavelength will generate a smaller spot size) at a magnification of x100 (Numerical aperture of 0.9) and a laser wavelength of 532 nm would in theory be 361 nm. In practice, various factors, such as the flatness of the sample, the loss of light through the holes of the samples used in this work need to be taken into account and as a result, the spot size would be expected to be about 1 µm.

After passing through the microscope, the signal is reflected from the sample back on the same trajectory but will now carry the Raman scattering signal from the sample. This signal and the remaining half of the original beam will go through a notch filter which attenuates the Rayleigh band in a narrow range (about 2 nm for a holographic one and 10 nm for a dielectric one). In the case of our system the filter was a holographic filter which allows for detection of signals closer to the Rayleigh wavelength. The beam is then passed through a slit which collimates its. The light then hits a diffraction grating (an arraw of fine lines on a reflective surface), this leads to constructive and destructive interference combinations which will depend on the wavelength. These will therefore reflect at a slighly different angle, which will then hit the CCD detector at different spatial points. These points can then be reconstructed according to diffraction laws into the corresponding wavelengths.

A direct consequence of this setup is that the wavelength resolution will be dependent of the grating used and on the quality of the CCD.

3.6 Atomic Force Microscopy

This method is a characterisation technique [93] which scans and probes the forces on the surface of a sample in order to compute out a high resolution map of it. The properties mapped are probed using a sharp tip, of dimensions comparable or smaller than the structures to be probed on the sample. This is a very versatile technique, which can give information on topography, sample composition as well as other sample properties depending on the tip.

An AFM device can be broken down into three rough components: a sample holder, a scanner and a platform used to isolate the measurement system from external noise.

The most critical part of the apparatus is the scanner which consists of four key parts: the probe, the force sensor, the piezo scanner and the feedback control. These three components are connected in a loop, which can be controlled in order to change the resolution and the properties measured by the equipment. The resolution can also be influenced by the nature of the probe, which consists of a cantilever terminated at the end by a sharp tip as illustrated in Figure 4.13 c). The loop system is based on the sample principle in all AFM devices, and operates as follow: first, the probe is positioned in the desired area of the sample and then lowered down onto the sample using the piezoelectric motor, until the tip of the cantilever is close enough to the sample and starts interacting with it.

3.6.1 Cantilever and Tip

The tip-cantilever system [94] is used to sense the forces on the sample and is critical to the type of measurement carried. In fact, different types of tip-cantilever systems will experience different forces and properties from the sample.

Stiffer cantilevers that do not deform easily are used in applications where high forces are involved. On the other hand, soft and high elastic moduli cantilevers are used to sense lower forces due to their greater flexibility. These cantilevers have a lower force constant and are used to avoid damaging soft samples. Because of manufacturing

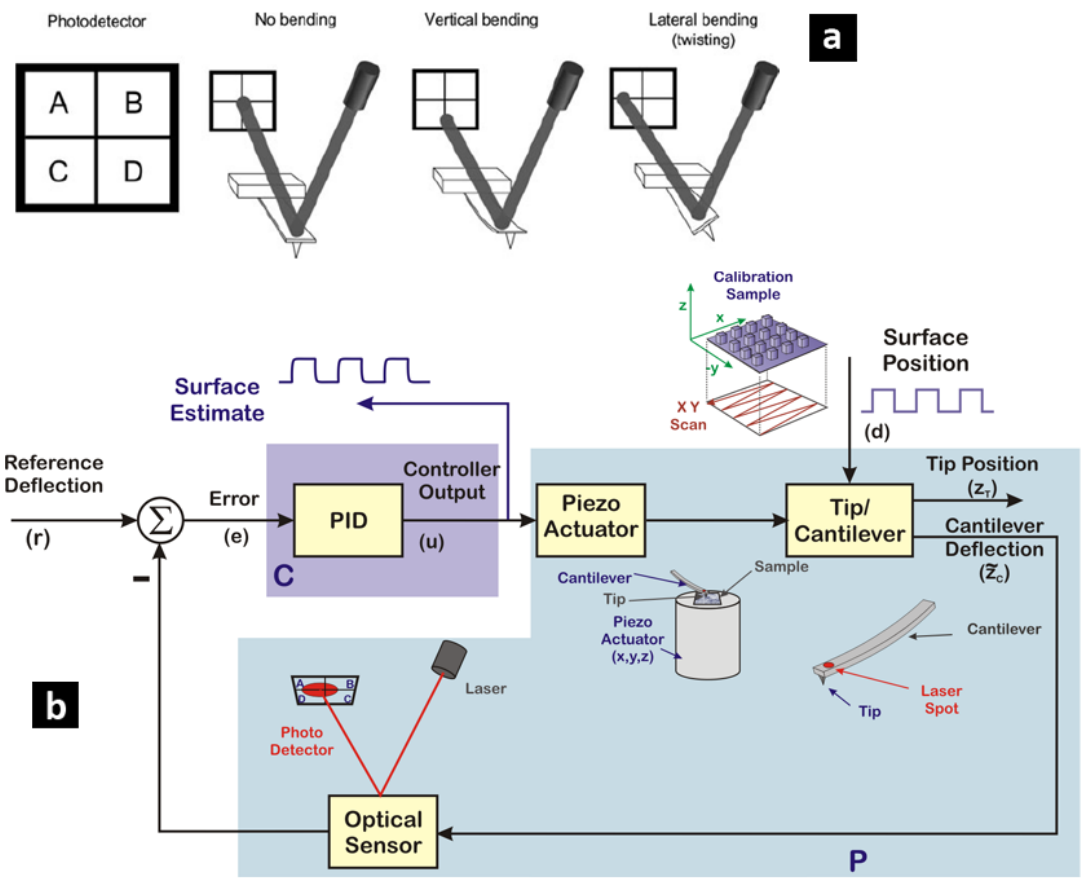

Figure 3.9: a) Diagram illustrating how the cantilever deflection is measured by the laser in non-contact mode from reference [94]. b) Diagram of the control loop for a typical AFM (image credits: Daniel Y. Abramovich).

defects, it is estimated that the properties of a cantilever such as spring constant, force constant and resonance frequency can differ from each other to about 10 % even within the same manufacturer.

In theory the tips used are refined so that the end is atomically sharp, for optimal sensitivity (as shown in 3.9 c)). However because of the great sharpness of the tips, exposure to air and to unclean environments may cause a certain degree of contamination on the sharp end. This contamination enlarges the effective area of contact between the tip and the sample and therefore the amount of force experienced by the probe. This eventually leads to a lower resolution of the image and can cause artefacts and irregular features to appear when the tip drags the contaminants across the surface. This is the case in multiple-tip imaging where the tip is contaminated resulting in two or more atoms sharp spaced equally. In that case every feature on the

sample will appear twice or more (if there are more atoms) on the resulting image. Contamination of the tip is very difficult to remove but can be cleared by applying a voltage pulse or by applying the tip on the sample lightly.

The sharpness of the tip is therefore critical to obtain high lateral resolution images. Because tips tend to blunt after a certain number of scans it is necessary to change and clean the tips relatively often. The two most used materials for AFM tips are silicon (Si) and silicon nitride (Si_3N_4). Tips made with silicon nitride have lower force constants and resonance frequencies, but because of their residual stress they tend to bend with use whereas Silicon tips are more resistant.

3.6.2 Piezoelectric Motor and Feedback Loop

The forces on the tip upon interaction range of the sample is then measured by a force sensor which feeds the data back into the loop. The details of the processing done by the force sensor will be discussed in the next section. The measured force, converted into a height, is then fed back to the piezoelectric controller which will correct for the z-direction movement of the probe accordingly. The links between the components of the loop are described in diagram b) of 3.9.

The piezoelectric scanner is a part of the device that is critical to the vertical resolution of the scan (whereas the tip and cantilever systems only determine the lateral resolution). It consists of two pieces of piezoelectric material that contracts or expands when subject to an electric potential. This expansion converts the electric signal into mechanical movement to operate the raster scan. A typical value [94] for the displacement of the material is 0.1 nm for an applied voltage of 1 V. This fine movement which is the typical vertical resolution for an AFM can therefore be used to resolve nanometre-sized features. The scan rate of the AFM is also determined by the properties of the piezoelectric material. Indeed, the higher the resonance frequency of the material, the faster scans can be performed. There are two ways of implementing the piezo scanner, the first one is called sample scanning and the sample is supported by the piezoelectric motor while the probe stays still. The second way is called probe scanning and the probe itself is driven by the motor and the sample kept still. The latter build has more versatility as more features can be added to a moving probe.

However it is also more difficult to build as the force sensor system has to be moved with the probe during a scan.

In order to avoid damaging the tip as well as for higher sensitivity, there is a feedback loop controlling the z-axis movements of the probe. Because piezoelectric materials exhibit hysteresis and creep, position sensors can also used in the x and y axis in a feedback loop system to correct for the deformations of the piezoelectric ceramic. The correction for this non-linearity in the expansion or contraction of the material is important for higher accuracy of the measurements.

3.6.3 Tip-Sample Convolution

The shape and aspect of the tip also has a consequential impact on the measurements. The tip and the sample surface are convoluted and the resulting measurements are therefore a combination of the surface features and the features of the tip (see Figure 3.10). As a consequence, when a low aspect ratio tip (blunt) is used to image features that are smaller, the resulting image will only be an image of the tip. Similarly, the inverse situation with a very sharp tip will only image the sample.

The convoluted signal measure can be deconvoluted mathematically by taking into account the tip geometry. However, because of the high variability between the tips shapes (even within one manufacturing process) and the technical difficulty that arises from measuring the shapes, the process become quite complex. In fact scanning electron and transmission electron microscopes (SEM and TEM) have been used in many attempts to determine the tip shape but were shown to alter the tip at high voltages. Another way of characterizing the tip would be to make use of convoluted images of known features to estimate the size and shape of the tip.

3.6.4 AFM Modes

AFM can be used in a wide variety of modes by changing the type of probe used or the way the sample is scanned. Because of the differences in preparation and scanning method, this leads to different interpretation of the results and a different suitability depending on the property and material probed. Applications include the removal of materials, or positioning of small particles on a surface, force imaging, topography,

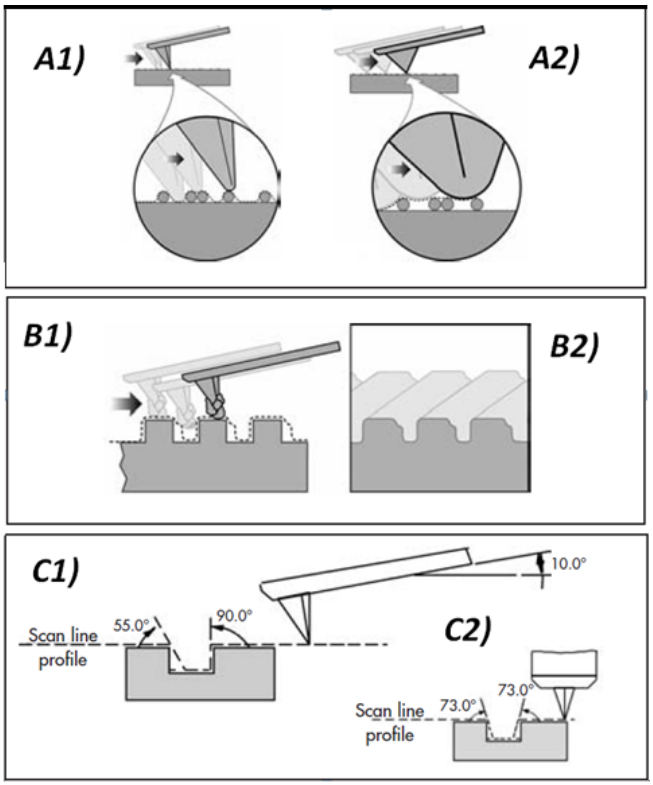

Figure 3.10: A1) Diagram of the effects of a sharp tip and A2) a blunt tip. B1) Diagram of the effects of tip contamination on computed topography. B2) Dependence of features on the geometry of the tip and scanning direction (adapted from: Veeco)

spectroscopy etc. There are in fact more than 20 modes [94] used for various purposes and by modifying various parts of the AFM, however this report will only cover the three main modes: contact mode (also called static mode), intermittent mode (or tapping mode) and non-contact mode. These modes operate in different regimes and can measure different properties of the material. Assuming a Lennard-Jones-like potential on the surface of the material, the area of operation of each AFM mode can be represented on a diagram as shown in Figure 3.11.

3.6.4.1 Contact

In this mode, the tip is made to approach the sample until it reaches the repulsive force regime where both the tip and the sample apply. The tip is then considered 'in contact' with the sample and the feedback loop is used to keep the cantilever deflection constant; this constant value can be set by the user and is called the set-point.

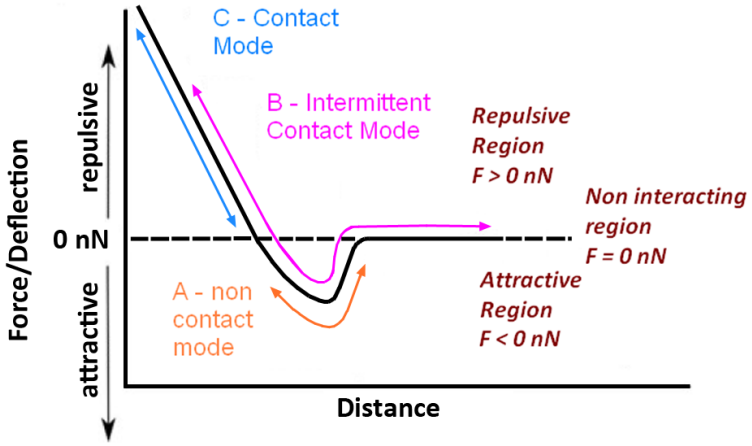

Figure 3.11: Diagram of the regions of interaction of the three main AFM modes plotted on a graph of deflection or force as a function of distance.

This mode is particularly interesting because the deflection of the cantilever can be used to monitor three quantities: the lateral deflection, the vertical deflection, as well as the height of the cantilever 3.9 a). For this reason and because of the close contact between the sample and the tip, this mode offers very high resolution and quite accurate measurements. However the tip and sample are also likely to be damaged by quick variations in forces on the sample surface. Indeed a slow feedback and a negative feature with attractive forces can suddenly bend the cantilever towards the surface and cause damages or alterations. This is the reason why this mode isn't suitable for weakly bound samples or soft samples. Another particularity of this regime is that the cantilever deflections are sensitive to the nature of the surface.

There is a sub-regime of this mode called constant-height contact mode AFM where the feedback loop is turned off and the tip is dragged across the surface. This is generally in cases where the scanning speed is faster than the feedback loop for instance when finding a particular area of a sample. The sub-regime with the feedback loop is called constant-force contact mode and is the default sub-regime in contact mode unless specified otherwise.

3.6.4.2 Tapping and Non-Contact Modes

In these two modes, the cantilever is made to oscillate above the surface of the sample and as a result, the cantilevers used have higher stiffness than in the contact mode.

Because the tip isn't in contact with the sample, softer and more delicate samples that in contact mode can be imaged. Those modes are usually used the amplitude modulation sub-regime where the changes in amplitude or in the phase of the signal are used in the feedback loop as errors. There is also a frequency modulation sub-regime mainly used for true atomic resolution imaging in ultra high vacuum.

In the non-contact mode, the frequency of oscillation used is much lower than the resonance frequency of the cantilever. Because the very low frequencies are used, the device operates in the attractive force region of the surface where Van der Waals forces dominate. In order to avoid falling within the repulsive range of the surface, the non-contact mode makes use of cantilevers with higher resonance frequency and higher stiffness than the contact and intermittent mode. Except for the latter application, non-contact mode generally has less accuracy than contact mode and is used rather than contact mode when soft samples are imaged.

In the tapping mode (also called dynamic mode or intermittent), the cantilever is driven at a frequency near its resonance frequency and the cantilever is driven back and forth from the non interacting region through to attractive region to finally the repulsive region. For higher frequencies, the tip is closer to the sample and the signal detected also contains information of the surface adhesion, elastic properties, topographic details and load force of the sample. This results in a complex mix that is difficult to interpret. If atomic resolution is achieved, the magnitude of those forces can be used to determine the chemical nature of the atoms as well as their bonding properties.

3.7 Particle Detector Test Measurements

3.7.1 Experimental Setup: the X-ray Set-Up

In this section, the experimental methods for the detector setup will be described. As discussed in section 2.4, the triple GEM is made out of 3 stacked GEMs in cascade. In this work, the GEMs had an area of $(10 \times 10)\,\mathrm{cm}^2$. The GEMs are powered using a single power source connected to a voltage divider. The values of the resistances decrease as it is closer to the anode, so that the voltage applied to the GEMs is also

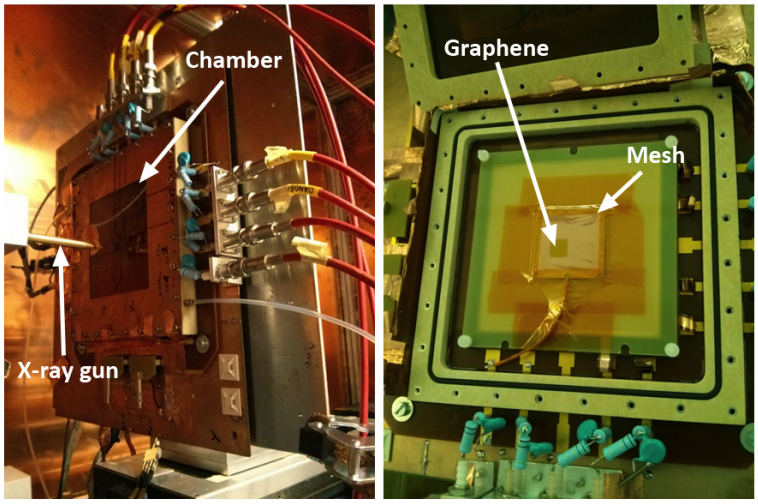

Figure 3.12: Pictures of the X-ray signal detector (based at CERN), left: setup with X-ray gun and chamber, right: the chamber was opened and a piece of graphene transferred onto mesh placed inside the chamber on top of electrode readouts.

decreased. Both the current from the cathode and the anode are monitored.

The anode used in this work was a printed circuit board (PCB), patterned with an array of metallic strips used to collect the electric signals. The strips were connected together to gather the overall signal. The cathode consisted in a $(10 \times 10)\,\mathrm{cm}^2$ copper support placed on top of the triple GEM. The chamber was flushed with inert gases from one side to the other of the chamber.

A micromesh, also called mesh in this report, was then integrated to the inside the chamber of this system in order to accommodate the addition of graphene. The introduction of this will be discussed in Chapter 6.

In the experimental setup used for this work to test the detector devices fabricated, an X-ray source acts to ionise particles from collision chambers. The X-ray gun was placed perpendicular to the chamber as shown in Figure 3.12.

The reliability of the signal in this system depends on the electron transparency of the whole system and on its ion channelling properties. These properties are measured by measuring the intensity of the ion current from the anode, the cathode, or from the GEMs.

3.7.2 Pulse Processing for a Basic Detector

A simple particle detection system can be described as a capacitor filled with an inert gas, across which a high voltage is applied. This would cause any charge carriers in the capacitor to move towards the plates. During an event, an incoming radiation passes through the capacitor and the gas can be ionised along the radiation path. From this, a small current ensues. In order to measure and process this small signal, a specific setup is commonly used in particle detection applications, as described in Figure 3.13. Punctual events give rise to short charge flows which can be converted into a proportional voltage pulse by a pre-amplifier. This in turn is then connected to an amplifier which increases the amplitude of the signal. A discriminator can then be used to set a threshold above which a pulse is considered a signal, or is otherwise noise. This allows for the filtering of background noise in the signals. The relevant pulses are then sent into a multi-channel analyser (MCA), which classifies each signal by height and saves them into a corresponding channel. Each channel is therefore used to 'count' the number of pulses of that height and the plot of the number of counts per channel results in a histogram. The MCA includes an analogue to digital converter (ADC) which converts the voltage pulse into a digital signal 1 or 0. The cumulative count of the signals per channel can then be plotted as a pulse height spectrum, which can be interpreted in terms of the number of events per given energy happening over the integration time of the MCA. If an event is know to happen at a given energy, the number of channels can be calibrated to fit the energy of the event, for instance in this work, channel 800 corresponds 8 keV (the energy of the X-rays used in this work), and therefore 700 would correspond to 7 keV.

The signal from the discriminator is also sent to a scaler, which counts the number of pulses per fixed unit time and gives a count rate in Hz.

In this basic detector description, the amplitude of each of the charge pulses collected by pre-amplifier is proportional to the energy lost in the ionisation processes caused by the initial particles, the histogram can therefore be interpreted as an energy distribution spectrum of the radiations collected within the detector. The energy of the charges collected can be calculated from the input range of the MCA divided by the number of channels used in the measurement and divided once again by the gain

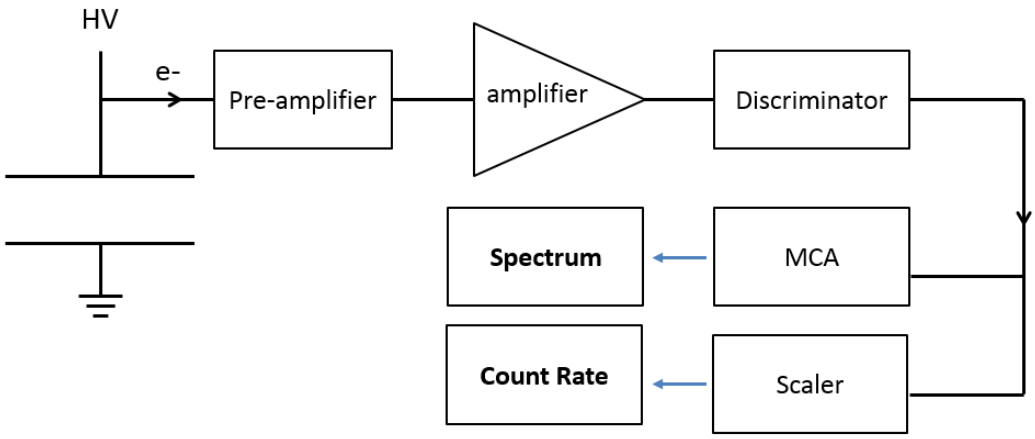

Figure 3.13: Basic counting setup for discrete events, starting with the charge collection from the detector, drawn as a capacitor on the left, all the way until the pulse height spectrum.

of the amplifier. Another information which can also be collected is the rate of these charge pulses which gives information on the frequency of the events occurring. This information is computed by the scaler.

3.7.3 Escape Peak

When an X-ray of energy E_i is incident on an Argon gas atom in the chamber, two events can result. The energy of the radiation can be transmitted to an electron with a lower binding energy than the incoming X-ray, resulting in ionization. These electrons will drift towards the cathode and be detected as an electric signal of proportional intensity to the incoming signal.

If the incident ray has energy E_i larger than $\phi = 3.203$ keV, the binding energy of the electron in the K shell of Ar, it will result in ionization and an electron emitted with an energy E_e of:

$$E_e = E_i - \phi \tag{3.3}$$

This process leaves a vacancy in the K shell, which will be filled by electrons from higher shells via release of a characteristic X-ray or an Auger electron as described in Section 3.4. These emissions will account for the remaining energy ϕ of the initial incident ray.

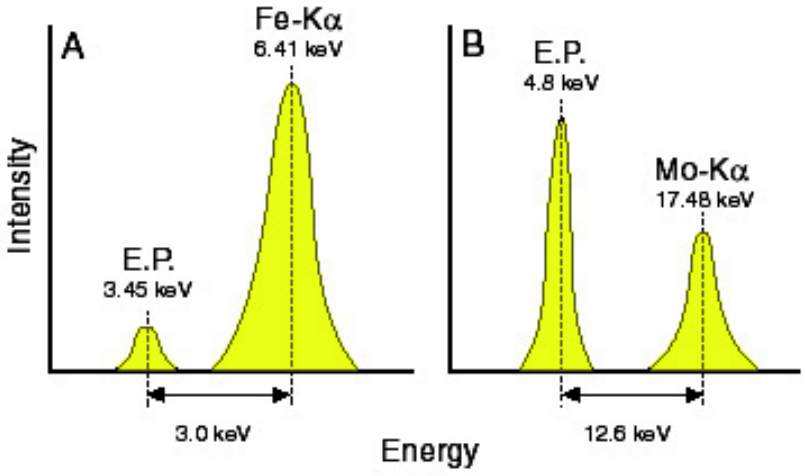

Figure 3.14: Right: Diagram of the Fe-Kα escape peak in an argon atmosphere and left: the Molybdenum escape peak in Krypton (adapted from Northern Arizona University).

If the energy of the emitted radiations is not re-absorbed by other processes in the detector and they leave the chamber, the energy of the electrons collected by the readout will be of energy E_e as stated in equation 3.3.

This effect will appear as a peak also called 'escape peak' of energy ϕ lower than the bulk energy of the incident X-rays. This energy difference is $\phi = 3.203\,\text{keV}$ in the case of the Argon atmosphere as described in Figure 3.14. The respective height ratio of the escape peak to the original peak depends on ω the fluorescent yield of the atom: for argon $\omega = 0.21$, and in the illustration for krypton it is $\omega = 0.65$.

This peak can be given two different names identifying its characteristics: the 'argon escape peak', which indicates the nature of the lost characteristic X-ray, or alternatively it can simply be called the 'Fe Kα escape peak', underlining only the energy of the main peak. Figure 3.14 shows a typical result, this graph is also called pulse height spectrum.

3.8 Protocols

This section will document the chemical protocols used in this work (see Section 4.4.9).

3.8.1 FITC Labelling

The following section will describe the protocol used for the FITC labelling (from Sigma):

1. Prepare a protein solution in 0.1M sodium carbonate Na_2CO_3, pH 9, at a concentration of at least 2 mg/mL

2. In a darkened lab, dissolve FITC (Pierce) in dry DMSO (dimethyl sulfoxide $(CH_3)_2SO$) at a concentration of 1 mg/mL. Do not use old FITC, as breakdown of the isothiocyanate group over time, may decrease coupling efficiency. Protect from light by wrapping in aluminum foil or using amber vials.

3. In a darkened lab, slowly add 50-100 µL of FITC solution to each mL of amine solution (at 2mg/mL concentration). Gently mix the protein solution as the FITC is added. 4. React for at least 8 h at 4°C in the dark.

5. The reaction may be quenched by the addition of ammonium chloride (NH_4Cl) to a final concentration of 50 mM. Some protocols include at this point the addition of 0.1 % xylene cylanol and 5 % glycerol as a photon absorber and protein stabilizer, respectively. React for a further 2h to stop the reaction by blocking the remaining isothiocyanate groups.

6. Purify the derivative by gel filtration using a PBS buffer (phosphate buffered saline) or another suitable buffer for the particular protein being modified. The use of Sephadex G-25 or similar matrices with low exclusion limits works well. To obtain complete separation, the column size should be 15-20 times the size of the applied sample. Fluorescent molecules often non-specifically stick to the gel filtration support, so reuse of the column is not recommended.

3.8.2 Ninhydrin

This section documents the protocol used for ninhydrin colorimetry for amines [95,96]:

The reagents used in this protocol were the following: Standard amino acid stock solution (150 micrograms of standard amino acid stock solution (150 µg/ml)), 0.2M Acetate buffer (pH = 5.5), 8% w/v of Ninhydrin reagent (preparation: weigh 8 g of ninhydrin and dissolve in 100 ml of acetone), 50% v/v ethanol.

The protocol is as follow:

1. Pipette out different volumes (0.1 ml - 1 ml) of standard amino acid solution to the respective labelled test tubes.

2. Add distilled water in all the test tubes to make up the volume to 4 ml.

3. Add 4 ml of distilled water to the test tube labelled Blank.

4. Now add 1 ml of ninhydrin reagent to all the test tubes including the test tubes labelled 'blank' and 'unknown'.

5. Mix the contents of the tubes by vortexing /shaking the tubes.

6. Put a few marble chips in each tube.

7. Cover the mouth of the tubes with aluminium foil.

8. Place all the test tubes in boiling water bath for 15 minutes.

9. Cool the test tubes in cold water and add 1 ml of ethanol to each test tube and mix well.

10. Now record the absorbance at 570 nm of each solution using a colorimeter.

Chapter 4

Large-area transfer of suspended monolayer, bilayer, and trilayer graphene with high coverage and reduced PMMA residues

4.1 Abstract

Graphene is a one-dimensional material with predicted and measured properties of an exceptional nature. However most of these properties are significantly deteriorated by the presence of an underlying substrate, making suspended graphene a very sought after material. As expected from a single-atom layer, suspending such a material has been a challenge and the largest areas obtained as of today have been in the range of 5 μm. Here, we present a new transfer method for mono-, bi- and tri-layer graphene which allows for reproducible transfer of suspended layers with high coverage over large areas and over periodic holes up to 70 μm diameter, a significant step from the previous suspended layers. We also show that the method yields less PMMA residues than usual transfer as well as excellent properties. This method paves the way for further applications of large-area suspended graphene such as nanoresonators [11,97], water desalination [98], photodetection, enhancement membranes for TEM imaging

[70, 99, 100], filters and trans-diffusion applications through graphene [50, 101–103], amongst others.

4.2 Introduction

Graphene is an allotrope of carbon arranged in a hexagon shape by sp^2 bonds, which ranges from a monolayer to a few layers. Since its isolation [1] in 2004, it has been the subject of intensive research due to its unique physical properties such its high mobility, high mechanical strength, optical transparency. The effort to integrate graphene into industrial methods has driven research into a wide variety of methods of graphene production, each producing an equally wide range of graphene with different sizes and properties. Of these, large area sheets of graphene show the highest potential as a replacement for ITO in commercial products and as suspended membrane for detection of filtering applications. To date, the most appropriate and promising way of growing this type of graphene is the CVD of graphene on low solubility substrates such as copper. Other metallic substrates have also been investigated but the low cost of copper compared to the supports which have been shown to yield high quality graphene, such as iridium, colbalt, ruthenium (list) make it the most ideal growth substrate. Due to the limitation imposed by the selective nature of the supports over which graphene can be grown, multiple ways of transferring graphene to a different material have been explored in order to obtain the highest quality, and highest coverage of graphene.

The original transfer method consisted in the mechanical exfoliation of graphene from highly ordered pyrolitic graphite (HOPG) using scotch tape and applying it to a silicon substrate. Despite the low graphene yield of the method, it led to the development [37] of the now commonly used polymer support method where PMMA or PDMS [104] are coated on top of the graphene. The original substrate is then removed and the graphene and polymer are adsorbed onto the new support. The sacrificial PMMA or PDMS can then be removed, leaving graphene on the new substrate. The main disadvantage of this method is the remaining residues which are reported [39] to be less than 2 angstroms even with an intermediate self-release layer. Thermal annealing methods [41] have been developed to reduce [40] these PMMA residues, but also induce graphene doping [42] and irreversible strain from substrate pinning [105],

which affects the properties of the layer.

Other transfer processes also exist, such as the electrochemical bubbling of graphene [43] which is limited to metallic destination substrates, a new marker frame support [106], thermal release [32], capillary bridges [44] which can avoid the manual transfer of graphene onto the destination substrate but requires nitrogen incorporation on the surface of the new support. A few methods [107,108] have been suggested by patterning the copper below the graphene but suffer from contamination and the limitation of the patterned substrate being copper. Despite this large number of transfer methods, the full coverage of suspended graphene over large areas has only been successful for holes [62] or features [97, 109] less than 5 μm size [98, 107, 110]. Any larger area or different method has yielded low partial coverage, or large amounts of PMMA residues which has helped the suspension [111]. In this work a new method was developed to suspend graphene onto large areas patterns, with significantly reduced PMMA residues, without disturbing the properties of the layer.

4.3 Methods

In this work, monolayer graphene was obtained from Graphene Supermarket, the single graphene layer is grown by chemical vapour deposition (CVD) on 25 μm thick polycrystalline copper. The full transfer method following the growth process is described in Figure 4.1. The sample of 15x15 mm^2 was first floated on nitric acid (17 %) for 1 min to remove the graphene grown on the backside. The sample was then rinsed with flowing DI water. A layer of 300 nm of PMMA was then spin-coated onto the graphene and baked at 180°C for 1:30 min to remove any remaining solvent. The sample was left floating on a solution of $Fe(NO_3)_3$ in DI water at 40 mg/mL to etch the copper layer. Once the copper was fully etched, the samples were gently moved to a DI water solution using a watchglass so as to not disturb the layer. In order to remove all etchant residues, this step was repeated until the DI water solution stayed clear after being left for an hour (generally 3 or 4 times). At this point other publications [112] have suggested the use of HCl-based solutions to remove metallic residues from the solution. This method was shown by other works to induce defects in the suspended graphene layer (increase in the height of the D peak after treatment) and

was therefore avoided for this transfer [113, 114].

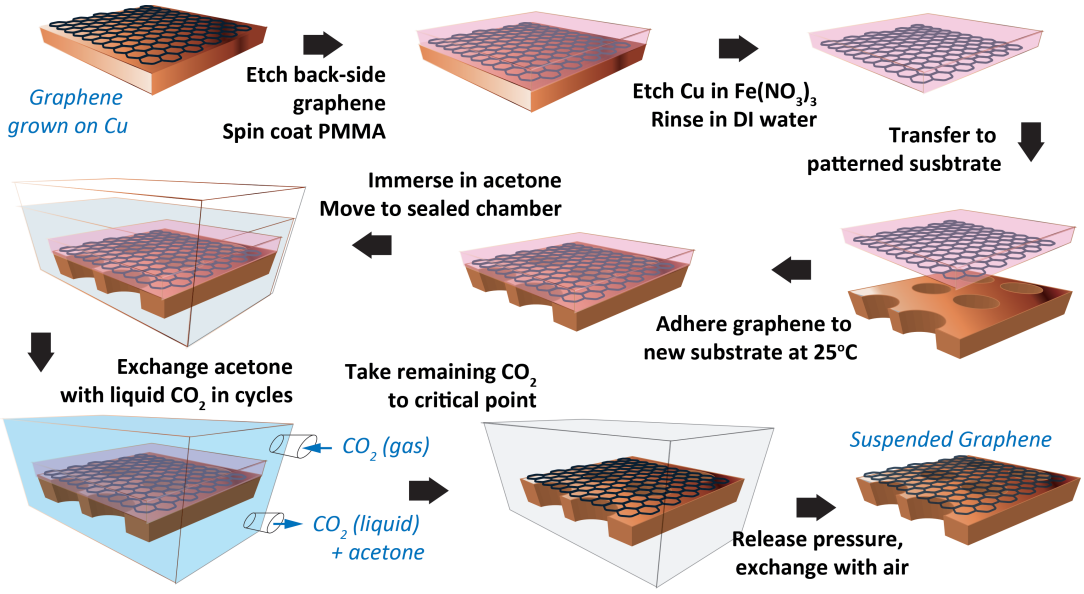

Figure 4.1: Diagram of the new transfer process used to suspend large area graphene.

The copper and gold supports were 25 μm thick and were fabricated (in CERN) by standard photolithography (see Figure 3.2) using masks with a regular hole pattern of diameter sizes varying from 30 μm to 75 μm and a pitch of 140 μm or 60 μm. The copper supports were cleaned with 1:3 acetic acid for 3 min to remove the oxide layer and both the gold and copper are degreased thoroughly with cotton in solutions of acetone (C_3H_6O), then isopropyl alcohol (IPA) (C_3H_8O) and rinsed in infinite running DI water. These cleaning steps are critical to obtain the best possible coverage as the adhesion of graphene and its likelihood to tear were found to be strongly influenced by impurities and irregularities (such as partial oxide) on the surface of the support. The floating graphene and PMMA were then adhered onto their new support taking care to not wrinkle the layers by using a needle [62]. The sample was then heated at 25°C for 10 min to adhere the graphene to the surface of the substrate and iron out any possible folds in the layer. Failure to adhere the graphene in this step resulted in near to no suspended graphene after the process. At this point, standard transfer [15] would require an adhesion and flattening step done by adding another layer of PMMA followed by curing. However this process would add extra strain onto graphene and the resulting suspended layers would not be flat, this step is therefore to be avoided.

The next step which consisted in the removal of the PMMA layer, was done by substituting acetone with supercritical CO_2 as a solvent in order to reduce the surface tension of the liquid to zero. Due to the absence of interface between the gas and the liquid phase, this process can therefore be used to remove the PMMA layer while drying the graphene membrane in one step without damaging it. The drying chamber used in this work was custom built to support the large samples used to support the membranes. The sample was gently immersed in a container filled with acetone and held stable at the bottom. The container is introduced in a chamber and cooled at atmospheric pressure to 10°C and subsequently sealed. Gaseous CO_2 at 5.5 MPa was then very slowly introduced inside the chamber and underwent a phase change upon contact with the acetone. The liquid CO_2 was then carefully exchanged with the acetone by evacuating part of the mixture while keeping the sample immersed. This way the acetone was removed in small cycles of CO_2 mixing. Once the chamber was fully acetone free, the CO_2 was taken to its critical point. At this point it was important to flush the mixture in order to remove the dissolved PMMA in solution. The CO_2 was therefore taken back down to liquid form by cooling the chamber down back to 10°C. The liquid CO_2 was then flushed with new liquid CO_2 in cycles until the whole mixture has been displaced. The new liquid is then taken back to critical point. Once in supercritical state, the pressure is decreased slowly releasing the gas until room-pressure and eventually replaced with air.

4.4 Characterisation and Discussion

4.4.1 Interpretation of Raman Spectroscopy Data: Background Signals

Raman spectroscopy is one of the most versatile and comprehensive ways of probing the properties and the quality of graphene [115]. The layer number and quality were characterised using an InVia Renishaw Raman Spectrometer. As most of the Raman signature peaks of graphene are strongly energy dispersive, all the following measurements are for a laser of 532 nm unless stated otherwise. This allows for the measurement of the peak shifts independently of the excitation energy ω_L, but also

consistency in the intensity of the G peak which is known to increase [116] with ω_L^4 while the other peaks stay at the same intensity. Care was also taken to not cause laser-induced damage by keeping the excitation power at 1 % of the 30 mW maximum on the sample.

A typical Raman spectrum obtained is shown in Figure 4.2 a), the graphene peaks were fitted with mixed Gaussian-Lorentzian curves using the patented algorithm on the Wire software. All the main expected peaks were observed: the D, G and 2D peaks. Additionally, the C, D+D" peaks were also present in most spectra, as well as G*, the overtone of the G peak [115]. Further details on Raman spectroscopy and on the peaks can be found in section 3.5.

The spectra obtained also showed two background signals aside from expected peak contributions from the graphene layers as shown in the top. These two contributions were also fitted with Gaussian-Lorentzian curves and were found to be centred at (1890 $\pm$ 40) cm^{-1} and (3300 $\pm$ 200) cm^{-1}. The centre of the second curve was found to vary a lot as most spectra were taken from 1000 cm^{-1} to 3000 cm^{-1} and the background had to be fitted with the centre of the peak outside that region. As these background curves were very consistently present throughout all samples, the origin of these curves was checked thoroughly in order to make sure that the signal did not originate from the graphene layer. To this end, a Raman spectrum was taken for the copper substrate alone, as well as for amorphous PMMA residues, the two other possible contributors to the signal. The latter sample was prepared by spinning PMMA over an intrinsic silicon substrate (which does not show any background signal at this laser wavelength) and then ultra-sonicating the sample in acetone for 5 min, and subsequently rinsing in IPA and DI water. The spectra are shown in Figure 4.2 c) and were also centred within statistical error of the two background contributions calculated above. This seemed to indicate that the background observed did not originate from graphene but from two different contributions: the copper support and PMMA residues. A cross-check of this result was done by taking the Raman spectra of the freestanding graphene layers, as well as suspended PMMA and it was found that the copper background contribution at (1890 $\pm$ 40) cm^{-1} did not appear on both suspended spectra as expected.

As Raman spectroscopy is an excitation technique, if the sample contains energy

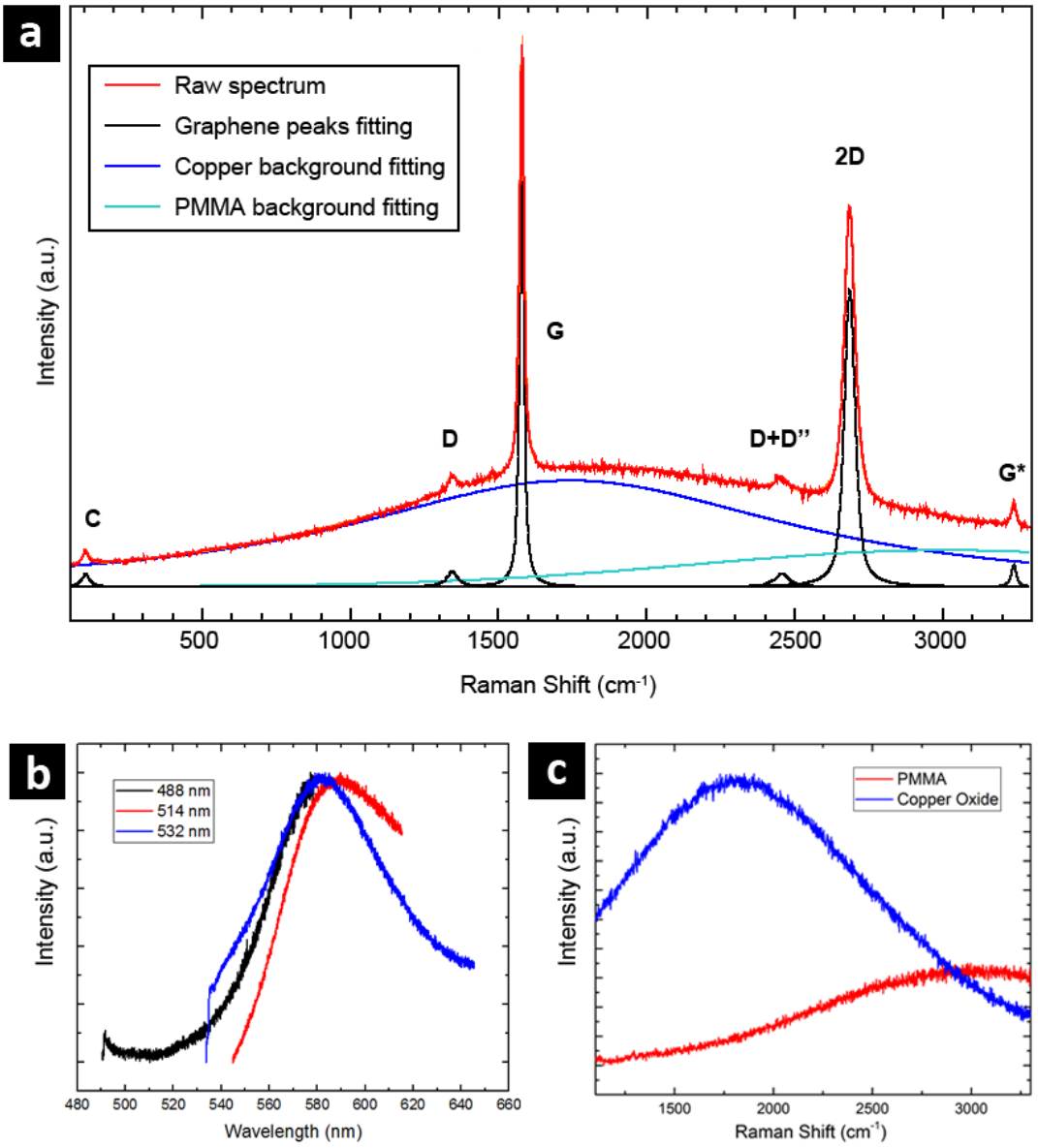

Figure 4.2: a) Typical Raman spectrum of trilayer graphene supported over copper with some PMMA residues. The red curve corresponds to the raw spectrum. Graphene peaks are fitted in black and the background is fitted in blue. The dark blue colour corresponds to the copper contribution and the light blue corresponds to PMMA. b) fluorescence data from the copper substrate calculated from Raman data. c) Raw PMMA and copper oxide Raman data.

bands near the exciting wavelength of the laser, this can give rise to fluorescence signals which will also be detected by the apparatus. However, unlike Raman signal, fluorescence appears at a fixed wavelength and will therefore shift on a Raman spectrum if the laser wavelength is changed. In order to verify this, both samples were probed using different laser wavelengths: 488, 514 and 532 nm. The centre of the signal was indeed found to shift significantly for both samples. As expected, as the laser wavelength was decreased, the centre of both peaks signal shifted towards larger Raman shifts. Unfortunately, as the PMMA signal was already on the edge of the spectra, the centre of that peak shifted out of the range of the spectrometer. On the other hand, the copper centre was found to shift very clearly to higher Raman shifts. These shifts were converted into wavelengths using the known laser energy. The Raman spectra for copper at different laser excitations was then re-plotted as a function of wavelength. This is shown in Figure 4.2 b). The peaks were indeed found to coincide and were centred at (580 $\pm$ 5) nm. This peak is in accurate agreement with the known photoluminescence [117, 118] from copper complexes and is expected to shift to higher wavelengths for rougher surfaces [119]. As the copper samples used in this work showed roughness to varying degrees, this explained the variation in the peak centre. The edge of the PMMA Raman signal exhibited a fluorescence peak extrapolated to (640 ± 20) nm which agrees with literature values [120], however this peak is expected to have variations in its centre depending on polymer chain lengths and structure, similarly to the case of the roughness in copper mentioned earlier. This dependence does not affect this application: assessing the amount of PMMA residues. As the fluorescence of a material is proportional to its concentration, the intensity of the peak is therefore directly proportional to the thickness of the polymer on the sample, given the same density. This experiment has therefore shown that the specific origin of each background luminescence contribution in the Raman spectra of the samples and that the photoluminescence background contribution from the PMMA residues is proportional to its thickness.

4.4.2 Assessment of PMMA Residues

In order to avoid fluorescence from the copper, the spectra were taken on suspended graphene only. The background contribution from PMMA residues is a semi-Gaussian due to broadening attributed to disorder induced by exposure to acetone. In the case of the residues left after simply subjecting the material to acetone, the spectra appeared as a fluorescence background centred beyond 3500 cm^{-1}. The position of the centre could not be determined accurately as it was not observed within the spectra for this laser energy and could only be extrapolated by fitting the tail of the signal. This contribution to the background fluorescence was used to show a significantly lower amount of PMMA in the new transfer than for a standard transfer. This is illustrated in Figure 4.3 with the Raman spectra of suspended graphene after a standard transfer, and after this method, compared with the spectra of bulk de-cross linked PMMA. All spectra showed in the figure are normalised to the same 2D peak intensity for ease of comparison but otherwise are raw spectra with no background modification. The spectrum of the suspended graphene using this method shows an almost perfectly clean background showing a very negligible amount of PMMA left.

Scanning electron microscopy (SEM) was also used to cross check the amount of PMMA residues. All close up SEM images of the suspended graphene layers and PMMA were characterised using a Carl Zeiss XB1540 focused-ion-beam with an integrated scanning electron microscope at an accelerating voltage of 5 kV unless stated otherwise. The detectors used were either the Inlens or SE2 detector. The residues of polymer appear as filament-like de-cross linked chains under electron microscopy. This is shown in image d) of Figure 4.4 where standard transfer was used to suspended monolayer graphene over a hole with a large amount of residues of polymer covering the membrane. In the same figure, image a) shows a suspended monolayer after transfer using this new method. The white arrow points out filament-like remaining PMMA which can be seen to account for the negligible background in the Raman spectra shown in Figure 4.3 amount compared to the usual PMMA residues. A similar observation can be made for transferred bilayer and trilayer graphene shown in insets b) and c).

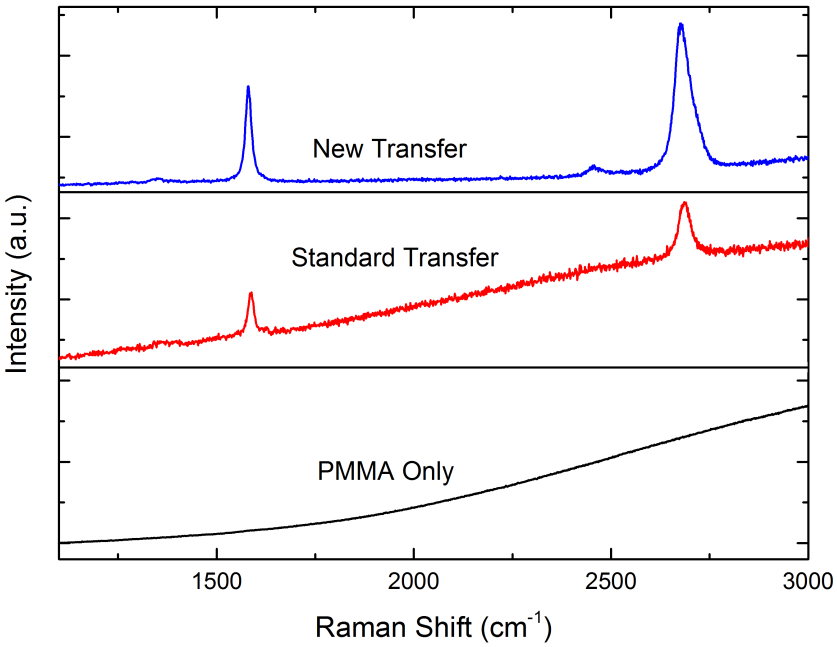

Figure 4.3: Raman spectra of suspended graphene using this transfer method compared to standard transfer, and to a spectrum of PMMA. The spectra are normalised for ease of comparison.

4.4.3 Mechanism of PMMA Removal

The explanation for this clean removal of PMMA was also investigated via a few key experiments. Given that the process involved was a solvation process, with the PMMA dissolving into the liquid environment provided, there were a few parameters to take into account in the system:

- the affinity and interaction between PMMA, the solvents: acetone and CO_2,
- the interaction between the underlying layer: graphene, with the solvents,
- the thermodynamic conditions used in the process.

The exact nature of the interface interactions between all these materials is a complex subject beyond the scope of this thesis, and therefore only a few relevant interactions will now be discussed in order to design the appropriate experiments to further understand the behaviour of PMMA.

The PMMA monomer consists of a hydrocarbon backbone with an ester (-COOH) termination, which makes its electronegativity similar to that of acetone (=O). How-

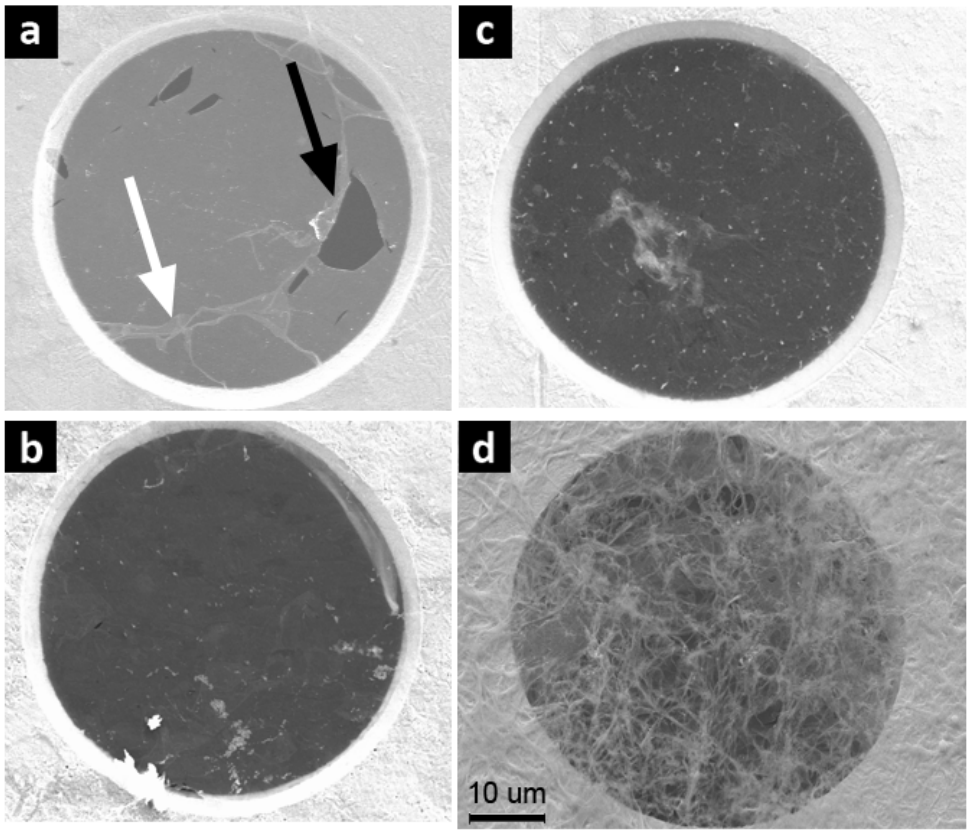

Figure 4.4: SEM images of holes of 35 upmum diameter covered with a) suspended monolayer graphene using the method presented in this paper, where the black arrow shows a crack in the layer and the white arrow points out some PMMA residues (white filament), b) suspended bilayer, c) suspended trilayer, d) monolayer graphene with large amounts of PMMA residues (light coloured filaments) after transfer without critical point drying. All images have the same scale bar and were taken at an accelerating voltage of 5kV.

ever, being a polymer chain rather than a monomer, this electronegativity is reduced by the entanglement of non-polar hydrocarbon chains, making the acetone wettability lower. Despite this factor, PMMA remains soluble in acetone with some flow.

On the other hand, due to the very symmetrical and aromatic carbon structure of graphene, the layers are expected to be highly non-polar and its wettability to acetone and other polar solvents is expected to be poor. This would therefore have a strong influence on the wetting of the polymer layer in direct contact with the graphene, explaining the few nm of PMMA remaing after a simple acetone cleaning process.

CO_2 is a small non polar molecule which would make it immiscible with polar solvents in its liquid state. This was clearly confirmed during all the critical point

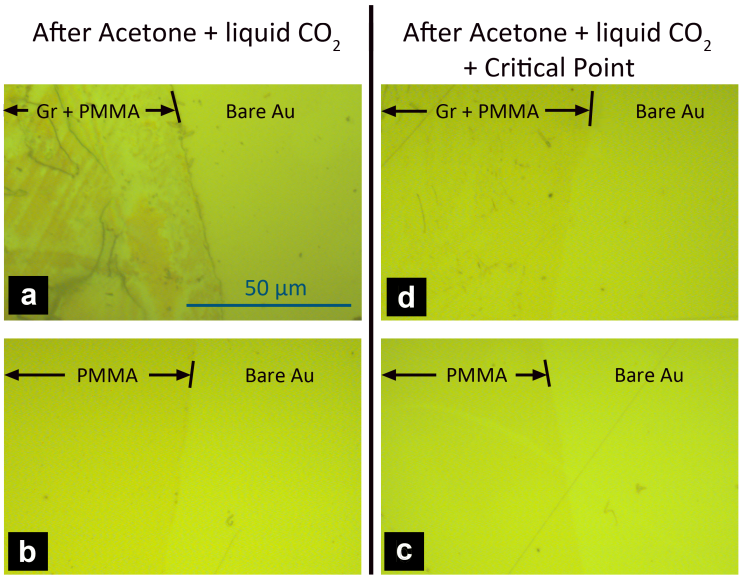

Figure 4.5: Optical microscope images of a gold substrate covered with a layer of a) PMMA + graphene, after undergoing a solvation in acetone, which was then exchanged with liquid CO_2; b) only PMMA, after the same process; c) PMMA + graphene after the full process used for this transfer method, d) PMMA only, after the full transfer method as well. The microscope images all have the same scale bar and are all taken near the edge of the deposited layers and bare gold in order to emphasize the visibility of each layer with respect to the same bare gold reference.

drying experiment as the liquid CO_2 and acetone always formed two phases in the chamber when not being heavily mixed. However its non polar nature would make its wettability on graphene very high, especially compared with acetone.

From the interactions between the materials previously mentioned, two hypotheses had to be tested in order to determine which interaction is responsible for the reduced PMMA residues. The aim of the following experiment was to determine whether the mixture of acetone + liquid CO_2 was responsible for the reduced PMMA residues, or whether taking the CO_2 to its supercritical fluid state was necessary for such enhanced residue removal. The second hypothesis tested was whether, as discussed in the previous paragraph, having graphene as a support for the PMMA could influence the removal of the polymer due to interaction of graphene with the various solvents.

Samples of (20 x 20) mm were prepared by evaporating a 10 nm adhesion layer of Cr, then 300 nm of Au onto a glass subtrate. Gold was chosen as a substrate due to its high conductivity, yielding a high SEM signal, but also due to its high acetone-

philicity. A graphene layer covered with 300 nm of PMMA was prepared as previously described and transfered onto two of the Au susbtrates. Two other susbtrates were also covered only with 300 nm of 950 PMMA A4, with the same parameters as done for graphene.

One of the gold samples with PMMA-covered graphene was submerged in acetone for 5 min. The acetone was then carefully exchanged with liquid CO_2 at 15°C. After fully exchanging the two solvents, the liquid CO_2 was exchanged once more with air. The second PMMA+graphene sample underwent the same process but the liquid CO_2 was then taken to its supercritical phase and then back to the gas phase, similarly to the full transfer process described in this work. If the interaction between the liquid CO_2 and acetone was responsible for the enhanced PMMA removal, the first sample would present the same amount of PMMA residue as the same sample. However, as shown in the optical microscope images in Figure 4.5, the sample which was not subjected to supercritical CO_2 was found to have visible PMMA residues remaining. In order to have a more quantitative measure of the residues, the thickness of the layers were measured using a DektakXT profiler, using a 120 s scan over 300 μm. The results are shown in Table 4.1.

Layers	Acetone + Liquid CO_2	Supercritical CO_2
PMMA + Graphene	45 nm +/- 10 nm	2 nm +/- 4 nm
PMMA only	10 nm +/- 4 nm	not distinguishable from bare Au

Table 4.1: Thickness of various layers after undergoing either a solvation in acetone and liquid CO_2 or the same process followed by a transition to the supercritical phase of CO_2, which corresponds to the full transfer process described in this work. The corresponding column is labelled 'supercritical CO_2 for clarity purposes. These thicknesses were collected using a Dektak profiler.

From an experimental point of view, it is important to note that when present, the PMMA residues were larger near the edge as expected from usual 'edge beads' formed during spin coating. As the edges beads were of negligible width (about 100 μm) compared to the bulk of the layers deposited, the results quoted were for the thickness of the main inner residues.

The results in Table 4.1 show that the amount of residues remaining after a solvation in acetone, then liquid CO_2 exhibited 15 % of the initially deposited polymer

remaining after the process. On the other hand, the full transfer process left less than 1 % of PMMA residues. This result therefore confirms the hypothesis that the supercritical phase of CO_2 plays a critical role in the removal of the polymer residues in this method.

The second part of the experiment, consisted in testing the hypothesis that the graphene affinity with the solvents and/or the polymer, also plays a role in the removal of the residues. From an organic chemistry point of view, solid clean Au was chosen as a substrate due to its metallic nature. This allows both polar and non polar molecules to rearrange more easily on its surface, making its wettability by most liquid solvents, whether polar or non polar, very easy. This is confirmed by the lower thickness of the residues PMMA after both processes compared with the thickness of the PMMA on graphene. This result therefore shows that the interaction of graphene with acetone is responsible for at least some amount of PMMA residue.

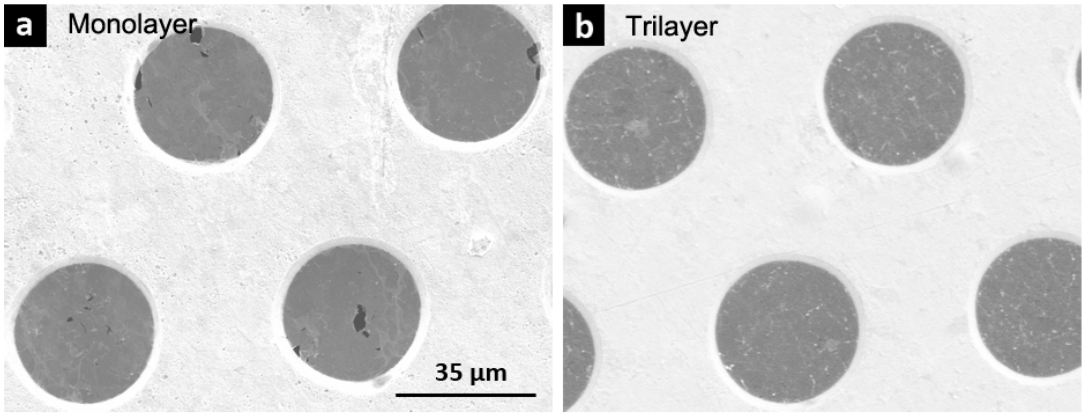

Figure 4.6: SEM images with enhanced contrast taken at a working distance (WD) of 7 mm at 8 kV showing an area of the patterned holes of 30 µm diameter and a pitch of 60 µm, a) covered with suspended monolayer graphene, showing a few defects of a micrometer or less in size, compared with b) a sample covered with completely defect-free suspended trilayer graphene. The white filament-like material present on some parts of the suspended layer corresponds to PMMA residues.

After narrowing down the interactions which were responsible for the lower amount of observed PMMA residues. The two mechanisms observed can now be safely correlated with what organic chemistry would predict. Indeed, from a more quantitative point of view, a liquid will be wettable on a solid surface if the surface energy (excess energy required to form a surface, compared to the bulk of the material) of the sub-

strate is $10\,\mathrm{mJ.m^{-2}}$ larger than the surface tension of the liquid [121]. Although it is easy to determine this value for liquids, for instance acetone has a surface tension of $25\,\mathrm{mJ.m^{-2}}$. On the other hand, for solids, the surface energy varies greatly depending on the crystalline orientation of the material, on surface adsorbates and on roughness. This can also create uneven wettability on the surface. The main advantage of this transfer method is that in the case of supercritical CO_2, the surface tension of the solvent is reduced to 0, and therefore will perfectly wet any surface. Adding to it the very small size of the CO_2 molecule, this leads to a very thorough penetration into all roughness details of the surface, and would therefore clean any soluble material.

4.4.4 Graphene Coverage

An analysis function was written in Matlab (see Appendix A) to compute the amount of unbroken suspended graphene over the holes, which will be referred to as graphene coverage henceforth. The method uses image segmentation based on the relatively higher secondary electron yield from areas with higher thicknesses and a significantly lower yield from defective areas which presented no support nor graphene. Segmented images were then separated into binary images using Otsus algorithm. SEM images were taken under a Zeiss EVO SEM, with slightly higher electron energy at $8\,\mathrm{kV}$ and with enhanced contrast in order to distinguish the different levels of electron yield. This allowed wider area survey while keeping the resolution at a maximum. In the interest of accuracy, the coverage of the layer over the holes was defined solely in terms of suspended material, without taking supported graphene on the substrate into account. A function was written in Matlab to determine the coverage of graphene using image segmentation. As a result, the coverage quoted in this work was defined by:

$$C = \left(\frac{A_{Gr}}{A_h}\right) \times 100 \tag{4.1}$$

where C was the coverage, A_{Gr} the total area of unbroken suspended graphene and A_h the total area of the patterned holes to be covered. The error to consider in this percentage therefore corresponded to the cumulative addition of the resolution of the SEM images and the subsequent error generated by the operations performed

by the function. As a result, the highest error in this measurement is mainly from the limitation of the SEM resolution over large areas as all holes of 35 μm cannot be checked individually over $(15 \times 15)\,\mathrm{mm}^2$. Consecutive SEM images were taken for the layers and mapped carefully in a grid fashion in order to measure the coverage. The coverages quoted do not include some occasional small defects of less than a few μm, which can be seen on a close-up graphene image in but not on the mapping. However it was found that these small defects only appeared on monolayer graphene, occasionally on bilayer, and were almost non-existent on trilayer graphene as illustrated in Figure 4.6. As these small broken holes are of negligible size compared to the overall covered area, only the largest ones are taken into account in the calculation of the coverage. This is illustrated in Figure 4.7, where image a) is a purposely chosen SEM image with a large amount of defects of different sizes. The corresponding segmented image obtained using the algorithm described above is shown in b) with the defects in the layer and coloured in dark blue, the covered holes in light blue. The images show that this method can be used to locate and take into account defects larger than 1 μm.

Aside from these small defects appearing on the monolayer, it was found that the other source of defects were either large scratches from manipulation of the samples or defects in the area on the edge of the transferred layers. The edges of the $(15 \times 15)\,\mathrm{mm}^2$ transferred graphene layers, presented a lot of defects over about 0.5 mm instead of a clear-cut edge between the layer and uncovered holes. Figure 4.7 a), for instance is an image extracted from one of the edge regions of a monolayer, with its corresponding segmented image. The coverage of the overall image was calculated to be 76 % but it can be seen that one side of the layer (which was further from the edge) is better covered than the other one, closer to the edge of the layer.

The pitch of the hole pattern was defined as the distance from one side of a hole to the same side of one of the nearest holes. Therefore, for obvious geometric reasons, the pitch had to be larger than the holes diameter, and the smallest hole size investigated were 35 μm, with a pitch of 60 μm and the largest hole size was 70 μm with a pitch of 140 μm. The data computed for the coverage showed that the values of coverage for different pitches were within error bars of each other and were therefore merged together in the plot presented in Figure 8. The graph shows the coverage of trilayer,

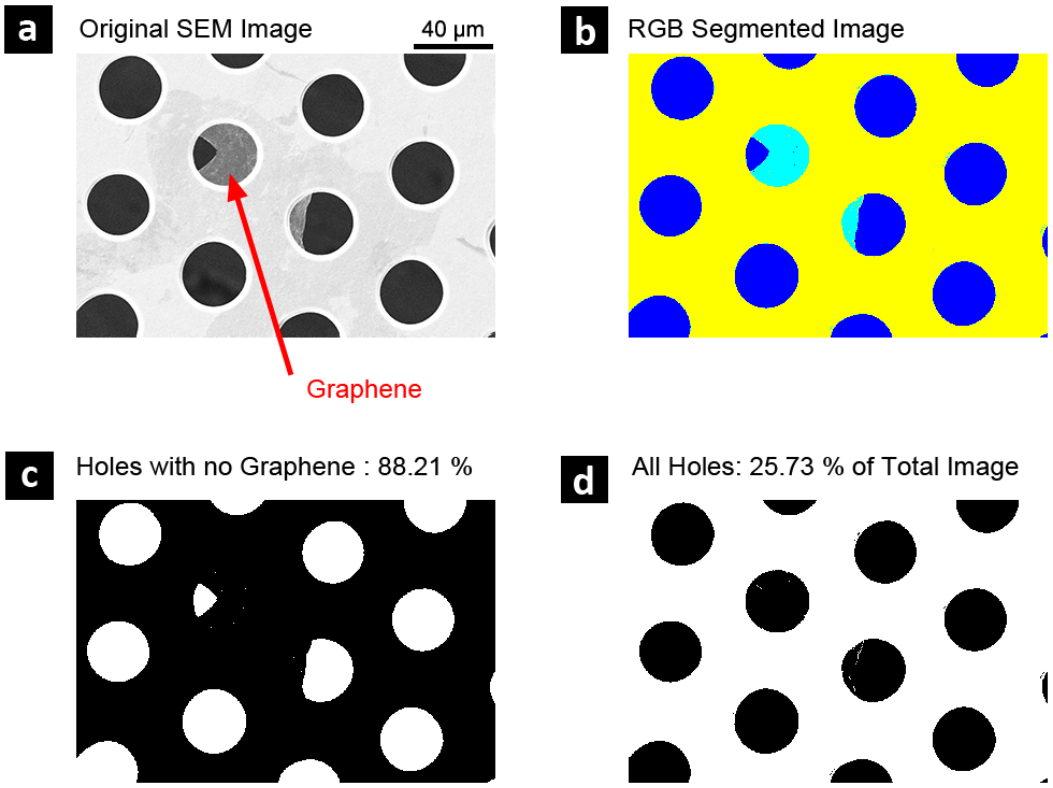

Figure 4.7: a) SEM image of suspended monolayer graphene on the edge of a transferred layer, illustrating a calculated 11.79 % coverage of the holes. The graphene is suspended over 35 µm holes with a 60 µm pitch, the hole areas with no graphene appear in black in the picture whereas covered holes appear light grey (as shown by the red arrow) b) Segmented version of the SEM image, used to detect defects in the layer for the calculation. The image is RGB coloured in order to enhance the differences between the different areas: the defective zones appear as dark blue, the suspended graphene appears as light blue while the copper substrate appears in yellow. c) shows the image computed by the function for the areas that have no graphene with the percentage of these areas with respect to d) the total areas covered by the holes on the image.

bilayer and monolayer graphene as a function of hole diameters. For all hole sizes and pitches investigated, we report a coverage of at least $(98 \pm 1)\,\%$ for suspended trilayer graphene over the full area transferred ($(14 \times 14)\,\mathrm{mm}^2$ on average, not including the edges of the layer which presented a lot of defects as discussed previously) up to an almost perfectly defect-free coverage of $(99.6 \pm 0.1)\,\%$. Bilayer graphene was found to have a very similar coverage as trilayer graphene for all hole sizes investigated, with values of at least $(98.1 \pm 0.5)\,\%$ up to $(99.7 \pm 0.5)\,\%$. Figure 4.8 shows an image of a very good quality bilayer graphene with 99.9 % coverage over 35 µm holes with a few occasional defects.

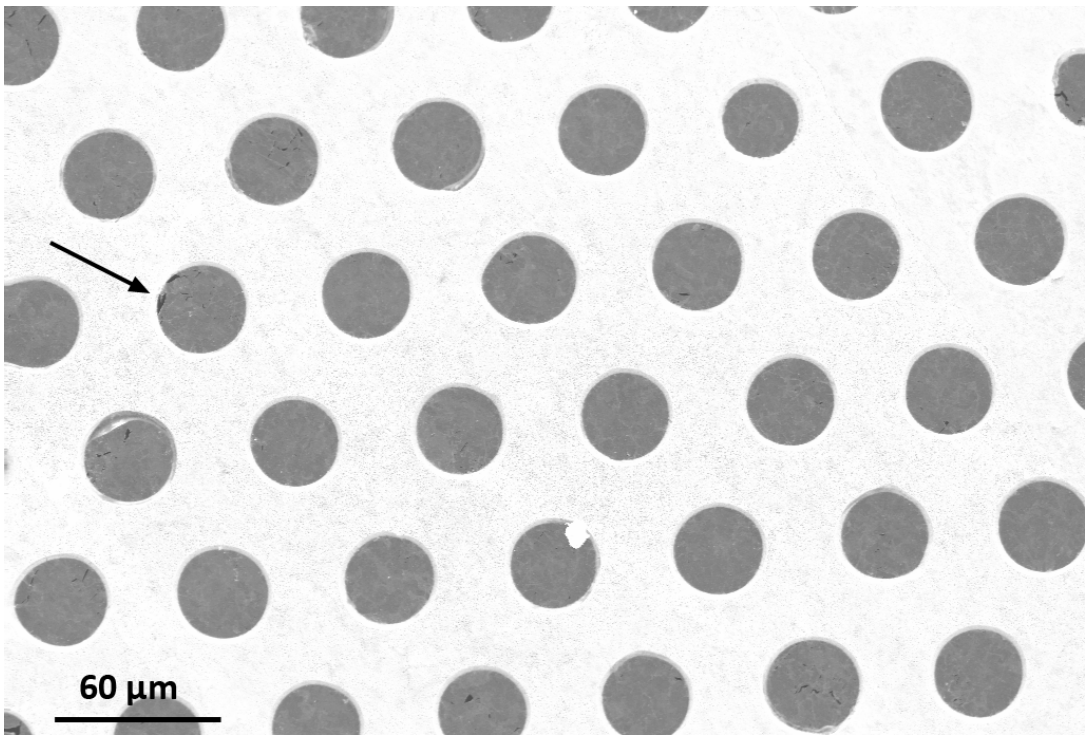

Figure 4.8: a) SEM image taken at 8 kV at a working distance of 7 mm of suspended bilayer graphene over. The layer exhibits 99.9 % covered holes, appearing in a grey colour on the image with very few occasional defects in black. One of them is highlighted by an arrow for clarity.

On the other hand monolayer graphene did not show full coverage like the other layers and presented an even lower coverage for larger holes. The coverage of monolayer was found to be irregular throughout a same sample and could vary between a very good coverage comparable to the multilayer one, to a much sparser coverage. This disparity is reflected in the error bars in the average values calculated for a

monolayer, which are plotted in Figure 4.9. Typical values for monolayer over 35 μm holes were found to range from 74.3 % to 90.2 %. For the largest hole size of 70 μm, the coverage was found to vary even more and could range between 30 % and 70 %. Some large defect contributions were found to be arising from manipulation scratches as the layer was extremely fragile. However the main contribution to this lower coverage percentage was from the existing imperfections of the layers from its growth on copper, before transfer. The layers are quoted by the provider to have a guaranteed $>$ 95 % coverage [122] on the original copper growth substrate, which makes our transfer of the layers almost defect free despite existing imperfections. By layering the graphene layers, into two and three layers, perfect coverage was therefore obtained as not only the layer was strengthened by the presence of more support, but the original imperfections from growth were also covered by the extra layers.

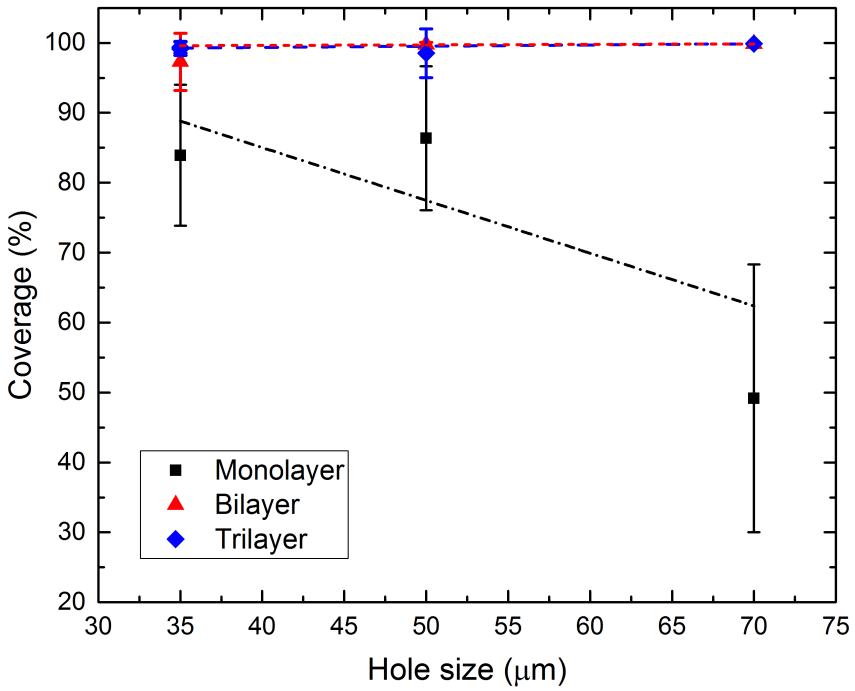

Figure 4.9: Graph of the coverage of monolayer, bilayer and trilayer graphene as a function of hole diameter. The data takes into account different pitches as they did not show a significant difference in coverage and were within error bars of each other. The dashed lines are linear fits of the data.

We have therefore shown that this method can be reproducibly used to produce virtually defect-free large area suspended bilayer and trilayer graphene. These layers were successfully suspended over holes of at least to 70 µm diameter and below, a size that has not been achieved before. Monolayers presented a larger amount of defects which showed an increase with increasing hole size, as expected. A large contribution to these defects is due to the imperfect growth of graphene of at least $> 95\,\%$ depending on the sample, and therefore there were existing defects prior to transfer. As a result, the coverage of suspended monolayer can be improved by enhancing on the coverage during growth.

4.4.5 Graphene Quality

Disorder and defects in graphene activates the so-called D peak in the Raman spectrum of graphene located around $1250\,\mathrm{cm}^{-1}$. This peak is not influenced by strain nor intercalated dopants and is only sensitive to structural and active defects [115]. The presence of these structural defects is in fact a necessary condition for the activation of this peak, which makes it a unique tool to assess the presence of damages and reconstruction in the lattice which may affect the properties of the layer. The Raman spectra of transferred monolayer, bilayer and monolayer on copper all showed either the absence or the presence of a weak D peak as shown in Figure 4.10. The ratio $\mathrm{I_D/I_G}$ of the intensity of the D peak, to that of the G peak was taken only for monolayer graphene in order to avoid influences to the spectra from stacking orientations [123, 124], and only for supported monolayers in order to rule out G peak intensity changes from strain [115]. The distance between defects on the sample can be calculated using the following formula [91, 115]:

$$L_D^2(nm^2) = \frac{4.3 \times 10^3}{\omega_L^4(eV^4)} \left(\frac{I_D}{I_G}\right)^{-1} \tag{4.2}$$

where L_D is the average distance between structural defects in nm and ω_L is the energy of the laser in eV. From this L_D was found to be 70 nm or more, which lies beyond the validity of the formula quoted above for defects between 3 nm and 30 nm apart [91]. This indicates that the process has not damaged the graphene structurally and the low intensity of the D peak indicates a high crystallinity and quality in the

layer.

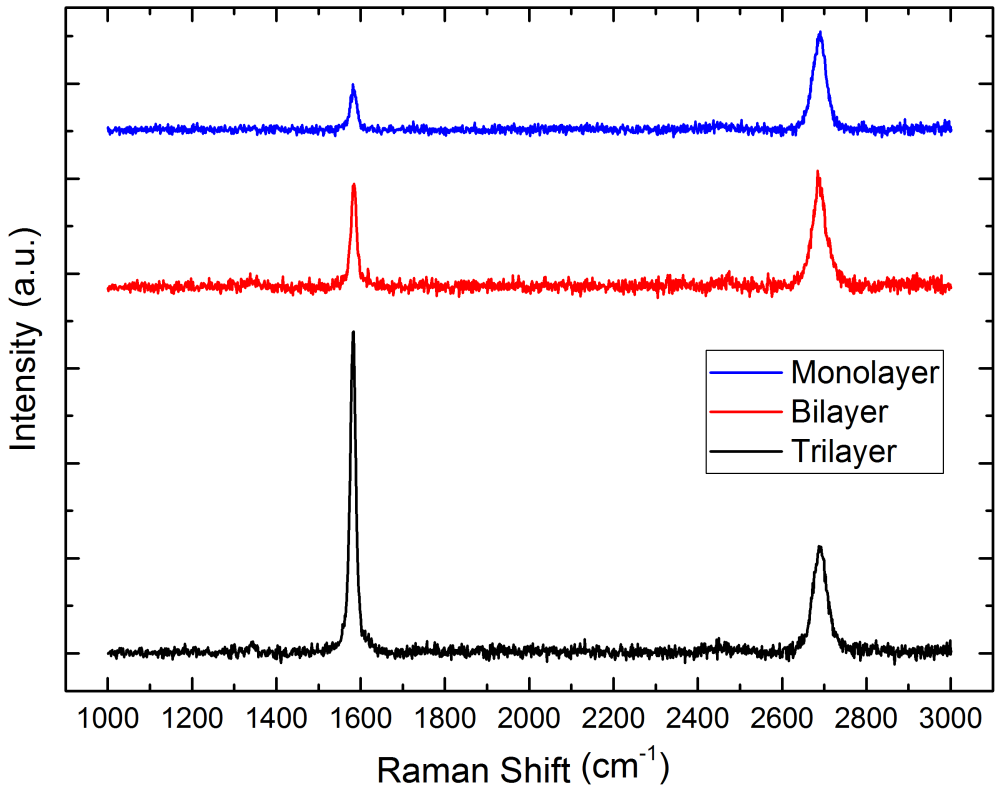

Figure 4.10: Typical Raman spectra of graphene monolayer, bilayer and trilayer showing a small D peak around 1350 cm^{-1}, the G peak around 1580 cm^{-1} and the 2D peak at about 2700 cm^{-1}.The graphs are offset for clarity.

4.4.6 Strain

Suspended samples have been shown in other works [51, 62] to be subject to non-negligible amounts of strain, which affects the properties [125] of the layer. In this work we show that this process can suspend graphene without inducing a measurable amount of strain on the layer. Raman spectroscopy is a tool that has been widely used [62,126–132] in the past for the measurement of strain on suspended graphene. For the same reasons as in the previous section, the following measurements were performed on monolayer graphene in order to avoid convolution from interlayer coupling and other effects related to multiple layers, which can affect the Raman spectra.

Figure 4.11 shows a Raman line scan across a hole with a suspended monolayer.

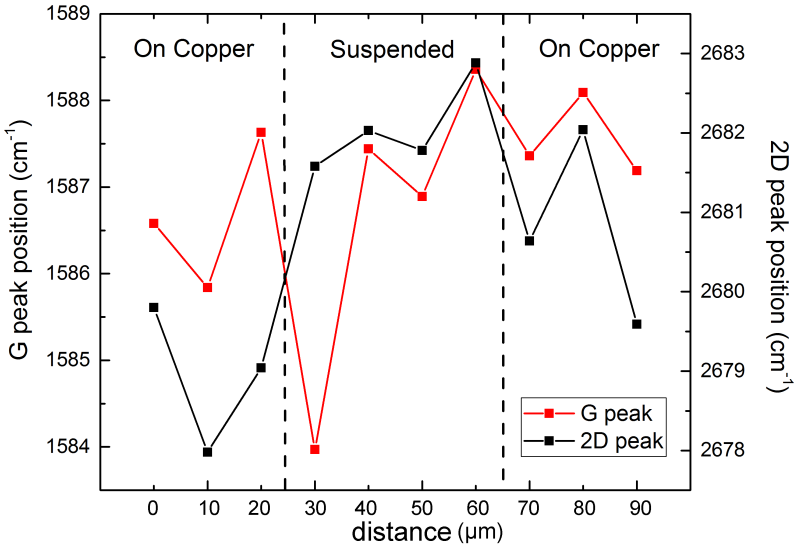

Figure 4.11: Raman line scan across a hole with suspended monolayer graphene showing no significant increase nor decrease in the G peak position, and in the 2D peak position, indicating the amount of strain on the suspended layer to be less than 0.1 %.

The positions of the G and 2D peaks are plotted as a function of distance. This graph shows that the shift in the peaks varied across the line scan, but that there was no significant difference between suspended graphene and supported one. Further calculations are shown below in Table 4.2, with an average of G and 2D peak positions ω_G and ω_{2D}, and their full width at half maximum (FWHM): Γ_G and Γ_{2D}. The slightly higher error in the values for the G peak is due to the lower intensity of the G peak compared to the 2D peak for monolayer graphene, which made the fitting of the peak less accurate.

	Suspended	Error	Supported	Error
ω_G (cm^{-1})	1586.7	1.9	1587.1	0.8
ω_{2D} (cm^{-1})	2682.0	1.0	2680.0	2.0
Γ_G (cm^{-1})	14.7	5.5	16.1	2.7
Γ_{2D} (cm^{-1})	33.2	2.4	33.5	1.5

Table 4.2: Positions of G and 2D peaks, as well as their FWHM compared for suspended graphene and supported graphene on copper, with their standard deviation. All numbers in the table are in cm^{-1}

.

The overall change in the respective positions of the peaks was found to be within standard deviation from one side to the other of the hole, as well as for the FWHM of the peaks. The measured difference between the positions was also much smaller than measurable values from literature. Indeed, for tensile uniaxial strain [62, 126, 127] of 0.01 %, we expected a G peak and 2D peak downshifts of a least $\Delta\omega_G = -10\,\mathrm{cm}^{-1}$ and $\Delta\omega_{2D} = -20\,\mathrm{cm}^{-1}$, or an increase [128, 129] in their full with half maximum Γdue to splitting of the bands into two components with increasing tensile uniaxial strain. Similarly for biaxial strain, which is what would be expected in this work due to the isotropic nature of the concentric pattern used to suspend graphene, we expected comparable, if not larger downshifts [130–132] of the same peaks. Using the Grüneisen parameter γ, a measure of the strain on the layer can be derived from the peak shifts according to the following formula:

$$\gamma = \frac{-1}{2\omega_0}\frac{\partial\omega}{\partial\epsilon} \tag{4.3}$$

Where ϵ is the biaxial strain on graphene, ω_0 is the strain-free frequency of the Raman vibration and ω is the frequency of the same vibration under biaxial strain. Using the parameters determined by previous works [130–132]: $\omega_G = 1.8, \omega_{2D} = 2.6$, and taking the two extreme values of ω_G and ω_{2D} to be the relaxed and strained values, the biaxial strain ε was found to be less than 0.001 % in all samples. Finally the ratio of the intensity of the 2D to G peaks I_{2D}/I_G did not show any further discrepancy between suspended and supported monolayer, which indicates that the layer deposited using this technique was not subjected to any measurable amount of strain.

4.4.7 Topography of the Layer

Atomic force microscopy (AFM) was also used to characterise the topography of the suspended layers in order to investigate further the findings on strain. The imaging was done on a Bruker Dimension Icon, with an amplitude-oscillation silicon tip of 40 µm wide, also called point probe plus non-contact long cantilever (PPP-NCLR) with a resonant frequency of 160 kHz, tuned at 5 % of the maximum resonance. In order to minimise damage, the scan rate used was the lowest possible: 0.10 Hz for a surface area of $(70 \times 70)\,\mu\mathrm{m}^2$. A suspended atom thick layer over such large areas

being undoubtedly very fragile, characterising the layer with AFM without breaking them or adhering the broken graphene onto the tip proved to be a challenge, and the parameters presented in this work were found to be changeable only within a very narrow range if damage was to be avoided. The effects of too high tip-sample interaction is shown in Figure 4.12, where the tip was approached onto the sample from the bottom right corner, breaking the layer immediately in that area. The scan continued further upwards, showing an initially pristine graphene layer being damaged by the tip. Confirmation of the breakage was done on the microscope. Suspended graphene is not distinguishable under microscope illumination, however the reflection from some leftover PMMA strands can be seen by changing the focus. Where some suspended PMMA strands were visible originally under the microscope, none were distinguishable in the same holes after the AFM measurement. This suggested any suspended material was removed during the scan.

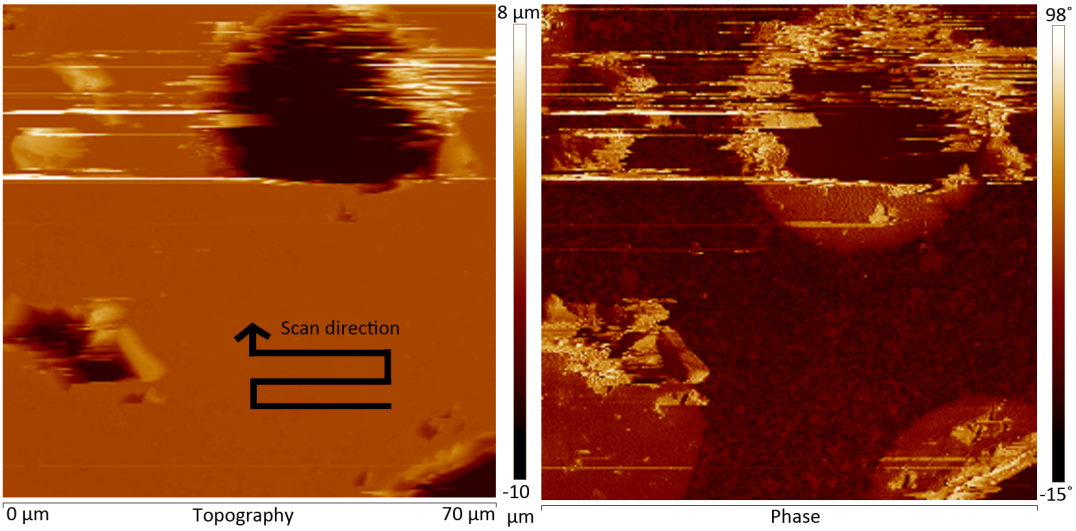

Figure 4.12: Typical AFM image showing the graphene layer breaking and being dragged along by the tip during the scan due to a too low setpoint to free amplitude ratio. The scanning direction is upwards, and the approach was performed from the bottom right corner. Left image: topography image showing the holes in the suspended layer, right: phase image distinguishing between the high damping over suspended graphene and the low damping on the copper substrate.

The two main challenges that had to be addressed were therefore to not break the suspended graphene during the scan, and the second one was to not incur damage to the tip. Two types of damage were found to occur throughout the scan of these

samples: the tip was found to either be broken by encountering a deep hole or to be contaminated by broken graphene adhering to it. A broken tip is shown in 4.13 compared to a sharp tip, this occurs because the holes used in the sample are infinitely deep comparatively to the size of the tip/cantilever, and the tip will be driven to oscillate at its maximum capacity in order to probe the empty surface. As the tip is moved along by the scanner, this causes it to break upon contact of one of the sides of the holes. In order to prevent tip damage, care was taken to choose areas where there were as few defects as possible. Tip contamination was more difficult to avoid due to the initial fine tuning required to prevent graphene from breaking. A typical image of graphene breaking and subsequent dragging of the layer by the tip is shown in 4.12. Unbroken graphene is recognisable from the very light colours on the phase image. Scanning over the suspended graphene induces higher amounts of damping in the AFM resonant frequency compared to the scan over copper. This translates into a large phase shift in the signal feedback when scanning over graphene. Pieces of graphene breaking below the tip and being dragged along during the scan enhances this damping even further, resulting in very large phase shifts which can be used to determine the composition of the image as a complement to the topographic information.

The topography image shows two pieces of graphene poorly adhered onto the sample in the top left corner (in white) appearing as a result of the hole breaking and dragging to the left of pieces of graphene, shown as white lines.

In order to limit the disturbance of the layer to a minimum, an extremely delicate balance between tip-sample force and resolution had to be achieved in order to obtain an image. In order to reduce the force applied to the layer [93], the free amplitude of the tip was decreased from the default 350 mV value down to 100 mV. This value was the minimum value for which the loss in resolution was still negligible. Similarly, a high setpoint to target amplitude ratio of 0.9 was used to minimize the force [133] by keeping the tip at a reasonable height from the layer. With these two fixed parameters, the drive amplitude applied to the tip had to be increased from the default value in order to keep the trace and retrace matching. The minimum values found to match the tip traces without inducing noise or graphene breaking, were found to

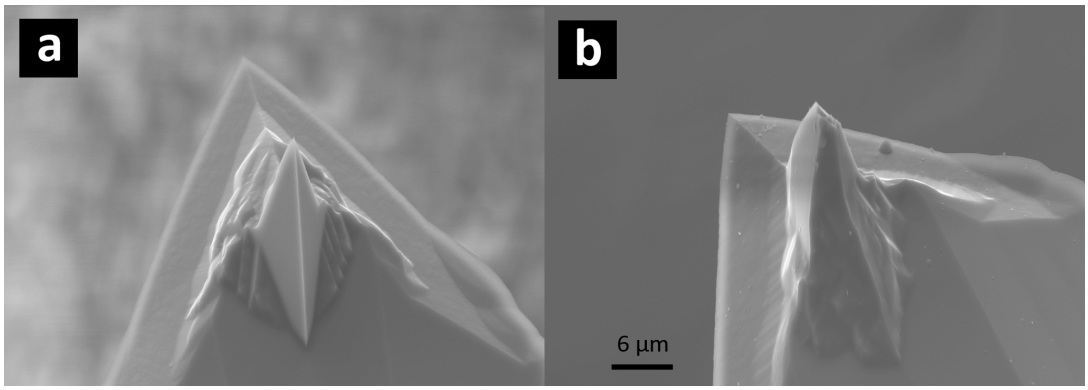

Figure 4.13: SEM images of n-doped silicon tips used in this work for non-contact mode measurements, both images were taken at an accelerating voltage of 10 kV and at a working distance of 10 mm. The first image shows a) a new AFM tip showing a sharp tip and the second image shows b) a broken AFM tip after being wedged into the side of one of the copper holes. The images were taken using a mixed signal of 50 % - 50 % from the Inlens and SE2 detectors.

lie very consistently between 15.70 mV to 15.90 mV. Typical values for the integral gain were found to be variable and would change between 1 and 6 depending on the sample. A successful AFM image is shown in Figure 4.14 a), with the corresponding topographic interpretation of the forces measured by the tip and the phase difference image between the free amplitude oscillation of the tip and the damped oscillation due to sample interaction. The phase image is shown in inset b) where the holes are easily distinguishable from the copper substrate due to the larger damping induced by the softer suspended layer.

Due to the atomic thickness nature of the suspended layer, very strong interactions with the tip could not be avoided. These interactions are evidenced in the cut out of a topography image shown in Figure 4.14 c). The suspended graphene was found to have much stronger interaction forces with the tip, which is translated into an apparent "higher" topography. This strong interaction is also evidenced in the phase image by large damping of the tip oscillation over the holes, which colour is clearly distinguished from the brown low damping colour of the hard copper substrate. The layer was also found to have an oscillation driven by the tip appearing as very regular spikes in the cut-out topography c). The AFM phase image shows holes with an imperfect spherical shape. These imperfections are defects from the photolithographic fabrication of the holes and are not related to graphene. This is clearly shown in inset d) where a

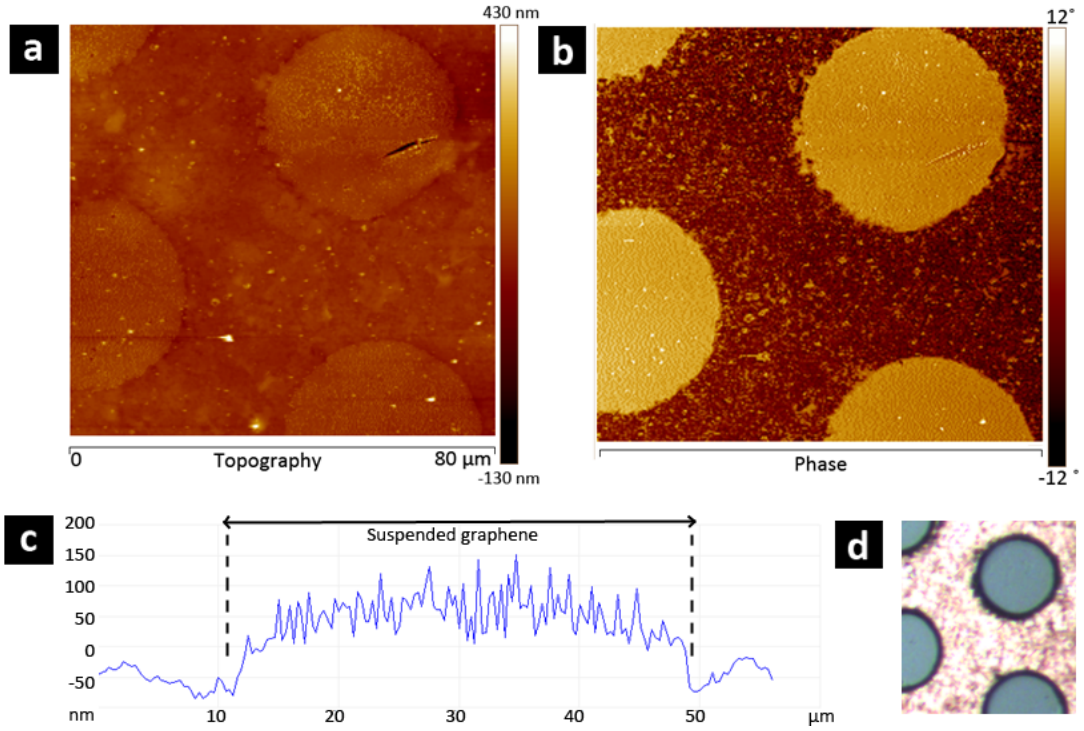

Figure 4.14: a) Topography image of suspended graphene over 35 µm holes showing a defect in the upper right hole, indicated by the arrow, b) phase image of the same AFM image showing the high damping of the tip over the holes, c) a cross section of the AFM image across a hole, showing the large interaction of the tip with the sample, d) a microscope image of the area investigated, showing that despite the AFM image showing the clear presence of a layer across the hole, this cannot be evidenced under simple microscope illumination.

microscope image of the same AFM region is shown. The dark ring around the hole shows the exact same shape as the irregularities of the hole in the AFM image. These are a result of over-etching, eroding the upped sides of the hole and are therefore also covered in suspended graphene as seen by the yellow colour in the AFM phase image. The information on strain from this type of measurement was found to be difficult to correlate with Raman measurements due to the strong tip-graphene interaction forces. On the other hand, the AFM images gave a decisive confirmation of the SEM measurements showing the full coverage of graphene over the holes, and evidenced the fragile nature of the layers.

4.4.8 Doping

Within the constraints of the experimental conditions described previously, the position and FWHM of the G peak, ω_G and Γ_G can only have contributions from doping and strain. The latter having been ruled out previously, the remaining contribution would be from doping. On the other hand, the 2D mode can also have contributions from interlayer coupling between graphene sheets. This appears as extra mode contributions to the 2D peak, which is usually centred around 2685 cm^{-1}, and can therefore increase the FWHM Γ_{2D}. The multilayer graphene transferred using this technique showed 2D modes of similar shapes regardless of the number of layers as shown on the normalised spectra of Figure 4.15 a). The values of Γ_{2D} for bilayer, trilayer and monolayer were found to be within standard deviation of each other with an average value of (37 $\pm$ 3) cm^{-1} and could be fitted with a single Lorentzian. The details of the values for the FWHM of each layer are shown in Table 4.3. This single 2D peak is characteristic of artificially stacked multilayer graphene [123, 124, 134] and denotes a weak interlayer coupling. This was checked by calculating the ratio I_{2D}/I_G which was found to vary greatly across the bilayer and trilayer due to different grain orientations stacked at varying angles. For this reason, although the doping of the layers influences the intensities of the G and 2D peaks, this information cannot be used to identify doping contributions without separating the contribution from layer orientation.

Layers	Γ_G (cm^{-1})	Γ_{2D} (cm^{-1})
Monolayer	16.1345	40.2014
Bilayer	17.0903	33.6564
Trilayer	18.2847	36.5221

Table 4.3: FWHM Γ_G and Γ_{2D} of the average G and 2D peaks for monolayer, bilayer and trilayer graphene.

The plots of the G and 2D peaks in Figure 4.15, are averaged over 100 μm^2 area in order to rule out local statistical variation, and were integrated over an exposure of 120 s. ω_{2D} is observed at 2688.54 cm^{-1} for single layer graphene and shifts up with an increasing number of layers while ω_G downshifts for increasing layers. After ruling out strain effects from suspension, effects from defects, and interlayer coupling in the

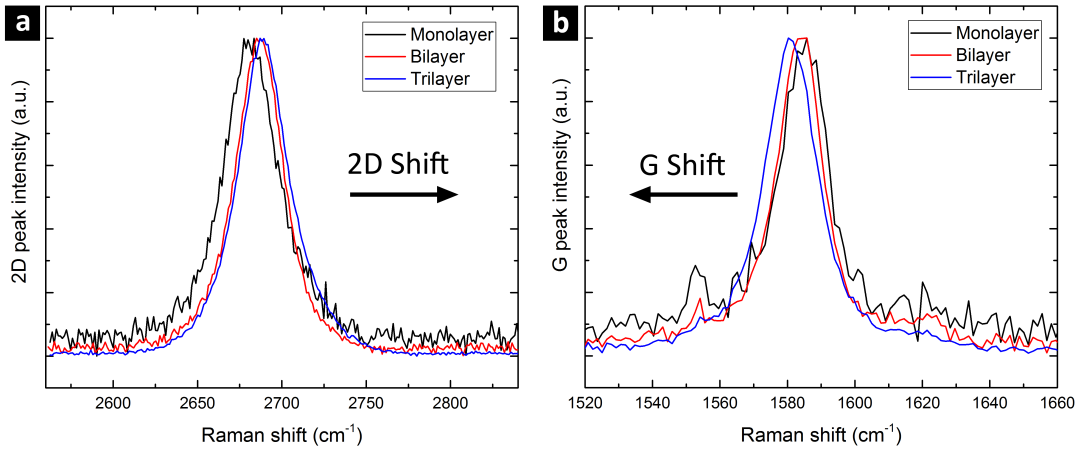

Figure 4.15: Raman spectra showing: a) the 2D peak for monolayer, bilayer and trilayer graphene showing a shift to higher values for more layers: $\Delta\omega_{2D} > 0$. The single Gaussian shape for the multilayer Raman indicates weak interlayer coupling between the extra layers. b) the G peak for monolayer, bilayer and trilayer graphene, showing a negative $\Delta\omega_G$.

previous discussions, the only remaining contribution to this shift $\Delta\omega_{2D}$ would be doping. A more quantitative plot of the observed shifts is shown in Figure 4.16. As shown in Figure 4.16 a), the G peak assigned to the high-frequency E_{2g} vibrational mode [115] was observed around 1586 cm^{-1} for monolayer graphene and showed a downshift $\Delta\omega_G$ = -2 cm^{-1} as the number of layers increased.

As all other contributions have been ruled out in previous discussions, this change in ω_G can be safely attributed to doping. The negative shift $\Delta\omega_G$ is a well investigated effect of a decrease in charge (either positive or negative) doping [135–137]. Such decrease in doping is also expected to yield a widening of the G peak, which is expected to be at its widest around the charge-neutral Dirac-point [135,138]. Another expected result of a change in doping is an upshift in ω_{2D} for hole doping. On the other hand, electron doping is not expected to affect ω_{2D} [135] for doping below 3 x 10^{13} cm^2. Table 4.3 indeed shows an increase of 1 cm^{-1} in Γ_G as expected, while Γ_{2D} does not exhibit any obvious trend. On the other hand, ω_{2D} is found to increase with number of layers, with a consistently larger increase of about 5 cm^{-1} between one and two layers, and a smaller increase of about 2 cm^{-1} between bi- and trilayer. This stiffening and sharpening of the G peak, and softening of the 2D peak as the number of layers decrease, are typical effects of a light increase in doping [135,139].

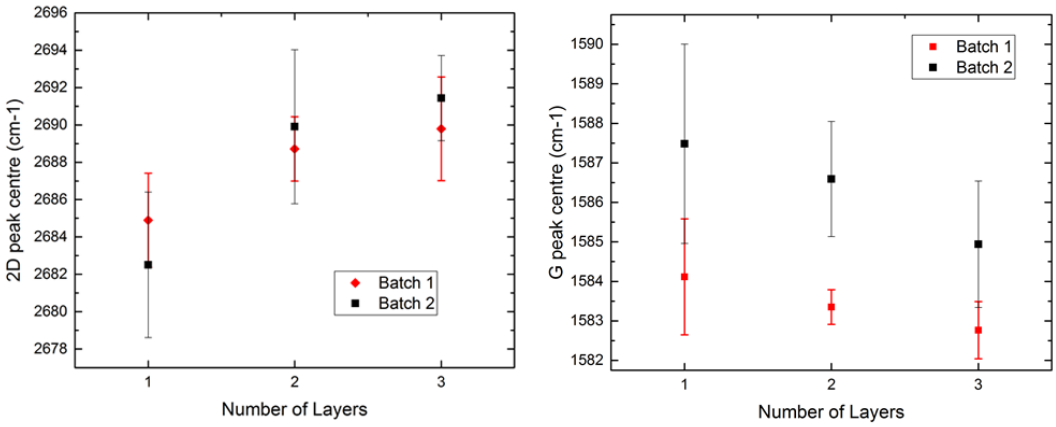

Figure 4.16: Graphs showing a) a downshift in the position of the G peak with an increasing number of layers, b) a shift of the 2D peak towards higher values. Both graphs show two samples where each point correspond to the average of the peak positions for all the spectra taken for that layer.

This doping decrease with an increasing number of layers has been observed in previous works, and has been interpreted as doping from the supporting substrate. One layer would be more doped by the substrate while a larger number of layers are less influenced by the underlying support.

4.4.9 Grain Boundaries

As previously discussed in Section 1.5.1 one of the main causes of deterioration of the mechanical and electrical properties in grown graphene is the formation of islands of graphene with different orientations during the growth process called grains [17, 140]. At the boundary where these grains meet, the usual structure of graphene is altered. Such graphene is called polycrystalline graphene and exhibit deteriorated mechanical and electronic properties compared with single crystal graphene [17, 58, 59, 141].

Zhang et al. [142] have reported the finding of two types of grain boundaries: "flat" and "inflected" (where the grain forms an out-of-plane inflexion) and predict that flat grain boundaries would decrease the intrinsic tensile strength of the layer linearly with increasing formation energy of these boundaries. Similarly, they show that the tensile strength of inflected boundaries will decrease with increasing angle of inflexion.

The presence of such boundaries would therefore deteriorate the mechanical strength of the layers suspended in this work. For this reason it was important to quantify the

amount of grain boundaries of the layers. For this, multiple solutions which have been presented in literature will be discussed here along with whether they are applicable to this work.

4.4.9.1 Oxidisation

The easiest technique at first sight would be the optical characterisation using microscope by oxidising the copper substrate [143, 144]. The papers describe an annealing method using oxygen radicals produced by UV irradiation of O_2 gas at room temperature and room pressure.

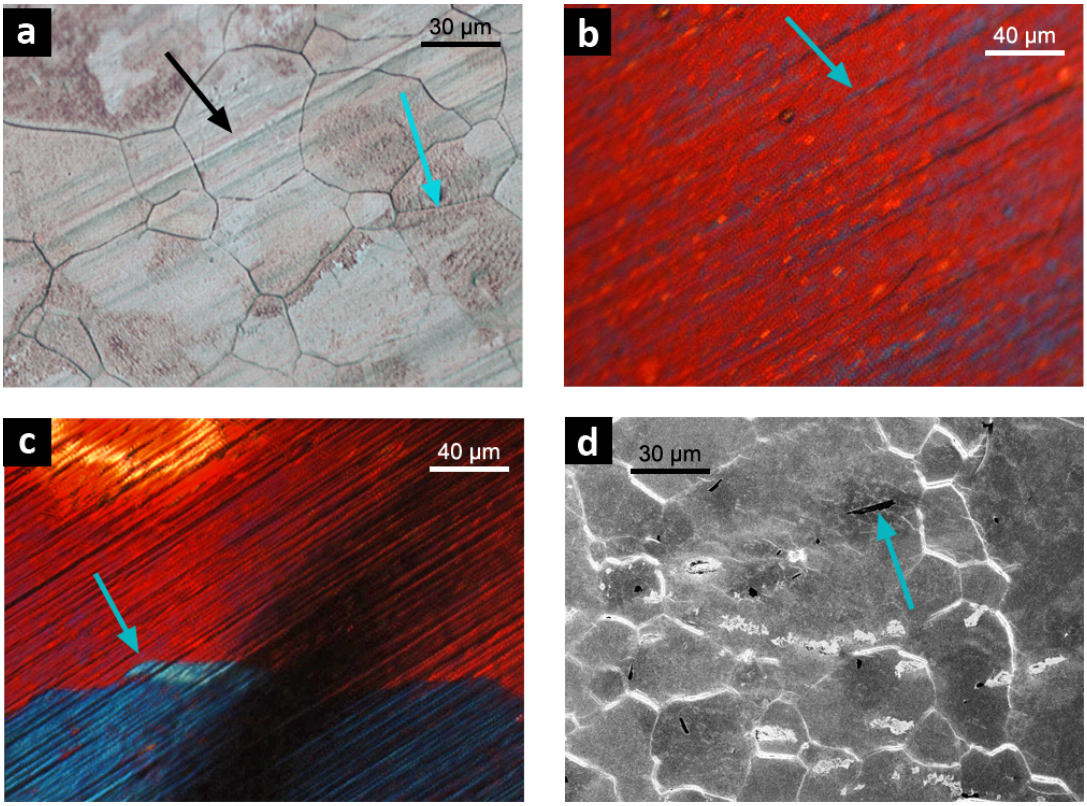

Figure 4.17: a) Optical microscope image showing a sample of commercial graphene used in this work, the black arrow indicates a copper inflexion while the blue arrow indicates a copper grain boundary. b) A microscope of a sample of commercial graphene annealed at room temperature using Ozone (O_3) radicals produced under UV (as described in [144]) for 5 min. The blue arrow the selective annealing of copper inflections. c) Another microscope image of an annealed sample for 10 min. The arrow shows the annealing of a copper grain (in blue). d) An SEM image of a graphene sample showing in white the copper grain boundaries. The arrow indicates an area where the graphene was scratched away.

The setup used in this experiment consisted of a steady O_2 flow through an Ozone generator (where UV light is used to break O_2 into oxygen radicals). The sample cleaned with acetone and IPA and was put under vacuum, and a steady of O_2 was flowed through at 10 Torr, the Ozone generator was then turned on for 5 min for some samples and 10 min for other samples. It was found that the oxidation was produced preferentially along the copper grain boundaries and inflexions of the copper as shown in Figure 4.17. Image d) shows an SEM of the graphene on its native copper, with the copper grain boundaries as well as areas of bare copper (where the graphene was scratched away). As the graphene was not grown-in house as described in the papers, nor was the information provided in the paper very thorough in terms of the setup used, this method was not pursued further.

4.4.9.2 Fluorescence Labelling

Another method explored for the estimation of grain boundaries was to label grain boundaries with fluorescent markers. As grain boundaries are more reactive than pristine graphene [145, 146], similarly to the preferential oxidation technique along grain boundaries described in the previous subsection, we attempted to functionalise the boundaries with primary amines (-NH_2) instead of the very reactive Oxygen radicals. The aminated grain boundaries would then be labelled with FITC (Fluorescein isothiocyanate) [147], a commonly used fluorescein derivative used to label amino-acids in biology. This molecule is very reactive towards amine radicals and forms a bond with the functional group. This would allow for the fluorescent labelling of the grain boundaries using a confocal microscope.

The procedure consisted in cleaning a sample in IPA and acetone and putting it under vacuum in a chamber. A flow of ammonia (NH_3) gas is then passed through the chamber to clean any remaining oxygen (care must be taken to remove as much gas a possible as ammonia is highly reactive). The chamber is then filled with NH_3 up to 150 Torr at room temperature. A 300 W UV lamp is then shone directly onto the sample through a UV-clear window on the chamber for 1h30 for some samples and for 5 h for other samples. The samples are then labelled with FITC. The preparation protocol used for the labelling is described in Section 3.8.1. The samples were then

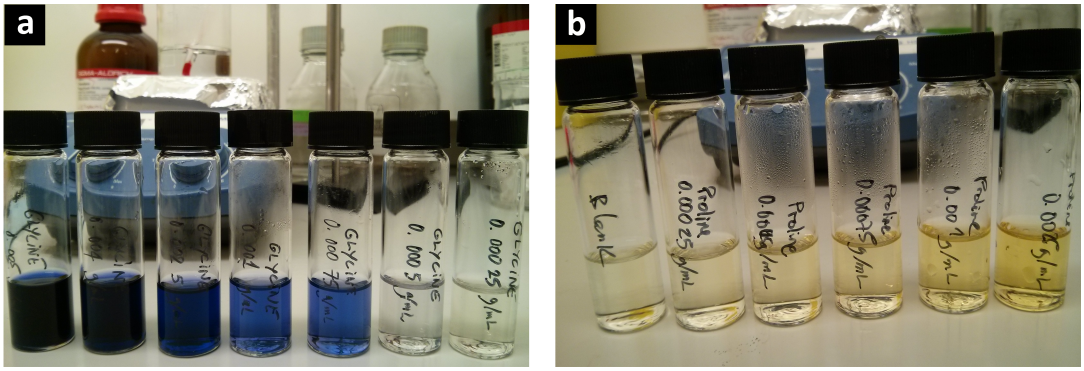

Figure 4.18: a) This photo shows solutions with concentrations of glycine between 0.25 mg/mL to 5 mg/mL and their colour after reaction with ninhydrin. b) This photo shows solutions with concentrations of proline between 0.25 mg/mL to 5 mg/mL and their colour after reaction with ninhydrin, along with a blank (just ninhydrin) solution.

investigated under confocal microscope and were found to have no labelling.

In the light of that results, the first step was to check whether the amination process was successful. For this a different graphene was used: AO3 graphene flakes which has a larger reactive surface due to the small flake (12 nm average size) nature. The flakes underwent the same amination treatment described previously. As it was difficult to separate the labelling molecules and the small flakes in solutions, another method was used to assess whether amines were present on the sample: ninhydrin colorimetry. Ninhydrin ($C_9H_6O_4$) is an aromatic molecule generally used to determine the presence of amines. It is a destructive method as it will bind to the amine function to form a new coloured composite which is soluble in alcohol. The solution will therefore take a purple colour in the presence of primary amines (-NH_2) and an orange colour in the presence of secondary amines (-NH). The protocol used in this work is described in 3.8.2.

The controls used were commercial amino-acids: glycine (a primary amine) and proline (a secondary amine) as shown on Figure 4.18. Preliminary results were conducted and were not conclusive in determining whether the AO3 graphene samples were successfully functionalised either with -NH_2 or -NH terminations. Further work would be needed to reach a definite conclusion.

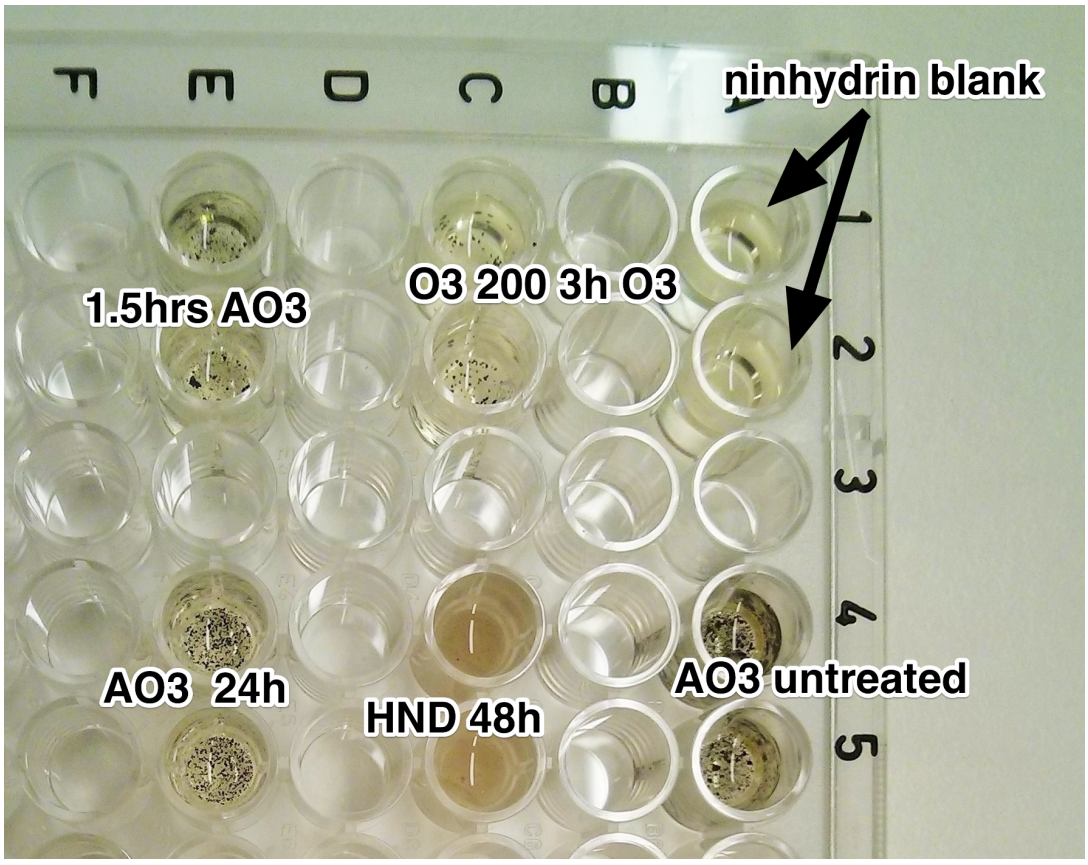

Figure 4.19: This photo shows an assay with ninhydrin blanks, AO3 graphene in a ninhydrin solution (untreated), AO3 graphene treated for 1.5 hours in Ammonia, and for 24 hours. The two samples in the middle (O3 and HND) are unrelated to this work but were not removed from the image to keep to full picture and show that the samples were measured on the same day.

4.4.9.3 Carrier Mobility

Another method attempted to determine grain boundaries in this work was the fabrication of a suspended graphene device to measure the carrier mobility in the layer. The process used to fabricate the samples are outlined in Figure 4.20 a). The process was conducted with the help of Nuno Braz who operated the Argon mill and EBL exposure.

This process was designed as a preliminary process used to assess whether the graphene could be suspended over gaps of different sizes. Six 5 x 5 mm preliminary samples were produced using gold (the gold surface would be easier to ground to obtain SEM measurements, this was planned to be changed at a latter time when the

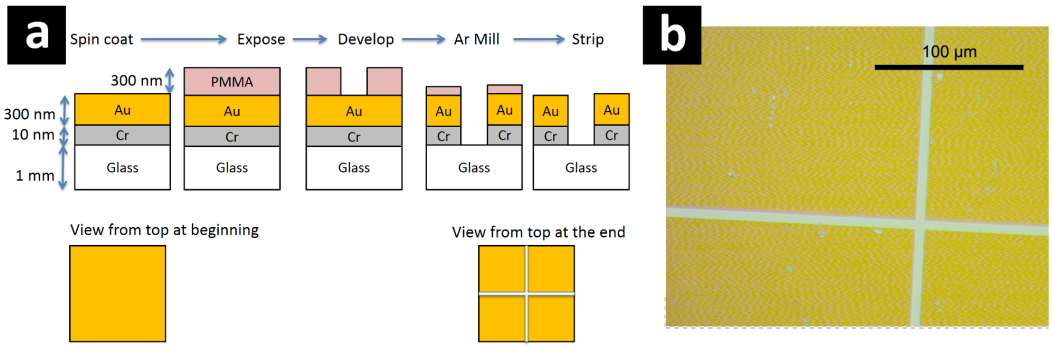

Figure 4.20: a) Diagram illustrating the process used to produce the test samples for suspended mobility measurements, b) Microscope image of the sample illustrating one of the samples produced using this method.

suspension process was established). The EBL settings were as follow: a voltage of 10 kV, a current of 1.75 nA and an aperture of 120 µm. The samples were then developped using MIBK:IPA 1:3 for 1 min, then IPA 1 min and dried with N_2. The widths of the crosses obtained after Argon Mill (5 sccm, 120 min, 58 rpm, 390 V acceleration voltage, 200 V beam voltage and 9 mA current) were 5 µm, 1.4 µm and 600 nm.

The samples were all checked for shorts between the 4 gold pads and showed a resistance which was beyond the scale of the voltmeter. Graphene was then transferred onto the samples across the lines using the same method as previously described in this chapter. The graphene was found to curve towards the bottom of the shape and further work would be required to investigate the reason for this. Future developments and exploration paths will be discussed in Chapter 8.

4.5 Conclusion

To summarise, a new method to transfer graphene was successfully developped and refined during this project and presented in this chapter. This method was shown to suspend graphene, grown natively on copper onto supports patterned with holes up to 70 µm diameter, a very large step from the usual sizes achieved so far in literature: 5 µm. In this chapter, the quality of the single, bi and trilayer suspended graphene obtained were assessed using Raman spectroscopy, scanning electron microscope and atomic force microscopy. The experiments have shown not only that this method

produces clean graphene, but also good quality layers which have reduced amount of PMMA residues. The origin of the residues were also discussed, and finally the coverage of the layers and some key properties: strain and doping were investigated. A few methods were explored for the assessment of grain boundaries in graphene and will be discussed further in Chapter 8.

Chapter 5

Optimisation, Calibration and Behaviour of Parameters in a Modified Triple GEM Detection Chamber

5.1 Abstract

The measurement setup was custom built at CERN by the group of Prof. L. Ropelewski. The system is based on the currently investigated triple GEM system described in section 3.7. The system used in this work is very similar but parameters and components had to be tuned to adapt to the presence of the graphene layer. In this chapter, the systematic variation of parameters used further in this thesis was conducted. Subsequently, measurement methods developed for the measurements as well as new parameters resulting from setup modification were characterised systematically.

5.2 Introduction

Detector physics is a complex subject which could take multiple books to describe in detail (for further interest one can refer to the following books: [80] [76]). However

the aim of this work is to understand the behaviour of graphene as a potential ion backflow membrane for particle detectors, in particular GEMs and therefore only the physics relevant to the understanding of such behaviour will be discussed. In interest of clarity, experimental results will be discussed here at the same time as the relevant theoretical equations and interpretations, as separating them into a separate section would require constant cross-referencing of equations.

The basic GEM was invented by Fabio Sauli in 1997 [79], as a potential replacement for the most commonly used particle detectors: the wire chambers. The GEMs were shown to be potentially able to overcome most of the drawbacks of the wire chambers: less expensive structure and maintenance, better resolution and track separation, less ion backflow [79].

As the triple GEM setup is a very complex system with a multitude of parameters which influence the radiation detection signal in varied ways, it is extremely important to understand the influence of each of the parameters on each other, and various effects observed independently of the presence of graphene. This will firstly allow for a more accurate optimisation of the parameters for the characterisation of the layer. Secondly it will also enable an accurate interpretation of the results of the characterisation as any difference observed can be compared with the absence of layer and be deconvoluted from unwanted side effects of the variations of a parameter. Finally as the mechanical resistance of an one atom thick layer of graphene in the operating regimes of the detector was almost completely unknown, it was important to tune all parameters to the lowest energy configurations possible in order to avoid damage.

5.3 Methods: The Detection Chamber and Setup

In this experiment the GEMs were all fabricated by the CERN workshop using standard lithographic techniques: 5 μm of copper or gold (depending on the GEM) is evaporated onto both sides of a 50 μm thick kapton foil, so an overall thickness of 60 μm. The GEM is then covered on both sides with SU-1818 resist and exposed to UV light and then developed. The holes are then dry-etched away from the top side, and then from the back side. The holes are therefore shaped in an hourglass shape with the smaller inner diameter of 30 μm and the outer diameter of 35 μm. The holes are

arranged in a periodic honeycomb-like pattern, with a pitch of 60 µm. The copper mesh used to support graphene has an active area of (3 x 3) mm^2, a thickness of 5 µm, with the same pattern as the GEM: holes of 35 µm diameter arranged in a honeycomb fashion with a regular pitch (distance from the centre of one hole to the nearest ones) of 60 µm. Because the films are etched from one side, the holes are not cylindrical but the diameter shrinks from 35 µm to 30 µm on the bottom side of the mesh. This narrowing and its relative size is illustrated clearly in the SEM image taken from the top of a mesh hole covered with graphene in Figure 4.4, with the bottom rim of the hole appearing in as an apparent inner diameter of the hole.

On the contrary to Chapter 4, where transferring graphene onto the top side of the meshes and GEMs need to take into consideration the top larger diameter of 35 µm. In the detector, the effective area seen by an incoming perpendicular radiation will be the smaller area of 30 µm diameter, and consequently this size will be used in this chapter in calculations.

The detector used in this work has an active area of 10 cm x 10 cm (surface area of the chamber). All the readout strips on the anode were connected together so as to integrate all the current collected into one signal.

The three GEMs could each be powered individually however this can damage the setup as any large discharges occurring through one of the GEMs would only shut down that one GEM and not the others, causing the discharge to be transferred further along the triple GEM, possibly causing further damage. For this reason, the three GEMs are powered together via a voltage divider using the resistors with values labelled in Figure 5.1.

For a given voltage applied on the triple GEM stack, a fixed current will flow through the voltage divider on the left of Figure 5.1, which can be easily calculated using:

$$I_{GEM} = \frac{V_{GEM}}{\Sigma R} = \frac{V_{GEM}}{(0.55 + 0.5 + 0.45 + 3) \times 10^6} \tag{5.1}$$

Due to a maximum current limitation on the power supply connected to the GEM stack, monitoring the current I_{GEM} on this voltage divider rather than the voltage V_{GEM} was slightly more practical. Relevant calibration graphs will therefore be plot-

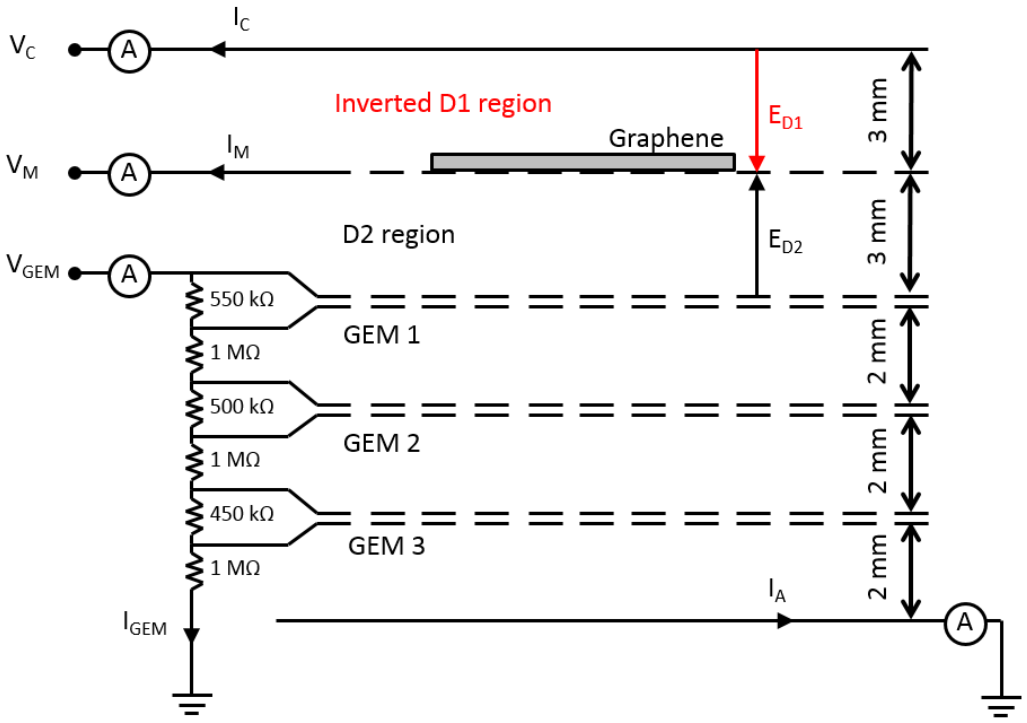

Figure 5.1: Diagram of the measurement setup used in this chapter. The field in region D1 is inverted in order to not have any contribution from ion-electron pairs generated above the mesh.

ted as a function of current on the GEM stack. However both quantities I_{GEM} and V_{GEM} are directly proportional and can be easily computed if needed.

The other quantities labelled on Figure 5.1 correspond to: the voltage V_C and current I_C on the cathode, the voltage V_M and current I_M on the mesh, and the ones on the anode V_A and I_A.

As the ultimate aim of the experiment was to calibrate the setup to study the charge transmission properties of graphene for potential integration in particle detector, and not to study GEMs for radiation detection in general, the source of radiation was fixed for simplicity and was a PANalytical commercial X-ray gun with a variable interaction rate which can be changed by varying the current applied to the gun up to a few mA, while keeping the voltage fixed to 16.00 kV. The X-rays used in this setup were copper characteristic alpha X-rays (K_α) and therefore had an energy of 8.04 keV, corresponding to a wavelength of 0.154 nm.

For a given triple GEM configuration, with a determined spacing between the

GEMs as described in the previous section, and a given gas mixture, the gain and rates of the detector still needs to be calibrated in order to operate the detector setup in the proportional regime. As described in Chapter 2, gains between 10^3 and 10^5 are situated in the proportional region where the energy of the signal collected at the anode is directly proportional to the energy of the incident particles. Therefore even by increasing the gain in the same regime, the rate of the detector is expected to be constant.

Unless stated otherwise, the gas used in the detector chamber was argon-carbon dioxide in a mass ratio of 70% argon and 30% CO_2. This quantity will be labelled Ar-CO_2 70-30 from now on. All measurements were done at room pressure and temperature. The chamber was always flushed for at least 2 hours (or overnight if possible) at high flow of 9L/h before any measurements in order to clean the chamber of gas impurities and obtain a homogeneous mixture. The flow is then reduced to 5L/hour for the measurements. The voltages used to power up the detector were very high, in the range of 3000 V to 5000 V with electric fields up to 10^4 V.cm^{-1}. It was therefore necessary to set a ramp up rate of 25 V.s^{-1}.

The MCA used in this measurement was an: MCA8000D AmpTek Pocket MCA, the software used to transfer the data from the MCA to the computer was DPP MCA and the input range was 10 V for 2048 channels with a threshold set at channel 20 on the software.

In order to understand the behaviour of the parameters independently of the presence of graphene, and in order to calibrate the triple GEM accurately, the Drift region above the mesh supporting the graphene layer needed to be disabled. By doing so, the setup reduces to a simple triple GEM with only one drift region above it: D2. In order to disable the drift region D1, the field E_{D1} across the region can be inverted to be pointing in the direction opposite to E_{D2}. This causes all electrons generated by the X-rays in D1 to be drifted the opposite way towards the cathode, therefore not contributing to the current collected at the anode after amplification. The reason for the inversion rather than keeping the voltages across D1 the same (equipotential), which would also prevent the drift of the electrons, is that by implementing the latter, ions produced in D2 will still drift back up to D1 through collisions and not get

collected on the mesh, therefore changing the current collected on the mesh (I_M). In this chapter E_{D1} is therefore kept inverted with a value of -100 V.cm^{-1}, unless stated otherwise.

5.4 Variation of Parameter V_{GEM}: Voltage across the Triple GEM

5.4.1 Influence on Rate and Gain

As discussed in Chapter 2, the voltage across the GEM will directly influence the amount of amplification of the electrons in the detector. In this work, the detector was to be operated in the proportional regime, and therefore the voltage needed to be varied in order to identify the different regions and therefore to calibrate the setup accordingly.

The number of primary electron-ion pairs n_0 produced by the interaction of an X-ray with a gas molecule, in this case can be approximated by:

$$n_0 = \frac{\Delta E}{W} \tag{5.2}$$

where ΔE is the energy lost in the material and W is the energy required to create and electron-ion pair, this number is 26 eV for Ar and 34 eV for CO_2 [79]. For a mixture of gases A, B, C etc., the expression can be modified to take into account the gas mass ratio of each components ρ_A, ρ_B, ρ_C, etc.:

$$n_0 = \sum_n \frac{\Delta E}{W_n} \rho_n \tag{5.3}$$

For a gas mixture of Ar-CO_2 70-30, the number of primary electrons ejected upon complete conversion of an 8 keV X-ray into electrons would therefore be about 289 primaries. These primary electrons resulting strictly from the energy lost by the X-rays are then amplified. The effective gain of the triple GEM detector at a given applied voltage V_{GEM} is defined as the ratio of the electrons collected after amplification n_a to the number of initial primaries n_0 and can be calculated from experimental parameters

as follow:

$$G = \frac{n_a}{n_0} = \frac{I_A}{n_0 e R} \tag{5.4}$$

where I_A is the current collected at the anode, e is the electron charge and R is the count rate, also called interaction rate.

The current and the rate therefore needed to be measured in order to calculate the gain of the detector. For this, the GEM was powered up to a given applied current I_{GEM} in steps of 10 μA while the X-ray was kept off. Once all the induced currents from the change in electric field weree settled, the X-ray was turned on and the quantities I_A and R were monitored for that given I_{GEM}. It was important to keep the X-ray off and X-ray on times consistent as the detector was subject to charging up effects, which will be discussed later, on top of induced currents from the change in voltage across the detector. These systematic measurements as a function of time are shown in Figure 5.2.

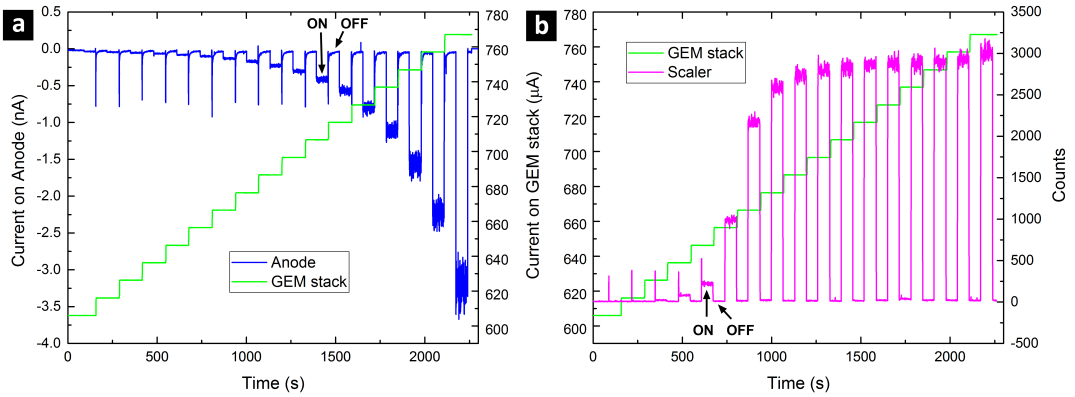

Figure 5.2: a) Plot of current collected on the anode as a function of time during a systematic measurement of the collected current I_{anode} while varying the current I_{GEM} on the triple GEM stack. The X-ray gun shutter was closed at regular intervals in order to avoid charging up in the detector. This is shown by the arrows as ON and OFF. b) Plot of the count rates recorded on the scaler as a function of time, while increasing I_{GEM}, the current on the triple GEM stack in steps of 10 μA. Similarly, the X-ray gun shutter was closed at regular intervals indicated by the arrows, reducing the counts to noise close to 0.

As expected, the current I_A collected increases with an increased amplification voltage. The measured rate R is expected to be constant with time (with some random

fluctuations varying according to Poisson's distribution as discussed in Chapter 2, which also manifests in the anode current), the reason for the observed '0' rate at for low voltages is due to the set amplitude threshold above which a pulse is considered as a count. As amplification is increased, the most energetic signals will be registered as a count and the signal distribution will slowly shift out of from the threshold, until the full signal is within the detection range, and the count rate will therefore reach its maximum. The current I_A was averaged over 100 measurement points as well as the rate R, when the X-ray was ON. The same was done for both quantities when the X-ray was OFF. The net current I_A was systematically calculated using $I_{A(ON)} - I_{A(OFF)}$, and R was given by $R = R_{ON} - R_{OFF}$ in order to avoid potential contribution from baseline shift effects (if any) and background noise. The averaged and net values for both quantities are plotted with their respective standard deviation in Figure 5.3 a and b.

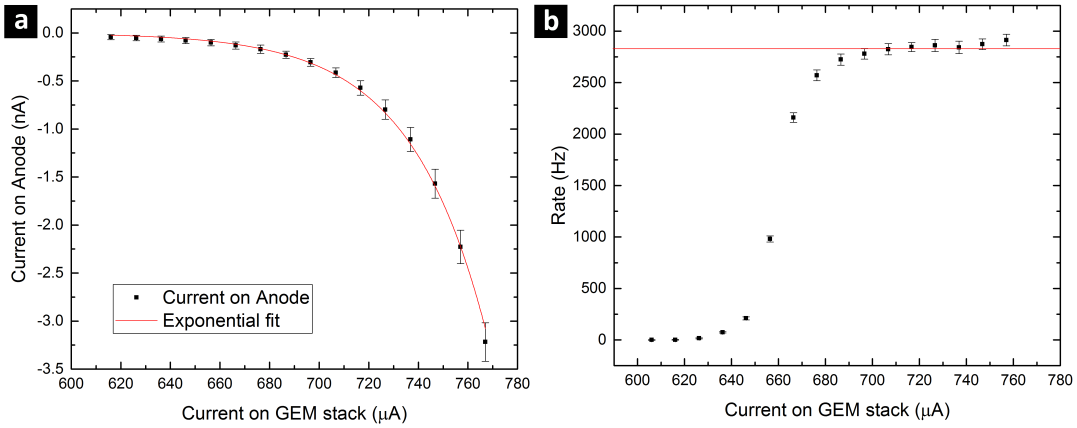

Figure 5.3: a) Plot of I_{anode}, the current collected on the anode as a function of the current I_{GEM} on the triple GEM stack. b) Plot of the count rates recorded on the scaler as a function of I_{GEM}, the current on the triple GEM stack.

The graph of the current I_A as a function of the current on the triple GEM, I_{GEM} is fitted with an exponential function and can be seen to not fit very well below 660 μA. This indicates that the proportional region as illustrated previously in 2.3 starts after that amplification voltage. Indeed the count rate R starts increasing at about the same voltage, indicating that the initial ion-electron signal starts being amplified enough to be counted within the system. R reaches a plateau when all the counts are being

amplified beyond the threshold. The gain was computed from using the values of I_A shown in the graph, and using the value for R averaged in the saturated regime above 690 µA: $R = (2.85 \pm 0.04)$ kHz. The gain G was then replotted on a logarithmic scale with a linear fit as shown in Figure 5.4. The linear fit can be seen more clearly to start diverging very slightly at lower values below 660 µA and the slope eventually becomes almost flat below 620 µA. The linear fit through ln(Gain) shows that the region of true proportionality lies between 660 µA and 770 µA.

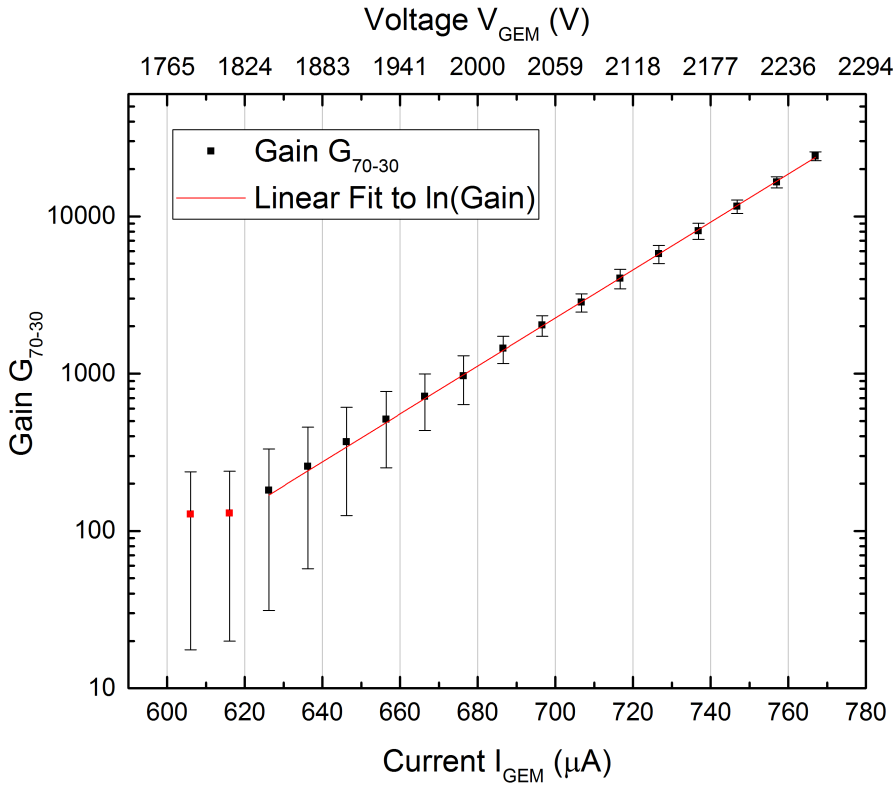

Figure 5.4: Logarithmic plot of I_A, the current collected on the anode as a function of the current I_{GEM} on the triple GEM stack. The corresponding V_{GEM} is also plotted on the upper axis for comparison. A linear fit through the data is shown in red excluding the two lowest points marked in red, which are towards the end of the ionisation chamber regime.

For a gas mixture of $Ar - CO_2$ 70 − 30, at a rate of 2800 Hz, under the current settings, the gains reached in the proportional regime vary between 2×10^3 to 2×10^4.

The equation of the linear fit is given by:

$$ln(G) = (0.035 \pm 0.01) \times I_{GEM} - (16.7 \pm 0.1) \tag{5.5}$$

The value for the current used in this work for the Ar-CO_2 70-30 mixture was chosen to match $G = 10^4$ in order to simplify further calculations, using equation 5.5, this corresponds to a current of $I_{GEM} = (740 \pm 1)\,\mu A$. An effective Townsend coefficient α_{eff} can be calculated for each gain G but this is not of interest to this work. For the value of $I_{GEM} = 740\,\mu A$ which will be used from now for a mixture of Ar-CO_2 70-30, the effective Townsend coefficient can be calculated in order to give an idea of the mean free path. For an avalanche region of 3 GEMs of 50 µm this yields $\alpha_{eff} = (0.061 \pm 0.001)\,\mu m^{-1}$, which corresponds to a mean free path of ionisation of $\lambda_{i,eff} = 16\,\mu m$. After discussing the influence of the applied voltage V_{GEM} on the gain G and the rate R, the influence on the energy spectrum will now be discussed.

5.4.2 Influence on Energy Spectrum

The energy spectra recorded for each amplification current I_{GEM} are plotted in Figure 5.5 (see Section 3.7.2 for more information on the axis and on the setup). The main energy peak starts appearing fully for an applied current $I_{GEM} = 670\,\mu A$. This correlates with the result in Figure 5.3b, where the count rates start increasing. When the Ar escape peak fully appears within the readable range of the electronics after $I_{GEM} = 690\,\mu A$, the count rate reaches its maximum point.

The spectrum then shifts to higher energies as the current is increased and the gain increases. On the other hand, for too high gain after 730 µA, the spectrum starts showing a small broad peak at the highest end of the spectrum, which keeps increasing as the gain is increased. This peak is a manifestation of the dead time as described in Section 2.5.3, where a pulse (or many) can appear within the decay time of a first pulse, leading to an pulse with an apparent higher energy. This effect is also called pile-up. As the subsequent pulse appears randomly within the decay time of the first pulse, the amplitude of the resulting pulse is also a random distribution and will appear as a distribution of counts rather than a very sharp peak. As the energy of the pulses is amplified by the GEM, the pulses have a higher amplitude,

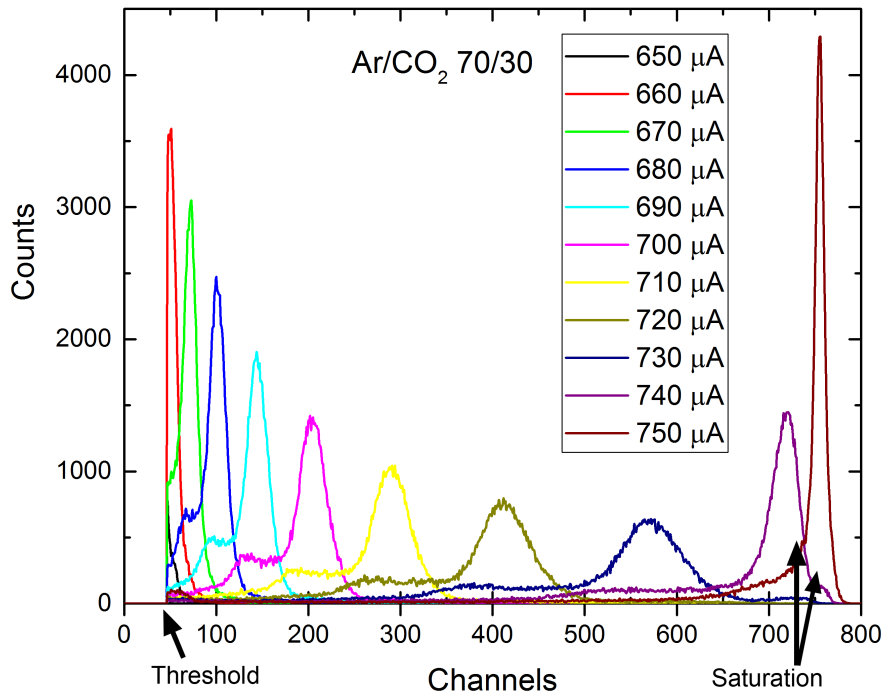

Figure 5.5: Graph of energy spectra as a function of current applied to the triple GEM stack. Increasing the current on the triple GEM is expected to increase the amplification of the signal. The spectra were cumulated over 30 s.

also a larger distribution and are therefore more likely to overlap. Finally as the gain is increased further the main peak starts merging with the increasing pile-up signals at the end of the spectrum. As there is also a maximum pulse amplitude detectable, which is limited by the electronics, the amplitude of the pulse is simply saturated and just appears as a narrower peak at the highest end of the detection range. The two spectra at 740 µA and 750 µA therefore show main peaks which have a high convolution with pile-up signals, this is why they seem narrower and have a higher amplitude than the spectra at 740 µA, while in theory they would be expected to be broader and lower. The Argon peak for the 740 µA spectra on the other hand, is not yet subject to convolution with pile-up and can be seen to be broader and lower than its equivalent in the 740 µA spectra as expected.

The main energy peaks of the spectra and their Ar peak can be fitted with two Gaussians. The fittings were done using the Wire Renishaw software, and graph of the main peak centre P measured from the Gaussian fittings is shown in Figure 5.6 on

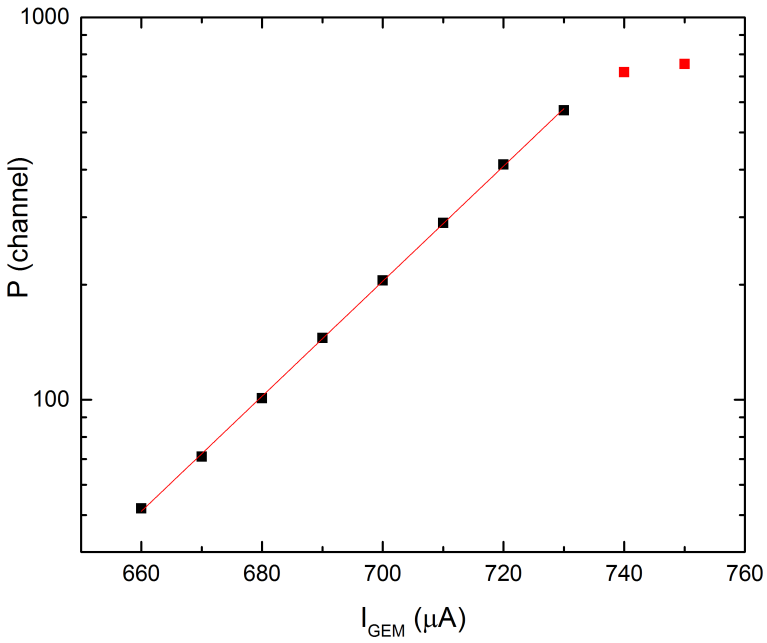

Figure 5.6: Graph of the main peak position P of the energy spectra as a function of current applied to the triple GEM stack I_{GEM} on a logarithmic scale. A linear fit through the data points marked in black is fitted by a red line on the graph. The data points marked in red are expected to deviate from the trend due to pile-up effects as seen in Figure 5.5 and are therefore not considered.

a logarithmic scale. As expected the energy of the current pulses collected increases exponentially. As discussed in the previous paragraph, the two points at 740 μA and 750 μA, where expected to not fit the trend due to pile-up effects and are indeed found to deviate from the line. A linear fit to ln(P) is plotted through the other points and yield the same slope as found in the graph of the gain G as a function of I_{GEM} in Figure 5.4.

As discussed in Chapter 2, the electron-ion production is a random independent event following Poisson's distribution due to the distance between the gas molecules in the system. The pair generation from the avalanche mechanism is also due to random independent events, we expect that therefore the probability distribution of the result X of all of these random independent events A, B, C... is related to the probability distribution of these random independent events. If all these independent variables A, B, C... all follow Poisson's distribution, then X will also follow Poisson's

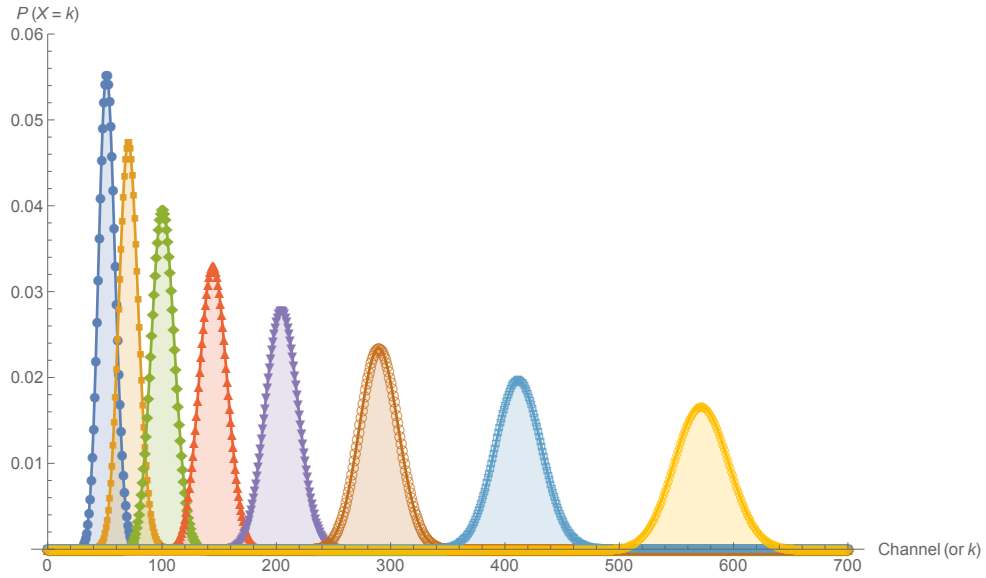

Figure 5.7: Plot of the P(X=k), the probability distribution of a random variable X taking a value k (or channel number in our case) according to Poisson's distribution where the values of λ, the expected values were taken to be the centre of the measured peaks as measured in graph 5.6. The plot was computed using Mathematica.

distribution [80].

Figure 5.7 is the probability distribution P(X=k) calculated using Mathematica, for a variable X to take the value k for a series of expected values λ. The values of λ used were the channel numbers measured in our experiment as shown in Figure 5.6. The trend can be seen to agree quite well trend-wise with the experimental energy spectra measured in Figure 5.5. The main differences (in height and shape of the distributions) are due to the fact that the argon escape peak was not taken into account into this distribution plot. This calculation however, has shown in a qualitative way that the changes in shape of the spectra and its evolution at increasing energies is directly dictated by the probabilistic nature of the counting events. From the measurements in this section, the range of currents which can be used for measurements in the proportional regime but while keeping the gain low enough to avoid pile-up therefore lies between 670 μA and 730 μA in this configuration and using Ar-CO_2 70-30.

5.5 Variation of Parameter E_{D2}: Electric Field below the Mesh

After discussing the influence of amplification inside the triple GEM, by varying V_{GEM} while keeping all other variables constant, the influence of the voltage V_{D2} applied in the drift region of the triple GEM, i.e. in the region labelled D2 on Figure 5.1, will be discussed. The current of the triple GEM was set to operate in the region of true proportionality as measured in the previous section and I_{GEM} was set to 676 µA. The gas mixture used was Ar-CO_2 70-30, and the electric field in region D1, E_{D1} is still kept inverted in order to separate the effects of the two regions. The voltage V_{D2} was varied systematically in this section in order to assess its influence, however the results will be plotted and discussed as a function of the electric field E_{D2} as this quantity does not depend on the distance between the mesh and the first GEM, and is therefore valid for any separation.

By varying the electric field in that region, the number of electrons collected by the triple GEM could be varied. As defined in Chapter 2, the collection efficiency ε is the ratio of the electrons collected to the number of electrons produced originally. To measure this quantity, the electric field E_{D2} was varied systematically, while the current collected on anode I_A was monitored. The measurements were taken in a similar fashion to the previous section, where the X-ray was turned ON/OFF at regular intervals to avoid charging up effects. I_A was then averaged over 100 points while the X-ray was ON and plotted with its standard deviation as a function of E_{D2} as shown in Figure 5.8. Three different regimes with a different trend can be seen and are labelled in the graph.

The explanation of the behaviour of the collected current is explained by diagrams in Figure 5.9. I_A was seen to increase as E_{D2} was increased from zero. This is because at low values of E_{D2}, the field is not strong enough to prevent recombination of electrons with ions. The more the field is increased, the more electrons are collected, and therefore amplified, reaching the anode. The amount collected will stop increasing and reach a plateau when an optimum field configuration is reached (as illustrated in Figure 5.9a, where all electrons in the drift region are collected, reaching an efficiency

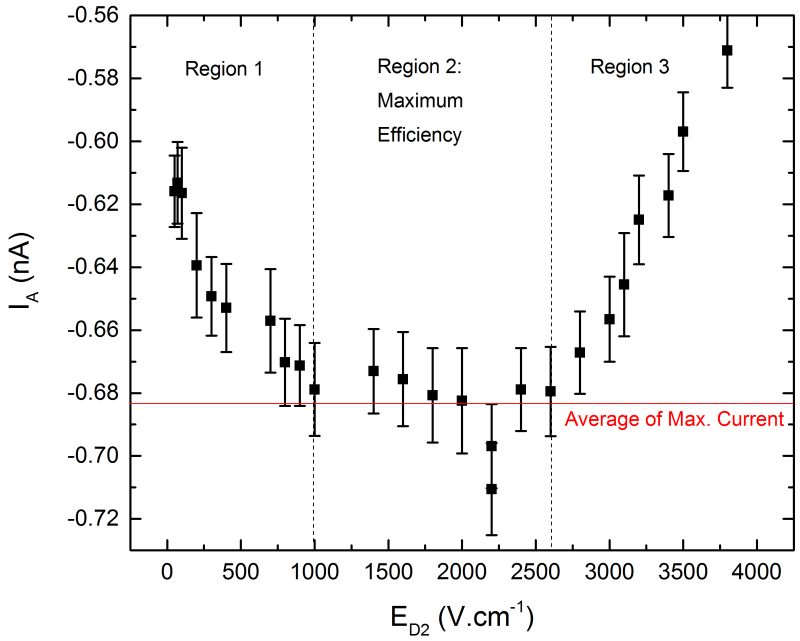

Figure 5.8: Graph showing the current collected on the anode I_A as a function of varying E_{D2}, the Drift field between the mesh and the triple GEM stack. Three regions can be distinguished and are labelled on the graph. The average maximum current collected is labelled as a red line. The data was taken for Ar-CO_2 70-30, at a fixed GEM amplification current I_{GEM} of 676 μA, with E_{D1} inverted.

of 100 %. If the field is increased further however, the field lines will become so dense in D2 that some of the lines will start ending on the conductive metal coating on top of the GEM as illustrated in b). This will cause electrons to be collected on the top of the GEM rather than through the holes, and therefore the current I_A collected on the anode will start decreasing. The variation of E_{D2} can therefore be used to change the number of primary electrons in the drift region which will reach the next amplification stages in the triple GEM. This will therefore also affect the apparent pulse amplitude and the spectrum position. Optimum operation of the triple GEM for a maximum collection efficiency therefore lies in the range of 1000 $V.cm^{-1}$ to 1500 $V.cm^{-1}$ for the applied electric field E_{D2}.

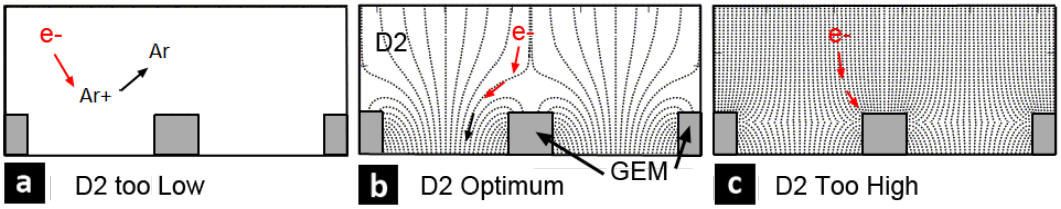

Figure 5.9: Diagram illustrating the effects of varying E_{D2} in the three regimes delimited in Figure 5.8. a) when E_{D2} is optimum, all electrons in D2 will be collected through the holes of the GEM, b) when E_{D2} is too high, electrons are lost to the conductive layer on top of the GEM and c) when E_{D2} is too weak, electrons do not gain enough kinetic energy and recombine with ions. Simulations illustrating this effect can be found here: [82, 148, 149]

5.6 Variation of Parameter I_{xray}: X-ray Current

The X-rays used in this experiment are produced by a commercial X-ray gun where a current is passed by a wire/filament until the temperature of the wire is high enough to reach thermionic emission. The electrons generated by this 'electron gun' are accelerated towards a copper target, resulting either in back-scattered electrons, the production of secondary electrons, or the generation of characteristic X-rays. As each electron striking the target has the same chance of producing an X-ray, an increase in the number of electrons is expected to yield an linear increase in the X-ray produced. A copper collimator with an opening of 0.5 mm diameter was fitted to the source in order to filter out X-ray which were not parallel to the axis of the gun, and also to partially reduce the high rate of the gun.

Figure 5.10 shows a graph of the rate measured for the X-ray gun at varying applied I_{xray}. As illustrated by the linear fit plotted with a red line, the measurement indeed shows a linear trend for low values of applied current. However the slope of the graph starts decreasing after 1.5 mA. Indeed at very high count rates, there is a higher chance of loosing counts to dead-times. When the effects starts becoming noticeable, increasing the rate will only increase the lost counts even further, making the slope of the graph decrease further. For this reason, spectra at count rates above an I_{xray} of 1.5 mA, are expected to not have accurate count rates and any measurements requiring a reliable rate were made with $I_{\text{xray}} < 1.5\,\text{mA}$. These measurements will be referred to as 'low rate' measurements, while the ones taken at $I_{\text{xray}} > 1.5\,\text{mA}$, will be referred

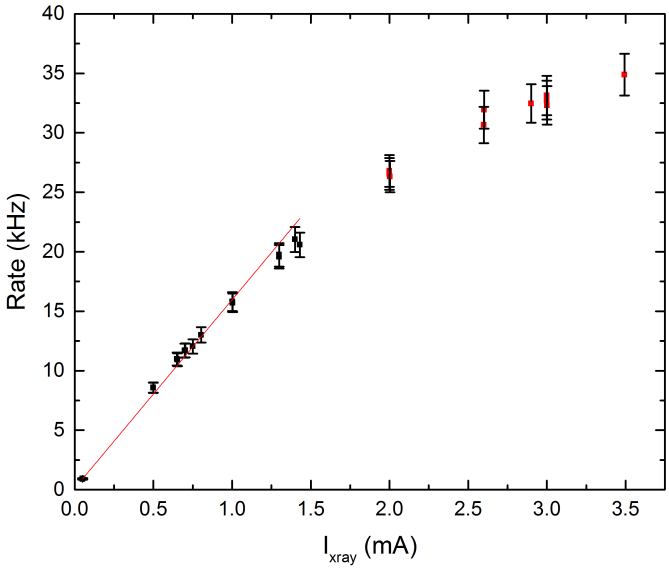

Figure 5.10: Graph of the rate R with increasing I_{xray}, the current through the X-ray gun with a collimator of 0.5 mm diameter. The red line is a linear fit through the data points marked in black, while the data points marked in red are not taken into account in the fit.

to in the rest of this work at 'high rate' measurements. The linear fit through the data points not marked in red yielded a slope of (15.8 ± 0.2) kHz for the points below 1.5 mA. Globally, varying this quantity I_{xray} does not influence any other parameters than the count rate, which simply increases as I_{xray} is increased. This therefore will affect the number of events counted on the energy spectra, but as it doesn't affect other variables, the shape and position of the peaks are expected to be the same. Figure 5.11 shows a few selected spectra at varying X-ray currents, this illustrates that indeed the spectra has the same energy but an increasing number of counts as expected.

5.7 Variation of Parameter: Gas Mixture

The last parameter to be discussed before moving on to the effects of the added mesh on top of the triple GEM is the gas mixture. In this work argon was used as the main source of ion-electron pairs with the addition of CO_2 as a quencher. The two

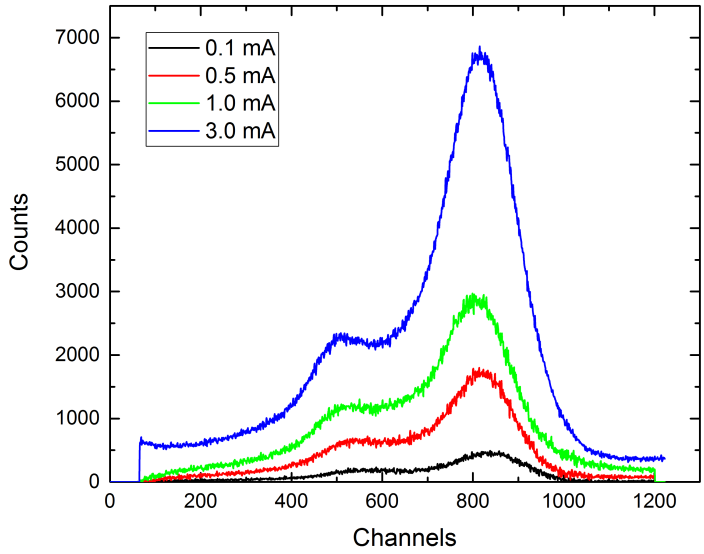

Figure 5.11: Graph of the rate R with increasing I_{xray}, the current through the X-ray gun with no collimator.

gas mixtures used were: Ar-CO_2 70-30 and Ar-CO_2 93-7.

At the same pressure and temperature conditions (room-conditions at 20°C, and 1 atm), changing the proportion of Ar to CO_2 will change the number of primary electrons produced by the same radiation according to equation 5.3. The energy deposited by each radiation is therefore expected to change, and the position of the peaks in the resulting energy spectra should shift accordingly. Furthermore, not only the interaction cross-section σ_γ with the incoming radiation will change, but the interaction cross-section for the electrons in the avalanche production process σ_a is also expected to change accordingly. Argon is used in the mixture as the main ion-electron pair production source (the energy required to produce electron-ion pairs is 26 eV, whereas for CO_2 for example is it 34 eV [80]) and is also used rather than other noble gases due to its high ion mobility of $1.7\,cm^2.V^{-1}.s^{-2}$ (as opposed to $10.2\,cm^2.V^{-1}.s^{-2}$ for He for example [80]), allowing for accumulated local charges due to ions to dissipate faster. CO_2 also has a low ion mobility $1.09\,cm^2.V^{-1}.s^{-2}$ and is used in the mixture as a gas quencher. Indeed CO_2 by vitue of its two very electronegative oxygen atoms, acts as a common electron acceptor in chemical reactions. In this gas mixture, its presence

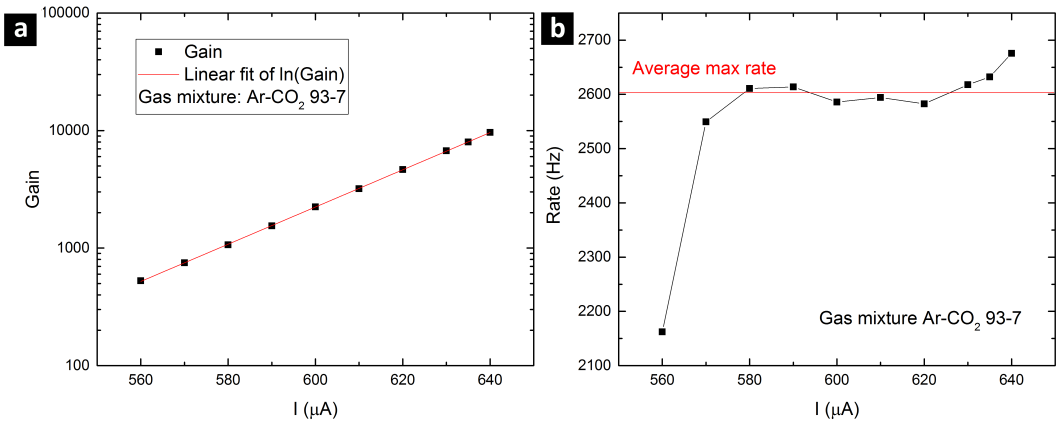

Figure 5.12: a) Logarithmic plot of the gain G for a gas mixture of Ar-CO_2 93-7 as a function of I_{GEM} on the triple GEM stack, with a linear fit through the data points shown in red b) Plot of the count rate R recorded on the scaler as a function of I_{GEM}, the current on the triple GEM stack. The average value for the measured rate is shown as a red line. The X-ray current used was 0.05 mA.

would reduce the number of electrons collected at the anode. This allows to reduce the energy deposited by the incoming radiation, and given the same experimental settings it the presence of more CO_2 would shift the energy spectrum further towards zero. This means that while the maximum rate stays the same, a higher voltage is required to reach the maximum rate measurable by the system. Similarly, a higher voltage is also needed to achieve the same gains with more CO_2.

Comparing the calibration graphs for Ar-CO_2 93-7 shown in Figure 5.12, with the ones for Ar-CO_2 70-30 in section 5.4 shows that indeed for a lower proportion of CO_2 the current I_{GEM} needed to obtain the same gains, is lower by 75 μA. The rate measured was $R = 2600 \pm 10$. The slope given by the linear fit to the gain data gave $\alpha = (0.341 \pm 0.01)$ m^{-1}. This slope is higher than the value found for Ar-CO_2 70-30: $\alpha = (0.035 \pm 0.01)$ m^{-1}, indicating a much faster increase in gain. This is in agreement with experimental results in literature as shown in Figure 5.13. The graph shows the evolution of the pulse height or amplitude of the pulse as a function of applied voltage for different ρ_{CO_2}. This is roughly equivalent to the energy of the main peak P of the energy spectrum as a function of V_{GEM}. The plot shows the exponential trend discussed previously and shows that a higher voltage is needed to obtain the same gain for increasing ρ_{CO_2}, and it also shows a steeper increase in the gain G for lower

ρ_{CO_2}, which is expected as the molecule is expected to quench the avalanche process.

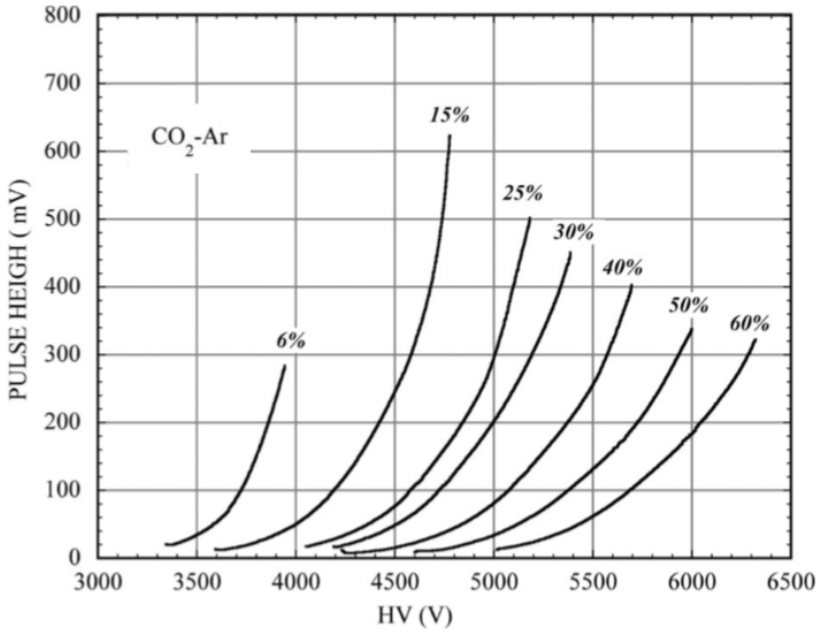

Figure 5.13: Plot of the average pulse heights measured in mV, as a function of applied voltage V_{GEM} across the detector in V for different percentages of CO_2 in the Ar-CO_2 gas mixture. Adapted from reference [150].

As CO_2 acts as an electron acceptor, the effective cross sections σ_γ and σ_a are both expected to decrease as ρ_{CO_2} increases so the amount of energy deposited by one radiation will be lower. The addition of different amounts of quencher gas therefore has the benefit of being able to modify and control the dynamics of electron production inside the chamber, modifying their speed and therefore modify the pulse collection time in order to change deadtimes. Another benefit of modifying the gas mixture is that the quenching process can increase the threshold of the beginning of the arc-discharge regime therefore allowing for operation at higher gains without the appearance of discharges. The dependence of these benefits is complex, non linear and previous experimental results have shown [80, 150] that a minimum exists for an addition of between 30 % and 40 % of quenching gas, where the amount of discharges is lowered. The calculations for this are beyond the scope of this thesis and can be found in the following references: [80, 150–152], however this explains the reason for the use of Ar-CO_2 70-30 in this work, and in other detectors work as a standard gas mixture. The use of Ar-CO_2 93-7 will be explained in the next chapter.

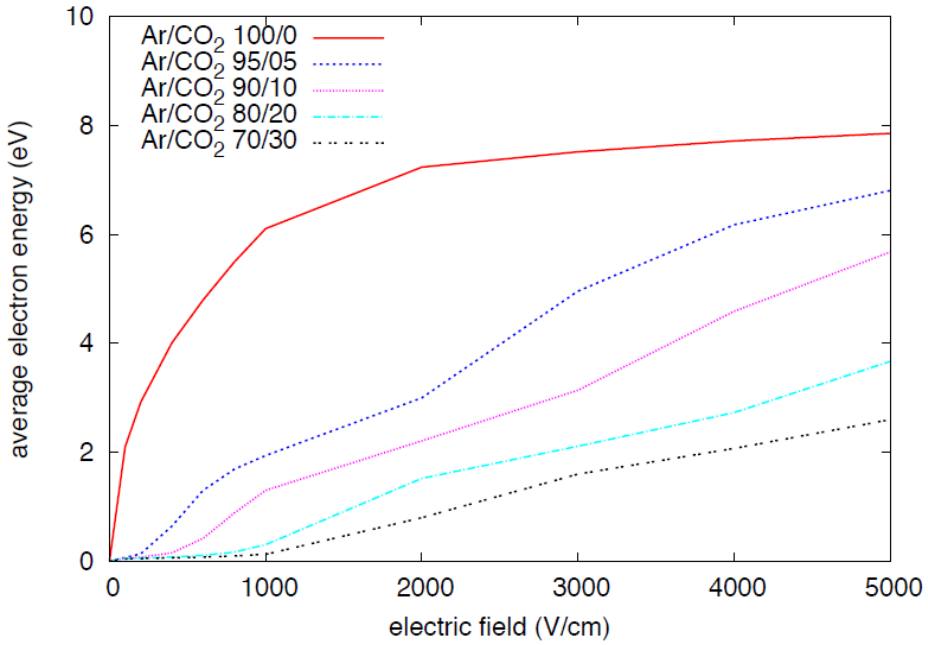

Figure 5.14: Plot of the average electron energy in Ar-CO_2 gas mixtures with varying ratios, as a function of applied electric field across a drift region. Simulations by Filippo Resnati (CERN) (co-author in the publication).

5.8 Variation of Parameter E_{D1}: Electric Field above the Mesh

After discussing the effects which would influence a standard triple GEM while keeping the electric field in region D1 inverted in order to avoid any contribution from it, it is now important to understand the new setup designed in this work without the presence of graphene before integrating the layer. It is now important to discuss what to expect from this second drift region on top of the standard GEM, as well as measuring the effects of a varying E_{D1} field on the rest of the setup.

The addition of an extra drift region of 3 mm height, on top of the existing drift region D2 also of 3 mm height would be equivalent to having a drift region of 6 mm height. The path of an incoming X-ray is therefore effectively doubled and the energy loss of the X-ray which can now be collected is expected to increase according to the Beer-Lambert law. Considering an incoming X-ray beam of intensity I_i upon entering region D1, the beam will be attenuated after passing by the gas in region D1. After which the beam hits the mesh layer. This is important to take into account as the

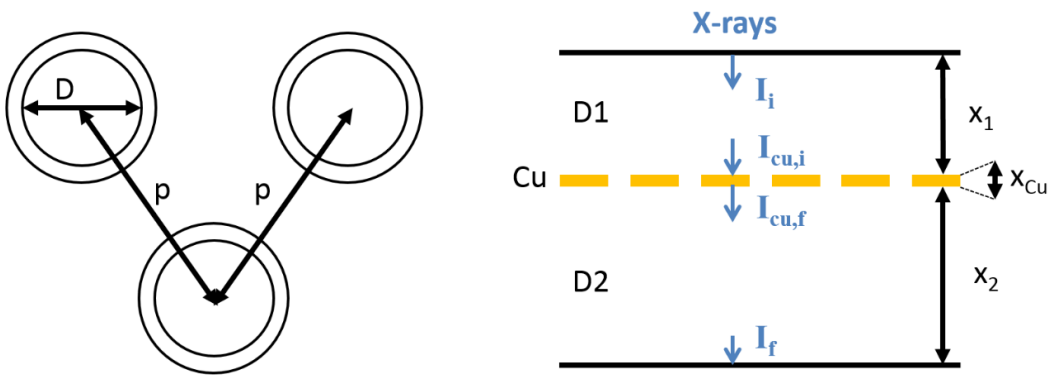

Figure 5.15: Diagram illustrating the quantities used in the equations in section 5.8, describing the D, the diameter of the holes, p, the pitch, and the intensities used.

stopping power of copper is high. It will then be attenuated by the copper, and then upon leaving it, will be attenuated a third time after passing by region D2. According to Beer-Lambert law, as the distance travelled by the X-rays in each region is the same: $x_{D1} = xD2$, the ratio of intensity lost in D1 should be equal to the one lost in D2. We call ratio A_{gas} and by rearranging equation 2.1, the following relation is obtained:

$$\frac{I_{Cu,i}}{I_i} = \frac{I_f}{I_{Cu,f}} = e^{-\mu_{gas} x_{D1}} = A_{gas} \tag{5.6}$$

Where I_i is the initial X-ray intensity entering region D1, and $I_{Cu,i}$ the attenuated intensity upon leaving D1, before entering copper. Similarly, $I_{Cu,f}$ is the intensity after passing in copper, and I_f, the intensity upon leaving D2. For clarity purposes, these quantities in the equation are described in Figure 5.15. The attenuation constant of the Ar-CO_2 mixture μ_{gas} can be expressed as a function of the mass attenuation coefficient $\frac{\mu}{d}$, the density d and the mass ratio ρ of each gas.

$$\mu_{gas} = \frac{\mu_{Ar}}{d} d_{Ar} \rho_{Ar} + \frac{\mu_{CO_2}}{d} d_{CO_2} \rho_{CO_2} \tag{5.7}$$

Similarly, the attenuation of the X-rays through the copper mesh can be described in terms of mass attenuation coefficient of copper $\frac{\mu_{Cu}}{d}$ and its density d_{Cu}. However, the copper layer is not continuous and has periodic holes through which attenuation is equal to attenuation by Ar/CO_2 . The optical transparency T_0 of copper is calculated

as follow for the hexagon lattice samples:

$$T_0 = \frac{D^2\pi}{(2\sqrt{3})p^2} \tag{5.8}$$

Where D is the diameter of the holes and p is the pitch separating them. The attenuation through the A_{Cu} mesh can the be expressed as follow:

$$\begin{cases} \frac{I_{Cu,f}}{I_{Cu,i}} = e^{-\mu_{Cu}x_{Cu}} = A_{Cu} \\ \mu_{Cu} = T_0\left(\frac{\mu_{Cu}}{d}d_{Cu}\right) + (1-T_0)\mu_{gas} \end{cases} \tag{5.9}$$

Assuming any radiation lost by attenuation is converted into an ion-electron pair which will be detected by the system (full efficiency), the rates R measured can be expressed as follow:

$$\begin{cases} I_i - I_{Cu,i} = R_{D1} \\ I_{Cu,f} - I_f = R_{D2} \end{cases} \tag{5.10}$$

where R_{D1} is the number of hits collected from region D1, and R_{D2} is the rate collected in region D2. Combining linearly and rearranging equations 5.6, 5.9 and 5.10 to solve for R_{D2}, we can write a linear relation between the two rates:

$$R_{D1} = \frac{R_{D2}}{A_{gas}A_{Cu}} \tag{5.11}$$

The values used for the calculations are as given in 5.1. Inputting numbers, this corresponds to $R_{D1} = 1.062R_{D2}$ for Ar-CO_2 70-30 and $R_{D1} = 1.075R_{D2}$ for Ar-CO_2 93-7. And the rate detected in region D1, is, as expected from gradual attenuation, slightly higher than the one detected in region D2. The total rate R detected in the spectra should therefore be $R = R_{D1} + R_{D2}$, i.e. 2.075 times more than the counts in the spectra collected for D2 in Ar-CO_2 93-7. This was confirmed experimentally, and for I_{xray} = 1.0 mA, the rate R_{D2} measured was 15400 ± 50, for inverted field in D1, while the rate R measured with positive D1 was averaged to 32900 ± 100. This number is slightly higher than the number expected 31900 ± 100.

We therefore expect the rate in region D1 to be slightly higher than the one measured from region D2. On the other hand, we expect the energy of the X-rays to be

Material	**μ/d ($m^2.kg^{-1}$)**	**d ($kg.m^{-3}$)**
Copper (Cu)	0.5062	8960
Argon (Ar)	11.80	1.666
Carbon Dioxide (CO_2)	0.9399	1.836

Table 5.1: Table of values used for the mass attenuation coefficient μ/d of 8 keV photons in relevant materials, the gas densities d quoted are for 21°C and 1 atm and calculated using the ideal gas law with $M_{Ar} = 39.95$ g.mol^{-1} and $M_{CO_2} = 44.01$ g.mol^{-1}. The values of μ/d for Cu and Ar are as of 2015 from the website of the National Institute for Standards and Technology (nist.gov) and for CO_2 are from: [153].

the same (i.e.: 8 keV) even though their intensity has been decrease. The energy of the peak measure should therefore be the same. However one important difference is that the electrons generated in region D1 have to travel through the copper mesh before reaching D2 and then be amplified. As obtaining a perfect 100 % transmission efficiency is extremely difficult even with the most optimal field configurations due to potential geometrical defects, we would expect a lower energy being detected from region D1. and any deviation between the energy of the X-rays measured from region D2 and the ones from region D1 can therefore be attributed to the electron transmission capability of the copper mesh, also 'electron transparency'. The behaviour of the energy spectra as a function of increasing E_{D2} is shown in Figure 5.16. The spectra from region D2 with inverted D1 is shown in bright yellow, and has its main energy peak was at channel 822 ± 3. On the other hand as soon as D1 is set to a positive field, a second set of energy peaks appear at lower energies with a main peak and its corresponding Ar peak, as expected from previous considerations.

As E_{D1} is increased up to the value of $E_{D2} = 2000$ V.cm^{-1}, the energy transferred from region D1 diminishes and the peak shifts to lower energies. Indeed for $E_{D1} < E_{D2}$, the field lines are less dense above the mesh than below and as changes in E have to be continuous, the field lines above the mesh will tend to 'focus' into the holes in order to match the denser field at these locations. This causes electrons to be drawn through the holes to region D2 rather than being lost on the mesh. When $E_{D1} = E_{D2}$ the field lines won't need to be matched in this case and will naturally line up straight. The transparency at equal fields is therefore expected to be equal to the amount of holes in the mesh i.e. the optical transparency. A graph of the peak positions from region D1 could be plotted as a function of E_{D1}, however, as this

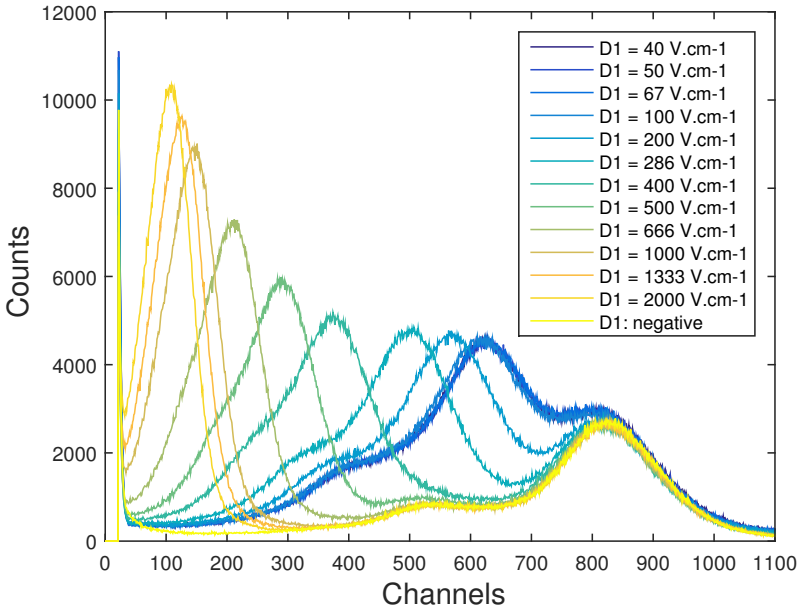

Figure 5.16: Plot of the energy spectra for at varying E_{D1} for fixed $E_{D2} = 2000$ V.cm^{-1}, including a plot of E_{D1} inverted in yellow showing only one main peak and its Ar peak, with no secondary peaks at lower energies. The spectra were taken with an Ar-CO_2 93-7 mixture at $I_{xray} = 1$ mA at $I_{GEM} = 635$ µA.

behaviour by varying E_{D1} is relative to the value of E_{D2}, it is more relevant to plot it as a function of E_{D2}/E_{D1}. This ratio can be interpreted in terms of focusing of the fields, drawing the electrons through the mesh. Indeed, as E_{D2}/E_{D1} is very high the field below the mesh is much larger than the one above, causing more focusing and inversely, as E_{D2}/E_{D1} is decreased, the field is less focused. Similarly, the peak shifts are with respect to the peak position of the energy spectra from D2, so plotting P1/P2 is more of interest. Such plot can be interpreted as the 'transparency' of the mesh with varying field focus. After discussing the influence of the new D1 region on the results. The electron transparency of the mesh will now be discussed in further detail in the next section as well as the influence of relevant parameters from previous sections on its variation.

5.9 Variation of Electron Transparency T_{e^-}

5.9.1 Optical Transparency

Before looking at the electron and ion transparencies, it is important to discuss the optical transparency and its relevance depending on the measurement. Here it will be defined as the percentage of holes per area of a copper mesh or a GEM. And for a mesh with holes arranged in a hexagonal pattern, it was defined earlier in equation 5.8. The reason for the importance of this value is due to the field focusing. Boundary conditions for electric field lines, dictates that a perfect conductor in an electric field will cause the lines to bend so that they are normal to the surface of the conductor. Similarly, a perfect insulator will cause the lines to flow parallel to its surface. As discussed in section 5.8, in the case of E_{D2}/E_{D1} decreasing and reaching a value close to 1, the field lines will not need to focus less and less into the holes to match the electric field below because of similar field densities. In this case, as both the surface of the GEMs and meshes are conductive, the field lines will tend to flow straight and end perpendicular to the surface of the conducting mesh. This means that in the case $E_{D2}/E_{D1} = 1$, with an ideal setup, we expect the number of electrons passing through the mesh to be equal to the area of the holes, i.e. the optical transparency. This value is therefore a limiting number for the minimum transparency of the mesh.

5.9.2 T_{e^-} Calculation Methods

As one may have noticed, the transparency of the mesh behaves in a very similar manner to the process described in Figure 5.9 for the influence of E_{D2} on the anode current. Because of this, it is important to fix E_{D2} if E_{D1} is to be varied in order to differentiate the two mechanisms. As discussed previously, a simple way to calculate the electron transparency would be to take the ratio of the centre of the two main energy peaks of the spectra P_1/P_2. This can be done by fitting the peaks with a mixture of Gaussian and Lorentzian curves as shown in Figure 5.17. The argon peaks also need to be fitted and their ratio can be checked in order to assess the goodness of fit in the case of non-negligible overlap.

However, in the case of low transparencies, part of the peak can disappear below

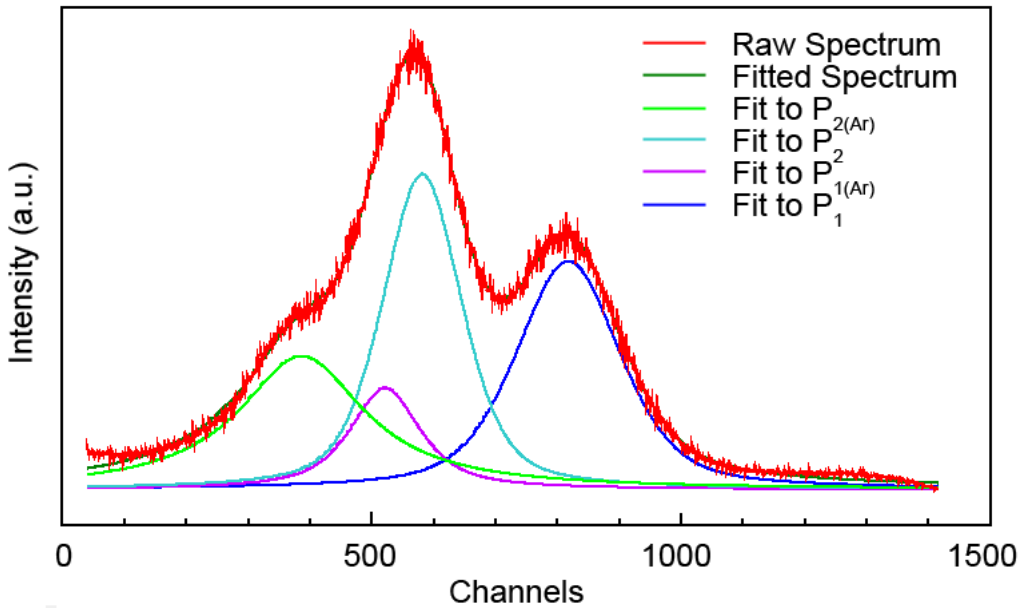

Figure 5.17: Graph showing a typical curve fit of an energy spectrum used to obtain the values for P_1 and P_2. The fitting of the argon peaks are also necessary in order to get an accurate value, especially when the transparency is high and the peaks overlap significantly.

the measurement threshold and only the decaying tail of the main peak will be visible. This makes it much more difficult to measure the centre of the peak and extrapolations would be required. Another drawback of this method is the fitting of the secondary peak as the peak moves closer to zero. Indeed, due to the probabilitic distribution of the spectra discussed in Section 5.4, the Argon peak of P_2 will start merging with P_2, creating a double peak which yields higher fitting errors. In order to remedy to these drawbacks and to cross-check measurements, a second T_{e^-} calculation method was required.

The electron transparency can be defined in stricter terms as the number of electrons measured from D1 to the number of electrons which should be collected from region D1. For a given gain G, the electron transparency can be calculated by rearranging equation 5.4 in terms of I_{D1} and I_{D2} the currents collected due to region D1 and D2 and their respective rates R_{D1} and R_{D2}. As the current I_A collected at the anode is the amplified signal from both D1 and D2: $I_A = I_{D1} + I_{D2}$, and D1 can be inverted to to determine the I_{D2} and R_{D2}, this means a simple subtraction could be used to determine I_{D1} and R_{D1}. The electron transparency can therefore be calculated

using:

$$T_{e-} = \frac{I_A - I_{D2}}{R_{D1+D2} - R_{D2}} \times \frac{R_{D2}}{I_{D2}} \tag{5.12}$$

Despite the stated advantages of this method, one of the drawbacks is the high error carried in this calculation, not only from error propagation with all the experimental values, but mainly from the high errors associated with the values of the rate. Indeed, although the current collected I_A and I_{D2} take into account the total number of electrons from all pulses, the measurement of the rate is limited by the speed of the electronics and as the real rate increases, the counts lost to pile-up will increase. This means R_{D1+D2} will be most affected and will be lower than it should be, consequently T_{e-} will appear larger than with the calculation from the peaks. This effect is therefore also expected to be more prominent with larger overall rates.

Comparatively, the total error in the calculation of T_{e-} from P_1/P_2 is effectively the error in the two peak positions. This error will increase at very high transparency close to 100 % as the two peaks merge and at very low transparencies when the peak starts disappearing. below the threshold. A graph of T_{e-} as a function of $\mathrm{E_{D2}/E_{D1}}$ is plotted for Ar-CO_2 70-30 and illustrates both methods for different rates and shown in Figure 5.18. As shown in b) the transparency of the mesh in % is independent of the rate, and the curves for all three I_{xray} show a trend within each other's error with a maximum value of 75.7 %. On the other hand, Figure a) shows that a) at highest I_{xray}, T_{e-} reaches values of 78.3 % for lower rates and up to 80.3 % for a higher rate at $I_{xray} = 3.0mA$. The deviation between the two methods was found to be a percentage of T_{e-} with a value of 4.7 $\pm$ 2.7 %.

This section has therefore illustrated the two methods determined for this setup for the calculation of T_{e-} of the mesh meant to support the graphene layer on top of the detector. As the deviation between the two diminishes at lower transparencies a combination of the two methods can be used for high and low transparencies.

5.9.3 Effect of Gas Mixture on $\mathbf{T_{e-}}$

As discussed in Section 5.7, the gas mixture is expected to affect the number of primaries generated from the X-rays and the dynamics of the electrons in the gas mixture.

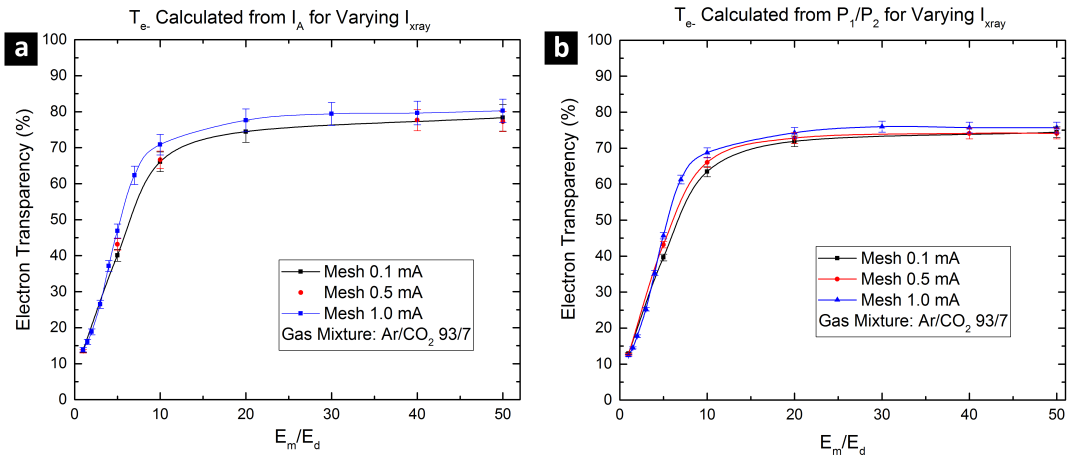

Figure 5.18: Graphs of the electron transparency of a mesh as a function of the ratio E_{D2}/E_{D1} the electric field below the mesh over the electric field above it. The higher positive ratio therefore indicates a stronger field below the mesh. Both graphs were taken at different X-ray currents, (the higher current, the stronger the signal) at a gas mixture of Ar/CO_2 93/7. The graphs illustrate the difference between a) the calculation of the electron transparency from the anode current and b) the electron transparency from the peak position.

As shown in Figure 5.19, for a higher Ar concentration, the electron transparency is overall lower. This is because CO_2 acts as a light quencher and as described in section 5.7, will allow charges to dissipate faster, and allow a higher collection of electrons, this will overall decrease the loss of electrons from one region to the other.

5.10 Measurement of Ion Backflow

5.10.1 Ion Backflow Measurements

Along with the electron transparency, the second main quantity which was critical to monitor was evidently the ion backflow. The ions drifting back following field lines, from the amplification stages to the drift zone D2 will partly be collected onto the mesh, generating a current I_M. The remaining, which will follow further field lines through the holes of the mesh will drift back to zone D1, where they will be collected onto the cathode, producing a current I_C. As the number of ions collected is dependent on the number of electrons collected on the anode I_A, ion backflow is usually defined as the ratio of the I_C to the I_C in the case of a normal triple GEM detector. As in

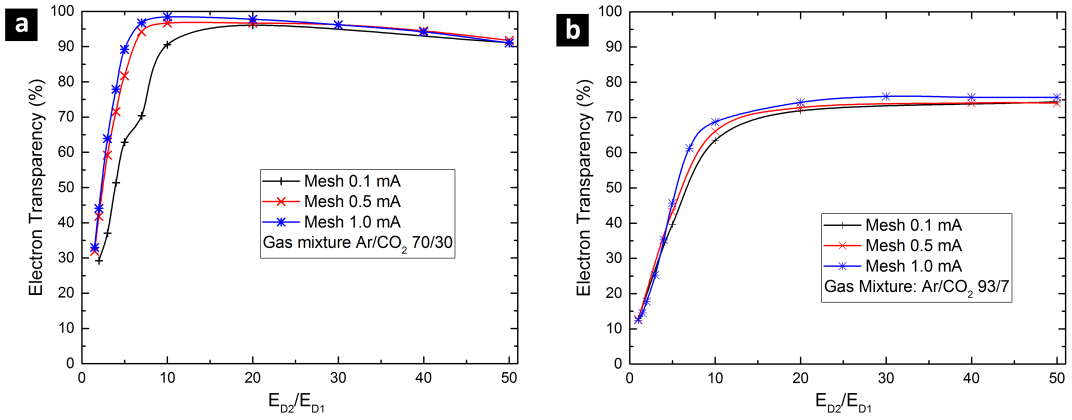

Figure 5.19: Graphs of the electron transparency of a mesh as a function of the ratio E_{D2}/E_{D1} the electric field below the mesh over the electric field above it. The higher positive ratio therefore a stronger field below the mesh. Both graphs were taken at varying X-ray currents, (the higher current, the stronger the signal) and illustrate the effect of the gas mixture on the transparency of the mesh for a) Ar/CO_2 70/30 and b) Ar/CO_2 93/7.

this work the mesh collects part of the ions drifting back from the triple GEM, the ion backflow can be rewritten:

$$IBF = \frac{I_C}{I_A} = \frac{I_M + I_C}{I_A} \tag{5.13}$$

However, the aim of this work was to measure the properties of graphene, supported on the mesh, as an effective ion collector, not the measure of the ion backflow itself. We therefore define another quantity of more interest: the ion transparency of the mesh T_{ions}. If the graphene did block some of the ions, they would contribute to the ones collected on the mesh as part of I_M, while the ones drifting back to I_C would be considered gone through the graphene layer. The ion transparency of the mesh is therefore defined as a fraction of the ion backflowing from the GEM:

$$T_{ions} = \frac{I_C}{I_M + I_C} \tag{5.14}$$

As this quantity is defined as a fraction of the ions flowing back from the amplification region, this quantity is not expected to be affected by the gas mixture, V_{GEM}, nor I_{xray} but only by the field lines and the geometry of the mesh. T_{ions} was therefore monitored as a function of E_2/E_{D1} along with T_{e-}. The measurements were

done simultaneously with the measurements for T_{e-} in a similar fashion. Figure 5.20 shows the ion transparency T_{ions} measured with Ar/CO_2 70-30 and 93/7, confirming the independence on the gas mixture. On the other hand, the measurements with the same E_{D2}/E_{D1} as for T_{e-} (labelled 'normal GEM operating region') show that an ion backflow below the optical transparency of the mesh, indicating that the mesh already collects most of the electrons. It was then necessary to increase further E_{D1}, until $E_{D1} > E_{D2}$ in order to reach a high ion backflow region to test the graphene for T_{ions}. The resulting measurement are labelled accordingly in Figure 5.20.

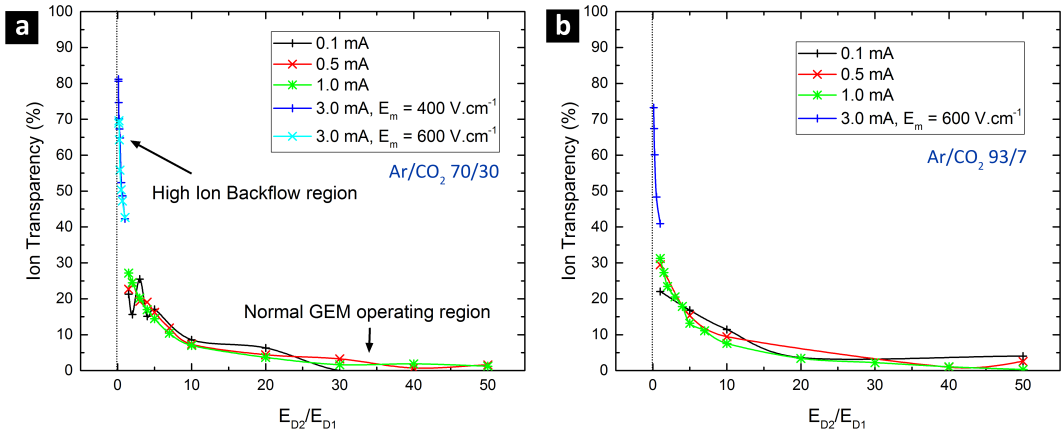

Figure 5.20: Graphs of the ion transparency of a mesh as a function of the ratio E_{D2}/E_{D1} the electric field below the mesh over the electric field above it. The higher positive ratio is therefore a stronger field below the mesh. Both graphs were taken at varying X-ray currents, and illustrate the effect of the gas mixture on the ion transparency of the mesh for a) Ar/CO_2 70/30 and b) Ar/CO_2 93/7. The lines connecting the points are a guide to the eye.

The graph shows an increasing trend for the ion backflow as E_{D2}/E_{D1} is decreased. Indeed, the focusing works in an inverse way for the ions as for the electrons, as the field below the mesh increases, the field lines below will be denser and will end straight into the mesh, causing the maximum amount of ions to go through to be equal to the optical transparency: 22.67 % in this work. Conversely, as E_{D2}/E_{D1} reaches values below 1, the field above the mesh becomes higher, hence drawing ions through the mesh. This causes an increase in the ion backflow below 1. Another point to notice is that the ion backflow at low rates below $I_{xray} = 1.5\,\mathrm{mA}$ as seen on the graph show high fluctuations due to the low currents collected. For this reason as well as for the observation of a higher ion backflow than the optical transparency, the measurements

for ion backflow will be done in the next chapter at $I_{xray} = 3.0\,\mathrm{mA}$. This high rate did not affect the ion measurements as the rate is not needed in the calculation, while more accurate and higher currents were critical in order to assess the transparency of graphene layer. For ease of comparison with the electron transparency measurements, the graphs for the ion backflow will be plotted as a function of E_{D1}/E_{D2} so that an increasing x-axis will be equivalent to a higher focusing for ions.

5.11 Conclusion

In this chapter, the effects of the key parameters $\mathrm{V_{GEM}}$, $\mathrm{E_{D2}}$, $\mathrm{I_{xray}}$ and the gas mixture on relevant results were discussed for the standard triple GEM, as well as the relevant links between them for this experiment. A new measurement setup was introduced with its specific measurement methods and calculations, all of which were developed progressively during this work as the need arose: these consisted in suspending the graphene above the triple GEM on a copper mesh, therefore separating the drift region D into two: D1 and D2. Measurements of the variation of the electric field in both drifts regions were investigated without the presence of graphene, the effect of which will be treated in the next Chapter. The quantities $\mathrm{T_{e^-}}$ and $\mathrm{T_{ions}}$, the electron and ion transparency of the mesh were defined with their relevant calculation methods, and investigated systematically. The influence of graphene on these parameters will then be investigated in the next Chapter.

Chapter 6

Integration and Charge Transmission Properties of Graphene as a Membrane in a Triple GEM at Low Field Configuration

Publication of results from this chapter:

- *Charge Transfer Properties Through Graphene Layers in Gas Detectors*, P. Thuiner, R. Hall-Wilton, R. B. Jackman, H. Muller, **T. T. Nguyen**, E. Oliveri, D. Pfeiffer, F. Resnati, L. Ropelewski, J. A. Smith, M. van Stenis, and R. Veenhof, IEEE 2014 Transactions.

6.1 Introduction and Aims

The resilience of graphene in high electric fields was unknown and it was therefore important to test the behaviour of graphene under such conditions. For this the design discussed in Chapter 5 keeps the graphene in a low electric field region with E ranging from $0\,\mathrm{V.cm^{-1}}$ to $2000\,\mathrm{V.cm^{-1}}$. The first systematic steps consisted in the measurement of the electron and ion transparencies at low field and checking

their repeatability for the same layer in order to address potential damage due to the electric field. Secondly, the second set of measurements consisted in measuring the electron and ion transparencies at high electric field and assess its repeatability. For this graphene was transferred onto the backside of GEM and placed on top of the triple GEM. The detailed reasons for this configuration will be explained further in this Chapter.

6.2 Methods

The layers used in this chapter were transferred using the method described in Chapter 4. This separation allowed for the measurement of the four different regions within the same detector setup and the same environmental conditions, without having to open the detector between all the measurements. The pressure and temperature were $(21 \pm 1)^{o}$C and atmospheric pressure, the gases were flushed for at least two hours (when possible overnight) at 9 L/h, then the experiments were conducted at 5L/h. Graphene was transferred onto the top side of copper (Cu) meshes with an active area of 30 mm x 30 mm using the technique developed in Chapter 4. The meshes were fabricated by the CERN workshop by stretching a 5 µm thick copper foil onto a 40 mm x 40 mm kapton frame. Periodic holes of 35 µm size and a pitch of 60 µm were then etched onto the active suspended area by standard photolithography: SU-1818 resist was coated onto the layer, then exposed to UV light and subsequently developed. The holes were then etched away using $FeCl_3$ (further details can be found in the following reference: [154]).

The presence of graphene required a much slower ramp up rate of $10\,V.s^{-1}$ in order to check systematically for discharges and therefore avoiding damage to the very fragile layer. The first part of the experiment consisted in measuring the transfer properties of the graphene at low fields, in order to avoid damage. The setup for this was the same as the one described in Section 5.3 except for a slower ramping rate and for the addition of monolayer and trilayer graphene.

The setup was optimised so that the graphene was not exposed to the high fields within the GEMs as its strength needed to be proven for low fields first. For this, a micromesh was added above the GEMs in the primary ionization zone as shown in

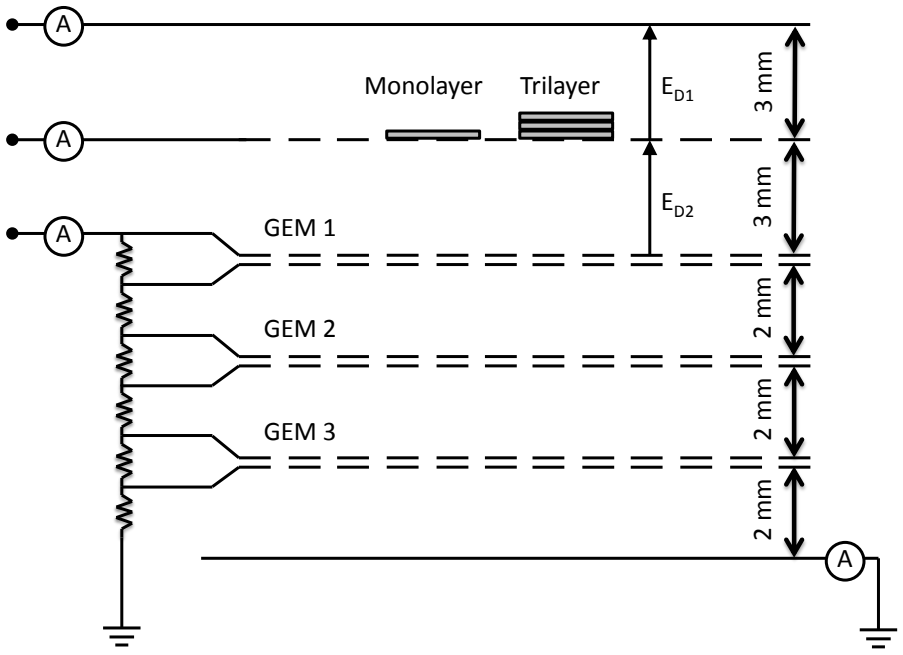

Figure 6.1: Diagram of the measurement setup used in this chapter. Monolayer and trilayer graphene were transferred onto the top of a mesh to avoid large fields. This mesh was placed in the drift region D of the triple GEM, dividing it into D1 and D2.

Figure 5.1. This allowed its use as a support for the graphene without exposing it to the high field density within the GEM holes. As described in Chapter 5, the triple GEM was calibrated to operate in the region of true proportionality, the current used on the voltage divider was 740 µA. The meshes were divided into four quadrants with either monolayer graphene or trilayer graphene covering one of the quadrants, leaving the rest of the mesh graphene-free. The reason for this was so that the graphene and the bare mesh could be directly compared without having to open the detector and re-calibrate all the settings, this would not only cause a difference in calibration parameters, which would make results slighty different but would also be significantly more time consuming. The graphene coverage over the holes of the mesh was determined using the method described in section 4.4.4. The following measurements will now present the results for the measurements in this low field configuration.

6.3 Measurements on Suspended Monolayer Graphene

The monolayer was deposited on a mesh with 35 µm holes and 60 µm pitch. For this measurement, this mesh had a graphene coverage over the holes of 75.8 ± 0.8 % as shown on Figure 6.2 a). The mesh active area was 30 mm wide and the graphene covered the area between 15 mm and 25 mm as shown on Figure 6.2 b). The first measurements were done to determine the electron transparency T_{e-} and the layer was scanned across the x-axis as labelled in Figure b), at $E_{D1} = 20\,\mathrm{V.cm^{-1}}$ and $E_{D2} = 800\,\mathrm{V.cm^{-1}}$ at $I_{GEM} = 740\,\mu\mathrm{A}$ and at a fixed $I_{xray} = 0.05\,\mathrm{mA}$. The gas mixture used was Ar-CO_2 70-30.

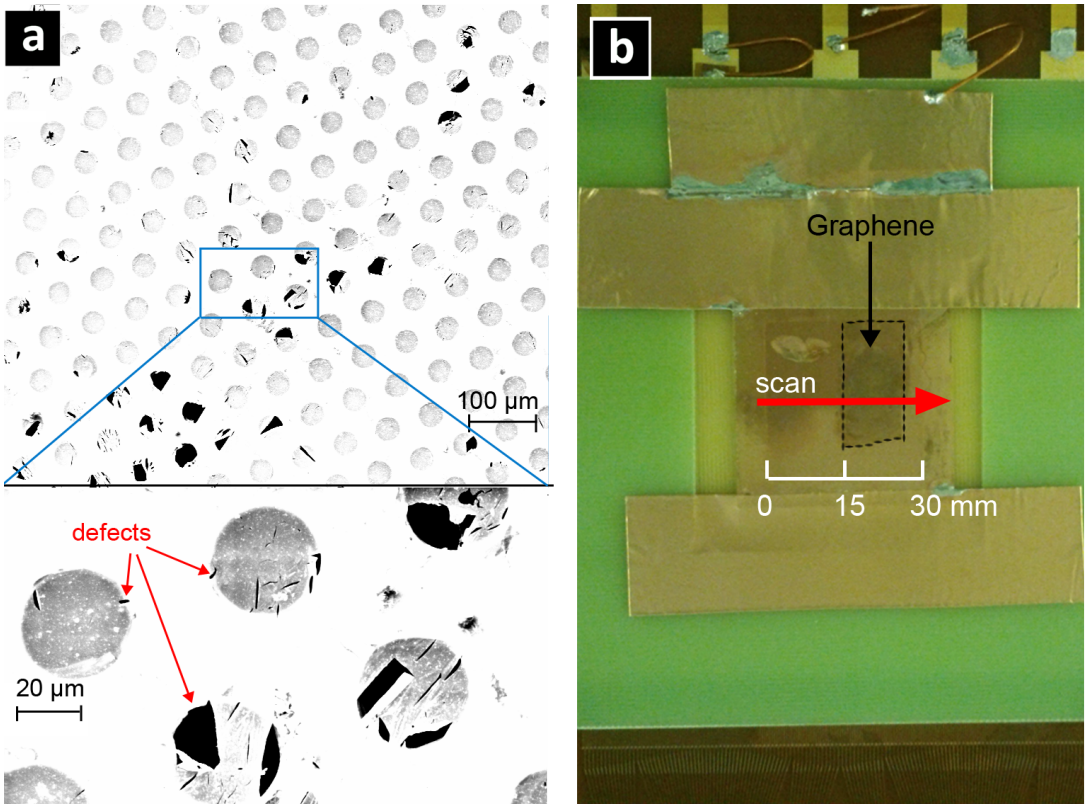

Figure 6.2: a) SEM image taken at 2 keV accelerating voltage, of the monolayer graphene used for this measurement. Below shows an magnified image of a zone in the centre of the SEM image, illustrating some defects present on the layer. b) Photo of the mesh within the detector, showing the size of the graphene layer (dashed lines), as well as the scan direction for the measurements and the x-axis for the position.

The resulting anode current I_A at constant rate is plotted in Figure 6.3. As shown on the graph, there is a clear decrease in the anode current from the graphene layer

compared with the bare mesh. The subsequent calculation of the electron transparency from P_1/P_2, is also plotted on the same graph T_{e-} and shows the same correlation as the anode current: the transparency to electrons is lower in the presence of graphene. The average current collected on the anode from the Mesh was $4.4 \pm 0.2\,\mathrm{nA}$ and it is decreased to $3.3 \pm 0.3\,\mathrm{nA}$. Similarly, T_{e-} on the mesh was $61.5 \pm 0.9\,\%$ while on the graphene layer: $T_{e-} = 23 \pm 7\,\%$. From this result, the mesh with graphene covering the holes seems to exhibit a lower T_{e-} than the mesh.

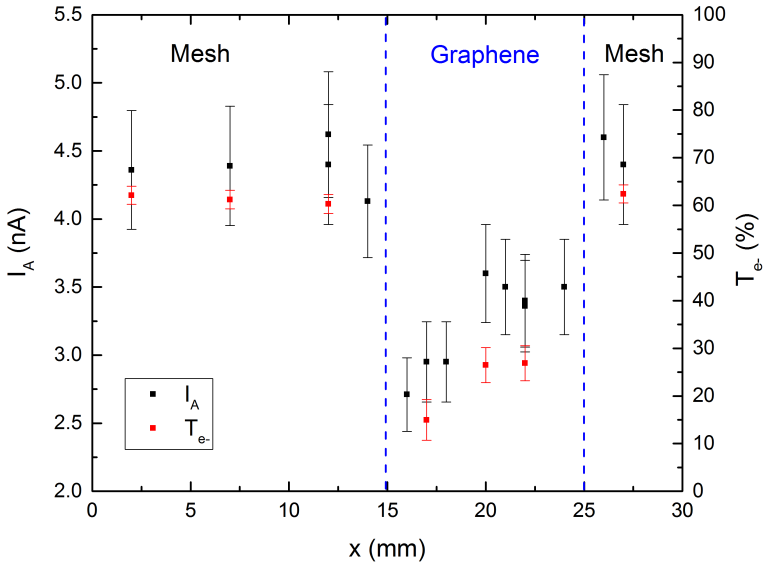

Figure 6.3: Graph of I_A and T_{e-} as a function of the position on the x-axis as labelled in Figure 6.2 for $E_{D2}/E_{D1} = 40$. The position of the graphene with respect to the bare mesh is labelled as dashed lines for clarity. The anode current measured in the setup is actually negative but the absolute value is plotted here for a more meaningful comparison with the transparency.

The next step was to assess the behaviour of T_{e-} as a function of the field focusing. If the graphene layer behaved as a perfect conductor, the electric field above the layer E_{D1} would be expected to have its field lines normal to the layer regardless of density of the field, and T_{e-} would be expected to be close to the optical transparency, and constant as a function of E_{D2}/E_{D1}. Even in the case of a semiconducting behaviour, the high fields applied in this setup are enough to overcome any potential opened bandgap in graphene, and the layer would eventually behave as a metal. However, as

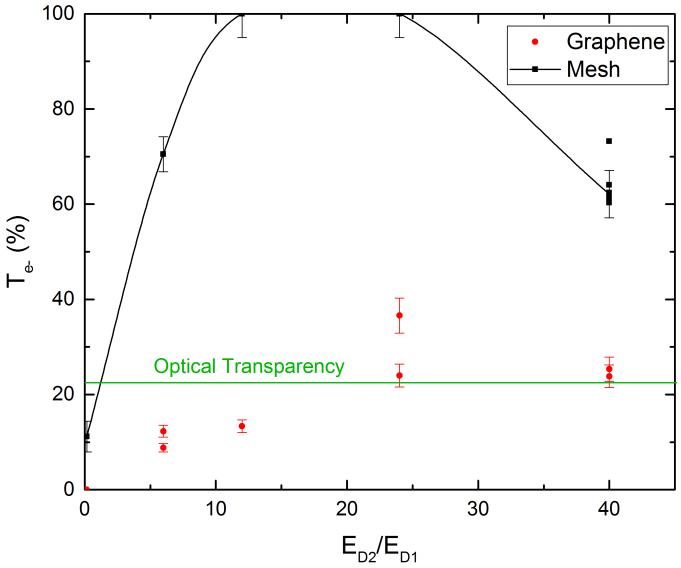

Figure 6.4: Graph of T_{e-} as a function of E_{D2}/E_{D1} for the bare mesh in black and graphene in red. The line is a guide to the eye to locate the points for the mesh.

the fields also need to be continuous, in the case of $E_{D2} > E_{D1}$, some field lines will still be focused into the holes covered with graphene. So we expect a T_{e-} for graphene to behave in a similar manner to the mesh but with a lower transparency.

The behaviour of T_{e-} for both graphene and the mesh is illustrated in Figure 6.4. The transparency of this mesh behaves a expected from the results of Chapter 5. And T_{e-} on the mesh covered with graphene is observed to have a transparency which increases with increasing E_{D2}/E_{D1}. This seems to confirm the observation from Figure 6.3 and the qualitative discussion in the previous paragraph, that graphene is expected to behave as a mesh with lower electron transparency.

The graphene monolayer seems therefore to behave as expected: in its presence, the electron transparency is slightly lower. Next the ion backflow was measured. The graphene layer is expected to be completely opaque to ions and regardless of the field configuration, T_{ions} is expected to stay constant.

The results of the ion measurements are presented in Figure 6.5. The mesh behaves as expected and T_{ions} increases with decreasing E_{D2}/E_{D1}. On the other hand, the ion measurements for the graphene layer also show an increase at decreasing E_{D2}/E_{D1}.

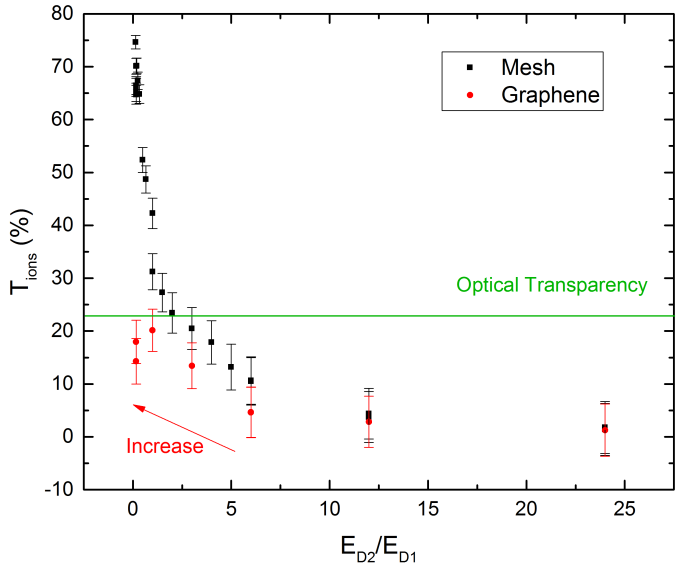

Figure 6.5: Graph of T_{ions} as a function of E_{D2}/E_{D1} for the bare mesh in black and graphene in red.

Despite the lesser number of points the trend of T_{ions} for graphene seems to follow very closely the trend for the mesh when no dependence was expected.

Combining this information with the increasing trend from the electron transparency of graphene, overall, this monolayer of graphene seemed to behave in the same way as a mesh but with a lower transparency both for T_{ions} and T_{e-}. Such behaviour was expected for T_{e-} but not for T_{ions}, which was expected to stay constant.

In an ideal case, the optical transparency of the graphene layer would be zero. However, as stated above, the coverage of the holes was $75.8 \pm 0.8\,\%$, therefore modifying the effective optical transparency of the graphene+mesh to be $5.5\,\%$. A hypothesis for the behaviour of the ion and electron transparencies observed would be that the field lines also need continuity in these defective zones, and to remedy to that, the field lines from D1, will focus into the defects preferentially causing the graphene+mesh to behave as a mesh with a lesser optical transparency.

In order to verify this hypothesis, and in order to suppress the ion backflow still observed, the next step was to improve the transfer of graphene so as to eliminate defects on the layer. As discussed in Chapter 4, the defects arise mainly from already

existing defects on grown graphene combined with some defects which arise from mechanical manipulation of the layer during the transfer process. Let N be the probability of getting a defect, the probability of which is assumed to be random. In which case by transferring one graphene layer on top of another layer to form a bilayer would make the probability of getting a defect N^2. As $N < 1/2$, then the probability is expected to diminish significantly. For a probability of $N = 0.242$ as in our case, transferring two layers would yield $N_{bi} = 0.059$ (so 5.9 %), and in the case of a trilayer, the probability would be significantly lower with $N_{tri} = N^3 = 0.014$, yielding 1.4 % of defects. Probabilities aside, the resistance of a bilayer, and trilayer to tear during mechanical manipulation was expected to reduce the experimental defects even further. For these reasons, in order to reduce the number of defects as much as possible while keeping the suspended surface area high, the next step consisted in transferring trilayer graphene onto a mesh, and monitoring the behaviour of T_{ions} and T_{e-} on the layer.

6.4 T_{ions} on Trilayer Graphene

The trilayer was transferred onto a mesh with a coverage of 99.7 ± 0.5 % onto a Cu mesh with 35 µm holes and 60 µm pitch as discussed in Chapter 4. An SEM image of the trilayer is shown in Figure 4.8, and its quality is further discussed in Section 4.4.5. The first measurements were done to determine the ion transparency T_{ions} at $I_{GEM} = 740$ µA for Ar-CO_2 70-30 and at a fixed $I_{xray} = 3.0$ mA. The gas mixture was then changed to Ar-CO_2 93-7 with a current of $I_{GEM} = 635$ µA, also corresponding to a gain of 10^4. E_{D2} was kept fixed while E_{D1} was varied systematically.

Firstly the standard GEM operation regime was investigated, by varying E_{D1} between 0 and E_{D2}. These measurements yielded only residual ion backflow close to zero, a promising result, possibly indicating complete ion-blocking properties. However for this regime, the ion extraction field (i.e. E_{D1}) is low: E_{D1}/E_{D2} is lower than 1. It was therefore critical to check the ion backflow blocking for a high extraction field. For this, E_{D1} was varied between the values of E_{D2} and 3600 V.cm^{-1}. The E_{D2} used to this end had to be lower than that used in the electron transmission measurements (2000 V.cm^{-1}) for practical purposes as increasing the extraction field much higher

than 2000 in order to reach respectable E_{D1}/E_{D2} ratios can cause large discharges and become un-manageable. But in order to cross-check the independence of the results on the value of E_{D2}, two values were chosen: $400\,\mathrm{V.cm^{-1}}$ and $600\,\mathrm{V.cm^{-1}}$ and measured systematically.

The results of the ion measurements are shown in Figure 6.6. Graph a) shows the results in Ar-CO_2 70-30, the mesh behaves as expected and increases with increasing E_{D1}/E_{D2}. On the other hand, for comparison graphene was measured on two different points on the layer labelled Gr1 and Gr2 as well as for two values of E_{D2}. The collimator used had a diameter of 0.5 mm, making the area investigated at both points roughly a disk of 500 µm diameter. In both cases T_{ions} on trilayer graphene did not show any dependence on E_{D1}/E_{D2} and remained below 10 % transparency, within error bars of zero. This behaviour was checked at the same two points in Ar-CO_2 93-7, after flushing with the gas overnight. This independence on E_{D1}/E_{D2} seems promising as it was the expected behaviour for graphene as discussed in the previous section. The ion measurements investigated on monolayer graphene in the previous section, showed a dependence in T_{ions} as a function of E_{D1}/E_{D2}, similar to the behaviour of the mesh. The independence found in on trilayer graphene seems to confirm the hypothesis that the behaviour observed for monolayer was related to the number of defects. The next step consisted in the measurements of the electron transparency T_{e-} of the layer.

6.5 T_{e^-} on Trilayer Graphene in Ar-CO_2 70-30

The measurements for the electron transparency were done at low rate with $I_{xray} = 0.1/0.5/1.0\,\mathrm{mA}$ in the same conditions as the ion transparency at the same points Gr1 and Gr2. First the gas mixture Ar-CO_2 70-30 was investigated. Figure 6.7 shows an energy spectra taken at $E_{D1} = 666\,\mathrm{V.cm^{-1}}$ $E_{D2} = 2000\,\mathrm{V.cm^{-1}}$ for a point on the Mesh, and for points Gr1 and Gr2. The respective positions of the points are described in the inset. This graph illustrates how low T_{e-} for graphene was, compared with the bare mesh but also shows that the transparency in Gr1 was slightly lower than the transparency in Gr2. For illustration purposes, the energy spectra for point Gr2 is shown in Figure b), with P_1 shifting to higher energies for higher E_{D2}/E_{D1}. The

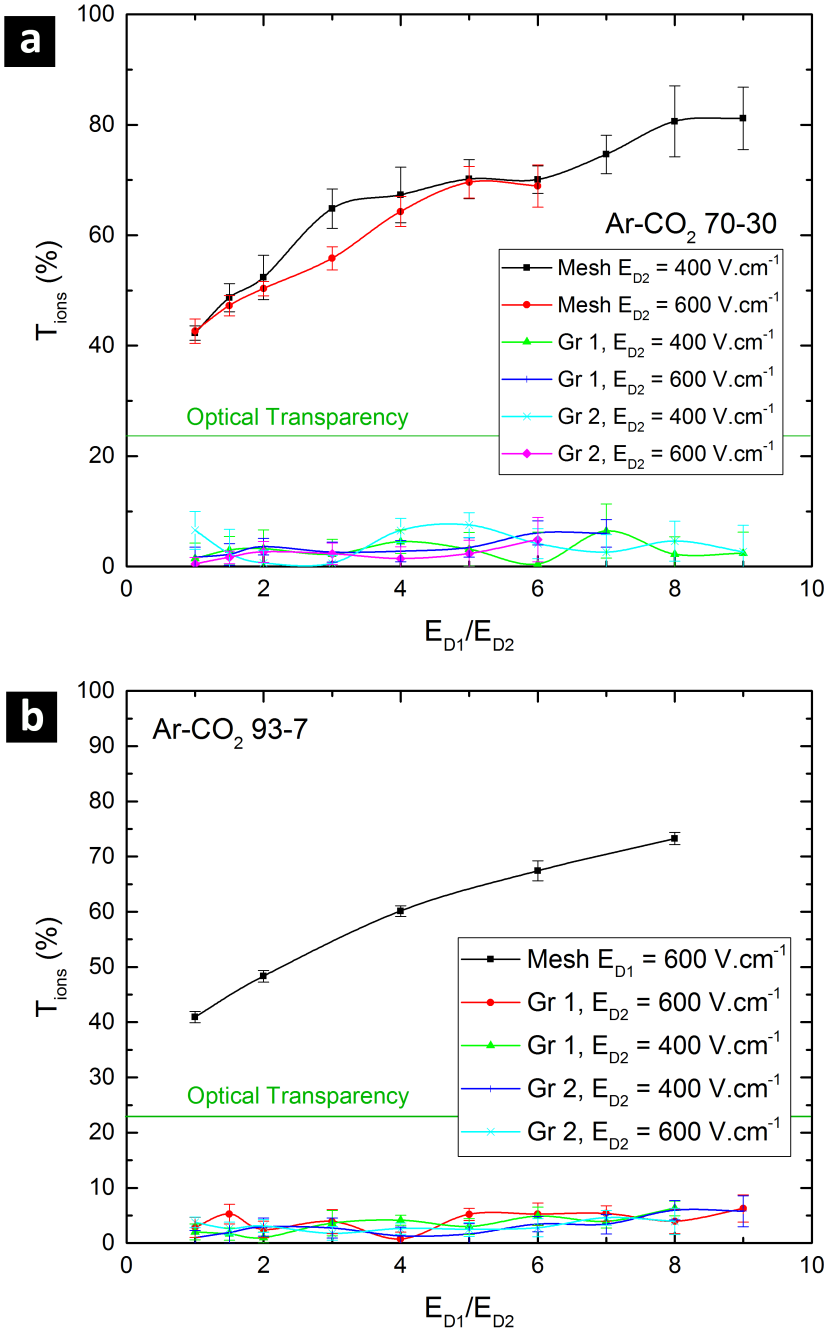

Figure 6.6: Graphs of the ion transparency T_{ions} as a function of E_{D1}/E_{D2}, at varying I_{xray} comparing a part of the mesh covered with trilayer graphene at two different arbitrary points: Gr1 and Gr2 with the bare mesh. In graph a) the gas mixture used was for Ar-CO_2 70-30 and in b) Ar-CO_2 93-7.

electron transparencies were then computed from the position of the peaks for all points.

The results for the electron transparency are plotted in Figure 6.8 for the position Gr1 on the trilayer. Figure a) shows the results calculated from the peak positions in the spectrum P_1/P_2. T_{e-} on the mesh exhibits the expected behaviour. On the other hand, measurements on graphene first did not show any apparent peak P_1 suggesting the layer was either completely opaque, i.e. the peak was below the noise, or the layer was completely transparent, i.e. peaks P_1 and P_2 overlapped perfectly. Integration of the counts on the spectrum eventually displayed the same number of counts a the measurements with inverted E_{D1}, suggesting the first hypothesis: the layer was completely opaque to electrons. By increasing E_{D2}/E_{D1} beyond 20, the tail of P_1 started appearing, the peak eventually started appearing enough to be fitted with a Gaussian after $E_{D2}/E_{D1} = 40$. The fitting results are plotted on the graph showing a very low T_{e-}, which seems to exhibit an increasing transparency trend with increasing field focusing. This behaviour was cross-checked using the measurements from I_A, allowing to obtain the lower values of the transparency as shown in Figure b), which shows the clear increasing trend of T_{e-}.

The results were checked once again at the separate point Gr2 using the same settings and the results are plotted on Figure 6.9. Point Gr2 on the layer exhibited the same increasing behaviour, visible for both caculation methods, and a slightly higher transparency by up to 5 %. This difference could be due to local variations on either the trilayer itself or some differences in geometrical defects on the mesh itself, but overall the values for were within calculation errors and most importantly, the increasing behaviour was still observed below the optical transparency. This suggested once more that the effective optical transparency of the mesh was reduced and that a large amount of field focusing was occurring in the defects despite their low percentage of 0.3 ± 0.5 %. This conclusion points at two issues: the first one is that if field focusing occurs for electrons through these defects, this means inverse field focusing is likely to occur for the ions the other way. The reason for which the effect could not be observed in this experiment is simply due to the fact that T_{e-} measured for graphene is very low compared to that of the mesh, making the ion backflow residual and very

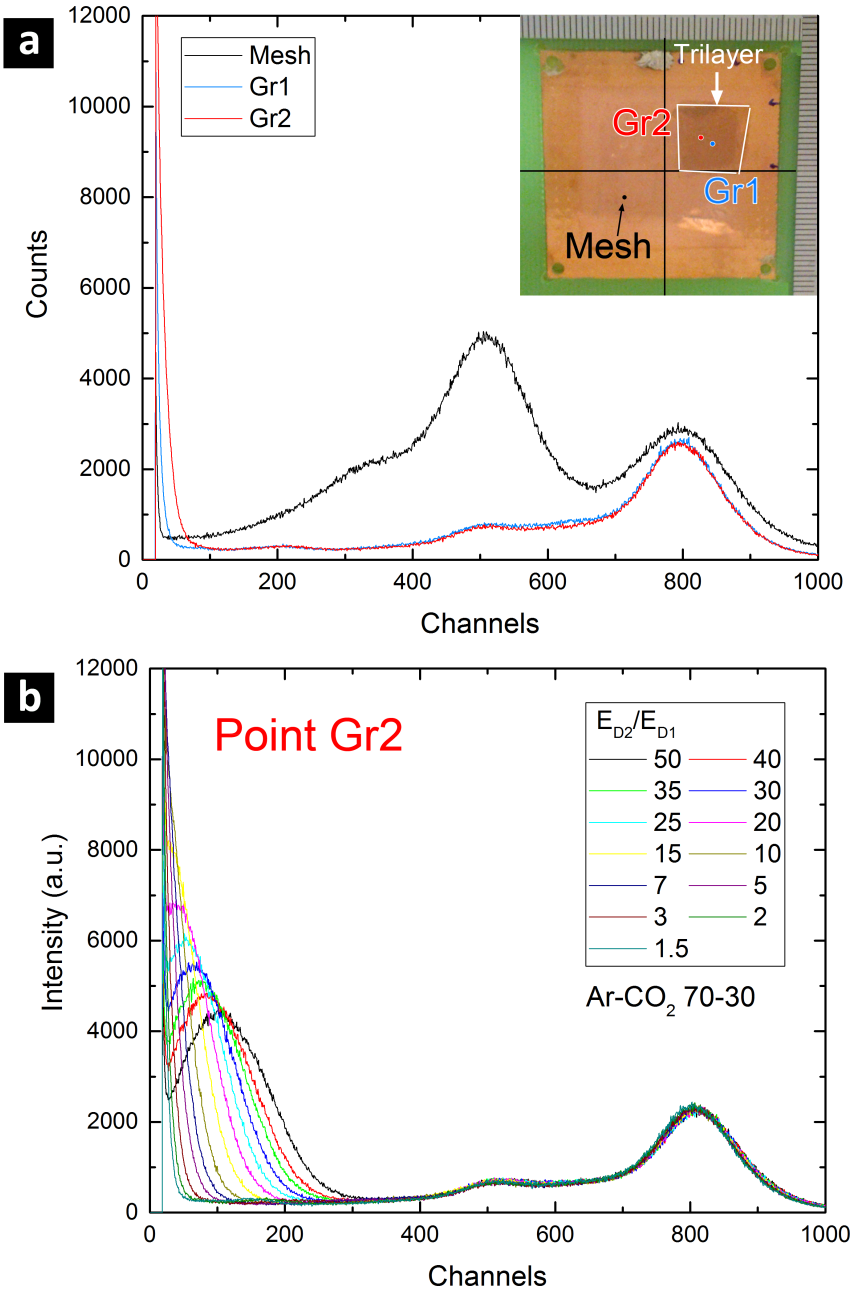

Figure 6.7: a) Energy spectra of the mesh, the points Gr1 and Gr2 at $E_{D2}/E_{D1} = 3$. Inset shows a photo of the mesh with the position of the trilayer on the mesh outlined in white, with coloured points corresponding to the respective positions of the measurements. b) Energy spectra of point Gr2 with varying E_{D2}/E_{D1} showing P_1 shifting to higher energies for increasing E_{D2}/E_{D1}.

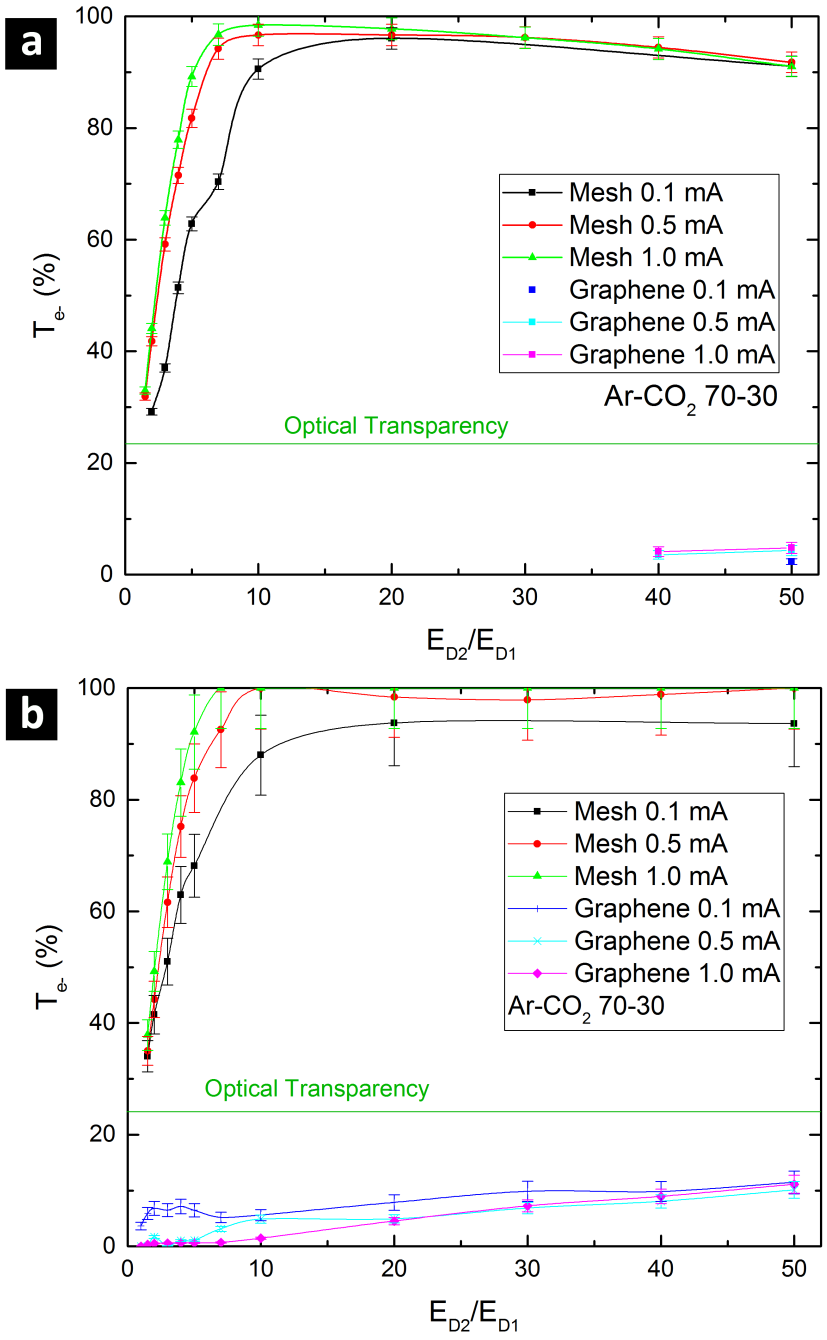

Figure 6.8: Graphs of the electron transparency T_{e-} at point Gr1 as a function of E_{D2}/E_{D1} for Ar-CO_2 70-30, at varying I_{xray} comparing a part of the mesh covered with trilayer graphene with the bare mesh. In graph a), T_{e-} was calculated using P_1/P_2 and in b) with the anode current I_A .

difficult to measure using this method. On the other hand, the finding of this field focusing into defects also reveals an overall wider point to be investigated: that of the electron transmission through graphene. Indeed if graphene did transmit 100 % of electrons as originally hypothesized, then the T_{e-} would be at least equal to the optical transparency, or even slightly higher with the addition of the field focusing of extra electrons through the holes. However, in this case, as the value lies below the optical transparency, this meant that if trilayer graphene did transmit electrons, it was only a fraction of them. For this reason an experiment needed to be set up in order to differentiate the electrons transmitted through the layer from the ones which were focused through the holes, to assess the actual T_{e-} of the layer.

This field focusing side-effect through the defects would not be of importance in this application of graphene, provided the electron transparency could be high enough to have a readable signal at lower field, while still blocking all ions with no field dependence as demonstrated in the previous section. However the electron transparency measured through graphene in this section even due to field focusing would make it too low to resolve any radiation below the 8 keV X-rays used in this work. For this, the next step was to work further on the transfer of graphene to reduce the amount of defects without increasing the number of layers in order to measure the effective electron transmission of the layer independently from the defects. And in parallel, the electron transparency needed to be improved by increasing the energy of the electrons through the layer. Alternatively another method of assessing the real T_{e-} of the layer would be to increase the kinetic energy of the electrons. For this, the gas mixture can be changed inside the chamber in order to increase the average drift velocity of the electrons. For this purpose, the gas mixture was changed to Ar-CO_2 93-7, and will be discussed in the next section.

6.6 T_{e-} on Trilayer Graphene in Ar-CO_2 93-7

The purpose of changing the gas mixture in the set-up was to increase the average drift velocity of the electrons inside the setup in order to measure a change in the T_{e-} of graphene. Any change could then be quantified and separated from the field focusing effects in the defects discussed in the previous section. This would allow

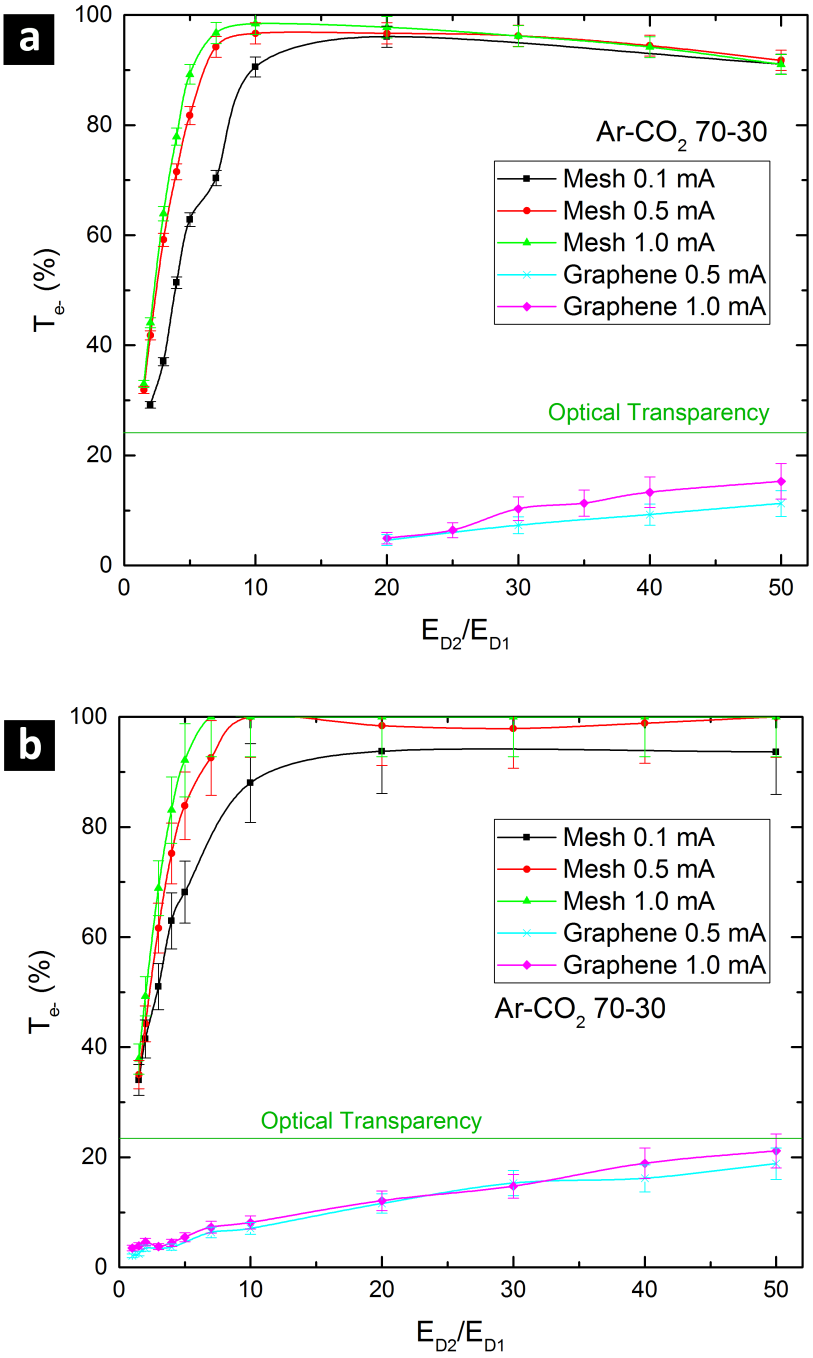

Figure 6.9: Graphs of the electron transparency T_{e-} at point Gr2 as a function of E_{D2}/E_{D1} for Ar-CO_2 70-30, at varying I_{xray} comparing a part of the mesh covered with trilayer graphene with the bare mesh. In graph a), T_{e-} was calculated using P_1/P_2 and in b) with the anode current I_A .

to measure the real transmission properties of graphene. The gas mixture inside the chamber was changed from Ar-CO_2 70-30 to Ar-CO_2 93-7. The distribution of the electron drift velocities inside the chamber are slightly different upon changing the quantities inside the chamber and are not simple Gaussians. The detailed description of such distributions are not of interest in this work and only the average drift electron velocity v_e was relevant to this experiment. For an increasing proportion of argon in this mixture, v_e will increase as shown in Figure 5.14. As discussed in Section 5.7, the current used to operate this gas mixture in the proportional regime was $I_{GEM} = 635\,\mu\text{A}$, for a gain of 10^4 as well.

The measurements are shown in Figure 6.10. The mesh behaved as expected, with an overall lower electron transparency than for the Ar-CO_2 70-30 mixture as explained in Section 5.7. The transparency was measured at the same points Gr1 and Gr2 as in the previous section. For Gr1, P_1 could not be measured at all, and the transparency measured from the anode was consistently below 5 % within error bars of zero. As a consequence, the graph for Gr1 was not presented here, instead, point Gr2 is shown in Figure 6.10. The transparency of graphene to electrons at point Gr2 was found to be slightly lower than the transparency in Ar-CO_2 93-7, but with the same increasing trend for increasing E_{D2}/E_{D1}. This behaviour is the opposite one to the one expected naturally, that is, the transparency would increase with increasing electron kinetic energy.

6.7 Discussion of the Results

First of all, these measurements have shown one important point: the repeatability of the measurements. The measurements were found to be repeatable when the points measured were changed, and when moving back to the same points, the results were found to be the same within random fluctuations. The transparency measurements for the monolayer were found to vary greatly depending on the point measured as the distribution of defects within a layer was not homogeneous even for a similar average coverage. On the other hand, the trilayer measurements were found to be repeatable at least twice on two separate samples, and for all measurements on different points of one sample. As a consequence, these results also show the non-destructive nature

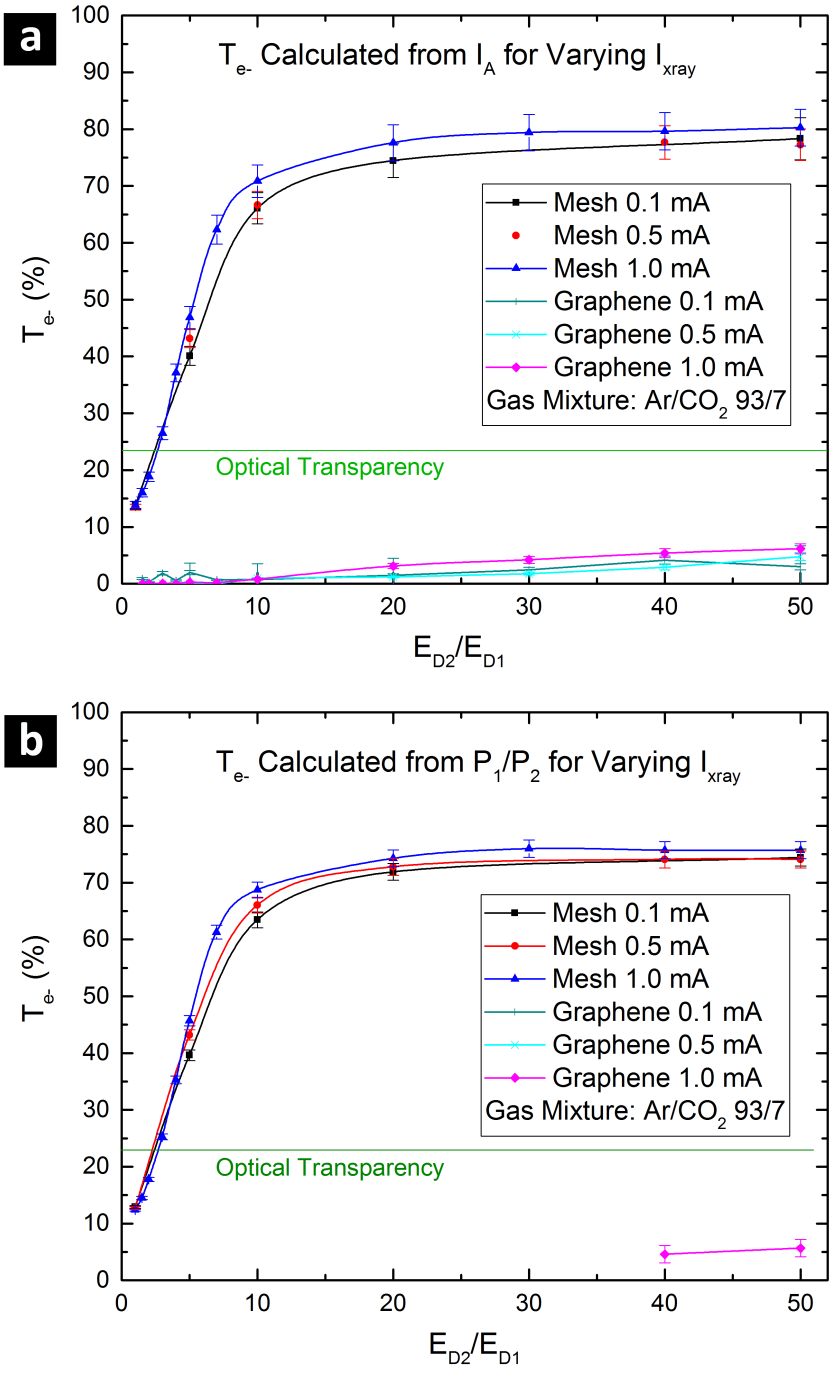

Figure 6.10: Graphs of the electron transparency T_{e-} at point Gr2 as a function of E_{D2}/E_{D1} for Ar-CO_2 93-7, at varying I_{xray} comparing a part of the mesh covered with trilayer graphene with the bare mesh. In graph a), T_{e-} was calculated using P_1/P_2 and in b) with the anode current I_A .

of the measurement on graphene and its resilience in large field differences up to a ratio of 50.

Secondly, in terms of findings, these measurements have revealed the complex behaviour of charge transmission through large areas of suspended graphene. To summarise the results before discussing them, the transmission measurements were found to be strongly influenced by the presence of defects on graphene. Indeed, multiple experiments have previously shown that graphene is completely opaque to ions and molecules [48], making graphene a good membrane for transdiffusion applications [50, 98, 102, 103, 155–158] as previously discussed. However in ion diffusion measurements in monolayer graphene, the layer showed a very large ion transparency at high E_{D1}, a similar behaviour to the ion transparency of the bare mesh. T_{ions} for the monolayer was slightly lower than that of the mesh, almost within error bars, indicating that the ions were field focused through the graphene layer. As the layer should be opaque but presented a non-negligible percentage of defects: 24.2 %, this large ion transparency could only be attributed to field focusing through holes, leading to the conclusion that electrons were therefore also field focused through the holes. Indeed the T_{e-} of the monolayer was found to exhibit the same trend as the one for the mesh but lower, and most importantly, below the optical transparency of the mesh. The percentage of defects compared to the hole mesh was 5.5 %, and indeed, taking that value as the effective optical transparency then T_{e-} did indeed stay above that lower limit, confirming the field focusing of electrons.

Subsequent measurements on trilayer graphene with 99.7 % coverage showed that the layer was indeed completely opaque to ions within random fluctuations even at very high ion extraction field E_{D1}. On the other hand, the electron measurements showed an increasing dependence on their extraction field E_{D2}. This behaviour would be expected if electrons were transmitted through graphene. Indeed increasing their extraction field will increase the number of electrons being drawn through the layer. However the T_{e-} was low, and below the mesh optical transparency once more, indicating the effective transparency was reduced and that field focusing was occurring also for the trialyer. The effective transparency of the trilayer taking into account defects would be 0.07 % making this lower limit unresolvable with the existing errors.

However this very low limit, explained the decreasing behaviour observed even for very low E_{D1}.

Finally in order to determine the real transparency of the mesh, and deconvolute it from field focused electrons, the energy of the electrons was modified by changing the gas to Ar-CO_2 93-7 instead of Ar-CO_2 70-30. The kinetic energy of the electrons was therefore increased. T_{e-} was observed to decrease systematically even lower, close to complete opacity for the same points measured in Ar-CO_2 70-30, suggesting that most, if not all of the electrons measured through the mesh were field-focused and that the trilayer was likely to be completely opaque to electrons at these energies.

Another point that this experiment has demonstrated, was the potential mechanism for the electron transmission through graphene. As shown by the graphs of the electron transparency of the layer as a function of I_{xray}, the T_{e-} of graphene does not depend on the rate (i.e. the intensity of the electron beam). At this point a few possibilities are possible for the transmission of graphene, transmission of the electrons could occur as a conducting mechanism due to allowed states above a certain bandgap. Or the second mechanism could be tunnelling. As any band-gap occurring in graphene would be expected to be of the order of a few eVs as discussed in Section 1.5.2 and as the energy of the electrons in this experiment are of the same order of magnitude as the bandgap, we expect either full transmission (above the bandgap energy) or a transmission probability of 0 - 10 % below that depending on the electron energy. If no transmission occurs, this would mean that the energy of the electrons need to be increased.

6.8 Conclusions

As a conclusion this chapter has demonstrated the resilience of graphene in field ratios up to 50 through the repeatability of the measurements. Both ions and electrons were found to be subject to field dependence in the presence of large amounts of defects. This field dependence was correlated with field focusing effects through the holes and can be verified through the effective optical transparency measured in the T_{e-} graphs. Measurements on trilayer graphene showed a complete opacity to ions, but electrons were found to exhibit an optical transparency lower than the one of

the mesh, indicating once more that field focusing was occurring, suggesting that this was potentially true for the ions as well. Unfortunately the resolution of the equipment was not enough to resolve such a small dependence. However, this effect has little importance in this application, and provided the electron transparency can be increased to more functional levels, while keeping the ion transparency below the resolution of the equipment, this would show that graphene can be used to lower the levels of ion backflow without disturbing the measurements beyond functionality. By functional levels, it is understood that the transparency will be high enough that the peak signal can be distinguished from the noise and can be located accurately. The threshold will depend on the noise level of the measurement and on the broadening of the peaks but assuming a typical noise level as shown in Figure 6.7 b), a transparency of at least 30 % would be necessary.

The next steps for this work will therefore focus on the resilience of graphene at high electric field ratios, as well as increasing the electron transparency of graphene while keeping the ion backflow residual.

Chapter 7

Transmission Properties under High Field Configuration

Publication of results from this chapter:

- *Charge Transfer Properties through Graphene for Applications in Gaseous Detectors*, S. Franchino, D. Gonzalez-Diaz, R. Hall-Wilton, R. B. Jackman, H. Muller, **T. T. Nguyen**, R. de Oliveira, E. Oliveri, D. Pfeiffer, F. Resnati, L. Ropelewski, J. A. Smith, M. van Stenis, C. Streli, P. Thuiner, and R. Veenhof, Proceedings of the 13th Pisa Meeting 2015

7.1 Introduction and Expectations

The transmission properties of electrons and ions through graphene in gaseous detectors were measured in Chapter 6 for low field configurations in order to assess the resilience of graphene in electric fields ratios up to 50, while measuring the transmission properties of graphene. The ion-blocking properties of the graphene layer were established within the resolution of the equipment, as well as the electron transparency dependence of graphene on the amount of defects. This effect was identified to occur due to field focusing into these defects, an effect measureable from the effective optical transparency. However this field focusing finding is not critical to the purpose of graphene in this setup provided the electron transparency (effective or real) can be improved to functional levels, i.e. at least above the optical transparency of the

mesh. In this Chapter the resilience of graphene in high electric field ratios will be investigated while studying the electron transparency of graphene in order to improve it. To this end, graphene will be integrated in a GEM.

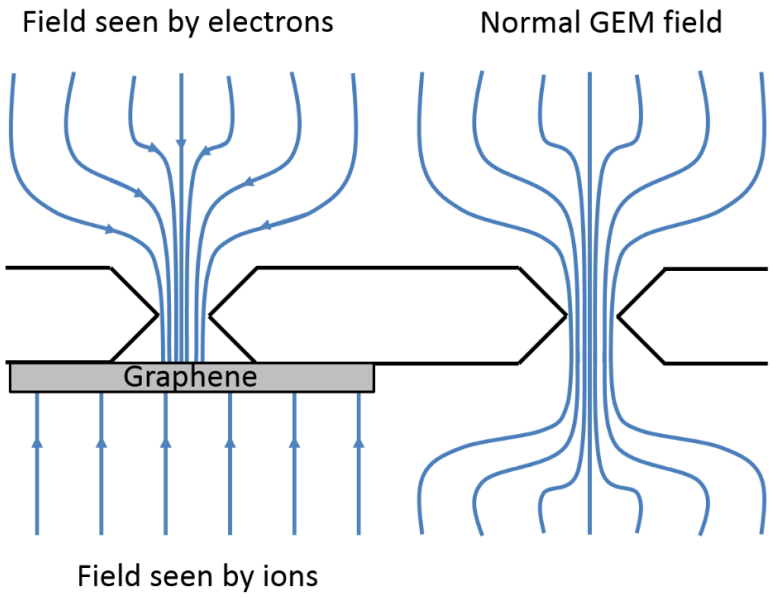

Figure 7.1: Diagram of the electric field in a GEM with graphene at the bottom, compared with the field in a normal GEM. In the presence of graphene the field 'seen' by the ions is different from the one 'seen' by electrons. The diagrams are for illustration of concept only.

The motivations behind this integration are explained in Figure 7.1. The diagram shows the electric field below and above a GEM in the presence of graphene compared with the field in a normal GEM. As graphene is a semi-metal, the field lines are expected to be perpendicular to it. Therefore by placing the graphene on the backside of the GEM, the field lines below it are expected to line up perpendicular to the layer, and no field focusing to occur. The ions drifting upwards towards the cathode are therefore expected to be all collected by the graphene layer, preventing ion backflow to the drift. On the other hand, field focusing is expected to still occur at the transition from the drift region into the high field region of the GEM. This should allow electrons to still be drawn through the graphene. As the the fields inside the GEM can be up to 25 times larger than the fields in the drift regions D1 and D2, the electron transparency is expected to be significantly improved by this setup. The second benefit of this setup

lies in the large fields within the GEM: as a GEM is 50 μm thick, therefore an applied voltage of 10 V already yields an electric field of 2000 V.cm^{-1}. Due to the small size of the fields, if optimal D1 and D2 fields were used, the density of electrons within the holes will also be very high, causing multiplication. So not only high field would allow for further field focus, but would also allow for enhancement of the electron transmission.

Another advantage of this measurement would be to avoid field focusing of the electrons through defects, a side effect discussed in the previous chapter. Indeed, as the transition from high to low field occurs at the upper entrance of the GEM for electrons, the particles drifting down will be drawn into the holes. Two situations can be expected once these electrons reach the amplification area inside the holes: if a defect is present, all the electrons in that hole will then be drawn through the defect in the graphene on the bottom of the GEM, then reaching region D2. And in the second case, the graphene in that hole would have no defect. In such situation, the electrons will then be forcefully drawn through the graphene layer and the transparency measured would then be the real transparency of graphene under these field conditions. These two cases mean that the transparency measured will be a convolution of the real transparency of graphene along with a transmission due to defects, which would be an improvement from the previous measurement. Indeed if an area with little defects can be achieved, then the transparency observed will mainly be the real transparency of graphene. Further methodological details are now discussed in the following section.

7.2 Methods and Experimental Challenges

For these measurements at high electric field, monolayer, bilayer and trilayer graphene were transferred using the method described in Chapter 4 onto the backside of copper coated GEMs with hole sizes of 35 µm with and effective inner diameter of 30 µm and a pitch of 60 µm. The GEMs had an active area of $30x30\,\mathrm{mm}^2$, which were divided into four rough quadrants with the monolayer, bilayer and trilayer each occupying one quadrant. The last one is kept graphene-free for direct comparison and cross-checking purposes.

The main difficulty in this change from a mesh to a GEM lied in the need for the

GEM to keep the top and bottom metallic layers well insulated to avoid discharges and damage. The GEMs were therefore checked for short-circuits before graphene transfer and after transfer. For this first batch, the three GEMs were all non-conductive before transfer. After transfer, samples 1 and 2 showed a variable resistance of about 200 Ω across the sample indicating that defective graphene may have lodged in the holes across the sample. Such low resistance would make applying a across the GEM impossible without a very large current and could therefore not be used for measurements as the large power supplies used had maximum current rating of 3mA.

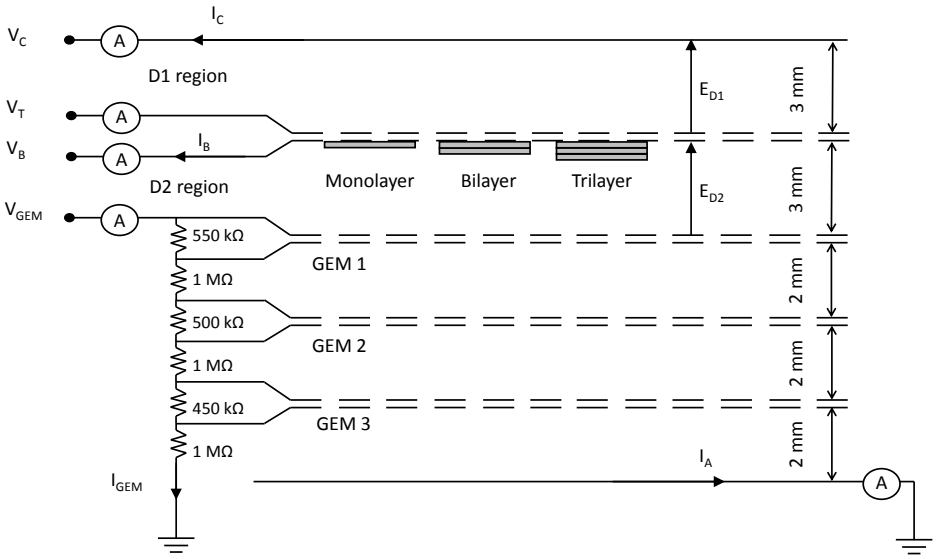

Figure 7.2: Diagram of the measurement setup used Section in this chapter. The graphene was transferred on the backside of a GEM with 35 µm diameter holes and a pitch of 60 µm

Sample 3 showed no conductivity across after transfer, but exhibited a resistance of $(10 \pm 2)\,\mathrm{M\Omega}$ after integration into the detector. The resistance was checked regularly in between trial voltage ramp ups and was found to be consistent. The GEM was integrated in the detector along with the triple GEM as described in Figure 7.2. As illustrated on the diagram, the top and bottom part of the GEM were powered separately by V_T and V_B in order to control the field applied to the GEM.

The voltage across the GEM used as support, $V_T - V_B$, will be labelled V_G in order to distinguish it from the voltage applied on the triple gem V_{GEM}. Due to the short across the GEM, a net current was expected to flow through the sample. A resistance

in MΩ with an applied voltage of 100V would yield a current of about 100 μA. As such a current is much larger than currents measured for ion backflow (a few nA), on a power supply with low current resolution (CAEN N1470 with a resolution of $\pm$ 50 nA) and additionally had significant fluctuations due to the instability of the resistance, the ion transparency of the GEM could not be measured with this setup. A way of monitoring the ion backflow in a qualitative way was to measure the differences on the cathode current (CAEN N1471H, $\pm$ 50 pA resolution) between the bare GEM and the GEM with graphene.

The second batch of samples consisted of two successful samples, which exhibited large resistance values (beyond the range of the voltmeter) after transfer. However upon integration and ramp up to the required voltages, one of them exhibited a too low resistance to be used, and the second GEM eventually exhibited a resistance of 200 kΩ and was successfully integrated into the system. The results from Sample 3 from the first batch are presented in section 7.3 and the sample from the second batch are presented in section 7.4.

On the setup shown on the diagram, graphene could have directly been integrated into the triple GEM however, this would have complicated the setup further and the effects of graphene would have to be de-convoluted from the effects of a missing stage of amplification. And a new setup would have to be re-characterised with one GEM less (a double GEM) and the results would also not be comparable with the previous ones.

On the other hand, by simply replacing the mesh with a GEM, we obtain a setup in which the triple GEM setup was already well characterised, and the division of the drift into two stages: D1 and D2 was well investigated in Chapter 5. This would leave the only new effects which may be observed, due to either the presence of graphene and/or the high field inside the GEM (as opposed to the absence of field difference across the mesh).

The gas mixtures used in this Chapter were Ar-CO_2 93-7, and 70-30 with I_{GEM} = 635 µA and I_{GEM} = 740 µA for the reasons explained in Chapters 5 and 6. The same care was taken to not ramp up too quickly the voltages to avoid large field differences, the gas was flushed for at least two hours. The voltages were settled in steps and left

running in the presence of discharges. The X-ray gun was turned ON and OFF at regular intervals between the measurements as was done in the previous chapter.

7.3 Irreversible Damage

The behaviour of the electron transparency of a GEM in the configuration is illustrated above is shown through Figure 7.3 for low fields. The graph describes the behaviour of T_{e-} of a GEM with varying voltage V_G. As the aim of this experiment was to improve the electron transparency of graphene, considerations that were not relevant to this application will not be discussed.

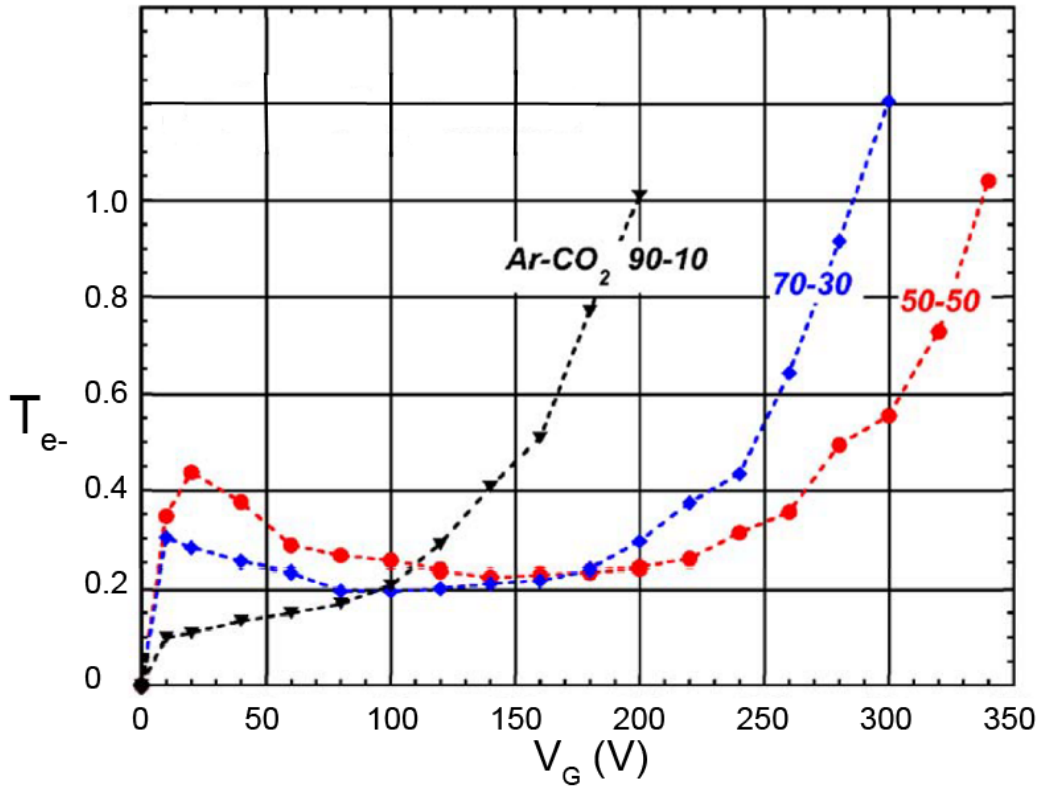

Figure 7.3: Graph of the electron transparency T_{e-} of a GEM as a function of applied voltage V_G for different gas mixtures of Ar-CO_2. The fields in the two drift regions were $E_{D1} = 150\,\mathrm{V.cm^{-1}}$ and $E_{D2} = 300\,\mathrm{V.cm^{-1}}$. Graph adapted from [159].

The electron transparency was measured here using the same peak ratio method as in Chapter 6. It is important to notice at this point that the transparency values shown on Figure 7.3, grow steadily until reaching a value beyond 100 %. This is due

to the multiplication effects discussed previously. This measurement therefore does not constitute the real electron transparency of a GEM and the results cannot be compared to those of the mesh. Even though, multiplication effects and transmission ones are not resolvable from each other, [159] this convolution can be beneficial to determine the presence of lower values of transparency as they will be amplified. It was shown in the previous chapters (confirmed in literature [159]) that the electron transparency increases with increasing transfer to drift E_{D2}/E_{D1} field ratio. Previous values of E_{D1} and E_{D2} were used. The values were consistently kept at $50\,\mathrm{V.cm^{-1}}$ and $2000\,\mathrm{V.cm^{-1}}$ respectively unless stated otherwise. These fields gave a high ratio of $E_{D2}/E_{D1} = 40$ for maximum transparency while staying in the proportional region.

Measurements were taken for the GEM up to 120 V as beyond this voltage, large discharges started appearing due to the large field, potentially damaging the GEMs. Interestingly, for the measurements on the graphene trilayer under the same conditions, the discharges started appearing from 70 V onwards. The behaviour of the anode current as a function of time is shown in Figure 7.4. The graph shows the systematic measurement of the ON and OFF values of I_A for increasing applied voltage V_G as a function of time. Towards 70 V onwards, the I_A shows very large punctual current peaks at least 20 times larger than the current measured from the X-rays. At $100\,V$ the I_A value was lost in the large amount of discharges. The measurement could not be carried further as repeated discharges caused very large currents to be drawn which the power supplies could not support, causing shutdown of the whole system.

The results of the measurement on the trilayer and on the bare GEM are shown in Figure 7.5. The GEM behaved as expected from Figure 7.3. On the other hand the trilayer exhibited no transparency up to 90 V. The consistence of the result shows the successful resilience of the layer under high field measurement conditions. On the other hand, the measurement seemed to show a transparency worse than the one measured on the mesh previously, with no transparency even up to a field inside the GEM of $18\,000\,\mathrm{V.cm^{-1}}$. This discrepancy with the measurements from the mesh indicates a need for repeat measurements, first at the same points to check the repeatability, then at different points of the same trilayer and eventually different batches.

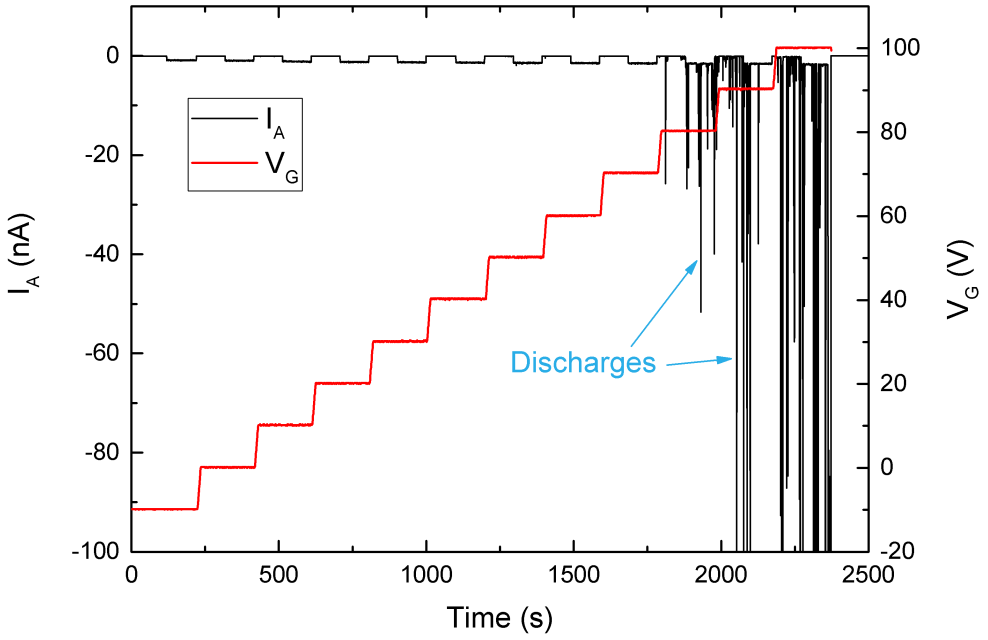

Figure 7.4: Graph of the anode current I_A as a function of time during a systematic variation of V_G, illustrating the large discharges occurring at large values of V_G from 70 V onwards.

A repeat measurement was made at the same trilayer point under the same conditions and it was found that the voltages could reach the same voltages V_G as the GEM. The energy spectra result for the repeat measurement at $V_G = 110$ V is shown in Figure 7.6, along with the spectrum of a bare GEM. As seen on the spectra, not only the transparency was higher than expected (an absence of the peak P_2 was expected from the previous measurements corresponding to a zero transparency), but it was also the same transparency as the bare GEM within some errors. After repeating the measurements at varying voltages, the measurements were taken once again under the same conditions at two other points of the trilayer, and then at a point on the bilayer and on the monolayer. All spectra are normalised and plotted on the same graph. All points have an average transparency of 18 % characteristic of the GEM transparency, indicating the graphene was not present anymore, whether it was monolayer, bilayer and trilayer.

This irreversible damage to the graphene layers could have originated from a few

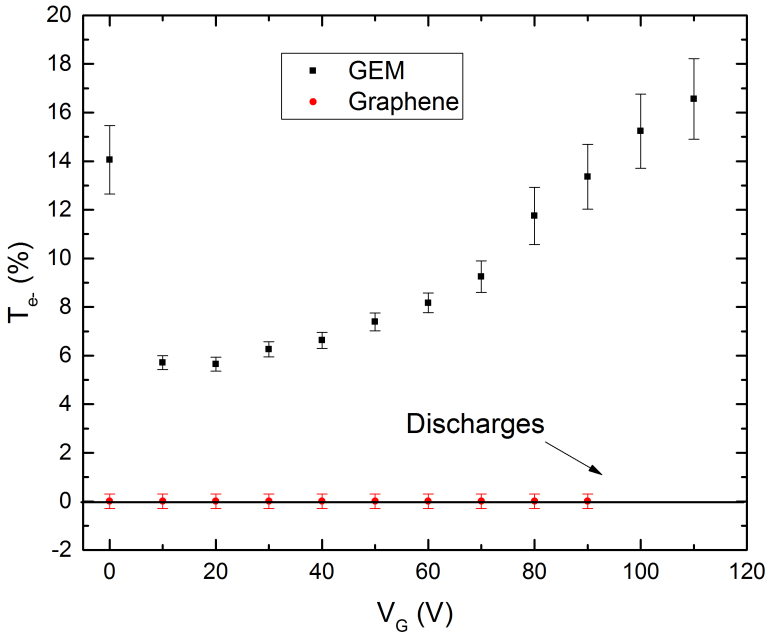

Figure 7.5: Graph of the electron transparency T_{e-} of the supporting GEM as a function of the voltage applied across it V_G. The gas mixture was Ar-CO_2 93-7, with $V_{GEM} = 635\,\mu A$. The T_{e-} of graphene is also shown in red under the same conditions.

effects. Damage from X-ray could be ruled out due to the fact that the X-ray irradiation was local: with a collimated beam of 1 mm diameter in direct contact with the chamber, so that the broadening of the beam could be neglected. This localisation of the X-ray irradiation was not consistent with the fact that the graphene was damaged in other areas of the trilayer and across the rest of the GEM, away from the measurement point. Damage in the presence of high electric fields up to 60 V could also be ruled out as initial measurements were repeatable multiple times during the initial tuning of the chamber before the systematic measurements. The only possibility left for the source of this damage was either the high electric fields from $V_G = 70\,V$ onwards or the large discharges observed at these fields, which could both account for the damage across all the GEM. The two effects are linked and it is difficult to distinguish them as the discharges start appearing with increasing applied field.

Further investigation of the damage was undertaken with an SEM scanning of the

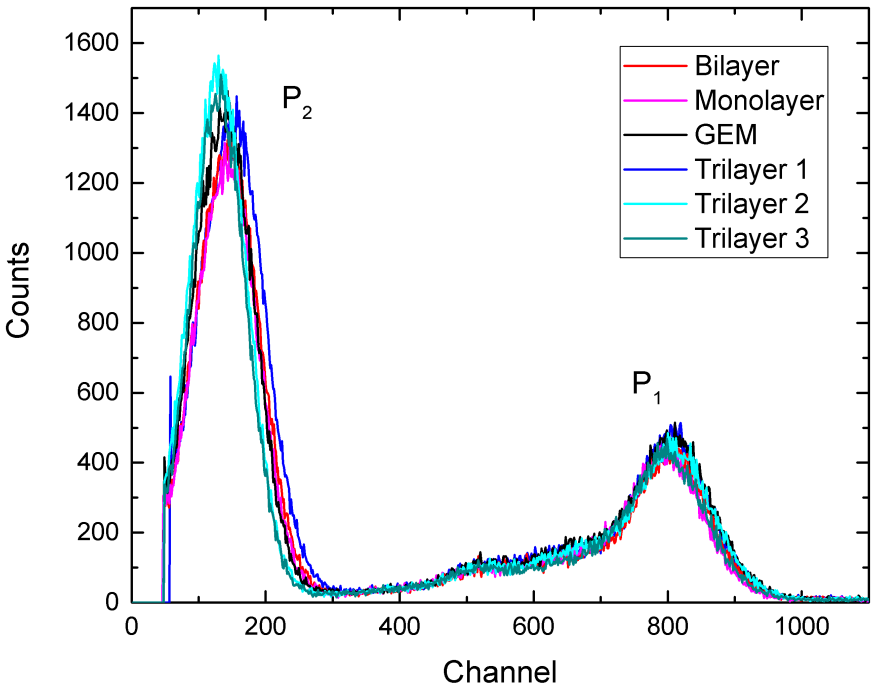

Figure 7.6: Energy spectra at $V_G = 110\,\mathrm{V}$, in Ar-CO_2 93-7, comparing various points of a graphene-covered GEM after damage by discharges.

GEM. Some SEM images are shown in Figure 7.7, showing no suspended graphene at all. The rest of the sample was scanned through and no sign of suspended graphene was found. After a closer zoom onto the sample the areas with mono-, bi- and trilayer graphene could be identified but the graphene was found to have no continuity as shown in b). The graphene was patchy and torn, indicating that the discharges were more likely the cause of the tearing of the layers, as a high field would mainly cause the suspended graphene to break, and would not affect the supported layer.

Additionally to this observed effect, after the removal of the GEM supporting the graphene, the triple GEM was also found to have a non functionning bottom GEM. Further cleaning of the chamber showed that the remains of the broken suspended graphene had propagated to the bottom triple GEM, shorting the three stages. These damaged graphene remains were only found directly below where the graphene was originally placed in the quadrants.

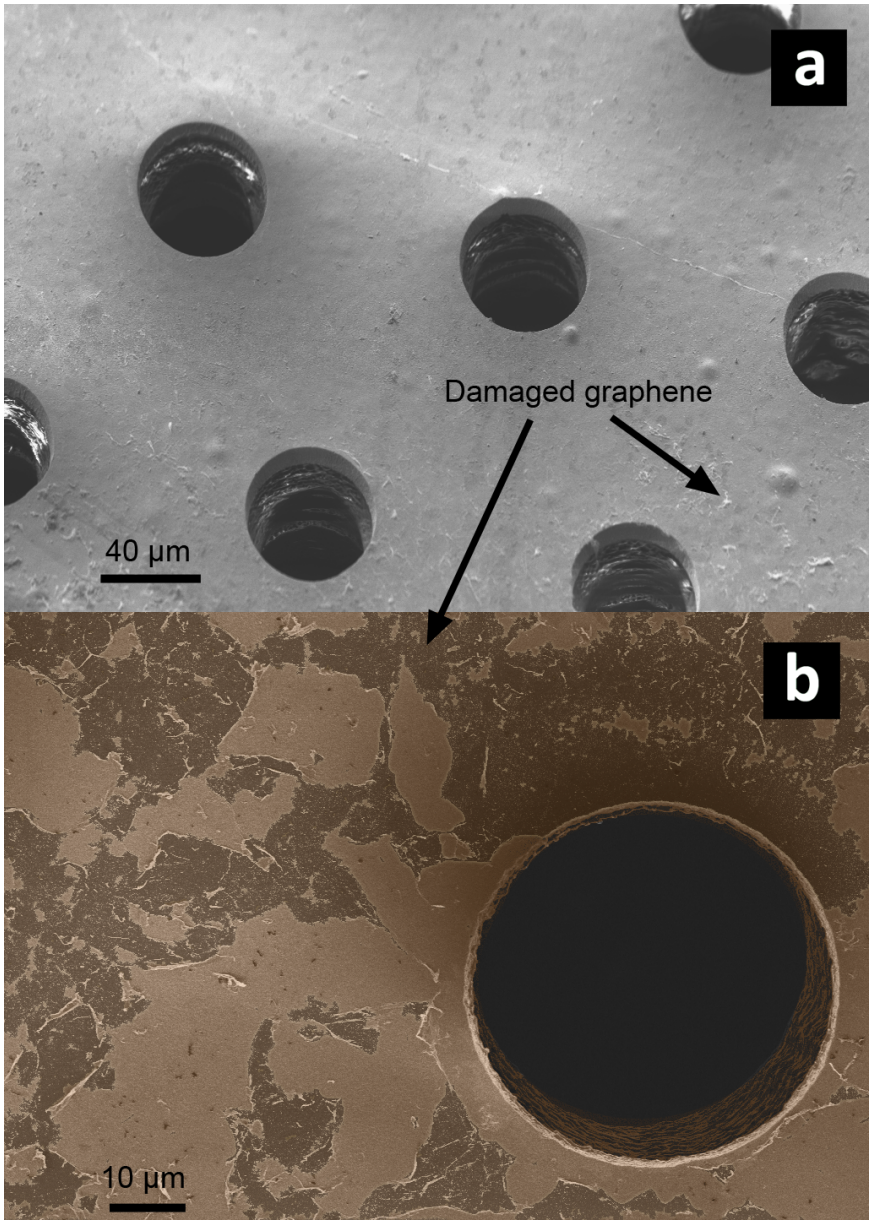

Figure 7.7: SEM images of the GEM after the damage, taken at 5 kV accelerating voltage, a working distance $WD = 5.0$ mm at a tilt angle of 54^o. Figure a) shows an SEM image in a trilayer region showing some light residues indicated with an arrow, corresponding to remaining graphene. Figure b) is a zoomed in image artificially coloured in a copper colour to enhance the graphene presence. The remaining graphene is shown by the arrow and appears as a dark greyish colour on top of the support coloured in copper.

These findings on the damage generated by the large discharges are crucial to the intergration of graphene for detector applications. Transferred layers were shown to not be suitable for use in systems with high electric fields, as very large discharges of the order of mA, even in very clean gas flow were shown to damage the layers irreversibly, with the damaged residues propagating to lower stages. In the next section, the transparency of the layer will be investigated in the light of these findings, and care was taken to halt the measurements as soon as significant discharges started appearing.

7.4 T_{e-} Measurements

The measurements were made in the same conditions as previously except the gas mixture was changed to Ar-CO_2 70-30. The reason for the change was that although higher voltages overall were required for the operation of the system, a higher voltage difference inside the GEM could be reached due to the higher amount of CO_2 quencher, in theory reducing the amount of discharges. The measurements were done on a GEM which was conductive, similarly to the previous sample with a resistance of 200 kΩ.

Two points on the GEM, labelled GEM 1 and GEM 2, were measured as reference and the electron transparency was measured for four different random points on the trilayer. The results are plotted in Figure 7.8. The trilayer exhibited a very different behaviour for each points. Point 3 showed a transparency slightly lower than that of the GEM but reaching similar values at higher voltages, while points 2 and 4 were completely opaque up to 90 V and point 1 showed and intermediate transparency. Further understanding of these results could be achieved by correlating these results with a map of the GEM, represented in Figure 7.9 a). The position of every point measured was redrawn on the map, with the colours of each plot matching the colour of the point for clarity. As seen on the map more clearly, the trilayer transfer was slightly off centred and point 3 lies at the very edge of the trilayer, explaining for the behaviour of the transparency very similar to that of a bare GEM. In theory, all three points 1, 2, and 4 were expected to all be completely opaque to the electrons from their position. Indeed from the measurements in the previous section, a measured complete opacity of the point can only mean a perfect-coverage trilayer is completely opaque.

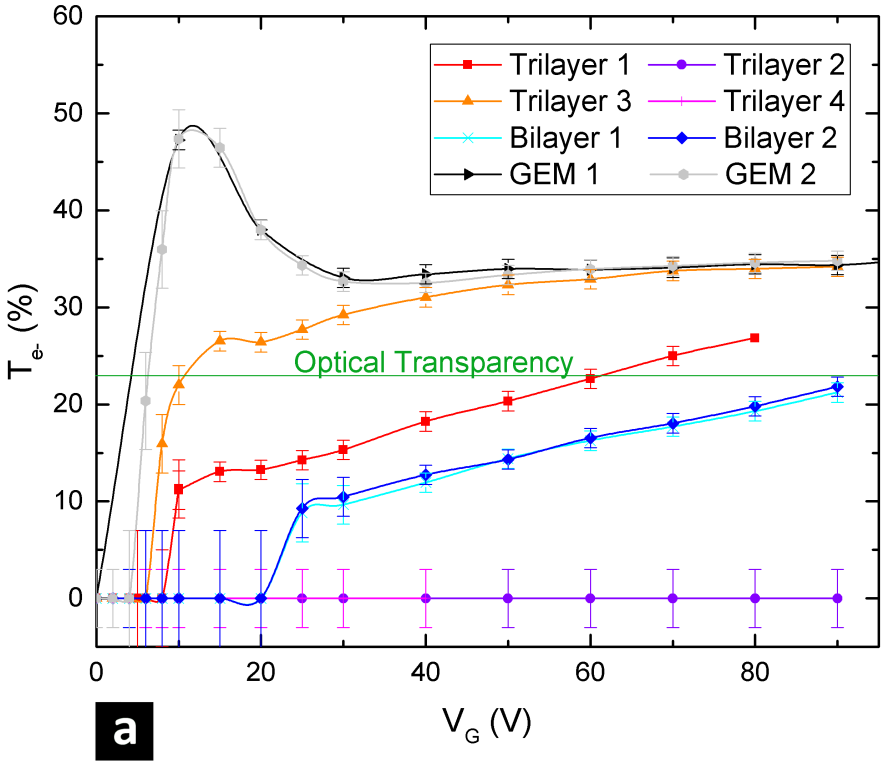

Figure 7.8: a) Graph of the electron transparency T_{e-} of the bare GEM, as well as various points on the bilayer and trilayer as a function of the voltage applied across it V_G. The gas mixture was Ar-CO_2 70-30, with $V_{GEM} = 740\,\mu A$. Each of the graph is colour-coded with a point indicating its exact position in figure b), on a photo of the GEM covered with monolayer, bilayer, and trilayer. The numbers in quadrants 0, 1, 2 and 3 indicate the number of layers deposited on each: i.e. 0 is no graphene, 1 is monolayer, etc. The black arrow indicates direction of the line-scan discussed next and the x-axis used for the scan is defined at the bottom of the GEM in mm.

In the event of the presence of defects as the electrons are not only amplified, but also completely field focused through the defect in the graphene, the number of electrons observed would rise very quickly. A complete opacity would therefore require either a perfect coverage or a very negligible amount of defects. From these results, any points on the trilayer can therefore be expected to be completely opaque as observed for points 2 and 4. The semi-transparency of point 1 indicates the presence of partial defects.

As a good quality trilayer was confirmed to be opaque to electrons in these measurement conditions, it was important to lower the number of layers in order to obtain an electron transparency for this application. The reason for which the monolayer was not investigated was due to the low coverage: although the SEM measurements of the GEM layers have shown the trilayer and the bilayer both had a very good coverage (98 % at least), the coverage of the monolayer was always too low to avoid the amplified field focusing effects expected with this setup. For this reason, only points on the bilayer were investigated. The results of the measurements for the bilayer at two random points are also plotted in Figure 7.8 a). The two points were found to be repeatable but also match each other perfectly, suggesting either a similar amount of defects at both points, or alternatively that the transparency measured was the intrinsic transparency of the bilayer.

In order to confirm this further, a measurement of every point in a line, at intervals of 1 mm (the diameter of the collimator) was made as illustrated in Figure 7.8 b). The measurements were made at $V_G = 50\,\mathrm{V}$ just below the onset of small discharges in order to keep the voltage the same for all measurements. Before discussing the results of the line-scan, a graph of the expected T_{e^-} for varying percentage of defects is plotted for bilayer and trilayer graphene in Figure 7.9 a). The graph is an estimation and assumes a maximum possible transparency of 35 % when no graphene is present as measured on the bare GEM in Figure 7.8 a), and assumes the lowest values of transparency measured for bilayer and trilayer to be the transparency at 0 defect.

The results of the line scan are plotted in Figure 7.9 b) along with two of the points measured previously (bilayer 2 and trilayer 1). The trilayer area showed highly varying transparencies between that of the GEM to no transparency. Between 40 mm and

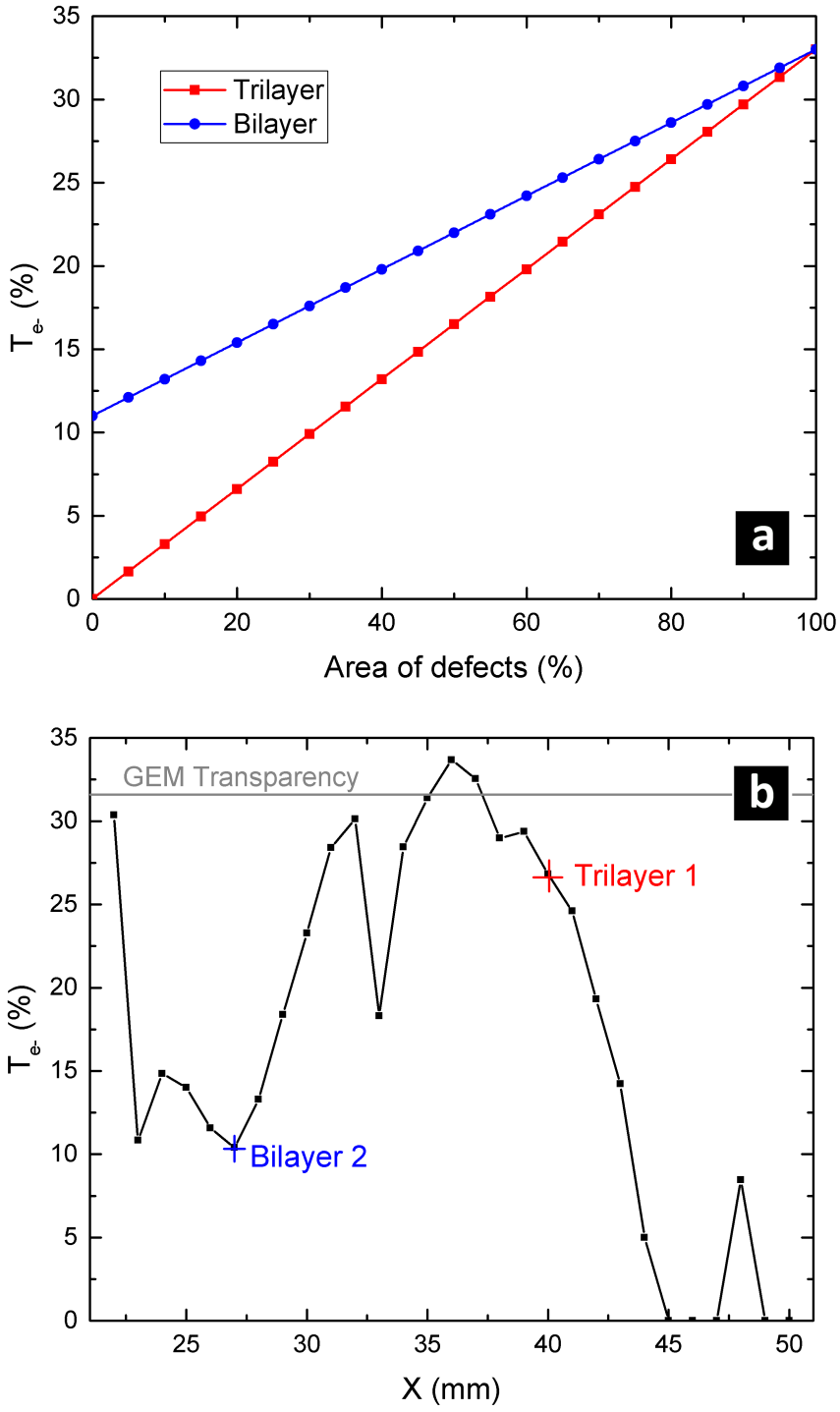

Figure 7.9: a) Plot of an estimation of the expected T_{e^-} for a given percentage of defects, using the data from Figure 7.8 a). Graph b) is the line-scan of the electron transparency at $V_G = 50\,\mathrm{V}$ as a function of the x-axis defined 7.8 b).

45 mm, the results show a very consistent decay of the transparency value, indicating either a homogeneous gradient of defects, which was unlikely or a convolution of the measurement points. The latter is much more likely as it is also observed towards the end of the bilayer after 30 mm. This finding is important as it means a completely opaque measurement would indicate that the effective opaque area measured is larger than the diameter of the X-ray beam. A quick comparison with the plot of the defects in graph a) would suggest the amount of defects measured on the bilayer is about 30 %, a very large number compared with the coverage measured on the SEM (indicating about 5 % defects on average). A similar observation can be made for the trilayer. This effect is to be investigated further and would require a systematic SEM mapping of the layers to be compared with a similar mapping of the transparency in order to draw further conclusions. Finally, the most interesting part of the graph was that quite a few points on the bilayer exhibited a consistent electron transparency between 11 % and 15 %, a promising result for this application.

7.5 X-ray Mapping

After having understood the behaviour of this graphene-covered GEM, and assessed its limitations (from damage) in these measurement conditions. The measurement was automated. The computer interface used to record the data systematically was designed in CERN. Instead of shorting the circuit board on the anode in order to collect all the current from the board into one signal, the current was collected separately. The anode circuit board consisted of perpendicular gold strips as represented in Figure 7.10 manifactured at the CERN workshop. The signals are collected on separate channels and the hits collected of was mapped using the respective channels into a "hit map".

The data was collected and was converted into the format of the data analysis framework ROOT, using the AMORE software at CERN. The data was subsequently analysed in the ROOT environment. The cumulated pulses collected on the x-strips and y-strips are recorded with their respective locations. A 2D histogram of the distribution of the cumulated hits as a function of their position in x and y can then be plotted, such distribution is called a "hit map". A photo of the real graphene

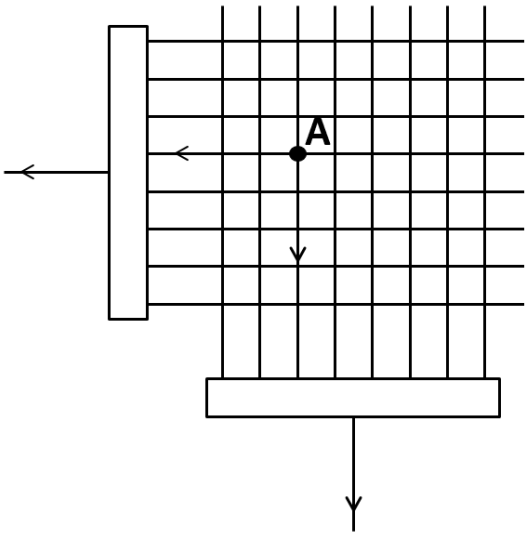

Figure 7.10: a) Diagram of the circuit board used for the localised detection of signals. If a current signal arrives in point A for example the data is

map, with the location of previous measurement points, is shown alongside a hit map collected after 209 626 hits in Figure 7.11 a) and b) respectively. The number of hits per location was colour coded with a resolution of 256 bins, corresponding to the relevant colour on the scale on the diagram.

There are quite a few interesting conclusions to be drawn from this successful mapping. Before doing so, it is important to understand the physical meaning of this graph. The equipment was configured to measure and store a few select quantities as a follow: each time a hit is measured, its position is recorded in x and y as well as its height. The graph in Figure 7.11 corresponds to the number of hits, per position (x,y) and therefore does not contain any information about the energy/height of the pulses. However it is very interesting to notice the correlation between a) and b) where very clearly, in the presence of the trilayer and bilayer, in quadrants 2 and 3, the number of hits varies between 0 and 30. While on the bare GEM, the number of hits collected lies between 40 and 80. Interestingly, the monolayer, which was assessed to have a poor coverage $< 40\,\%$ in SEM scans, shows a similar hit count to the bare GEM except a few patchy areas showing a similar hit count to the other layers. This behaviour is indeed what would be expected: as explained in the previous chapter, in the case of a high transparency, the number of pulses collected should be much higher

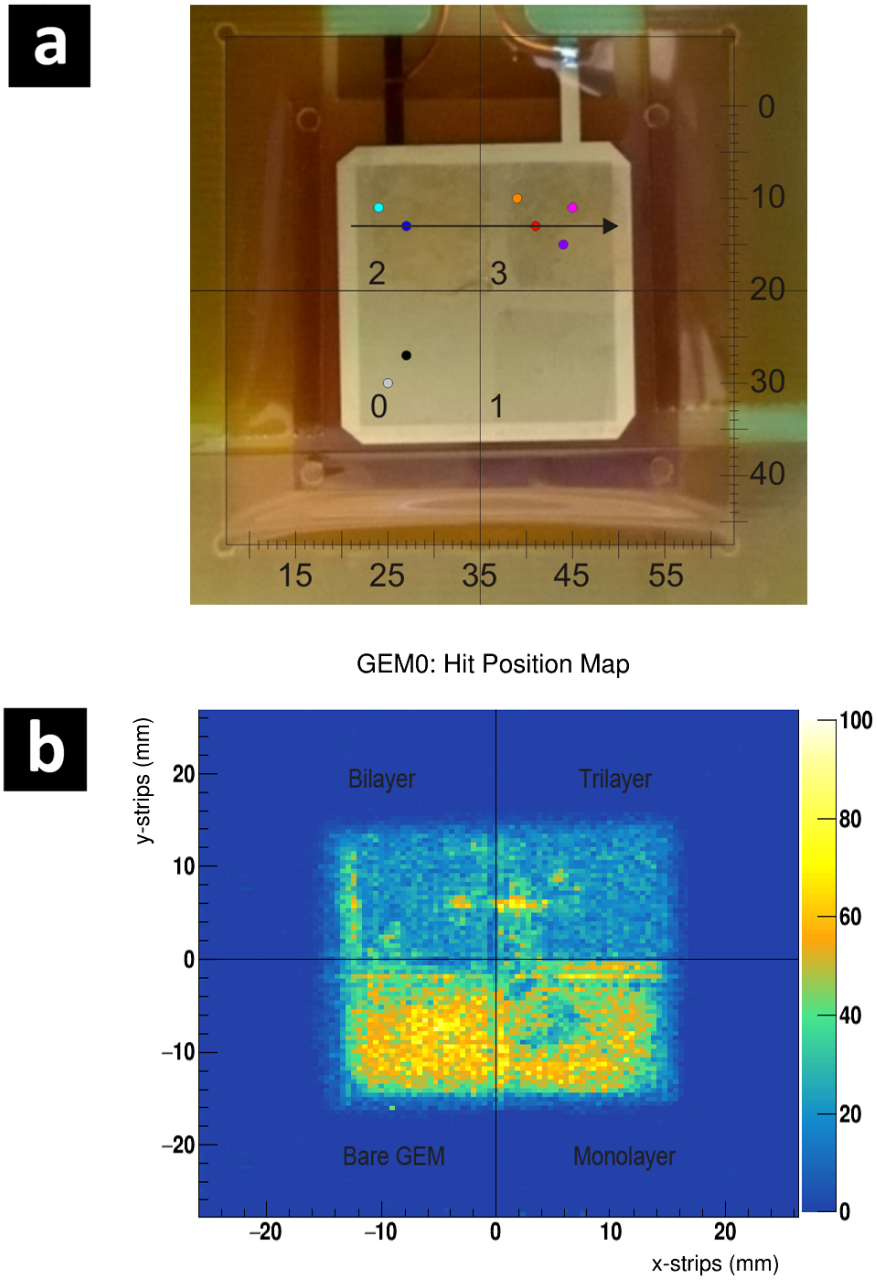

Figure 7.11: a) Photo of the GEM covered with monolayer, bilayer, and trilayer. The coverage corresponds roughly to the quadrants 0, 1, 2, 3 drawn on the photo. b) 2D histogram of the subsequent X-ray hit map of the GEM shown without collimator after 209 626 counts collected. The colour scale indicates the number of hits at the corresponding (x,y) location.

than when the transparency is poor (the number of counts collected at 100 % should be more than double).

This hit map also agrees very strongly with the previous measurements: if the graph in this image is correlated with the data taken in Figure 7.8. The measurements on the red and orange points (also shown again in Figure 7.11 a) for ease of comparison) had a high transparency, and this can be understood better from the new results: the red point corresponded to an unfortunate anomaly in the layer coverage, and the orange one was on the very edge of the trilayer, giving a slightly lower transparency than the red point but not quite the opacity of the trilayer. On the other hand, the two points taken on the bilayer agreed perfectly, and both correspond to random but typical points as seen from the mapping. Finally the two points on the GEM which also match within errors, correspond to typical points on the bare GEM. The hit map was found to be repeatable with a reproducible number of hits per area which scaled with the amount of time the run was left for.

The same data is replotted differently in a 3D map in Figure 7.12 in a): instead of the number of hits as a function of position, the mean ADC is plotted as a function of position, along with two histograms. They represent the mean ADC plotted as a function of position. Indeed, for each given position (x,y), a spectrum could be plotted with the energy distribution at that given point. However such a plot/information gathering would require very large integration times and very fast and precise electronics to achieve. Instead, the mean energy of all the hits collected at a given position (x,y), can be computed and plotted. The resulting map is shown in a). The graph in b) corresponds to the "mean ADC" for each position X, and c) is the one for each position Y. It is important to note that the two histograms are not projections of the 3D map but correspond to the average energy of all the hits collected along an X or Y strip, and are therefore cumulated histograms of the data on the map.

Due to the fact the energies are averages, the information of whether the pulse comes from D1 or D2 can be thought of as partially lost. However this information can be found easily in the graph due to the fixed position of P2. Indeed, for high transparencies, P2 is very close to P1, and the average ADC will therefore be high, whereas for low transparencies, P1 will shift to lower ADC values therefore bringing

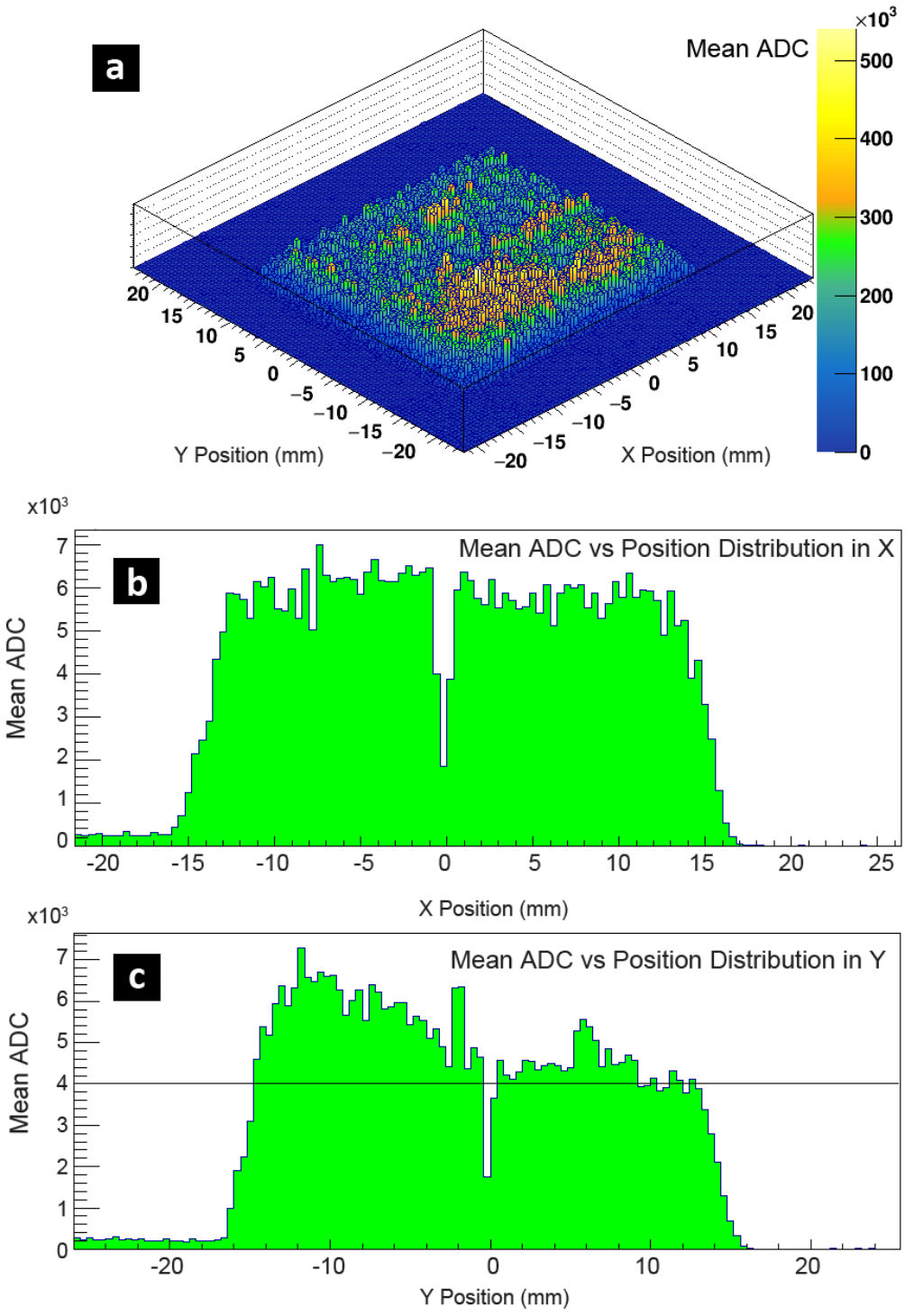

Figure 7.12: a) 3D plot of the mean ADC as a function of position (x,y), b) histogram of the cumulated mean ADC for each position X, c) histogram of the cumulated mean ADC for each position Y.

the mean ADC value down as well.

The results shown on the map correlate well with the hit map, but as expected, due to the fact that the information is averaged over the ADCs, the difference in the layers are visible but not as pronounced as in the hit map. In graph b) for example the cumulated mean ADCs look the same on both sides of the GEM as the distribution is symmetrical in with respect to $X = 0$. On the other hand the distribution in Y shows the clear asymmetry (shown by the black line) between the half which was covered with bilayer and trilayer graphene and the one which had a poor monolayer coverage and the bare GEM.

In both Figures, whether the hits or the mean ADCs were plotted, the bilayer and the trilayer both showed some variation in the transparency (shown by a variation in colour) across their $1.5\,\mathrm{cm}^2$ area. But most importantly, the two sides seem to exhibit the same average transparency. An RGB colour sampling of the most homogenous area in the bilayer, and in the trilayer was done. For both Figures, the colour distribution in R, G and B were found to be the same with some negligible differences: an average of 122 ± 71 over 255 for the trilayer and 123 ± 72 over 255 for the bilayer (the bare GEM for example gives 155 ± 98 over 255, a very different result). This result is confirmed in Figure 7.12 b) on the cumulated graph where no significant difference (within the errors) is found between the trilayer+monolayer and bilayer+bare GEM side. The latter result needs to be considered with care as the data is convoluted with small patches of monolayer on the trilayer side. But in this case one would expect the average ADC to be much lower than on the bilayer side. But instead no significant difference can be found. This similarity shown in the maps seem to indicate that the transparency of the bilayer needs to be investigated further in order to assess its suitability for this application.

7.6 Conclusions

In this chapter, a new setup was tested in order to assess the resilience of graphene in high electric fields as well as to improve the electron transparency of the layer. In conclusion, it was shown that permanent damage can be caused to graphene layers (up to three) in high electric field environments. The damage was attributed to the

presence of large discharges and was thought to not be due to electrostatic pressure from the field difference. It was also found that upon damage, the damaged graphene layers detach from the bottom of the GEM and propagate through the holes of the triple amplification stage. Such behaviour caused the shorting of the amplification and subsequent permanent damage to the triple GEM.

Secondly, it was found that trilayer graphene was completely opaque to electrons even under very high electric fields up to $18\,000\,\mathrm{V.cm^{-1}}$. On the other hand, the bilayer showed very promising repeatable results with a transparency of 10 % at $V_{GEM} = 30\,\mathrm{V}$ going up to 25 % at $V_{GEM} = 90\,\mathrm{V}$. These measurements were confirmed to be repeatable in two local point measurements and a line scan. Finally a full x,y mapping of the whole GEM was done in order to confirm this result. Many conclusions can be drawn from this mapping. The first one would be that the layers show a small fluctuation in transparency across their surface which is attributed to statistical variation. The second would be that the trilayer is most likely to be completely opaque to electrons under such conditions and the two previous measurements showing some potential transparency are points outside the trilayer. And finally the final observation was that according to the maps, the trilayer and the bilayer seem to show the same average transparency from colour sampling of the maps, this result was then confirmed by the plot of the mean ADC as a function of x position. However these results are not as accurate as the results taken by single measurements and the electron transparency of the bilayer remains to be investigated with care.

Chapter 8

Conclusions, Ongoing and Future Work

8.1 Conclusions of this Work

To summarise the achievements in this work, firstly a method to suspend graphene over large circular holes of sizes from 35 µm up to 70 µm with pitches of 60 µm to 140 µm was developed. Such sizes would correspond roughly to 22.5 % of suspended layers on the surface of the substrate. This suspension of the layers is a transfer technique where the graphene was initially grown in multigrain quality separately on a copper substrate. The copper substrate was then etched away, and the graphene was moved to the new substrate, a 50 µm thick metal foil which was patterned with a periodic hole pattern with the sizes mentioned. Monolayer, bilayer and trilayer graphene transfer were investigated, single layers exhibited coverages up to 90 % for the smaller 35 µm holes down to about 50 % for the 70 µm sizes. On the other hand, the thicker two and three layers showed coverages varying between 95 % and 100 %.

Such work is a very large step up from previously suspended layers in literature which only achieved sizes up to 5 µm [62, 97, 98, 107, 109, 110]. The layers were subsequently characterised using SEM, AFM and Raman spectroscopy and showed very good quality, low strain and reduced amounts of residues. The mechanism for the residues deposition was also investigated, revealing a complex interaction between the graphene layer, the PMMA polymer used for transfer purposes and the liquids used

for transferring the layers. This new method paves the way for large improvements in applications of graphene such as nanoresonators [11, 97], water desalination [98], photodetection, enhancement membranes for TEM imaging [70, 99, 100], filters and trans-diffusion applications through graphene [50, 101–103], amongst others.

As graphene has been shown in previous work to have ion blocking properties, and to be transparent to electrons under transmission electron microscope irradiations, in this work, the suspended graphene was then integrated as a potential membrane with the final aim of blocking ions feeding back into the drift conversion area while letting through the electrons necessary for the radiation detection. Before integrating the graphene layer, it was crucial to set up a preliminary integration environment in order to measure the charge transfer properties of the layer independently of the triple GEM: the drift area was divided into two drifts zones D1 and D2 by a mesh, destined to support graphene and fully characterised in order to understand the system without the presence of graphene. Methods to calculate the charge transfer properties of the mesh were also developed.

Single graphene layers were then successfully transferred onto these patterned copper meshes for preliminary tests in a low electric field environments in order to assess its viability under attenuated detection conditions. Results were highly repeatable and showed that graphene was very resilient in these electric field conditions, on the other hand, ions and electrons were found to be very sensitive to the presence of small defects in the graphene monolayer. It was shown that the electric field lines focused into such defects acting overall as small mesh holes. The ions were therefore found to feed through the layer and higher coverage of the layer was required in order assess the real charge transmission properties. After transferring bilayers and trilayers in order to obtain a near perfect coverage, the trilayer was then shown to be opaque to electrons and ions. Further modification of the setup to increase the transmission of the electrons still showed electron opacity for the trilayer while results were mixed for the bilayer. Furthermore, it was shown that graphene was very weak to discharges occurring in high field environments, and that damage to graphene layers transferred below a supporting GEM propagated to the triple GEM stages below, inducing further damage.

In the light of these results, the next steps to be investigated are the following: in order to probe the electron transparency at low energies of the monolayers and bilayers further a few possibilities of investigation are to be explored: the monolayer coverage can be improved by improving the transfer technique. A new setup could also be investigated in order to increase the electric field strength while avoiding discharges. A few of these possibilities are currently being explored and some of the work is either ongoing (started either by myself and having been taken over by other PhD students, or started by other collaborators) or are planned to be implemented shortly. The next section will briefly discuss the future directions of this work, including some the results of preliminary work (only results which I have worked on will be presented).

8.2 Ongoing Work and Preliminary Results

The work in this thesis as well as projects and ongoing work pioneered in the course of this thesis, were taken over by a student in UCL: Abdulkareem Afandi, and a student in CERN (to be announced once Patrik Thuiner finishes his PhD). Some preliminary results obtained but with further work required will be presented in this section.

As a remedy to the detachment of the graphene layers at the bottom of the GEM, and the consequent induced damages, a potential solution would be to improve the graphene adhesion. For this the best method would be to directly fabricate the meshes and GEMs directly from the growth substrates of graphene. Additionnally, this would allow to reduce the amount of defects in the suspended layers from less manipulation, but also would pave the way for an industrial fabrication process for the graphene covered devices.

Single layer graphene grown on 25 µm thick copper foils were used in this process. The graphene at the bottom of the layer was removed by floating the sample in a solution of nitric acid (17 %) for 1 min. The sample was then spin-coated with two layers of 300 nm, A4 950 PMMA at 2000 rpm for 1min, in order to protect the graphene layer in all of the following steps. The PMMA was baked at 180^{o}C for 1min30 to cure it. Three layers of HIPR 6512 (a much more viscous polymer resist) were then spin coated on top of the PMMA layer at 1000 rpm (dwell of 30 s) forming an overall 15 µm thick layer. The layers were baked at 120^{o}C for 1 h. The resist FX930 (30 µm thick)

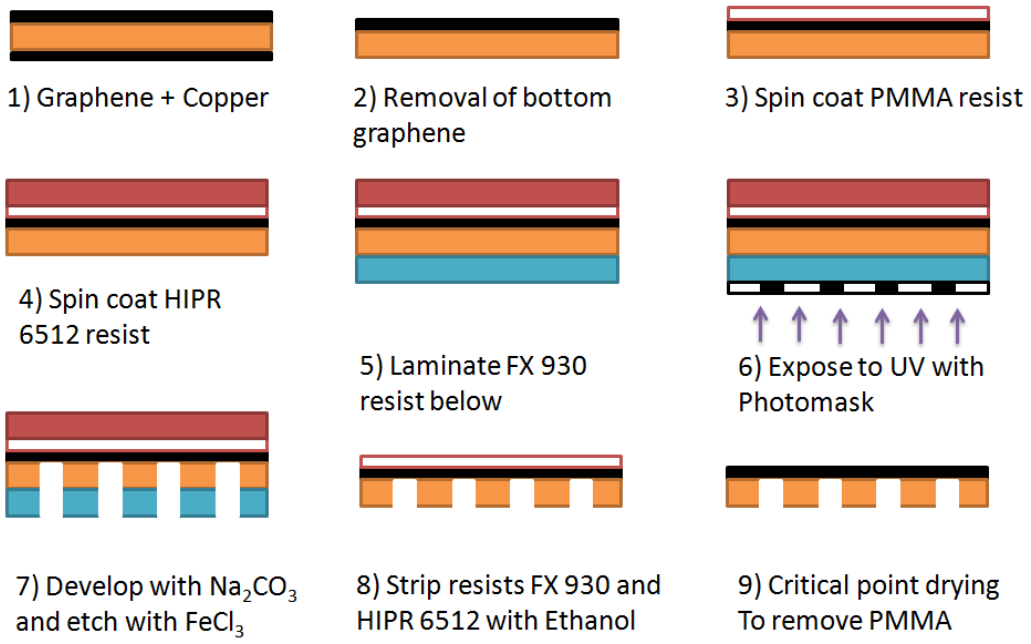

Figure 8.1: Diagram illustrating the etching process for the batch fabrication of suspended graphene on detector supports.

from Dupont was laminated on the copper backside, and exposed to UV light under a mask with varying hole sizes. A solution of sodium carbonite Na_2CO_2 was used to develop FX930 and areas with different hole sizes were blanked and etched separately. The spray etching was done with iron(III) chloride ($FeCl_3$) until the holes were fully etched. The laminated resist as well as the HIPR 6512 were then removed in a solution of ethanol, leaving only the PMMA layers on top of the graphene and the patterned copper. The samples were then critically dried as described in Chapter 4.

The samples were investigated using SEM and Raman spectroscopy to assess the amount of PMMA/polymer residues and the quality of the graphene. SEM images are shown in Figure 8.2, and revealed that the coverage was better in holes of larger size 70 µm than holes of smaller size (60 µm). The small holes had almost no coverage. Such surprising difference was attributed to the spray etching process. Indeed any damage occurring during the polymer removal processes (i.e. from surface tension or mechanical tears) would damage larger holes first. In this case however, if the etching process is considered: larger holes sizes etch faster and therefore required lower exposure time to the etching solution, while smaller holes had to be exposed at

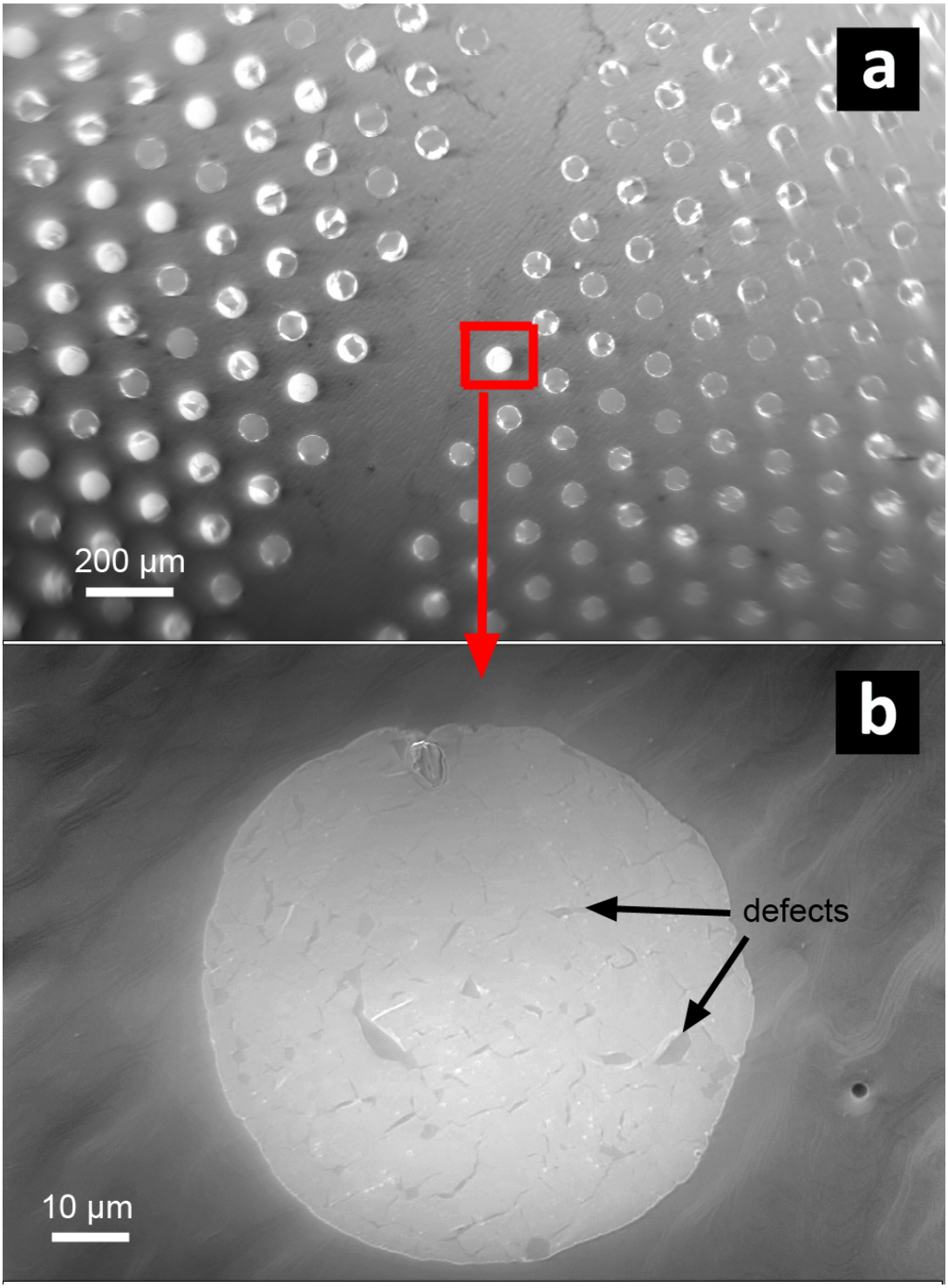

Figure 8.2: SEM images of the etched samples showing a) the boundary between two hole sizes (60 µm and 70 µm diameter holes) and b) a close up of one of the holes showing tears in the graphene (defects). The images were taken at 5 kV accelerating voltage and a working distance WD of 6 mm.

least a few sprays longer in order to all be etched.

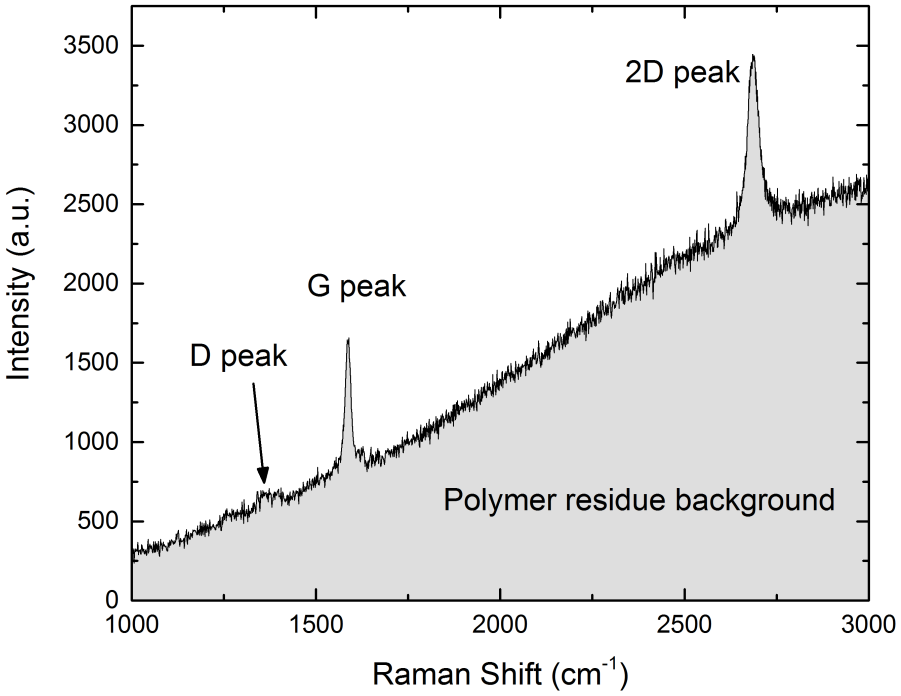

Figure 8.3: Raman spectra of suspended graphene after the whole process, taken using the 532 nm laser, at a magnification of x50, with an exposure time of 60 s.

A typical Raman spectrum of suspended graphene after the full process is shown in Figure 8.3. The layers showed a good intrinsic quality (a low D peak) despite the mechanical tears, indicating that the process did not structurally damage the layer. On the other hand, the use of the successive layers of polymer protective supports have left a quite high amount of residues shown as the background of the spectra.

The proposition to improve the process would be firstly to improve the coverage of the suspended layer and reduce the damage by implementing a new batch etching process which would involve exposure of the copper support to an etching solution in alternance with DI water rather than a mechanical spray. The polymer support residues due to the 5 consecutive layers of cured polymer on top of the graphene can then be addressed, by reducing the amount of support layers once the potential amount mechanical damage during the process has been reduced.

8.3 Future and Spin-Off Works

One of the next investigation points for this work remains to improve the toughness and resilience of graphene by not only reducing the amount of defects, but also by assessing the current amount of grain boundaries and working towards improving them. For this, the fabrication of a suspended hall bar of the graphene samples used in the work could be the first step towards estimating the amount of grain boundaries, and further methods could be developed further for more accuracy. Aside from improving the quality of graphene, its electron transparency remains a critical point to investigate. In order to achieve this, three specific courses of action are currently in progress. The first one being the building of an entire chamber dedicated to electron transmission measurements at low energies, using an electron gun. Such equipment would allow the systematic measurement of the electron transparency of graphene at controlled electron energies in vacuum without relying on the presence of various gas mixtures to attenuate the kinetic energy of the particles. The chamber will be equipped with high electric fields in the direction opposite to the electron path in order to slow the electrons emitted from the gun to functional energies (typical gun energies are in the 100 eV or more, while the energies needed for detection are 10 eV or less). This work will be directed by Dr. Filippo Resnati. The second course of action consists in a precise correlation between fully detailed SEM mapping of transferred graphene and therefore of the average amount of real defects per unit area, with a map of the number of counts obtained from each area. This would allow a more precise isolation of defect-free areas with transmission data. This work will be overseen by Abdulkareem Afandi and Patrik Thuiner (and his replacement in December 2015).

Publications

- *Thermal Dynamics of Graphene Edges Investigated by Polarized Raman Spectroscopy*, Y. N. Xu, D. Zhan, L. Liu, H. Suo, Z. H. Ni, **T. T. Nguyen**, C. Zhao, and Z. X. Shen, ACS Nano, 2011, 5 (1), pp 147152.

- *Electronic Properties of Graphene-Single Crystal Diamond Heterostructures*, F. Zhao, **T. T. Nguyen**, M. Golsharifi, S. Amakubo, K. P. Loh and R. B. Jackman, J. Appl. Phys. 114, 053709 (2013).

- *Charge Transfer Properties Through Graphene Layers in Gas Detectors*, P. Thuiner, R. Hall-Wilton, R. B. Jackman, H. Muller, **T. T. Nguyen**, E. Oliveri, D. Pfeiffer, F. Resnati, L. Ropelewski, J. A. Smith, M. van Stenis, and R. Veenhof, IEEE 2015 Transactions.

- *Charge Transfer Properties through Graphene for Applications in Gaseous Detectors*, S. Franchino, D. Gonzalez-Diaz, R. Hall-Wilton, R. B. Jackman, H. Muller, **T. T. Nguyen**, R. de Oliveira, E. Oliveri, D. Pfeiffer, F. Resnati, L. Ropelewski, J. A. Smith, M. van Stenis, C. Streli, P. Thuiner, and R. Veenhof, Proceedings of the 13th Pisa Meeting 2015.

- *Large-area transfer of suspended monolayer, bilayer, and trilayer graphene with high coverage*, **T. T. Nguyen**, June Sang-Lee, Patrik Thuiner, Eraldo Oliveri, Filippo Resnati, Lescek Ropelewski and Richard B. Jackman, to be submitted.

References

[1] K S Novoselov, a K Geim, S V Morozov, D Jiang, Y Zhang, S V Dubonos, I V Grigorieva, and a a Firsov. Electric field effect in atomically thin carbon films. *Science (New York, N.Y.)*, 306(5696):666–9, oct 2004.

[2] Yi Zhang, Luyao Zhang, Pyojae Kim, Mingyuan Ge, Zhen Li, and Chongwu Zhou. Vapor trapping growth of single-crystalline graphene flowers: synthesis, morphology, and electronic properties. *Nano letters*, 12(6):2810–6, jun 2012.

[3] Francesco Bonaccorso, Antonio Lombardo, Tawfique Hasan, Zhipei Sun, Luigi Colombo, and Andrea C. Ferrari. Production and processing of graphene and 2d crystals. *Materials Today*, 15(12):564–589, dec 2012.

[4] K. S. Novoselov, V. I. Falko, L. Colombo, P. R. Gellert, M. G. Schwab, and K. Kim. A roadmap for graphene. *Nature*, 490(7419):192–200, oct 2012.

[5] K.I. Bolotin, K.J. Sikes, Z. Jiang, M. Klima, G. Fudenberg, J. Hone, P. Kim, and H.L. Stormer. Ultrahigh electron mobility in suspended graphene. *Solid State Communications*, 146(9-10):351–355, jun 2008.

[6] Yenny Hernandez, Valeria Nicolosi, Mustafa Lotya, Fiona M Blighe, Zhenyu Sun, Sukanta De, I T McGovern, Brendan Holland, Michele Byrne, Yurii K Gun'Ko, John J Boland, Peter Niraj, Georg Duesberg, Satheesh Krishnamurthy, Robbie Goodhue, John Hutchison, Vittorio Scardaci, Andrea C Ferrari, and Jonathan N Coleman. High-yield production of graphene by liquid-phase exfoliation of graphite. *Nature nanotechnology*, 3(9):563–8, sep 2008.

[7] Goki Eda, Giovanni Fanchini, and Manish Chhowalla. Large-area ultrathin films of reduced graphene oxide as a transparent and flexible electronic material. *Nature nanotechnology*, 3(5):270–4, may 2008.

[8] Zhongqing Wei, Debin Wang, Suenne Kim, Soo-Young Kim, Yike Hu, Michael K Yakes, Arnaldo R Laracuente, Zhenting Dai, Seth R Marder, Claire Berger, William P King, Walter a de Heer, Paul E Sheehan, and Elisa Riedo. Nanoscale tunable reduction of graphene oxide for graphene electronics. *Science (New York, N.Y.)*, 328(5984):1373–6, jun 2010.

[9] Claire Berger, Zhimin Song, Tianbo Li, Xuebin Li, Asmerom Y. Ogbazghi, Rui Feng, Zhenting Dai, N. Alexei, Marchenkov Edward H Conrad, Phillip N. First, and Walt A. De Heer. Ultrathin epitaxial graphite: 2D electron gas properties and a route toward graphene-based nanoelectronics. *Journal of Physical Chemistry B*, 108(52):19912–19916, 2004.

[10] Konstantin V Emtsev, Aaron Bostwick, Karsten Horn, Johannes Jobst, Gary L Kellogg, Lothar Ley, Jessica L McChesney, Taisuke Ohta, Sergey a Reshanov, Jonas Röhrl, Eli Rotenberg, Andreas K Schmid, Daniel Waldmann, Heiko B Weber, and Thomas Seyller. Towards wafer-size graphene layers by atmospheric pressure graphitization of silicon carbide. *Nature materials*, 8(3):203–7, mar 2009.

[11] Shriram Shivaraman, Robert A. Barton, Xun Yu, Jonathan Alden, Lihong Herman, M. S V Chandrashekhar, Jiwoong Park, Paul L. McEuen, Jeevak M. Parpia, Harold G. Craighead, and Michael G. Spencer. Free-standing epitaxial graphene. *Nano Letters*, 9(9):3100–3105, 2009.

[12] Jinming Cai, Pascal Ruffieux, Rached Jaafar, Marco Bieri, Thomas Braun, Stephan Blankenburg, Matthias Muoth, Ari P Seitsonen, Moussa Saleh, Xinliang Feng, Klaus Müllen, and Roman Fasel. Atomically precise bottom-up fabrication of graphene nanoribbons. *Nature*, 466(7305):470–473, 2010.

[13] Xin Yan, Xiao Cui, Binsong Li, and Liang Shi Li. Large, solution-processable graphene quantum dots as light absorbers for photovoltaics. *Nano Letters*, 10(5):1869–1873, 2010.

[14] William J Arnoult and Rex B Mclellan. Solubility of Carbon in Rhodium, Ruthenium, Iridium and Rhenium. *Scripta Metallurgica*, 6, 1972.

[15] Xuesong Li, Yanwu Zhu, Weiwei Cai, Mark Borysiak, Boyang Han, David Chen, Richard D. Piner, Luigi Colomba, and Rodney S. Ruoff. Transfer of large-area graphene films for high-performance transparent conductive electrodes. *Nano Letters*, 9(12):4359–4363, 2009.

[16] B Y G L Selman, B Sc, P J Ellison, A Darling, D Ph, and M E Mech. Carbon in Platinum and Palladium at high temperatures. *Platinum Metals Review*, 14(1):14–20, 1970.

[17] Qingkai Yu, Luis a Jauregui, Wei Wu, Robert Colby, Jifa Tian, Zhihua Su, Helin Cao, Zhihong Liu, Deepak Pandey, Dongguang Wei, Ting Fung Chung, Peng Peng, Nathan P Guisinger, Eric a Stach, Jiming Bao, Shin-Shem Pei, and Yong P Chen. Control and characterization of individual grains and grain boundaries in graphene grown by chemical vapour deposition. *Nature materials*, 10(6):443–9, jun 2011.

[18] Joseph M. Wofford, Shu Nie, Kevin F. McCarty, Norman C. Bartelt, and Oscar D. Dubon. Graphene islands

on Cu foils: The interplay between shape, orientation, and defects. *Nano Letters*, 10:4890–4896, oct 2010.

[19] S. Marchini, S. Günther, and J. Wintterlin. Scanning tunneling microscopy of graphene on Ru(0001). *Physical Review B*, 76(7):1–9, aug 2007.

[20] E. Miniussi, M. Pozzo, A. Baraldi, E. Vesselli, R. Zhan, G. Comelli, T. Mente, M. Niño, A. Locatelli, S. Lizzit, and Dario Alfè. Thermal Stability of Corrugated Epitaxial Graphene Grown on Re(0001). *Physical Review Letters*, 106(21):2–5, may 2011.

[21] Gang Hee Han, Fethullah Güne, Jung Jun Bae, Eun Sung Kim, Seung Jin Chae, Hyeon-Jin Shin, Jae-Young Choi, Didier Pribat, and Young Hee Lee. Influence of copper morphology in forming nucleation seeds for graphene growth. *Nano letters*, 11(10):4144–8, oct 2011.

[22] Yufeng Hao, M S Bharathi, Lei Wang, Yuanyue Liu, Hua Chen, Shu Nie, Xiaohan Wang, Harry Chou, Cheng Tan, Babak Fallahazad, H Ramanarayan, Carl W Magnuson, Emanuel Tutuc, Boris I Yakobson, Kevin F McCarty, Yong-wei Zhang, Philip Kim, James Hone, Luigi Colombo, and Rodney S Ruoff. The role of surface oxygen in the growth of large single-crystal graphene on copper. *Science (New York, N.Y.)*, 342(6159):720–3, 2013.

[23] Adam W Tsen, Lola Brown, Mark P Levendorf, Fereshte Ghahari, Pinshane Y Huang, Robin W Havener, Carlos S Ruiz-Vargas, David a Muller, Philip Kim, and Jiwoong Park. Tailoring electrical transport across grain boundaries in polycrystalline graphene. *Science (New York, N.Y.)*, 336(6085):1143–6, jun 2012.

[24] Qing Hua Wang, Zhong Jin, Ki Kang Kim, Andrew J. Hilmer, Geraldine L. C. Paulus, Chih-Jen Shih, Moon-Ho Ham, Javier D. Sanchez-Yamagishi, Kenji Watanabe, Takashi Taniguchi, Jing Kong, Pablo Jarillo-Herrero, and Michael S. Strano. Understanding and controlling the substrate effect on graphene electron-transfer chemistry via reactivity imprint lithography, 2012.

[25] Zachary R. Robinson, Parul Tyagi, Tyler R. Mowll, Carl A. Ventrice, and James B. Hannon. Argon-assisted growth of epitaxial graphene on Cu(111). *Physical Review B - Condensed Matter and Materials Physics*, 86(23), 2012.

[26] Zhengzong Sun, Zheng Yan, Jun Yao, Elvira Beitler, Yu Zhu, and James M Tour. Growth of graphene from solid carbon sources. *Nature*, 468(7323):549–52, nov 2010.

[27] Daejin Eom, Deborah Prezzi, Kwang Taeg Rim, Hui Zhou, Michael Lefenfeld, Shengxiong Xiao, Colin Nuckolls, Mark S Hybertsen, Tony F Heinz, and George W Flynn. Structure and electronic properties of graphene nanoislands on Co(0001). *Nano letters*, 9(8):2844–8, aug 2009.

[28] J C Hamilton and J M Blakely. Carbon Segregation to Single Crystal Surfaces of Pt, Pd and Co. *Surface Science*, 91:199–217, 1980.

[29] G.a. López and E.J. Mittemeijer. The solubility of C in solid Cu. *Scripta Materialia*, 51(1):1–5, jul 2004.

[30] J Swartz. Solubility of graphite in cobalt and nickel. *Metallurgical and Materials Transactions B*, 2(8):2318–2320, 1971.

[31] Jorge M. Garcia, Ulrich Wurstbauer, Antonio Levy, Loren N. Pfeiffer, Aron Pinczuk, Annette S. Plaut, Lei Wang, Cory R. Dean, Roberto Buizza, Arend M. Van Der Zande, James Hone, Kenji Watanabe, and Takashi Taniguchi. Graphene growth on h-BN by molecular beam epitaxy. *Solid State Communications*, 152(12):975–978, 2012.

[32] Sukang Bae, Hyeongkeun Kim, Youngbin Lee, Xiangfan Xu, Jae-Sung Park, Yi Zheng, Jayakumar Balakrishnan, Tian Lei, Hye Ri Kim, Young Il Song, Young-Jin Kim, Kwang S Kim, Barbaros Ozyilmaz, Jong-Hyun Ahn, Byung Hee Hong, and Sumio Iijima. Roll-to-roll production of 30-inch graphene films for transparent electrodes. *Nature nanotechnology*, 5(8):574–8, aug 2010.

[33] Sasha Stankovich, Dmitriy a Dikin, Geoffrey H B Dommett, Kevin M Kohlhaas, Eric J Zimney, Eric a Stach, Richard D Piner, SonBinh T Nguyen, and Rodney S Ruoff. Graphene-based composite materials. *Nature*, 442(7100):282–6, jul 2006.

[34] Shuai Wang, Priscilla Kailian Ang, Ziqian Wang, Ai Ling Lena Tang, John T L Thong, and Kian Ping Loh. High mobility, printable, and solution-processed graphene electronics. *Nano Letters*, 10(1):92–98, 2010.

[35] Thomas Moldt, Axel Eckmann, Philipp Klar, Sergey V. Morozov, Alexander A. Zhukov, Kostya S. Novoselov, and Cinzia Casiraghi. High-yield production and transfer of graphene flakes obtained by anodic bonding. *ACS Nano*, 5(10):7700–7706, 2011.

[36] Alfonso Reina, Hyungbin Son, Living Jiao, Ben Fan, Mildred S. Dresselhaus, ZhongFan Liu, and Jing Kong. Transferring and identification of single- and few-layer graphene on arbitrary substrates. *Journal of Physical Chemistry C*, 112(46):17741–17744, 2008.

[37] Alfonso Reina, Xiaoting Jia, John Ho, Daniel Nezich, Hyungbin Son, Vladimir Bulovic, Mildred S. Dresselhaus, and Jing Kong. Large area, few-layer graphene films on arbitrary substrates by chemical vapor deposition. *Nano letters*, 9(1):30–5, jan 2009.

[38] Jae-Young Choi. Graphene transfer: A stamp for all substrates. *Nature Nanotechnology*, 8:311–312, 2013.

[39] Jie Song, Fong-Yu Kam, Rui-Qi Png, Wei-Ling Seah, Jing-Mei Zhuo, Geok-Kieng Lim, Peter K H Ho, and Lay-Lay Chua. A general method for transferring graphene onto soft surfaces. *Nature nanotechnology*, 8:356–62, 2013.

[40] Yung-Chang Lin, Chun-Chieh Lu, Chao-Huei Yeh, Chuanhong Jin, Kazu Suenaga, and Po-Wen Chiu. Graphene Annealing: How Clean Can It Be? *Nano Letters*, 12(1):414–419, jan 2012.

[41] Cheng Gong, Herman Carlo Floresca, David Hinojos, Stephen McDonnell, Xiaoye Qin, Yufeng Hao, Srikar Jandhyala, Greg Mordi, Jiyoung Kim, Luigi Colombo, Rodney S Ruoff, Moon J Kim, Kyeongjae Cho, Robert M Wallace, and Yves J Chabal. Rapid Selective Etching of PMMA Residues from Transferred Graphene by Carbon Dioxide. *The Journal of Physical Chemistry C*, 117(44):23000–23008, nov 2013.

[42] Kitu Kumar, Youn-Su Kim, and Eui-Hyeok Yang. The influence of thermal annealing to remove polymeric residue on the electronic doping and morphological characteristics of graphene. *Carbon*, 65(0):35–45, dec 2013.

[43] Sandeep Gorantla, Alicja Bachmatiuk, Jeonghyun Hwang, Hussain A Alsalman, Joon Young Kwak, Thomas Seyller, Jurgen Eckert, Michael G Spencer, and Mark H Rummeli. A universal transfer route for graphene. *Nanoscale*, 6(2):889–896, 2014.

[44] Libo Gao, Guang-Xin Ni, Yanpeng Liu, Bo Liu, Antonio H Castro Neto, and Kian Ping Loh. Face-to-face transfer of wafer-scale graphene films. *Nature*, 505(7482):190–4, 2014.

[45] Changgu Lee, Xiaoding Wei, Jeffrey W Kysar, and James Hone. Measurement of the elastic properties and intrinsic strength of monolayer graphene. *Science (New York, N.Y.)*, 321(5887):385–8, jul 2008.

[46] E.J. Pavlina and C.J. Tyne. Correlation of Yield Strength and Tensile Strength with Hardness for Steels. *Journal of Materials Engineering and Performance*, 17(6):888–893, apr 2008.

[47] Chuancheng Jia, Jiaolong Jiang, Lin Gan, and Xuefeng Guo. Direct optical characterization of graphene growth and domains on growth substrates. *Scientific reports*, 2:707, jan 2012.

[48] Vikas Berry. Impermeability of graphene and its applications. *Carbon*, 2013.

[49] A. Morin, D. Lucot, A. Ouerghi, G. Patriarche, E. Bourhis, A. Madouri, C. Ulysse, J. Pelta, L. Auvray, R. Jede, L. Bruchhaus, and J. Gierak. FIB carving of nanopores into suspended graphene films. *Microelectronic Engineering*, 97:311–316, sep 2012.

[50] J Scott Bunch, Scott S Verbridge, Jonathan S Alden, Arend M van der Zande, Jeevak M Parpia, Harold G Craighead, and Paul L McEuen. Impermeable atomic membranes from graphene sheets. *Nano letters*, 8(8):2458–62, aug 2008.

[51] Jannik C Meyer, A K Geim, M I Katsnelson, K S Novoselov, T J Booth, and S Roth. The structure of suspended graphene sheets. *Nature*, 446(7131):60–3, mar 2007.

[52] Hidetaka Sawada, Takeo Sasaki, Fumio Hosokawa, and Kazutomo Suenaga. Resolution enhancement at a large convergence angle by a delta corrector with a CFEG in a low-accelerating-voltage STEM. *Micron*, 63:35–39, 2014.

[53] P. R. Wallace. The band theory of graphite. *Physical Review*, 71(9):622–634, 1947.

[54] S V Morozov, K S Novoselov, M I Katsnelson, F Schedin, D C Elias, J A Jaszczak, and A K Geim. Giant Intrinsic Carrier Mobilities in Graphene and Its Bilayer. *Phys. Rev. Lett.*, 100(1):16602, jan 2008.

[55] K S Novoselov, A K Geim, S V Morozov, D Jiang, M I Katsnelson, I V Grigorieva, S V Dubonos, and A A Firsov. Two-dimensional gas of massless Dirac fermions in graphene. *Nature*, 438(7065):197–200, nov 2005.

[56] Guillermo Lopez-Polin, Cristina Gomez-Navarro, Vincenzo Parente, Francisco Guinea, Mikhail I Katsnelson, Francesc Perez-Murano, and Julio Gomez-Herrero. Increasing the elastic modulus of graphene by controlled defect creation. *Nat Phys*, 11(1):26–31, jan 2015.

[57] Ardavan Zandiatashbar, Gwan-Hyoung Lee, Sung Joo An, Sunwoo Lee, Nithin Mathew, Mauricio Terrones, Takuya Hayashi, Catalin R Picu, James Hone, and Nikhil Koratkar. Effect of defects on the intrinsic strength and stiffness of graphene. *Nature communications*, 5:3186, jan 2014.

[58] Xiao Huang, Zongyou Yin, Shixin Wu, Xiaoying Qi, Qiyuan He, Qichun Zhang, Qingyu Yan, Freddy Boey, and Hua Zhang. Graphene-Based Materials: Synthesis, Characterization, Properties and Applications. *Small*, 7(14):1876–1902, jun 2011.

[59] G.-H. Lee, R. C. Cooper, S. J. An, S. Lee, a. van der Zande, N. Petrone, a. G. Hammerberg, C. Lee, B. Crawford, W. Oliver, J. W. Kysar, and J. Hone. High-Strength Chemical-Vapor-Deposited Graphene and Grain Boundaries. *Science*, 340(6136):1073–1076, may 2013.

[60] Pinshane Y Huang, Carlos S Ruiz-Vargas, Arend M van der Zande, William S Whitney, Mark P Levendorf, Joshua W Kevek, Shivank Garg, Jonathan S Alden, Caleb J Hustedt, Ye Zhu, Jiwoong Park, Paul L McEuen, and David A Muller. Grains and grain boundaries in single-layer graphene atomic patchwork quilts. *Nature*, 469:389–392, 2011.

[61] Kwanpyo Kim, Vasilii I Artyukhov, William Regan, Yuanyue Liu, M F Crommie, Boris I Yakobson, and a Zettl. Ripping Graphene: Preferred Directions. *Nano letters*, dec 2011.

[62] Ji Won Suk, Alexander Kitt, Carl W. Magnuson, Yufeng Hao, Samir Ahmed, Jinho An, Anna K. Swan, Bennett B. Goldberg, and Rodney S. Ruoff. Transfer of CVD-Grown Monolayer Graphene onto Arbitrary Substrates. *ACS nano*, 5(9):6916–24, sep 2011.

[63] M I Katsnelson, K S Novoselov, and A K Geim. Chiral tunnelling and the Klein paradox in graphene. *Nature Physics*, 2(9):620–625, sep 2006.

[64] Andrea F. Young and Philip Kim. Quantum interference and Klein tunnelling in graphene heterojunctions. *Nature Physics*, 5(3):222–226, 2009.

[65] Shin-ichiro Tanaka, Masaharu Matsunami, and Shinichi Kimura. An investigation of electron-phonon coupling via phonon dispersion measurements in graphite using angle-resolved photoelectron spectroscopy. *Scientific reports*, 3:3031, 2013.

[66] Jean Nicolas Longchamp, Tatiana Latychevskaia, Conrad Escher, and Hans Werner Fink. Low-energy electron transmission imaging of clusters on free-standing graphene. *Applied Physics Letters*, 101, 2012.

[67] R. M. Feenstra, N. Srivastava, Qin Gao, M. Widom, Bogdan Diaconescu, Taisuke Ohta, G. L. Kellogg, J. T. Robinson, and I. V. Vlassiouk. Low-energy electron reflectivity from graphene. *Physical Review B - Condensed Matter and Materials Physics*, 87, 2013.

[68] K L Man and M S Altman. Low energy electron microscopy and photoemission electron microscopy investigation of graphene. *Journal of physics. Condensed matter : an Institute of Physics journal*, 24(31):314209, 2012.

[69] E Mimekova, H Bouyanfif, M Lejeune, I Mullerova, M Hovorka, M Uncovsky, and L Frank. Very low energy electron microscopy of graphene flakes. *Journal of Microscopy*, 251(2):123–127, 2013.

[70] Joshua D Stoll and Andrei Kolmakov. Electron transparent graphene windows for environmental scanning electron microscopy in liquids and dense gases. *Nanotechnology*, 23:505704, 2012.

[71] H Hibino, H Kageshima, F Maeda, M Nagase, Y Kobayashi, and H Yamaguchi. Microscopic thickness determination of thin graphite films formed on \mathrm{SiC} from quantized oscillation in reflectivity of low-energy electrons. *Phys. Rev. B*, 77(7):75413, feb 2008.

[72] Taisuke Ohta, Aaron Bostwick, Thomas Seyller, Karsten Horn, and Eli Rotenberg. Controlling the electronic structure of bilayer graphene. *Science (New York, N.Y.)*, 313(5789):951–954, 2006.

[73] Bart Van Zeghbroeck. *Principles of Semiconductor Devices*. University of Colorado, 2004.

[74] E Rutherford and H Geigerg. An Electrical Method of Counting the Number of Alpha Particles From Radio-Active Substances. *Proceedings of the Royal Society of London*, LXXXI(546), 1908.

[75] G. Charpak, R. Bouclier, T. Bressani, J. Favier, and Č. Zupančič. The use of multiwire proportional counters to select and localize charged particles. *Nuclear Instruments and Methods*, 62(3):262–268, jul 1968.

[76] Glenn F Knoll. *Radiation detection and measurement / 4th edition*. Wiley, New York, 4th edition, 2010.

[77] Robley D (Robley Dunglison) Evans. *The atomic nucleus*. McGraw-Hill, New York, 1955.

[78] Pam Cherry and Angela Duxbury. Practical Radiotherapy: Physics and Equipment. *Radiology*, 214(1):120, jan 2000.

[79] F. Sauli. GEM: A new concept for electron amplification in gas detectors. *Nuclear Instruments and Methods in Physics Research Section A: Accelerators, Spectrometers, Detectors and Associated Equipment*, 386(2-3):531–534, feb 1997.

[80] Fabio Sauli. Gaseous radiation detectors fundamentals and applications, 2014.

[81] E. Dané, G. Penso, D. Pinci, and A. Sarti. Detailed study of the gain of the MWPCs for the LHCb muon system. *Nuclear Instruments and Methods in Physics Research Section A: Accelerators, Spectrometers, Detectors and Associated Equipment*, 572(2):682–688, mar 2007.

[82] S. Bachmann, A. Bressan, L. Ropelewski, F. Sauli, A. Sharma, and D. Mörmann. Charge amplification and transfer processes in the gas electron multiplier. *Nuclear Instruments and Methods in Physics Research Section A: Accelerators, Spectrometers, Detectors and Associated Equipment*, 438(2-3):376–408, dec 1999.

[83] S. Bachmann, A. Bressan, M. Capeáns, M. Deutel, S. Kappler, B. Ketzer, A. Polouektov, L. Ropelewski, F. Sauli, E. Schulte, L. Shekhtman, and A. Sokolov. Discharge studies and prevention in the gas electron multiplier (GEM). *Nuclear Instruments and Methods in Physics Research Section A: Accelerators, Spectrometers, Detectors and Associated Equipment*, 479(2-3):294–308, mar 2002.

[84] A Bondar, A Buzulutskov, L Shekhtman, and A Vasiljev. Study of ion feedback in multi-GEM structures. *Nuclear Instruments and Methods in Physics Research Section A: Accelerators, Spectrometers, Detectors and Associated Equipment*, 496(2-3):325–332, jan 2003.

[85] P Colas, I Giomataris, and V Lepeltier. Ion backflow in the Micromegas TPC for the future linear collider. *Nuclear Instruments and Methods in Physics Research Section A: Accelerators, Spectrometers, Detectors and Associated Equipment*, 535(12):226–230, dec 2004.

[86] M Ball, K Eckstein, and T Gunji. Ion backflow studies for the ALICE TPC upgrade with GEMs. *Journal of Instrumentation*, 9:C04025–C04025, 2014.

[87] N L Aleksandrov and E M Bazelyan. Ionization processes in spark discharge plasmas. *Plasma Sources Science and Technology*, 8(2):285–294, may 1999.

[88] Weilie Zhou and Zhong Lin Wang. *Scanning Microscopy for Nanotechnology: Techniques and Applications*. Springer, xiv edition, 2007.

[89] Norman B Colthup, Lawrence H Daly, and Stephen E Wiberley. *Introduction to Infrared and Raman Spectroscopy*. Elsevier, 1990.

[90] Axel Eckmann, Alexandre Felten, Artem Mishchenko, Liam Britnell, Ralph Krupke, Kostya S Novoselov, and Cinzia Casiraghi. Probing the nature of defects in graphene by Raman spectroscopy. *Nano letters*, 12:3925–30, 2012.

[91] L. G. Cançado, A. Jorio, E. H Martins Ferreira, F. Stavale, C. A. Achete, R. B. Capaz, M. V O Moutinho, A. Lombardo, T. S. Kulmala, and A. C. Ferrari. Quantifying defects in graphene via Raman spectroscopy at different excitation energies. *Nano Letters*, 11(8):3190–3196, 2011.

[92] Pedro Venezuela, Michele Lazzeri, and Francesco Mauri. Theory of double-resonant Raman spectra in graphene: Intensity and line shape of defect-induced and two-phonon bands. *Physical Review B*, 84(3):35433, jul 2011.

[93] Holger Schönherr and G.Julius Vancso. Atomic Force Microscopy in Practice. In *Scanning Force Microscopy of Polymers SE - 2*, Springer Laboratory, pages 25–75. Springer Berlin Heidelberg, 2010.

[94] Peter Jonathan Eaton and Paul West. *Atomic force microscopy*, volume 10. Oxford University Press Oxford, 2010.

[95] Hyman Rosen. A modified ninhydrin colorimetric analysis for amino acids. *Archives of Biochemistry and Biophysics*, 67(1):10–15, 1957.

[96] Shih Wen Sun, Yi Cheng Lin, Yih Ming Weng, and Min Jane Chen. Efficiency improvements on ninhydrin method for amino acid quantification. *Journal of Food Composition and Analysis*, 19(2-3):112–117, 2006.

[97] N. Lindvall, J. Sun, G. Abdul, and A. Yurgens. Towards transfer-free fabrication of graphene NEMS grown by chemical vapour deposition, 2012.

[98] Sumedh P Surwade, Sergei N Smirnov, Ivan V Vlassiouk, Raymond R Unocic, Gabriel M Veith, Sheng Dai, and Shannon M Mahurin. Water desalination using nanoporous single-layer graphene. *Nat Nano*, 10(5):459–464, may 2015.

[99] Zonghoon Lee, Ki Joon Jeon, Albert Dato, Rolf Erni, Thomas J. Richardson, Michael Frenklach, and Velimir Radmilovic. Direct imaging of soft-hard interfaces enabled by graphene. *Nano Letters*, 9(9):3365–3369, 2009.

[100] Matthew G. Panthani, Colin M. Hessel, Dariya Reid, Gilberto Casillas, Miguel José-Yacamán, and Brian A. Korgel. Graphene-supported high-resolution TEM and STEM imaging of silicon nanocrystals and their capping ligands. *Journal of Physical Chemistry C*, 116(42):22463–22468, 2012.

[101] Christopher A. Merchant, Ken Healy, Meni Wanunu, Vishva Ray, Neil Peterman, John Bartel, Michael D. Fischbein, Kimberly Venta, Zhengtang Luo, A. T Charlie Johnson, and Marija Drndić. DNA translocation through graphene nanopores. *Nano Letters*, 10(8):2915–2921, 2010.

[102] S Garaj, W Hubbard, A Reina, J Kong, D Branton, and J A Golovchenko. Graphene as a subnanometre trans-electrode membrane. *Nature*, 467(7312):190–193, 2010.

[103] Kyaw Sint, Boyang Wang, and Petr Král. Selective ion passage through functionalized graphene nanopores. *Journal of the American Chemical Society*, 130(49):16448–16449, 2008.

[104] Kwang S Keun Soo Kim, Yue Zhao, Houk Jang, Sang Yoon Lee, Jong Min Kim, Kwang S Keun Soo Kim, Jong-Hyun Ahn, Philip Kim, Jae-Young Choi, and Byung Hee Hong. Large-scale pattern growth of graphene films for stretchable transparent electrodes. *Nature*, 457(7230):706–710, 2009.

[105] Zengguang Cheng, Qiaoyu Zhou, Chenxuan Wang, Qiang Li, Chen Wang, and Ying Fang. Toward Intrinsic Graphene Surfaces: A Systematic Study on Thermal Annealing and Wet-Chemical Treatment of SiO2-Supported Graphene Devices. *Nano Letters*, 11(2):767–771, feb 2011.

[106] I Pasternak, A Krajewska, K Grodecki, I Jozwik-Biala, K Sobczak, and W Strupinski. Graphene films transfer using marker-frame method. *AIP Advances*, 4(9), 2014.

[107] Benjamín Alemán, William Regan, Shaul Aloni, Virginia Altoe, Nasim Alem, Calar Girit, Baisong Geng, Lorenzo Maserati, Michael Crommie, Feng Wang, and A. Zettl. Transfer-free batch fabrication of large- Area suspended graphene membranes. *ACS Nano*, 4(8):4762–4768, 2010.

[108] Mark P. Levendorf, Carlos S. Ruiz-Vargas, Shivank Garg, and Jiwoong Park. Transfer-free batch fabrication of single layer graphene transistors. *Nano Letters*, 9(12):4479–4483, 2009.

[109] Yung Chang Lin, Chuanhong Jin, Jung Chi Lee, Shou Feng Jen, Kazu Suenaga, and Po Wen Chiu. Clean transfer of graphene for isolation and suspension. *ACS Nano*, 5(3):2362–2368, 2011.

[110] Xu Du, Ivan Skachko, Anthony Barker, and Eva Y Andrei. Approaching ballistic transport in suspended graphene., 2008.

[111] Leonhard Prechtel, Li Song, Dieter Schuh, Pulickel Ajayan, Werner Wegscheider, and Alexander W. Holleitner. Time-resolved ultrafast photocurrents and terahertz generation in freely suspended graphene, 2012.

[112] Xuelei Liang, Brent A. Sperling, Irene Calizo, Guangjun Cheng, Christina Ann Hacker, Qin Zhang, Yaw Obeng, Kai Yan, Hailin Peng, Qiliang Li, Xiaoxiao Zhu, Hui Yuan, Angela R. Hight Walker, Zhongfan Liu, Lian Mao Peng, and Curt A. Richter. Toward clean and crackless transfer of graphene. *ACS Nano*, 5(11):9144–9153, 2011.

[113] Ayrat Dimiev, Dmitry V Kosynkin, Alexander Sinitskii, Alexander Slesarev, Zhengzong Sun, and James M Tour. Layer-by-layer removal of graphene for device patterning. *Science (New York, N.Y.)*, 331(6021):1168–1172, 2011.

[114] V A Coleman Eriksson, R Knut, O Karis, H Grennberg, U Jansson, R Quinlan, B C Holloway, B Sanyal, and O. Defect formation in graphene nanosheets by acid treatment: an x-ray absorption spectroscopy and density functional theory study. *Journal of Physics D: Applied Physics*, 41(6):62001, 2008.

[115] Andrea C Ferrari and Denis M Basko. Raman spectroscopy as a versatile tool for studying the properties of graphene. *Nature nanotechnology*, 8(4):235–46, apr 2013.

[116] L. G. Cançado, A. Jorio, and M. A. Pimenta. Measuring the absolute Raman cross section of nanographites as a function of laser energy and crystallite size. *Physical Review B - Condensed Matter and Materials Physics*, 76(6), 2007.

[117] A Mooradian. Photoluminescence of Metals. *Physical Review Letters*, 22(5):185–187, feb 1969.

[118] Nigam P Rath, Elizabeth M Holt, and Katsumi Tanimura. Fluorescent copper(I) complexes: structural and spectroscopic characterization of bis(p-toluidine)bis(acetonitrile)tetraiodotetracopper and bis[(p-chloroaniline)(acetonitrile)diiodocopper] tetrameric complexes of mixed-ligand character. *Inorganic Chemistry*, 24(23):3934–3938, nov 1985.

[119] G T Boyd, Z H Yu, and Y R Shen. Photoinduced luminescence from the noble metals and its enhancement on roughened surfaces. *Physical Review B*, 33(12):7923–7936, jun 1986.

[120] Kallepalli Lakshmi Narayana Deepak, Soma Venugopal Rao, and Desai Narayana Rao. Direct Writing in Polymers with Femtosecond Laser Pulses: Physics and Applications. In Igor Peshko, editor, *Laser Pulses - Theory, Technology, and Applications*, chapter 9. InTech, 2012.

[121] James J. Licari. *Coating Materials for Electronic Applications*. Elsevier, 2003.

[122] Graphene Supermarket. Continuous Wafer - Scale Graphene Films Prepared by Chemical Vapor Deposition: Production and Applications. Technical report, Graphene Laboratories, 2015.

[123] Ramakrishna Podila, Rahul Rao, Ryuichi Tsuchikawa, Masa Ishigami, and Apparao M Rao. Raman Spectroscopy of Folded and Scrolled Graphene. *ACS Nano*, 6(7):5784–5790, jul 2012.

[124] Kwanpyo Kim, Sinisa Coh, Liang Z Tan, William Regan, Jong Min Yuk, Eric Chatterjee, M F Crommie, Marvin L Cohen, Steven G Louie, and A Zettl. Raman Spectroscopy Study of Rotated Double-Layer Graphene: Misorientation-Angle Dependence of Electronic Structure. *Phys. Rev. Lett.*, 108(24):246103, jun 2012.

[125] Seon-Myeong Choi, Seung-Hoon Jhi, and Young-Woo Son. Effects of strain on electronic properties of graphene. *Phys. Rev. B*, 81(8):81407, feb 2010.

[126] T M G Mohiuddin, A Lombardo, R R Nair, A Bonetti, G Savini, R Jalil, N Bonini, D M Basko, C Galiotis, N Marzari, K S Novoselov, A K Geim, and A C Ferrari. Uniaxial strain in graphene by Raman spectroscopy: G peak splitting, Grüneisen parameters, and sample orientation. *Phys. Rev. B*, 79(20):205433, may 2009.

[127] Mingyuan Huang, Hugen Yan, Tony F Heinz, and James Hone. Probing Strain-Induced Electronic Structure Change in Graphene by Raman Spectroscopy. *Nano Letters*, 10(10):4074–4079, oct 2010.

[128] Otakar Frank, Marcel Mohr, Janina Maultzsch, Christian Thomsen, Ibtsam Riaz, Rashid Jalil, Kostya S Novoselov, Georgia Tsoukleri, John Parthenios, Konstantinos Papagelis, Ladislav Kavan, and Costas Galiotis. Raman 2D-Band Splitting in Graphene: Theory and Experiment. *ACS Nano*, 5(3):2231–2239, mar 2011.

[129] Duhee Yoon, Young-Woo Son, and Hyeonsik Cheong. Strain-Dependent Splitting of the Double-Resonance Raman Scattering Band in Graphene. *Phys. Rev. Lett.*, 106(15):155502, apr 2011.

[130] Fei Ding, Hengxing Ji, Yonghai Chen, Andreas Herklotz, Kathrin Dörr, Yongfeng Mei, Armando Rastelli, and Oliver G Schmidt. Stretchable Graphene: A Close Look at Fundamental Parameters through Biaxial Straining. *Nano Letters*, 10(9):3453–3458, sep 2010.

[131] Y C Cheng, Z Y Zhu, G S Huang, and U Schwingenschlögl. Grüneisen parameter of the G mode of strained monolayer graphene. *Phys. Rev. B*, 83(11):115449, mar 2011.

[132] Jakob Zabel, Rahul R Nair, Anna Ott, Thanasis Georgiou, Andre K Geim, Kostya S Novoselov, and Cinzia Casiraghi. Raman Spectroscopy of Graphene and Bilayer under Biaxial Strain: Bubbles and Balloons. *Nano Letters*, 12(2):617–621, feb 2012.

[133] Justin Legleiter. The effect of drive frequency and set point amplitude on tapping forces in atomic force microscopy: simulation and experiment. *Nanotechnology*, 20(24):245703, 2009.

[134] Robin W Havener, Houlong Zhuang, Lola Brown, Richard G Hennig, and Jiwoong Park. Angle-Resolved Raman Imaging of Interlayer Rotations and Interactions in Twisted Bilayer Graphene. *Nano Letters*, 12(6):3162–3167, jun 2012.

[135] A. Das, S. Pisana, B. Chakraborty, S. K. Piscanec, S.V. Saha, U.S. Waghmare, K. R. Novoselov, Krishnamurthy H. K., A.C. Geim, A.K. Ferrari, and A. Sood. Monitoring dopants by Raman scattering in an electrochemically top-gated graphene transistor. *Nature Nanotechnology*, 3(4):210–215, apr 2008.

[136] Young Jun Yu, Yue Zhao, Sunmin Ryu, Louis E. Brus, Kwang S. Kim, and Philip Kim. Tuning the graphene work function by electric field effect. *Nano Letters*, 9(10):3430–3434, 2009.

[137] Michele Lazzeri and Francesco Mauri. Nonadiabatic Kohn Anomaly in a Doped Graphene Monolayer. *Phys. Rev. Lett.*, 97(26):266407, dec 2006.

[138] Simone Pisana, Michele Lazzeri, Cinzia Casiraghi, Kostya S Novoselov, A K Geim, Andrea C Ferrari, and Francesco Mauri. Breakdown of the adiabatic Born-Oppenheimer approximation in graphene. *Nat Mater*, 6(3):198–201, mar 2007.

[139] Jun Yan, Yuanbo Zhang, Philip Kim, and Aron Pinczuk. Electric Field Effect Tuning of Electron-Phonon Coupling in Graphene. *Physical Review Letters*, 98(16):166802, apr 2007.

[140] Luis A. Jauregui, Helin Cao, Wei Wu, Qingkai Yu, and Yong P. Chen. Electronic properties of grains and grain boundaries in graphene grown by chemical vapor deposition. *Solid State Communications*, 151:1100–1104, 2011.

[141] Oleg V Yazyev and Steven G Louie. Electronic transport in polycrystalline graphene., 2010.

[142] Junfeng Zhang, Jijun Zhao, and Jianping Lu. Intrinsic strength and failure behaviors of graphene grain boundaries. *ACS Nano*, 6:2704–2711, 2012.

[143] Thuc Hue Ly, Dinh Loc Duong, Quang Huy Ta, Fei Yao, Quoc An Vu, Hye Yun Jeong, Sang Hoon Chae, and Young Hee Lee. Nondestructive characterization of graphene defects. *Advanced Functional Materials*, 23:5183–5189, 2013.

[144] Dinh Loc Duong, Gang Hee Han, Seung Mi Lee, Fethullah Gunes, Eun Sung Kim, Sung Tae Kim, Heetae Kim, Quang Huy Ta, Kang Pyo So, Seok Jun Yoon, Sang Hoon Seung Jin Chae, Young Woo Jo, Min Ho Park, Sang Hoon Seung Jin Chae, Seong Chu Lim, Jae Young Choi, and Young Hee Lee. Probing graphene grain boundaries with optical microscopy, 2012.

[145] Sami Malola, Hannu Häkkinen, and Pekka Koskinen. Structural, chemical, and dynamical trends in graphene grain boundaries. *Physical Review B - Condensed Matter and Materials Physics*, 81, 2010.

[146] Max Seifert, Jose E B Vargas, Marco Bobinger, Matthias Sachsenhauser, Aron W Cummings, Stephan Roche, and Jose A Garrido. Role of grain boundaries in tailoring electronic properties of polycrystalline graphene by chemical functionalization. *2D Materials*, 2(2):24008, 2015.

[147] H Maeda, N Ishida, H Kawauchi, and K Tsujimura. Reaction of fluorescein-isothiocyanate with proteins and amino acids. I. Covalent and non-covalent binding of fluorescein-isothiocyanate and fluorescein to proteins. *Journal of biochemistry*, 65(5):777–783, 1969.

[148] M. Killenberg, S. Lotze, J. Mnich, S. Roth, R. Schulte, B. Sobloher, W. Struczinski, and M. Tonutti. Modelling and measurement of charge transfer in multiple GEM structures. *Nuclear Instruments and Methods in Physics Research Section A: Accelerators, Spectrometers, Detectors and Associated Equipment*, 498(1):369–383, 2003.

[149] Andrej Sipaj. *Simulation, Design and Construction of a Gas Electron Multiplier for Particle Tracking.* Faculty of Energy Systems and Nuclear Science Program University of Ontario Institute of Technology, 2012.

[150] R Bouclier, G Charpak, Z Dimčovski, G Fischer, F Sauli, G Coignet, and G Flügge. Investigation of some properties of multiwire proportional chambers. *Nuclear Instruments and Methods*, 88(1):149–161, nov 1970.

[151] Y Assran and A Sharma. Transport Properties of operational gas mixtures used at LHC. *ArXiv*, page 36, 2001.

[152] A Sharma. Properties of some gas mixtures used in tracking detectors. *ArXiv*, 1998.

[153] R H Millar Greening and J R. Experimental X-ray mass attenuation coefficients for materials of low atomic number in the energy range 4 to 25 keV. *Journal of Physics B: Atomic and Molecular Physics*, 7(17):2332, 1974.

[154] S D Pringle. Patent WO2009068887 A2: Gas electron multiplier detector, 2009.

[155] L. Tsetseris and S. T. Pantelides. Graphene: An impermeable or selectively permeable membrane for atomic species? *Carbon*, 67:58–63, 2014.

[156] Evelyn N. Wang and Rohit Karnik. Water desalination: Graphene cleans up water. *Nature Nanotechnology*, 7(9):552–554, sep 2012.

[157] De En Jiang, Valentino R. Cooper, and Sheng Dai. Porous graphene as the ultimate membrane for gas separation. *Nano Letters*, 9(12):4019–4024, 2009.

[158] Steven P. Koenig, Luda Wang, John Pellegrino, and J. Scott Bunch. Selective molecular sieving through porous graphene, 2012.

[159] F. Sauli, L. Ropelewski, and P. Everaerts. Ion feedback suppression in time projection chambers. *Nuclear Instruments and Methods in Physics Research, Section A: Accelerators, Spectrometers, Detectors and Associated Equipment*, 560(2):269–277, 2006.

Appendices

Appendix A

Matlab Function for Graphene Coverage

```
function [ allCounts, legendInfo, allTimes ] = mca_import_only()

% Note: shortcut for execution (copy paste):
% [ data, legend, times ] = mca_import_only();
%
%This Function Imports .mca files for MCA counts
% only works if all data files in folder has same channel numbers
%
%   List of outputs of this function
% startRow: 1st row of data
% endRow: last row of data
%
% Note: will replace old graph files with the same name without asking
% Change line 36 if different channel number
%
% OUTPUTS:  allCounts - a matrix with all the mca files
%           legendInfo - cell with all the file names in the order they
%               were found (corresponds to legend on graph)
%           allTimes - matrix with first row: all live times, 2nd row:
    all
%               real times
%  To export Data as txt, use command: saves 'A' into my_data.txt
%   save my_data.txt A -ASCII
```

```
%
% NOTES:    Legend for graph has to be set before these axes uncomment
% and copy-paste the block labelled below into command window if legend
% needs to be fixed manually
%
%: ------------------------------------------------------------------
%% Open file

% 'pwd' is the current path
% open a command box to choose a new directory
folder = uigetdir(pwd);
oldFolder = cd(folder);
% creates a struct with all the dat files and 5 values:
% name, date, bytes, isdir, datenum
files = dir('*.mca');
% Define output variable

if isempty(files)
    disp('no .mca file found in that directory');
    return
end


%% Initialise variables

channel_number = 2048;
allCounts = zeros(channel_number, length(files));
allTimes = zeros(2, length(files));

% define saving directory
imageDirectory = 'ImageDirectory';

saveDirectory = exist(imageDirectory, 'dir');
if saveDirectory == 0
    mkdir(imageDirectory);
end


```

```
%% Getting Data

% length(files) gives the length of the struct
% ie the number of files foundz


for i=1:length(files)
    % GET counts DATA %%%%
```

```
95      return
96      end %end if
97
98  end % end for loop all files
99  hold all;
100 legendInfo = cell(length(files),1);
101 clear i a;
102 a=1;
103 i=1;
104 cc=parula(length(files));
105
106 while i <= (length(files));
107
108     %plot(allCounts(:,i));
109     % uncomment line below for color gradient, if not uncomment above
110     plot(allCounts(:,i),'color', cc(i,:));
111     % fix file name without '_', without extensions, replace Vcm by V.cm
        -1:
112     newName = strrep(files(i).name(1:end-4), '_',', ');
113     newName = strrep(newName,'Vcm','V.cm-1');
114     legendInfo{a} = newName;
115     a=a+1;
116     i=i+1;
117
118 end
119
120 % note: 'epsc' saves the data as .eps
121 saveGraph('Original Data', imageDirectory, legendInfo, 'northeast', 'epsc
        ');
122 hold off;
123
124 cd(oldFolder);
125
126 end % end function
127
128
129
130
```

```
131
132 % ------------------------------------------------------------------------
133 %                     FUNCTION SAVEGRAPH
134 % ------------------------------------------------------------------------
135
136 function [] = saveGraph(graphName, imageDirectory, legendContent,
        legendLocation, format)
137 % Function saves current figure and closes it
138 % LegendLocation:
139 % use 'SouthOutside' for legend outside graph
140 % otherwise 'northwest', 'northeast' etc.
141 %
142 % format:
143 % use 'epsc' for .eps output
144
145 if nargin<=2
146     legendLocation = 'SouthOutside';
147     format = 'png';
148 end
149
150 xlabel( '\fontsize{14} Channels' );
151 ylabel( '\fontsize{14} Counts' );
152
153 % setting axes parameters/format for the graph (OriginPro style)
154     % Box = box around the graph (alternatively, use
155     % box 'on';
156     % Ticklength [2Dgraphlength 3Dgraphlength]
157     % Xtick = 0:5:100 labels ticks up to 100, with a major tick every 5
158     % Fontsize: font size for axes numbering only, see Xlabel and Ylabel
159         % for axis legend. Originpro default is 18 which is 14 here
160
161 % set(gca,'box','on','ticklength',[0.01 0.02],'XMinorTick','on',...
162 %     'XTick',0:300:2800,'YMinorTick','on','YTick',0:1000:15000,...
163 %     'fontsize',14);
164
165 % Uncomment below for fixed axes size: [xmin xmax ymin ymax]
166 % axis([0 1500 0 12000]);
167 axis auto;
```

```
168
169 legend( legendContent, 'Location', legendLocation );
170 % use code below if legend needs to be hidden or code above for visible
171 % legend
172 % myLegend = legend( legendContent, 'Location', legendLocation );
173 % set(myLegend, 'visible', 'off');
174
175 %-------------------------------------------------------------
176 % Adding top and right axes:
177 % First, store the handle to those axes.
178 % Next create a second set of axes,
179 % position This on top of the first and make it transparent.
180
181 % ax1=gca;
182 % ax2 = axes('Position', get(ax1, 'Position'),'Color', 'none');
183 % set(ax2, 'XAxisLocation', 'top','YAxisLocation','Right');
184 %
185 %% set the same Limits and Ticks on ax2 as on ax1;
186 %
187 % set(ax2, 'XLim', get(ax1, 'XLim'),'YLim', get(ax1, 'YLim'));
188 % set(ax2, 'XTick', get(ax1, 'XTick'), 'YTick', get(ax1, 'YTick'));
189 % set(ax2, 'XTickLabel', [],'YTickLabel',[]); % delete axis tick numbers
190
191 %NOTE: Legend has to be set before these axes uncomment and copy-paste
      the
192 %block into command window if legend needs to be fixed manually
193 %-------------------------------------------------------------
194
195 savefig(gcf, graphName);
196
197 % if the format requested isn't png, save a png anyway
198 if ~strcmp(format,'png');
199     saveas(gcf, [imageDirectory '\' graphName], 'png');
200 end
201
202     saveas(gcf, [imageDirectory '\' graphName], format);
203
204 end
```

```
205
206
207
208
209
210 % ------------------------------------------------------------------------
211 %                     FUNCTION MCA_DATA_IMPORT
212 % ------------------------------------------------------------------------
213
214 function [A] = mca_data_import(filename, formatSpec, startRow, endRow)
215 % Function reads one file and creates vector array of variables
216
217
218 %% A outputs a <2 column double> with the data
219 %% Format string for each line of text:
220 %   column1: double (%f)
221 % column2: double (%f)
222 % For more information, see the TEXTSCAN documentation.
223
224 clear A;
225
226 %% Initialize variables.
227 delimiter = ' ';
228
229 if nargin<=3
230     startRow = 13;
231     endRow = 2060;
232     formatSpec = '%f%*s%*s%*s%[^\n\r]';
233 end
234
235 %% Open the text file.
236 fileID = fopen(filename,'r');
237
238 %% Read columns of data according to format string.
239 % This call is based on the structure of the file used to generate this
240 % code. If an error occurs for a different file, try regenerating the
    code
241 % from the Import Tool.
```

```
242 dataArray = textscan(fileID, formatSpec, endRow(1)-startRow(1)+1, '
    Delimiter', delimiter, 'MultipleDelimsAsOne', true, 'HeaderLines',
    startRow(1)-1, 'ReturnOnError', false);
243 for block=2:length(startRow)
244     frewind(fileID);
245     dataArrayBlock = textscan(fileID, formatSpec, endRow(block)-startRow(
    block)+1, 'Delimiter', delimiter, 'MultipleDelimsAsOne', true, '
    HeaderLines', startRow(block)-1, 'ReturnOnError', false);
246     dataArray{1} = [dataArray{1};dataArrayBlock{1}];
247 end
248
249
250 %% Close the text file.
251 fclose(fileID);
252
253 %% Output variable.
254 A = [dataArray{1:end-1}];
255
256 end
```